

# SEISMIC BEHAVIOR OF SEMI-RIGID STEEL FRAMES

BY

HUSSAM N. MAHMOUD

DISSERTATION

Submitted in partial fulfillment of the requirements  
for the degree of Doctor of Philosophy in Civil Engineering  
in the Graduate College of the  
University of Illinois at Urbana-Champaign, 2011

Urbana, Illinois

Doctoral Committee:

Professor Amr S. Elnashai, Chair  
Professor Billie F. Spencer, Jr.  
Associate Professor Daniel A. Kuchma  
Assistant Professor Paramita Mondal

## ABSTRACT

The widespread and unexpected damage to welded connections during recent earthquakes led to the investigation of alternatives for the construction of steel frames in seismic areas. Bolted semi-rigid connections have been recognized as an attractive alternative to welded connections. However, existing knowledge on the behavior of the connection is either from testing of beam-to-column subassemblies under idealized load and boundary conditions, or from analytical studies. In addition, the system-level experimental behavior of semi-rigidly connected frames using real earthquake motions to conclusively verify the full potential of semi-rigidity (implying also partial-strength) in earthquake resistance application is lacking. To this end, an advanced hybrid simulation approach for the seismic assessment of steel frames with semi-rigid connections was proposed and successfully completed. Furthermore, nonlinear dynamic response-history analyses of semi-rigid frames with varying design parameters were conducted to evaluate the system performance under seismic events. The results of the hybrid simulation and the parametric studies are used to quantify various fundamental code parameters needed for the seismic design of structures.

The hybrid simulation included the most reliable, realistic, and computationally efficient experimental and analytical modules, which were developed and successfully integrated in a closed-loop system-level simulation. Three hybrid simulations were conducted on three different partial-strength semi-rigid frames with connection capacities that are a percentage of the plastic moment capacity of the beam ( $70\% M_{p_{beam}}$ ,  $50\% M_{p_{beam}}$ , and  $30\% M_{p_{beam}}$ ). The simulations utilized the large-scale Multi-Axial Full-Scale Sub-Structured Testing and Simulation (MUST-SIM) facility at the University of Illinois and included a full-scale physical specimen for the experimental module and a 2D finite element model for the analytical module. The experimental component consisted of a beam-column subassembly with top-and seat-angle with double web-angle connecting the beam to the column. The analytical component is an inelastic finite element model with the connections modeled using a refined 2D continuum elements that is capable of capturing all relevant deformation and inelastic features of the connection.

In addition to the hybrid simulation, nonlinear dynamic response-history analyses were conducted, on frames with three different connection capacities ( $70\% M_{p_{beam}}$ ,  $50\% M_{p_{beam}}$ , and

30%  $M_{p_{beam}}$ ), using a collection of ground motion records scaled to the maximum considered earthquake (MCE). The analyses were aimed at investigating the effect of varying different design parameters on the seismic response and period elongation of the frames. The design parameters, in addition to connection strength, included yield strength of the angle material, coefficient of friction between faying surfaces, and the amount of slip allowed in the connection.

The results of the hybrid simulation along with the analytical studies were used to evaluate more realistic fundamental code parameters needed for the seismic design of frames. The parameters included the equivalent damping ratio,  $\zeta_{eq}$ , the inelastic period of the structure,  $T_{inelastic}$ , and a demand-based force reduction factor,  $R_{demand}$ . The evaluated parameters can be used to better estimate the design base shear using a simplified design spectrum, allowing for safer and economical design of semi-rigid frames under seismic events.

## ACKNOWLEDGEMENTS

To begin, I would like to sincerely thank Professor Amr Elnashai, the Chair of my Ph.D. committee, for his technical guidance, understanding, and patience, during my graduate studies at the University of Illinois at Urbana-Champaign (UIUC). Most importantly, I want to thank him for his friendship, which often times was my source of motivation. Whenever I was feeling frustrated, he was always there to offer his guidance and encouragement. I was very fortunate to have him as an advisor, mentor, and a friend.

Thanks are due to Professor Bill Spencer for his support throughout my studies. My questions ranged from technical to philosophical, and although he was not my official advisor, he was always there to offer his valuable insight. I also want to thank Professor Dan Kuchma for his generosity in allowing our experimental work to fit in between his laboratory testing and for his help on answering many of my concrete questions while studying for the qualifying exam.

The work conducted would have not been possible without the support I received from many more individuals at UIUC. Particular thanks go to David Bennier, who supported me on this project and was a vital part of its success while working on his Master's degree at UIUC. I would also like to extend my gratitude to the MUST-SIM staff, Greg Pluta and Michael Bletzinger, for their support throughout the project. This project could have not been completed without the support of Tim Prunkard and the machine shop staff of the Newmark Laboratory. Useful advice and commentary was received from many UIUC graduate students to whom I am very grateful. Special thanks to Dr. Oh-Sung Kwon (currently at the University of Toronto, Canada), Dr. Sheng-Lin Lin (currently at the University of Canterbury, New Zealand), Do Soo Moon, and Dr. Sung-Jig Kim (currently at the University of Connecticut, USA) for their help with many tasks tied to the project. Thanks are also due to Dr. Dođramacı Aksoylar and Dr. Cenk Aksoylar (currently at Fatih Sultan Mehmet Vakif University, Turkey) for their valuable insight and comments.

I want to also thank my wife, Sarah, for being very supportive and understanding on all levels and for her willingness to do whatever it takes to help me finish my work. In times when things were rough, she was always by my side. Heartfelt thanks go to my parents, Nabil and Camilia,



and my brothers, Ahmed and Diaa, in Egypt who supported me beyond measure, both financially and through their encouragement.

I would like to dedicate my thesis to my daughters, Layla and Zeyna. They are the driving force behind my dreams and ambitions. I owe them both many nights of bedtime stories and countless trips to the park. I also want to dedicate my thesis to my father who had always dreamed that one of his children would grow to earn a Ph.D.

Most importantly, it is only through God's blessings where dreams ever come true. I owe my deepest gratitude to God for all his blessings.

I would like to also acknowledge the financial and logistical contributions of the Mid-America Earthquake (MAE) Center, a National Science Foundation (NSF) Engineering Research Center funded under grant EEC-9701785. This project is also supported, in part, by the George E. Brown, Jr. Network for Earthquake Engineering Simulation (NEES) Program of the NSF under Award Number CMMI-0927178.

# TABLE OF CONTENTS

LIST OF TABLES .....	x
LIST OF FIGURES .....	xii
CHAPTER 1 INTRODUCTION .....	1
1.1 Statement of the Problem.....	1
1.2 Objectives and Scope of Research .....	4
1.3 Organization of Dissertation .....	8
CHAPTER 2 BACKGROUND AND LITERATURE REVIEW .....	9
2.1 Introduction.....	9
2.2 Existing Models for Predicting the Characteristics of Connections .....	10
2.2.1 Mathematical Expressions .....	10
2.2.2 Finite Element Models.....	20
2.3 Analytical Investigation of Semi-rigid Frames.....	26
2.4 Code of Practice for the Seismic Design of Semi-rigid Connections .....	29
2.4.1 American Institute of Steel Construction (2005) .....	29
2.4.2 Eurocode 3 (2005).....	30
2.5 Summary and Conclusion .....	32
CHAPTER 3 HYBRID SIMULATION ENVIRONMENT .....	34
3.1 Introduction.....	34
3.2 Overview of Pseudo Dynamic Testing .....	35
3.3 The Must-SIM Facility .....	37
3.4 Description of the Structure .....	38
3.5 Analytical Module .....	39
3.5.1 Overview of the Model and Its Components .....	40
3.5.2 Approach for Modeling the Various Inelastic Features .....	42
3.5.2.1 Hot Rolling Residual Stresses.....	42
3.5.2.2 Bolt Pretension.....	45
3.5.2.3 Friction and Slip.....	47
3.5.2.4 Bearing, Bending, and Shearing Stiffness .....	49
3.5.2.5 Web Angle Idealization .....	52
3.5.3 Validation of the Analytical Model .....	53
3.6 Experimental Module.....	54
3.6.1 Test Specimen Configuration .....	54
3.6.2 Consideration for Column and Beam Length .....	55
3.6.3 Connection Topology.....	57
3.6.4 Test Matrix.....	59
3.6.5 Material Properties.....	60
3.6.6 Experimental Setup and Instrumentation.....	62

3.6.7	Control .....	65
3.6.7.1	Elastic Deformations of the LBCBs .....	65
3.6.7.2	Relative Deformation Approach .....	67
3.7	Integration of the Analytical and Experimental Modules .....	70
3.8	Selection of Ground Motion .....	71
3.8.1	Duration of Motion and Time Step .....	73
3.8.2	Record Scaling .....	74
3.9	Verification of the Sub-structuring Scheme .....	77
3.10	Summary and Conclusion .....	80
CHAPTER 4 SIMULATION RESULTS AND OBSERVATIONS .....		82
4.1	Introduction .....	82
4.2	Loading Scenario .....	83
4.2.1	Initial Stiffness Evaluation .....	83
4.2.2	Gravity Loading Stage .....	83
4.2.3	SPSD Tests with Selected Ground Motion .....	86
4.2.4	Cyclic Tests with Different Rotation Levels .....	87
4.3	Frame with 70% $M_{p_{beam}}$ under Earthquake Loading .....	89
4.3.1	Comparison with Analytical Predictions .....	89
4.3.2	Experimental Observations .....	95
4.3.2.1	Connection Slip .....	95
4.3.2.2	Localized Deformation .....	97
4.3.2.3	Relative Deformation of Beam with Respect to Column ...	100
4.4	Frame with 50% $M_{p_{beam}}$ under Earthquake Loading .....	102
4.4.1	Comparison with Analytical Predictions .....	102
4.4.2	Experimental Observations .....	107
4.4.2.1	Connection Slip .....	107
4.4.2.2	Localized Deformation .....	109
4.4.2.3	Relative Deformation of Beam with Respect to Column ...	111
4.5	Frame with 30% $M_{p_{beam}}$ under Earthquake Loading .....	112
4.5.1	Comparison with Analytical Predictions .....	112
4.5.2	Experimental Observations .....	117
4.5.2.1	Connection Slip .....	117
4.5.2.2	Localized Deformation .....	119
4.5.2.3	Relative Deformation of Beam with Respect to Column ...	121
4.6	Cyclic Tests .....	122
4.6.1	Experimental Observations (50% $M_{p_{beam}}$ ) .....	123
4.6.1.1	Connection Slip .....	123
4.6.1.2	Connection Deformation .....	124
4.6.1.3	Relative Deformation of Beam with Respect to Column ...	126
4.6.2	Experimental Observations (30% $M_{p_{beam}}$ ) .....	127
4.6.2.1	Connection Slip .....	127
4.6.2.2	Connection Deformation .....	129
4.6.2.3	Relative Deformation of Beam with Respect to Column ...	130
4.7	Summary and Conclusion .....	131

CHAPTER 5 INTERPRETATION OF RESULTS .....	137
5.1 Introduction.....	137
5.2 Comparison of Hybrid Simulation Results .....	138
5.2.1 Global Drift and Base Shear .....	138
5.2.2 Interstory Drift Ratio and Compliance with ASCE 41-06.....	141
5.2.3 Connection Slip.....	144
5.2.4 Connection Deformation.....	145
5.2.5 Moment-rotation Relationship .....	148
5.3 Comparison of Cyclic Test Results.....	153
5.3.1 Connection Slip.....	153
5.3.2 Moment-rotation Relationship .....	154
5.4 Summary and Conclusion .....	158
 CHAPTER 6 ANALYTICAL INVESTIGATION AND DESIGN IMPLICATIONS ..	162
6.1 Introduction.....	162
6.2 Description of the Selected Building Structure .....	164
6.3 Eigen Value Analysis and Fundamental Periods .....	165
6.4 Selection of Ground Motion Records .....	166
6.5 Investigation of Frame Response.....	170
6.5.1 Global Drift and Base Shear .....	170
6.5.2 Interstory Drift Ratio.....	176
6.6 Design Approach and Methodology .....	182
6.7 Determination of the Equivalent Damping Ratio, $\zeta_{eq}$ .....	185
6.8 Investigation of Period Elongation .....	190
6.8.1 Fourier Transformation.....	190
6.8.2 Short-time Fourier Transformation.....	193
6.8.3 Wavelet Transformation .....	198
6.9 Proposed Response Modification Factor (demand).....	207
6.10 Summary and Conclusion .....	209
 CHAPTER 7 CONCLUSIONS AND FUTURE RESEARCH REQUIREMENTS .....	212
7.1 Summary of Current Work .....	212
7.2 Summary of Findings.....	214
7.2.1 Hybrid Simulation.....	214
7.2.2 Cyclic Tests.....	215
7.2.3 Analytical Study of Semi-rigid and Rigid Frames.....	215
7.2.4 Design Implications .....	216
7.3 Future Research Requirements .....	217
 REFERENCES .....	221
 APPENDIX A. SPECIMEN DESIGN AND CONSTRUCTION .....	226
A.1 Building Configuration .....	226
A.2 Frame Strength and Drift per ASCE 7-02.....	227

APPENDIX B. INSTRUMENTATION PLANS ..... 243

## LIST OF TABLES

Table 2-1	Curve-fitting and standardization constants for Frye-Morris polynomial model ..11	11
Table 2-2	Empirical equations for shape parameters n (Richard and Abbott 1975).....13	13
Table 2-3	Connection parameters of the Chen-Lui exponential model (Chen 2000) .....15	15
Table 2-4	Pertinent data of Figure 2-3 (test ID 14S2) (Kishi, Ahmed et al. 2001).....24	24
Table 3-1	Summary of the geometrical parameters of the connections .....59	59
Table 3-2	Test matrix geometrical parameters.....59	59
Table 3-3	Test matrix loading parameters.....60	60
Table 3-4	Material properties of beam, column, and angles .....62	62
Table 3-5	Breakdown of the specimen and LBCBs sensors .....65	65
Table 3-6	Characteristics of the selected ground motions for the hybrid simulation.....72	72
Table 3-7	Initial stiffness, yield, and ultimate base shear from pushover analysis .....76	76
Table 4-1	Distributed gravity loads applied to the frames during the simulations .....83	83
Table 4-2	Ground motion characteristics and scale factor .....86	86
Table 5-1	Maximum absolute bolt slip in the top angles during the simulations .....140	140
Table 5-2	Maximum and normalized IDR .....144	144
Table 5-3	Maximum absolute bolt slip in the top angles during the simulations .....144	144
Table 5-4	Maximum absolute bolt slip in the seat angles during the simulations .....145	145
Table 5-5	Maximum absolute strain in the top angle during the simulations .....146	146
Table 5-6	Normalized maximum absolute strain in the top angle during the simulations...146	146
Table 5-7	Maximum absolute strain in the beam web during the simulations.....147	147
Table 5-8	Normalized maximum absolute strain in the beam web during the simulations .148	148
Table 5-9	Characteristics of the connections during the simulations.....152	152
Table 5-10	Maximum absolute bolt slip in the top angles during the cyclic tests .....153	153
Table 5-11	Maximum absolute bolt slip in the seat angles during the cyclic tests .....154	154
Table 5-12	Absolute mean maximum bolt slip in the top-and seat-angles for all tests .....154	154
Table 5-13	Characteristics of the connections during the cyclic tests .....157	157
Table 6-1	Varied design parameters used in the parametric studies .....162	162

Table 6-2	First three natural periods of the structures.....	166
Table 6-3	Characteristics of the ground motion records used in the parametric study .....	168
Table 6-4	Average maximum absolute response for a model under all ground motions.....	173
Table 6-5	Average maximum absolute response of all models under a given earthquake ..	175
Table 6-6	Average maximum absolute IDR for a model under all ground motions.....	176
Table 6-7	Average maximum absolute IDR of all models under a given earthquake .....	178
Table 6-8	Equivalent damping for all three semi-rigid frames .....	188
Table 6-9	Average inelastic period and percent period elongation for all frames .....	205
Table 6-10	Proposed average force reduction factor, $R_{demand}$ .....	209
Table A-1	Reactions resulting from ELF analysis .....	232

## LIST OF FIGURES

Figure 1-1	Fractured connection in a steel moment frame .....	1
Figure 1-2	Typical approach used for the seismic evaluation of steel frames.....	3
Figure 1-3	Proposed system-level approach for the seismic assessment of semi-rigid steel frames.....	6
Figure 2-1	Three-parameter power model, after: (Richard and Abbott 1975; Chen 2000).....	13
Figure 2-2	Mechanical model for top-and seat-angle with double web-angle connection, after: (Chmielowiec and Richard 1987) .....	19
Figure 2-3	Comparison between different modeling approaches, after: (Kishi, Ahmed et al. 2001) .....	23
Figure 2-4	Three-dimensional FEM for top-and seat-angle with double web-angle connection (Citipitioglu, Haj-Ali et al. 2002) .....	25
Figure 2-5	Moment-rotation curve defined in EC3 for top-and seat-angle connection, after: (Eurocode 3 1998).....	31
Figure 3-1	Plan view of the structure considered and an elevation of the SMRF .....	39
Figure 3-2	Overview of the analytical module .....	41
Figure 3-3	Measured hot-rolling residual stresses, after: (Nuttall and Adams 1970) .....	42
Figure 3-4	Recommended residual stress distribution per the Eurocode, after: (European Convention for Constructional Steelwork (ECCS) 1985) .....	43
Figure 3-5	Simulated residual stresses in the top-and seat-angles .....	44
Figure 3-6	Two-dimensional model with residual stress distribution .....	45
Figure 3-7	T-stub model accounting for the bolt action, after: (Coelho, Silva et al. 2004)....	46
Figure 3-8	Simulating typical bolt preload (a) without pretension (b) with pretension .....	47
Figure 3-9	Simulating typical connection slip behavior (a) without slip (b) with slip (c) force deformation during slipping (friction excluded).....	48
Figure 3-10	Test setup for a single bolt on a single plate, after: (Rex and Easterling 2003) ....	50
Figure 3-11	Illustrated arrangement of springs to account for the existence of two plates.....	51
Figure 3-12	Transverse connection stiffness with all shear resistance mechanisms .....	52
Figure 3-13	Idealization of the web angle including the equivalent strip model .....	53



Figure 3-14	Elevation view of the SMRF with red-dashed line representing the physical specimen to be tested .....	54
Figure 3-15	Elevation view of the physical specimen with its final dimensions .....	56
Figure 3-16	Detailed geometry of the semi-rigid connections .....	58
Figure 3-17	Geometrical parameters of the connection, <i>after</i> : (Leon, Wan Hu et al. 2004).....	58
Figure 3-18	Tensile Testing of coupons specimens .....	61
Figure 3-19	Display of computer monitors used during testing .....	63
Figure 3-20	Overview of the experimental setup .....	63
Figure 3-21	Small-scale testing facility including the rubber and steel specimens used for control verification.....	66
Figure 3-22	Concept of relative deformation used to map the three-point information to two-point information and vice-versa .....	68
Figure 3-23	A snap shot of the LBCB plugin used during the simulation .....	69
Figure 3-24	Schematic of the hybrid simulation approach.....	71
Figure 3-25	Acceleration elastic response spectra with 2% damping of the selected records ..	72
Figure 3-26	Loma Prieta acceleration time-history record with time step of 0.005 seconds ....	73
Figure 3-27	Loma Prieta acceleration time-history record with time step of 0.02 seconds .....	74
Figure 3-28	Elastic spectral acceleration of the original and modified records .....	74
Figure 3-29	Pushover results for rigid and semi-rigid frames.....	75
Figure 3-30	Relationship between the strength of the connection and the beam, <i>after</i> :(American Institute of Steel Construction (AISC) 2005).....	77
Figure 3-31	Sub-structured analytical models for the 30% $M_{p_{beam}}$ frame with blue box enclosing the model representing the experimental component .....	78
Figure 3-32	Complete analytical model of the 30% $M_{p_{beam}}$ frame used for comparison against SPSD analytical simulation .....	78
Figure 3-33	Roof displacement comparison between the sub-structured and full ABAQUS model.....	79
Figure 4-1	Localized connection deformation due to gravity load application ( <i>deformation scale is set to 100x</i> ).....	85
Figure 4-2	Deformed shape of the analytical module due to gravity loading ( <i>deformation scale of the analytical module is set to 100x</i> ) .....	86
Figure 4-3	Motion path of LBCB2 during the cyclic tests .....	87

Figure 4-4	Deformation commands imposed at the LBCB connected to the beam end to achieve the desired connection rotation during the cyclic tests .....	89
Figure 4-5	Second-story displacement comparison between the hybrid simulation and the analytical predictions for the 70% $M_{p_{beam}}$ specimen .....	90
Figure 4-6	First-story displacement comparison between the hybrid simulation and the analytical predictions for the 70% $M_{p_{beam}}$ specimen .....	91
Figure 4-7	Base shear comparison between the hybrid simulation and the analytical predictions for the 70% $M_{p_{beam}}$ specimen .....	92
Figure 4-8	Rotation comparison between the hybrid simulation and the analytical predictions for the 70% $M_{p_{beam}}$ specimen .....	94
Figure 4-9	Moment comparison between the hybrid simulation and the analytical predictions for the 70% $M_{p_{beam}}$ specimen .....	95
Figure 4-10	Slip of the top angle bolts relative to the top beam flange during the hybrid simulation of the 70% $M_{p_{beam}}$ frame .....	96
Figure 4-11	Slip of the bottom angle bolts relative to the bottom beam flange during the hybrid simulation of the 70% $M_{p_{beam}}$ frame .....	97
Figure 4-12	Deformation of the specimen during the hybrid simulation of the 70% $M_{p_{beam}}$ frame .....	98
Figure 4-13	Strain measurements in the top angle legs connected to the beam flange and column flange during the hybrid simulation of the 70% $M_{p_{beam}}$ frame.....	99
Figure 4-14	Localized strain in the beam web measured by the rectangular rosette gauges during the hybrid simulation of the 70% $M_{p_{beam}}$ frame.....	100
Figure 4-15	Rrelative rotation measurements between the beam and column during the hybrid simulation of the 70% $M_{p_{beam}}$ frame .....	102
Figure 4-16	Second-story displacement comparison between the hybrid simulation and the analytical predictions for the 50% $M_{p_{beam}}$ specimen .....	103
Figure 4-17	First-story displacement comparison between the hybrid simulation and the analytical predictions for the 50% $M_{p_{beam}}$ specimen .....	104
Figure 4-18	Base shear comparison between the hybrid simulation and the analytical predictions for the 50% $M_{p_{beam}}$ specimen .....	105
Figure 4-19	Rotation comparison between the hybrid simulation and the analytical predictions for the 50% $M_{p_{beam}}$ specimen .....	106
Figure 4-20	Moment comparison between the hybrid simulation and the analytical predictions for the 50% $M_{p_{beam}}$ specimen .....	106
Figure 4-21	Slip of the top angle bolts relative to the top beam flange during the hybrid simulation of the 50% $M_{p_{beam}}$ frame .....	108

Figure 4-22	Slip of the seat angle bolts relative to the bottom beam flange during the hybrid simulation of the 50% $M_{p_{beam}}$ frame.....	108
Figure 4-23	Deformation of the specimen during the hybrid simulation of the 50% $M_{p_{beam}}$ frame .....	109
Figure 4-24	Strain measurements in the top angle legs connected to the beam flange and column flange during the hybrid simulation of the 50% $M_{p_{beam}}$ frame.....	110
Figure 4-25	Localized strain in the beam web measured by the rectangular rosette gauges during the hybrid simulation of the 50% $M_{p_{beam}}$ frame.....	110
Figure 4-26	Relative rotation measurements between the beam and column during the hybrid simulation of the 50% $M_{p_{beam}}$ frame .....	112
Figure 4-27	Second-story displacement comparison between the hybrid simulation and the analytical predictions for the 30% $M_{p_{beam}}$ specimen.....	113
Figure 4-28	First-story displacement comparison between the hybrid simulation and the analytical predictions for the 30% $M_{p_{beam}}$ specimen.....	114
Figure 4-29	Base shear comparison between the hybrid simulation and the analytical predictions for the 30% $M_{p_{beam}}$ specimen .....	115
Figure 4-30	Rotation comparison between the hybrid simulation and the analytical predictions for the 30% $M_{p_{beam}}$ specimen .....	116
Figure 4-31	Moment comparison between the hybrid simulation and the analytical predictions for the 30% $M_{p_{beam}}$ specimen .....	116
Figure 4-32	Slip of the top angle bolts relative to the top beam flange during the hybrid simulation of the 30% $M_{p_{beam}}$ frame .....	118
Figure 4-33	Slip of the seat angle bolts relative to the bottom beam flange during the hybrid simulation of the 30% $M_{p_{beam}}$ frame .....	118
Figure 4-34	Deformation of the specimen during the hybrid simulation of the 30% $M_{p_{beam}}$ frame .....	119
Figure 4-35	Strain measurements in the top angle legs connected to the beam flange and column flange during the hybrid simulation of the 30% $M_{p_{beam}}$ frame.....	120
Figure 4-36	Localized strain in the beam web measured by the rectangular rosette gauges during the hybrid simulation of the 30% $M_{p_{beam}}$ frame.....	120
Figure 4-37	Relative deformation measurements between the beam and column during the hybrid simulation of the 30% $M_{p_{beam}}$ frame .....	122
Figure 4-38	Slip of the top angle bolts relative to the top beam flange during the post-earthquake cyclic testing of the 50% $M_{p_{beam}}$ connection .....	123
Figure 4-39	Slip of the seat angle bolts relative to the bottom beam flange during the post-earthquake cyclic testing of the 50% $M_{p_{beam}}$ connection .....	124

Figure 4-40	Deformation of the specimen during the post-earthquake cyclic testing of the 50% $M_{p_{beam}}$ connection.....	125
Figure 4-41	Shear failure of bolt 2 including failure surface characterized by shear lips during cyclic testing of the 50% $M_{p_{beam}}$ connection.....	125
Figure 4-42	Shear failure of bolt 4 including failure surface characterized by shear lips during cyclic testing of the 50% $M_{p_{beam}}$ connection.....	126
Figure 4-43	Relative deformation measurements between the beam and column during the post-earthquake cyclic testing of the 50% $M_{p_{beam}}$ connection.....	127
Figure 4-44	Slip of the top angle bolts relative to the top beam flange during the post-earthquake cyclic testing of the 30% $M_{p_{beam}}$ connection.....	128
Figure 4-45	Slip of the seat angle bolts relative to the bottom beam flange during the post-earthquake cyclic testing of the 30% $M_{p_{beam}}$ connection.....	129
Figure 4-46	Deformation of the specimen during the post-earthquake cyclic testing of the 30% $M_{p_{beam}}$ connection.....	130
Figure 4-47	Relative deformation measurements between the beam and column during the post-earthquake cyclic testing of the 30% $M_{p_{beam}}$ connection.....	131
Figure 5-1	Comparison of the second-story displacement between all three frames during the hybrid simulations.....	139
Figure 5-2	Comparison of the first-story displacement between all three frames during the hybrid simulations.....	139
Figure 5-3	Comparison of the base shear between all three frames during the hybrid simulations.....	140
Figure 5-4	Comparison of the maximum interstory drift ratios between all three frames during the hybrid simulations.....	141
Figure 5-5	Comparison between the response spectrum of all three frames and the DBE and MCE spectrum of ASCE 41-06.....	143
Figure 5-6	Comparison between the moment-rotation relationships derived using the linear pots and the inclinometers resulting from the hybrid simulation of the 70% $M_{p_{beam}}$ frame.....	149
Figure 5-7	Comparison between the moment-rotation relationships derived using the linear pots and the inclinometers resulting from the hybrid simulation of the 50% $M_{p_{beam}}$ frame.....	149
Figure 5-8	Comparison between the moment-rotation relationships derived using the linear pots and the inclinometers resulting from the hybrid simulation of the 30% $M_{p_{beam}}$ frame.....	150

Figure 5-9	Comparison between the moment-rotation relationships derived using the linear pots resulting from the hybrid simulation of all three frames.....	151
Figure 5-10	Comparison between the moment-rotation relationships derived using the linear pots and the inclinometers resulting from cyclic testing of the 50% $M_{p_{beam}}$ connection.....	155
Figure 5-11	Comparison between the moment-rotation relationships derived using the linear pots and the inclinometers resulting from cyclic testing of the 30% $M_{p_{beam}}$ connection.....	155
Figure 5-12	Comparison between the moment-rotation relationships derived using the linear pots resulting from the hybrid simulation of all 50% $M_{p_{beam}}$ and 30% $M_{p_{beam}}$ connections.....	156
Figure 6-1	Linear kinematic hardening material model used in the parametric study.....	163
Figure 6-2	First three mode shape of vibrations for the 30% $M_{p_{beam}}$ frame (typical for the other two frames).....	165
Figure 6-3	Scaled records used in the parametric studies.....	169
Figure 6-4	Response spectra of the scaled records.....	169
Figure 6-5	Influence of connection flexibility on the fundamental period of vibration for frames with varying heights (Elnashai and Di Sarno 2008).....	171
Figure 6-6	Roof displacement response of the 50% $M_{p_{beam}}$ frame to the 1989 Loma Prieta earthquake (LP-CLS).....	172
Figure 6-7	Average maximum absolute response with varying design parameters under all ground motions.....	173
Figure 6-8	Average maximum absolute base shear and displacement from the dynamic analyses superimposed on the pushover results.....	175
Figure 6-9	Average maximum absolute IDR ratios with varying design parameters under all ground motions.....	177
Figure 6-10	IDR for the 70% $M_{p_{beam}}$ frame.....	179
Figure 6-11	IDR for the 50% $M_{p_{beam}}$ frame.....	180
Figure 6-12	IDR for the 30% $M_{p_{beam}}$ frame.....	181
Figure 6-13	Design elastic response spectrum, <i>after</i> : (American Society of Civil Engineers (ASCE 7-05) and Structural Engineering Institute (SEI) 2005).....	182
Figure 6-14	Schematic of the dissipated energy, $E_D$ , in a cycle of harmonic vibration and the strain energy, $E_{so}$ , <i>after</i> : (Chopra 2006).....	186
Figure 6-15	Cyclic response of the semi-rigid frames.....	188

Figure 6-16	Variation of ductility and damping ratio with peak ground acceleration, <i>after</i> : (Parulekar, Vaity et al. 2004).....	189
Figure 6-17	FFT of the roof acceleration response of the 30% $M_{p_{beam}}$ frame under the 1979 Imperial Valley earthquake (IV-HBCR).....	192
Figure 6-18	FFT of the roof acceleration response of the 30% $M_{p_{beam}}$ frame under the 1989 Loma Prieta earthquake (LP-CLS) .....	193
Figure 6-19	Spectrogram of the roof acceleration response of the 30% $M_{p_{beam}}$ frame under the 1989 Loma Prieta earthquake (LP-CLS) .....	195
Figure 6-20	Roof displacement response of the 30% $M_{p_{beam}}$ frame under the 1989 Loma Prieta earthquake (LP-CLS).....	196
Figure 6-21	A Zoom in image of the Spectrogram of the roof acceleration response of the 30% $M_{p_{beam}}$ frame under the 1989 Loma Prieta earthquake (LP-CLS).....	197
Figure 6-22	Three-dimensional spectrogram of the roof acceleration response of the 30% $M_{p_{beam}}$ frame under the 1989 Loma Prieta earthquake.....	198
Figure 6-23	Wavelet scalograms (left) and instantaneous frequency (right) of the roof acceleration response of the 30% $M_{p_{beam}}$ frame under the 1989 Loma Prieta earthquake .....	200
Figure 6-24	Instantaneous period of the structural response of the 30% $M_{p_{beam}}$ frame under the 1989 Loma Prieta earthquake .....	201
Figure 6-25	Extracted instantaneous fundamental period of the structural response of the 30% $M_{p_{beam}}$ frame under the 1989 Loma Prieta earthquake (LP-CLS).....	203
Figure 6-26	FFT of the roof acceleration response of the 30% $M_{p_{beam}}$ frame under the 1989 Loma Prieta earthquake (LP-CLS) showing the predominate mode two response and the average of the elongated first mode period .....	203
Figure 6-27	Scalogram (left) and instantaneous period of the structural response (right) of the 30% $M_{p_{beam}}$ frame under the 1994 Northridge earthquake (NR-LOS) .....	204
Figure 6-28	Scalogram (left) and instantaneous period of the structural response (right) of the 70% $M_{p_{beam}}$ frame under the 1995 Kobe earthquake (KB-SHI) .....	204
Figure 6-29	Ratio of the elastic to the inelastic period as a function of connection strength..	207
Figure A-1	Plan and side view of the building including the SMRF .....	226
Figure A-2	Design elastic response spectrum .....	228
Figure A-3	Distribution of base shear along the height to check columns and connections yielding using SAP2000 .....	231
Figure A-4	Distribution of base shear along the height to check drift using SAP2000 .....	233

# CHAPTER 1

## INTRODUCTION

### 1.1 Statement of the Problem

The integrity of fully-welded connections under earthquake loading has come under question because many steel and composite buildings suffered severe damage in connections during the Northridge (1994), and Hyogo-ken Nanbu (1995) earthquakes. Post-earthquake visual assessments revealed that numerous cracks were developed in the welded beam-to-column joints of steel frames. The damage was caused by the use of low toughness welds combined with a number of other connection detailing, material properties, and construction practices that were typical prior to the earthquake (SAC 2000). The cracks originated in the heat-affected zone of the weld and propagated in the flange and the web of the columns as shown in Figure 1.



Figure 1-1 Fractured connection in a steel moment frame

Interest in utilizing bolted connections in steel constructions in seismic areas has significantly increased as a result of the uncertain and often-inferior performance of welded connections during the earthquakes. With their lower construction costs and simple fabrication process, bolted partial-strength semi-rigid connections were evaluated as a viable alternative and their fundamental characteristics were assessed both experimentally and analytically. The common types of bolted semi-rigid connections include extended endplate connection, T-stub connection, and top-and seat-angle with double web-angle connection.

The advantages of utilizing semi-rigid connections in the construction of steel frames have been widely recognized, especially in Europe. Extensive work has been conducted by a number of researchers on the different types of bolted semi-rigid connections to assess their fundamental characteristics. Of specific interest in this project is the seismic behavior of top-and seat-angle with double web-angle connections. The cyclic behavior of the connection was evaluated through testing of beam-column subassemblies and the results demonstrated its large energy absorption capabilities with stable hysteretic behavior (Azizinamini and Radziminski 1989). In addition, 3D analytical models aimed at capturing the complicated behavior of this type of connection such as slip, friction between surfaces in contact and prying action were also investigated (Kishi, Ahmed et al. 2001) and (Citipitioglu, Haj-Ali et al. 2002).

The previously conducted experimental and analytical studies were aimed at assessing the behavior of the connection on component level bases. Assessment of the performance of whole structural system in a global frame analysis is then conducted using idealized action-deformation relationships obtained from the experimental results



or the finite element models. The drawback of using such approach is that idealizing the action-deformation relationships does not represent the true behavior of the connection and will result in an inaccurate assessment of frame response. Furthermore, the interaction between the beam and column flanges and the angles comprising the connection is not captured. Such interaction is essential as it influences the onset and spread of yielding in the beam and column, the ductility demand on the joint, and the global behavior of the structural system. Figure 1-2 shows the typical approach used for evaluating steel frames under seismic loading conditions.

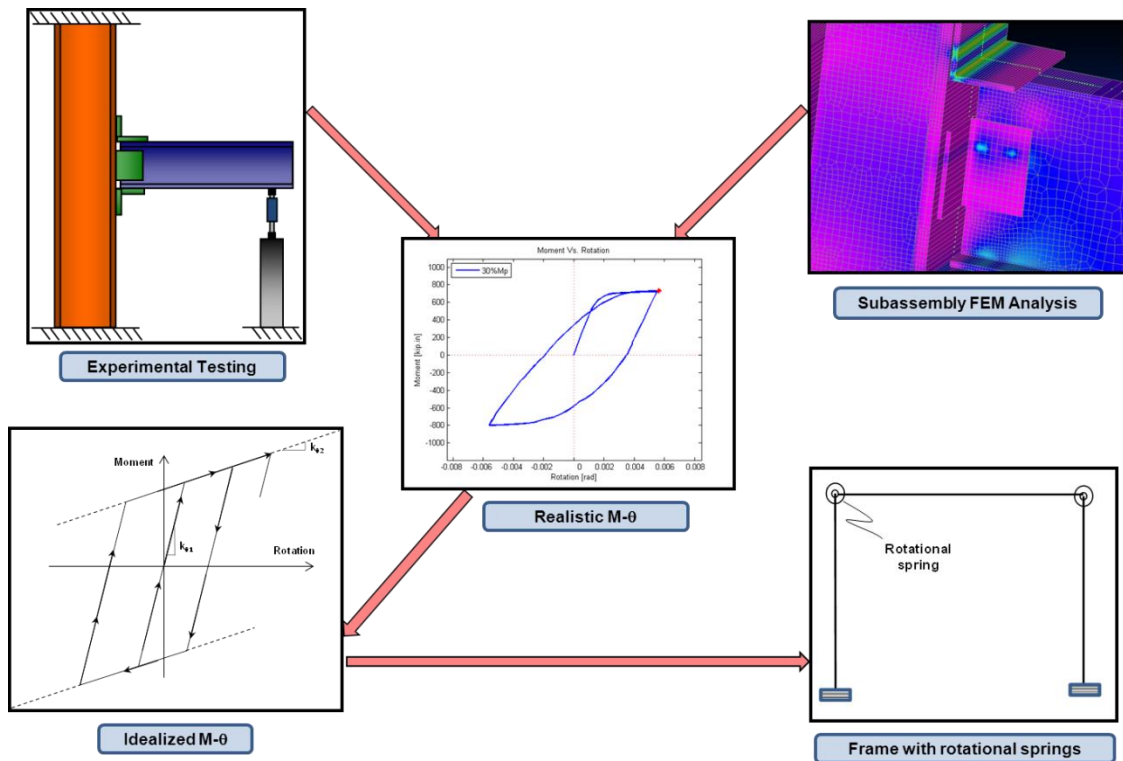


Figure 1-2 Typical approach used for the seismic evaluation of steel frames

Even from an economical point of view, utilizing semi-rigid connections for the construction of steel frames could lead to significant savings, particularly on erection cost.

Estimates from fabricators suggest about a 30% decrease in erection times, leading to less crane and labor time, and most importantly less trades on the job site (Barry 2004). In addition, since the connections are considered as the main energy dissipating elements of the structure, column overdesign could be eliminated by ignoring the strong-column weak-beam design criteria, which will lead to saving on material.

This research presents new system-level approach for the seismic assessment of steel frames with top-and seat-angle with double web-angle connections using hybrid simulation. In addition, nonlinear response history analysis is utilized in a parametric study to investigate the effect of various connection design parameters; including the yield strength of the angles, the coefficient of friction between surfaces, and the magnitude of bolt slip allowed, on the seismic behavior of semi-rigid steel frames. The implication of the results of the parametric study on the seismic response of semi-rigid frames is quantified through the determination of three main code-based design parameters including the equivalent damping ( $\zeta_{eq}$ ), the inelastic period ( $T_{inelastic}$ ), and the demand-based force reduction factor ( $R_{demand}$ ). The three fundamental design parameters can be used to construct a simplified design spectrum from which design base shear can be estimated more realistically to reflect actual forces likely to be experienced by the structure when subjected to a particular ground motion.

## **1.2 Objectives and Scope of Research**

As previously discussed, prior research aimed at investigating the potential use of semi-rigid connections in the construction of steel frames in seismic zones has been

conducted on a component level by assessing the behavior of a beam-column subassembly either experimentally or analytically. The moment-rotation relationship characterizing the connection behavior is then represented using idealized springs at the beam-to-column intersections in frame analysis. Idealizations of the connection behavior leads to inaccurate assessment of frame response as many of the inelastic features of the connections are not precisely represented including for example slip and pinching effects. Moreover, the effect of the interaction between the connecting elements including localized deformations and yielding in the beam or column, prying actions, and bolt-hole ovalization on the global frame behavior is not accounted for.

To make a near-fully realistic assessment of the demands upon and performance of semi-rigid steel frames that are subjected to seismic loadings, with a focus on the effect of top-and seat-angle double web-angle connection details. It was not possible to make such an assessment in the past due to limitations in experimental testing facilities and integrated analytical-experimental approaches. The research conducted in this project was made possible through the use of an expansion upon the unique hybrid-simulation testing capabilities that are part of the University of Illinois MUST-SIM facility.

In addition to conducting hybrid simulations, the scope of work includes conducting nonlinear dynamic response-history analyses on frames with varying design parameters using a collection of ground motion records. The results of the hybrid simulations along with the analytical studies are used to accurately predict fundamental code-based design parameters needed for constructing the design response spectrum. Accurate predictions of the code parameters allows for more realistic estimate of the design base shear whereby frame design to resist earthquake forces can be conducted in a

controlled and economical manner that has not been hitherto available. The proposed system-level Framework is illustrated in Figure 1-3.

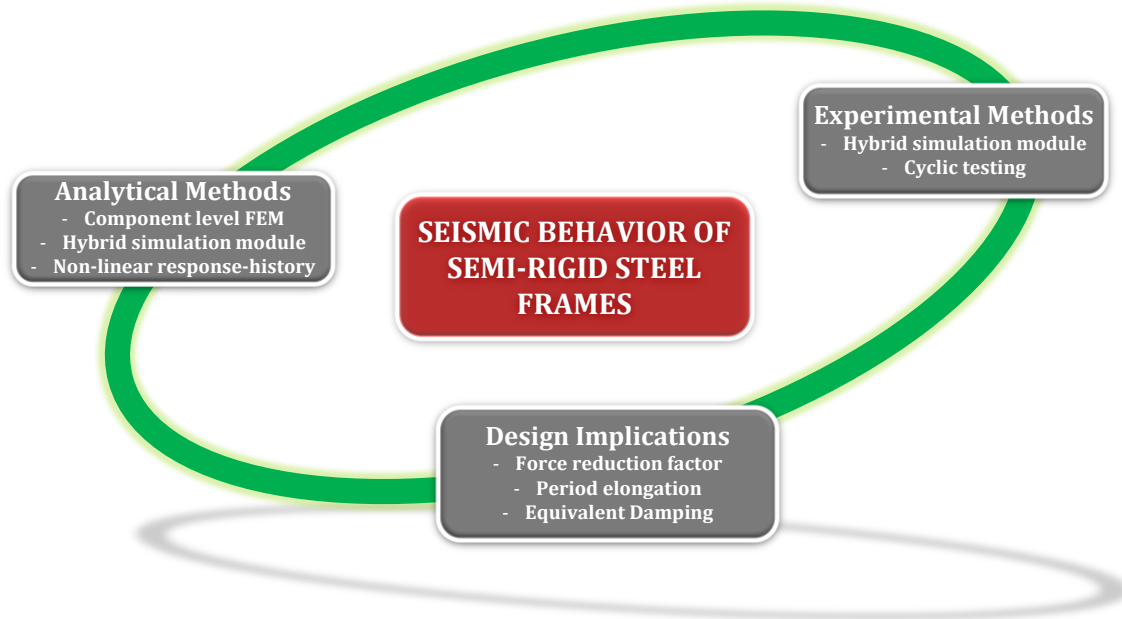


Figure 1-3 Proposed system-level approach for the seismic assessment of semi-rigid steel frames

Realizing the above objective requires the following tasks and subtasks to be accomplished:

- Task1: Conduct Comprehensive Literature Review
  
- Task2: Develop and Integrate the Hybrid Simulation Modules
  - Develop detailed analytical 2D finite element model capable of capturing the inelastic features of the connection
  - Develop an experimental beam-column setup with realistic loading and boundary conditions and dense instrumentation array
  - Conduct static pushover analysis
  - Select the ground motion record to be used in the simulations
  - Scale the record using the pushover analysis results

- Integrate the experimental and analytical modules in a closed-loop hybrid simulation
- Task3: Discuss the Simulation and Experimental Results
  - Conduct three independent full-scale simulations with varying connection capacities
  - Perform post-simulation cyclic tests of beam-column subassembly to quantify the residual characteristics of the connections after being subjected to an earthquake
  - Evaluate the effect of localized inelastic connection behavior on the resulting moment-rotation relationship
  - Evaluate the effect of the moment-rotation relationship on the global performance of the structure
- Task4: Interpret the Results
  - Perform comparison of the sub-structured pseudo-dynamic test results
  - Compare frame responses
  - Compare cyclic test results
- Task5: Conduct Analytical Investigation of Frame Response
  - Select an ensemble of ground motions
  - Conduct dynamic response-history analysis
- Task6: Investigate the Implication of the Analytical Study on the Seismic Design of Semi-rigid Steel Frames
  - Evaluate the equivalent damping ratio,  $\zeta_{eq}$
  - Assess and develop an equation to quantify the period elongation of the frame as a function of connection strength ( $T_{inelastic} = f(\%M_{p_{beam}})$ )
  - Determine the force-reduction factor,  $R$ , used in constructing the inelastic response spectrum

### **1.3 Organization of Dissertation**

A new approach for utilizing hybrid simulation to conduct system-level assessment of semi-rigid steel frames with top-and seat-angle with double web-angle connections are developed and implemented. Three hybrid simulations are successfully executed whereby an analytical and experimental module are integrated and subjected to a ground motion while taking into account the interaction at the interfaces of the two modules. The simulations are conducted using the state-of-the-art equipment at the MUST-SIM facility at the University of Illinois, part of the Network for Earthquake Engineering Simulation (NEES).

This dissertation includes seven different chapters. Chapter 1 introduces the problem statement and objective of this research. Chapter 2 discusses background and literature review in reference to evaluating semi-rigid connections with top-and seat angle with double web-angle connections and the seismic assessment of semi-rigid frames. Chapter 3 focuses on the development of the analytical and experimental modules and their integration in the hybrid simulations. Chapter 4 is an overview of the simulation and experimental results and discusses both the global behavior of the frames as well as the local behavior of the connection. Chapter 5 presents interpretation and comparison of results for the hybrid simulations and cyclic tests. Chapter 6 concentrates on the analytical investigation of frame response, with varying design parameters, using a collection of ground motion records. The implication of the analytical results on the seismic design of semi-rigid frames is investigated through assessing code-based parameters needed for constructing the design response spectrum. Chapter 7 summarizes the findings from current work followed by future research requirements.

## **CHAPTER 2**

### **BACKGROUND AND LITERATURE REVIEW**

#### **2.1 Introduction**

Post Northridge and Kobe earthquakes, alternative construction solutions for semi-rigid steel frames in seismic zones were heavily investigated. Design solutions were sought that would allow for ductility in all the connecting elements, as well as redundancy in failure modes. Due to their easy field installation, high ductility characteristics, and inherent redundancy, bolted connections were recognized as a viable solution to the seismic design of steel frames.

The literature review presented herein provides an introduction to the fundamental knowledge in moment-rotation relationship of connections while highlighting the models developed to represent and predict the characteristics of the connections. In addition to highlighting research conducted at the component level, research conducted on the performance of semi-rigid steel frames is then presented. The final section of this chapter represents the current code of practice for the design of semi-rigid connections with top-and seat-angle with double web-angle connections.

Major research on experimental testing of semi-rigid connections will not be the focus of the literature review. However, it is worth noting that various experimental programs were carried out to monotonically and cyclically test connections on component level basis. In all the tests, the beam was loaded with an actuator while the column was kept fixed. Early work on testing welded beam-to-beam and beam-to-column

connection using double web angle and top and seat angle connections was conducted by Johnson and Green (1940). In these tests, the connections sustained moment at a rotation of three times more than the full simple beam rotation was reached. Many other studies on semi-rigid connections included monotonic, cyclic, and dynamic loading carried out (Popov and Bertero 1973; Kukreti, Murray et al. 1987; Azizinamini and Radziminski 1989; Nader and Astaneh-Asl 1996; Sarraf and Bruneau 1996). The behavior of the connections was highlighted by “fat” and stable hysteretic behavior with high energy dissipation capabilities.

## **2.2 Existing Models for Predicting the Characteristics of Connections**

As previously mentioned, much research has been conducted to investigate and predict moment-rotation relationships of semi-rigid connections. The work included mathematical expressions comprising curve-fitting models, simplified analytical models, and mechanical models. Furthermore, detailed 3D finite element models were developed to capture the complex behavior of the connections. Description of the developed models and their distinct features are listed below.

### **2.2.1 Mathematical Expressions**

Mathematical models provide the ability to approximate the moment-rotation behavior of connections without the need for testing. Early models developed included curve fitting of test data using regression analysis. Frye and Morris (1975) proposed an odd-power polynomial empirical model whereby the rotation is expressed as a function of moment and other curve-fitting parameters. Curves are fitted to available experimental



data of connections subjected to monotonic loadings and the resulting  $M-\theta$  relationship is expressed as follows:

$$\theta_r = C_1(KM)^1 + C_2(KM)^3 + C_3(KM)^5 \quad (2.1)$$

Where  $M$  and  $\theta_r$  are the moment and rotation, respectively;  $C_1$ ,  $C_2$ , and  $C_3$  are curve-fitting parameters;  $K$  is a standardized parameter which is a function of important geometrical parameters such as the size of the connecting member and plate thickness. The curve fitting and standardization constants are listed in Table 2-1 below.

Table 2-1 Curve-fitting and standardization constants for Frye-Morris polynomial model

Connection types	Curve-fitting constants	Standardization constants
Single-web angle Connection	$C_1 = 4.28 \times 10^{-3}$ $C_2 = 1.45 \times 10^{-9}$ $C_3 = 1.51 \times 10^{-16}$	$K = d^{-2.4} \cdot t^{-1.18} \cdot g^{0.15}$
Double-web angle Connection	$C_1 = 3.66 \times 10^{-4}$ $C_2 = 1.15 \times 10^{-6}$ $C_3 = 4.57 \times 10^{-8}$	$K = d^{-2.4} \cdot t^{-1.18} \cdot g^{0.15}$
Top-and seat-angle - angle connection	$C_1 = 8.46 \times 10^{-4}$ $C_2 = 1.01 \times 10^{-4}$ $C_3 = 1.24 \times 10^{-8}$	$K = d^{-1.5} \cdot t^{-0.5} \cdot l^{-0.7} \cdot d_b^{-1.1}$
Top-and seat-angle - angle with double web-angle connection	$C_1 = 2.23 \times 10^{-5}$ $C_2 = 1.85 \times 10^{-8}$ $C_3 = 3.19 \times 10^{-12}$	$K = d^{-1.287} \cdot t^{-1.128} \cdot t^{-0.415} \cdot l^{-0.694} \cdot (g-d_b/2)^{1.350}$
End-plate connection with column stiffener	$C_1 = 1.79 \times 10^{-3}$ $C_2 = 1.76 \times 10^{-4}$ $C_3 = 2.04 \times 10^{-4}$	$K = d^{-2.4} \cdot t^{-0.6}$
T-stud Connection	$C_1 = 2.1 \times 10^{-4}$ $C_2 = 6.2 \times 10^{-6}$ $C_3 = -7.6 \times 10^{-9}$	$K = d^{-1.5} \cdot t^{-0.5} \cdot f^{1.1} \cdot l^{-0.7}$
Header-plate Connection	$C_1 = 5.1 \times 10^{-5}$ $C_2 = 6.2 \times 10^{-10}$ $C_3 = 2.4 \times 10^{-13}$	$K = t^{-1.6} \cdot g^{1.6} \cdot d^{-2.3} \cdot w^{0.5}$

The work also included proposed equations to predict the connection tangent stiffness,  $S_c$  and the initial stiffness,  $S_c^o$ , given by:

$$S_c = \frac{dM}{d\phi_c} = \frac{1}{C_1K + 3C_2K(KM)^2 + 5C_3K(KM)^4} \quad (2.2)$$

$$S_c^o = \left. \frac{dM}{d\phi_c} \right|_{M=0} = \frac{1}{C_1K} \quad (2.3)$$

The model has been noted by other researchers to represent the moment-rotation relationship reasonably well. The main drawback of this model is its prediction of negative tangent stiffness when the derivative of the polynomial function is taken within specific ranges since a polynomial function is characterized by peaks and valleys.

Richard and Abbott (1975) proposed a three-parameter power model to represent the moment-rotation behavior of the connection under monotonic loading. The model is represented by the following equation:

$$M = \frac{R_{ki}\theta_r}{\left[1 + \left(\frac{\theta_r}{\theta_0}\right)^n\right]^{1/n}} \quad (2.4)$$

Where  $R_{ki}$  is the initial connection stiffness;  $n$  is the shape parameter;  $\theta_0 = M_u/R_{ki}$  is the reference plastic rotation; and  $M_u$  is the ultimate moment capacity. Empirical equations for calculating the shape parameter  $n$  are listed in Table 2-2. The resulting moment-rotation curves for different values of  $n$  are shown in Figure 2-1.

Table 2-2 Empirical equations for shape parameters n (Richard and Abbott 1975)

Type No.	Connection types		N
I	Single web-angle connection	0.520	$\log_{10} \theta_0 > -3.073$
		0.695	$< -3.073$
II	Double web-angle connection	1.322	$\log_{10} \theta_0 > -2.582$
		0.573	$< -2.582$
III	Top- and seat-angle connection (without double web-angle)	1.398	$\log_{10} \theta_0 > -2.721$
		0.827	$< -2.721$
IV	Top- and seat-angle connection (with double web-angle)	2.003	$\log_{10} \theta_0 > -2.880$
		0.302	$< -2.880$

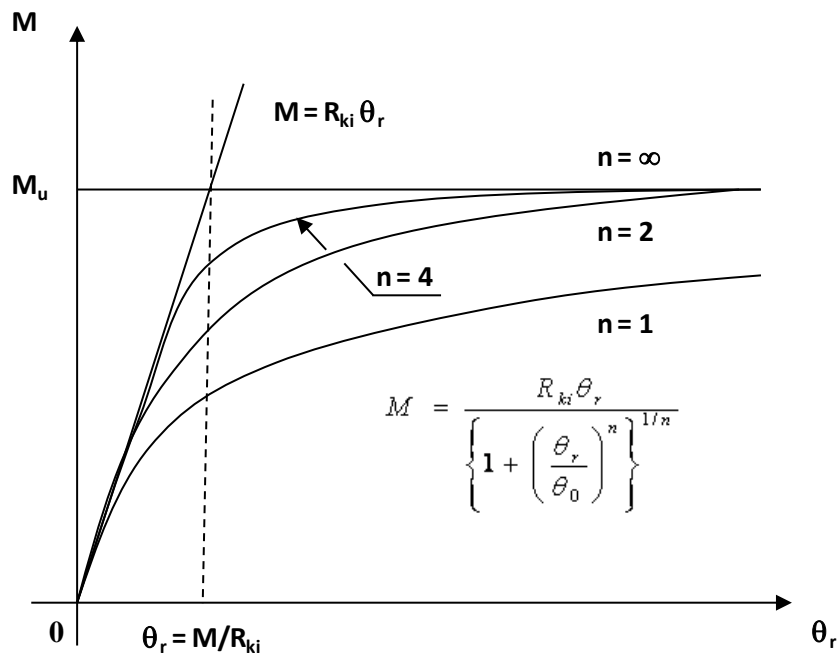


Figure 2-1 Three-parameter power model, after: (Richard and Abbott 1975; Chen 2000)

Since the tangent stiffness of the connection,  $R_k$  and the relative rotation  $\theta_r$  can be determined directly without iterations; this model is considered an effective tool for conducting a second-order nonlinear structural analysis. Unlike the Frye and Morris's model, however, this model requires a prior knowledge of the connection initial stiffness

and ultimate moment capacity for a complete prediction of the moment-rotation response of the connection. Therefore, its prediction of the response depends on two essential values that must be predicted by another tool or model.

$$R_k = \frac{dM}{d\theta_r} = \frac{R_{ki}}{\left[1 + \left(\frac{\theta_r}{\theta_0}\right)^n\right]^{(n+1)/n}} \quad (2.5)$$

To alleviate the problem with Frye and Morris's model associated with the prediction of negative tangent connection stiffness when the derivative of the polynomial function is taken within specific ranges, Ang and Morris (1984) proposed the use of a standardized Ramberg-Osgood model to express the moment-rotation behavior of five typical types of connections including single web angle, double web-angle, header plate, top-and seat-angle, and the strap angle connections. The proposed model is in the following form:

$$\frac{\theta}{\theta_0} = \frac{(KM)}{(KM)_0} \left[ 1 + \left[ \frac{KM}{(KM)_0} \right]^{(n-1)} \right] \quad (2.6)$$

Where  $\theta_0$ ,  $(KM)_0$ , and  $n$  are constants that depend on the geometry and type of the connection. The Ramberg-Osgood function has the advantage that its derivative, hence the slope of the M- $\theta$  curve, does not fluctuate which is contrary to the inherent oscillatory nature of polynomials.

Lui and Chen (1986) proposed an exponential model in the following form:

$$M = M_0 + \sum_{j=1}^n C_j \left[ 1 - \exp\left(-\frac{|\theta_c|}{2j\alpha}\right) \right] + R_{kf} |\phi_c| \quad (2.7)$$

In which  $M$  is the connection moment,  $M_0$  is the initial moment,  $|\phi_c|$  is the absolute value of the rotational deformation of the joint;  $R_{kf}$  is the strain-hardening stiffness of the connection,  $\alpha$  is a scaling factor,  $n$  is the number of terms considered, and  $C_j$  is the curve-fitting coefficients. The values of the curve fitting parameters were determined based on previous experimental data for four different types of connections including single web angle, top-and seat-angle, flush end-plate, and extended end-plate and are listed in Table 2-3. The tangent stiffness and the initial stiffness are represented by equations (2.8) and (2.9), respectively.

Table 2-3 Connection parameters of the Chen-Lui exponential model (Chen 2000)

	Connection type (kips-in)			
	A Single web angle	B Top-and seat-angle with double web-angle	C Flush-end plate	D Extended end plate
$M_0$	0	0	0	0
$R_{kf}$	$0.47104 \times 10^2$	$0.443169 \times 10^3$	$0.96415 \times 10^3$	$0.41193 \times 10^3$
$\alpha$	$-0.511678 \times 10^{-3}$	$0.31425 \times 10^{-3}$	$0.31783 \times 10^{-3}$	$0.67083 \times 10^{-3}$
$C_1$	$-0.43300 \times 10^2$	$-0.34515 \times 10^3$	$-0.25038 \times 10^3$	$-0.67824 \times 10^3$
$C_2$	$0.12139 \times 10^4$	$0.52345 \times 10^4$	$0.50736 \times 10^4$	$0.27084 \times 10^4$
$C_3$	$-0.58583 \times 10^4$	$-0.26762 \times 10^5$	$-0.30396 \times 10^5$	$-0.21389 \times 10^5$
$C_4$	$0.12971 \times 10^5$	$0.61920 \times 10^5$	$0.75338 \times 10^5$	$0.78563 \times 10^5$
$C_5$	$-0.13374 \times 10^5$	$-0.65114 \times 10^5$	$-0.82873 \times 10^5$	$-0.99740 \times 10^5$
$C_6$	$0.52224 \times 10^4$	$0.25506 \times 10^5$	$0.33927 \times 10^5$	$0.43042 \times 10^5$

$$S_c = \frac{dM}{d\phi_c} \Big|_{|\phi_c|=|\phi_c|} = \sum_{j=1}^n C_j \left[ \frac{|\theta_c|}{2j\alpha} \exp\left(-\frac{|\theta_c|}{2j\alpha}\right) \right] + R_{kf} \quad (2.8)$$

$$S_c^o = \sum_{j=1}^n \frac{C_j}{2j\alpha} + D_k H[-|\theta_k|]_{k=1} \quad (2.9)$$

The Chen-Lui model provides good representation of the nonlinear behavior of connections. However, the model does not represent the behavior well if there is sharp abrupt in the moment-rotation curve. Similar to Richard and Abbott's model, this model requires a prior knowledge of the different connection characteristics including the initial moment and the strain hardening stiffness.

Kishi and Chen (1986a) and (1986b) modified the Chen-Lui model so that a sharp change in moment-rotation curve can be accommodated. The moment-rotation relationship is described by the following equation:

$$M = M_0 + \sum_{j=1}^n C_j \left[ 1 - \exp\left(-\frac{|\theta|}{2j\alpha}\right) \right] + \sum_{k=1}^n D_k (|\theta| - |\theta_k|) H(|\theta| - |\theta_k|) \quad (2.10)$$

Where  $M_0$  is the starting value of the connection moment to which the curve is fitted,  $D_k$  is a constant parameter for the linear portion of the curve,  $\theta_k$  is the starting rotation of the linear component of the curve, and  $H[\theta]$  is a Heaviside step function.

In addition to the curve fitting approach, simplified analytical models were also developed to predict the connection initial stiffness and ultimate moment. The models use equilibrium, compatibility, and material constitutive relations based on the concepts of elastic structural analysis, to predict initial stiffness. Likewise, plastic analysis is used to predict ultimate moment.

Kishi (1988) predicted the initial stiffness and ultimate moment capacity of top-and seat-angle with double web-angle connections from its geometrical and mechanical properties using the following equations:

$$K_{\phi} = \frac{3EI_{ta}d_1^2}{g_1(g_1^2 + 0.78t_{ta}^2)} + \frac{3EI_{wa}d_3^2}{g_3(g_3^2 + 0.78t_{wa}^2)} \quad (2.11)$$

$$I_{ta} = \frac{L_{ta}I_{ta}}{12} \quad \text{and} \quad I_{wa} = \frac{L_{wa}I_{wa}}{12} \quad (2.12)$$

$$M_{j,u} = \frac{2V_{pu} + \frac{f_y t_{wa}}{2}}{6} L_{wa}^2 \quad (2.13)$$

Where  $d_i$  and  $g_i$  are geometrical parameters,  $f_y$  is the yield strength of the material,  $E$  is the elastic modulus,  $I_{ta}$  and  $I_{wa}$  are the moment of inertias for the leg adjacent to the column face of the top angle and the web angle, respectively,  $t_{ta}$  and  $t_{wa}$  are the thickness of the top angle and web angle, respectively, and  $V_{pu}$  is obtained from the following equation.

$$\left( \frac{2V_{pu}}{f_y t_{wa}} \right)^4 + \frac{g_c - k_a}{t_{wa}} \left( \frac{2V_{pu}}{f_y t_{wa}} \right) = 1 \quad (2.14)$$

It is important to note that simplified analytical models are only capable of describing key parameters of the moment-rotation relationships, mainly the initial stiffness and the ultimate moment. However, for a complete description of the moment-rotation curve, one still has to resort to the power model with the proper shape factor  $n$ .

The models described above were developed using old tests in which high degree of uncertainty exist regarding the level of bolt pretension and actual material properties. In addition, the tests were conducted on small specimens with shallow beams and thin angles and did not cover a wide range of specimen sizes. Test data for specimens comprising deep beams and thick angles did not show good agreement with the curve-fitting models (Leon, Wan Hu et al. 2004).

Recognizing the shortcomings of curve-fitting models, mechanical models were proposed as a viable approach for predicting the connection behavior based on physical meanings. In mechanical models, the various components of a joint are conceived as a set of rigid and deformable elements represented by springs with specified load-deformation characteristics. The constitutive laws describes the behavior of the various springs include both linear and nonlinear relationships; allowing for a complete moment-rotation curve to be constructed through the contribution of the various components modeled, while taking into account their deformation and progressive yielding. In the case of top-and seat-angle with double web-angle connections, the various components include angles, bolts, and the column panel zone. In addition to modeling the actual components, the interaction amongst them must also be modeled for accurate representation of the connection behavior which include contact nonlinearity, bolt slippage, and bolt hole ovalization. It is however important to note that an effective assembly of all components that adheres to equilibrium and compatibility is important to achieve desirable accuracy and robustness of the component-based model (Kim, Ghaboussi et al. 2010).

Early work on the development of mechanical models was conducted to represent the behavior of double web-angle connections under monotonic loading (Wales and



Rossow 1983). The model was further extended to the case of top-and seat-angle with double web-angle as shown in Figure 2-2 (Chmielowiec and Richard 1987).

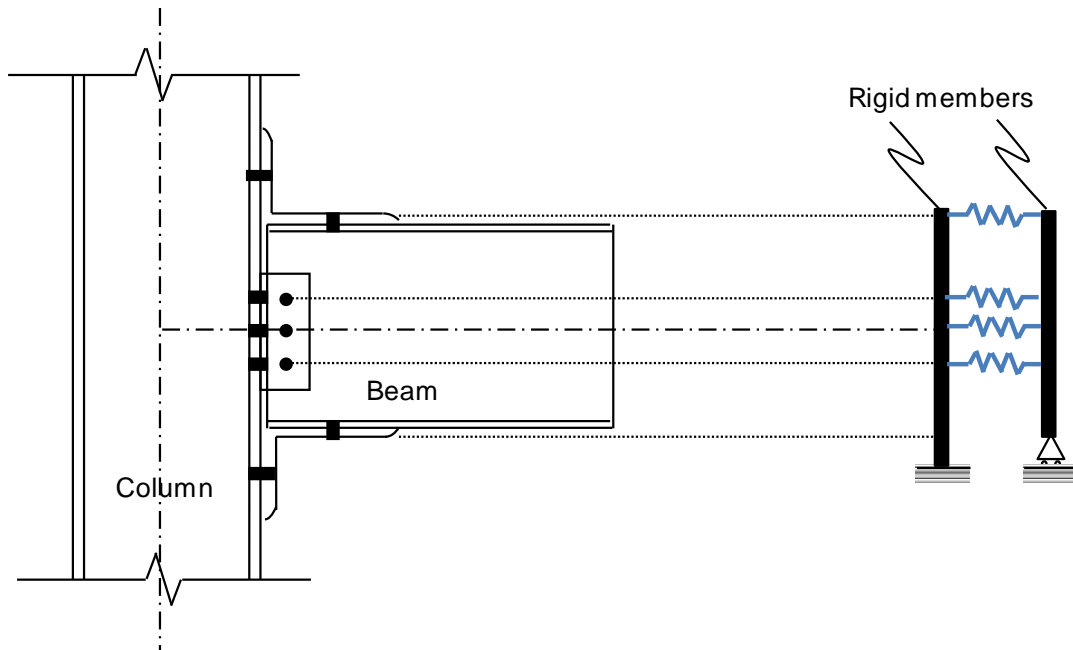


Figure 2-2 Mechanical model for top-and seat-angle with double web-angle connection, after: (Chmielowiec and Richard 1987)

Eurocode 3 provides a complete set of detailed rules to determine the structural properties of beam-to-column joints and base-plate joints using the mechanical model for an equivalent T-stub connection which is representative of top-and seat-angle connections. An extension to the model was proposed to account for the addition of double web angles (i.e. top-and seat-angle with double web-angle) and hardening (Pucinotti 2001). The model can predict the initial stiffness relatively well but it is not accurate in estimating the capacity of the joint.

To represent the cyclic behavior of double web-angle connections, a model was proposed which accounts for only material and geometric properties (De Stefano, De

Luca et al. 1994). The model was extended to include gap elements representing the slip effects (Shen and Astaneh-Asl 2000).

### **2.2.2 Finite Element Models**

Nonlinear finite element analysis is an attractive tool for modeling connections and its complex behavior. Early attempts to use finite element for analysis of partially restraint connections was a comparative study on extended endplate connections to correlate stresses and displacement obtained using 2D and 3D linear elastic models with bolt pretension alone (Krishnamurthy 1980). Similar procedure was proposed to reproduce moment-rotation relationships of end-plate connections (Kukreti, Murray et al. 1987).

Gendron (1989) developed a 2D finite element model for double-bolted joints and accounted for plasticity and contact. The model was calibrated against published test results and was shown to predict the behavior of the connection both before and after slip occurrence. The model, however, did not include the effect of friction, finite geometry, bolt clearance and different ratios of bolt loadings.

To the author's knowledge, no 2D continuum finite element models have been developed for top-and seat-angle connections or top-and seat-angle with double-web angle connections. With advancement in computational techniques and power, attention was shifted to developing 3D models which have proven, in some cases, to be capable of capturing the true behavior of the connections.

Early research on 3D modeling of bolted connections was conducted to develop a methodology to analytically evaluate the moment-rotation relationships for steel bolted

end-plate connections (Sherbourne and Bahaari 1994). The work included the development of an equivalent 3D analysis where the end plate, beam and column flanges, webs, and column stiffeners are represented as plate elements and each bolt shank is modeled using six spar elements. Contacts between the various surfaces were modeled using three-dimensional interface elements.

The stiffness and strength of a T-stub to the unstiffened column flange bolted connection was investigated in a 3D framework (Sherbourne and Bahaari 1996). Two T-stub connection models were developed for the validation of the modeling technique and included 3D T-stubs bolted to a rigid and flexible elements. The model was considered an improvement in investigating end-plate connections since most of the reported research has been performed on assemblies either attached to a rigid base or possessing symmetry about the interface of the connected elements.

Additional research on estimating the moment-rotation relationship of bolted connections was conducted and included 3D finite element analysis of extended end-plate connections for preloaded and non-preloaded bolted T-stubs (Bursi and Jaspart 1997). The bolts were preloaded with prestressing force and modeled with brick elements using an effective bolt length. The results of the analysis showed good correlation with test data and the modeling technique was proposed as a rational approach for accurate simulation of these types of connections.

Three-dimensional finite element models were also developed for angled connections. The first model was developed to study the response of double-angle connections subjected to axial and shear loads (Yang, Murray et al. 2000). In this study,

double web-angle connections with three different thicknesses were analyzed where the angles are welded to the beam web and bolted to the column flange. First, the results of the three-dimensional analysis were used to replace the angles by equivalent nonlinear springs. A two-dimensional finite element technique was then utilized to obtain response curves for the connections.

The behavior of top-and seat-angle connections was also simulated using 3D finite element models (Ahmed, Kishi et al. 2001). The model included bolt pretension and contact formulation with coulomb friction between contact pair surfaces. The results of the numerical analysis together with the prediction by the Kishi-Chen power model (Kishi and Chen 1990) were compared with experimental results and all three showed good correlation. It is important to note that the power model by Kishi and Chen is based on Richard and Abbott's model with strain-hardening being disregarded. Various parameters were then varied to study the effect of material properties of the connecting elements and magnitude of bolt pretension on the behavior of the connection.

The behavior of top-and seat-angle with double web-angle connections was investigated using four 3D models (Kishi, Ahmed et al. 2001). The four models included contact pair with Coulomb's friction coefficient of 0.1. The four models were noted as ND, NF, BM and BI where "N" denotes non-existence of bolts in the model; "D" denotes defined gage length ( $(g-w)/2$ ); "F" denotes full gage  $g$  where  $g$  is the gage distance from the bolt hole centerline to the angle heel and  $w$  is the width of the bolt head; "B" denotes the presence of bolts in the model; "M" denotes that the bolts are monolithic with the angle; and "I" denotes that the bolts act as independent component in the model. The results showed that all models can predict the strength of the connection with reasonable

accuracy except for the ND model. Less accuracy was achieved when estimating the initial stiffness of the connection.

A graphical comparison and the numerical results are shown and listed in Figure 2-3 and Table 2-4, respectively. As shown in Figure 2-3, model BI best represents the real interaction among the connection components, which emphasizes the need for including the bolts as independent components in the model. The analysis included a comparison between various experimental results (Azizinamini and Radziminski 1989), three-parameter power model (Kishi and Chen 1990), and the finite element analysis. It was concluded that the discrepancies on ultimate moment capacity between FE analysis and experimental results range from 15.4% to +6.1% and the power model predictions agrees fairly closely with test results with the exception of few cases. The accurate predictions using the power model are expected since the model was derived using the same test data.

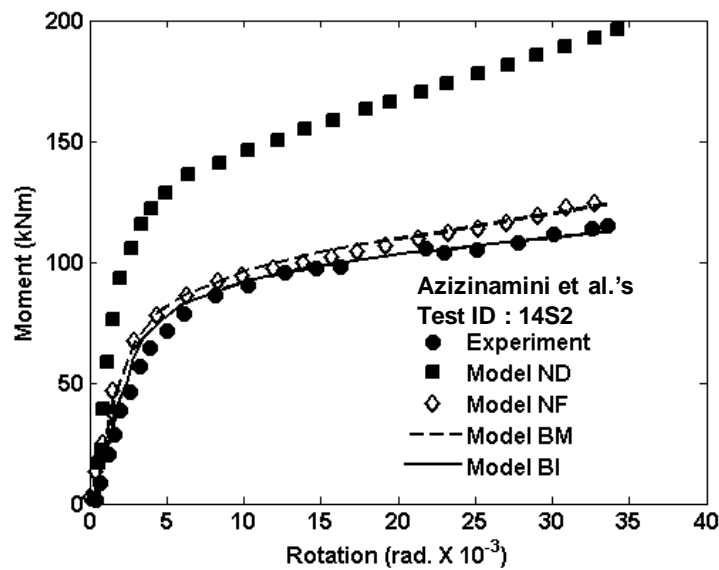


Figure 2-3 Comparison between different modeling approaches, *after:* (Kishi, Ahmed et al. 2001)

Table 2-4 Pertinent data of Figure 2-3 (test ID 14S2) (Kishi, Ahmed et al. 2001)

Connection capacity	Initial connection stiffness		Ultimate moment capacity	
	Result (kN.m/rad)	Error (%)	Result (kN.m/rad)	Error (%)
ND	69,619	+31.8	195.6	+70.5
NF	38,612	-26.9	125.3	+9.2
BM	40,025	-24.3	123.0	+7.2
BI	41,388	-21.7	112.5	-1.9
Test	52,839	-	114.7	-

Another 3D finite element model for top-and seat-angle with double web-angle connection was developed and included contact between all parts, friction, slip, and a method for applying pretension in the bolts (Citipitioglu, Haj-Ali et al. 2002). The models were compared with the experimental results in the literature by Azizinamini and Radziminski (1989). The results of the analysis highlighted the effect of blot pretension on the behavior of the connection as it could vary the ultimate moment-rotation by 25%. The 3D model developed is shown in Figure 2-4.

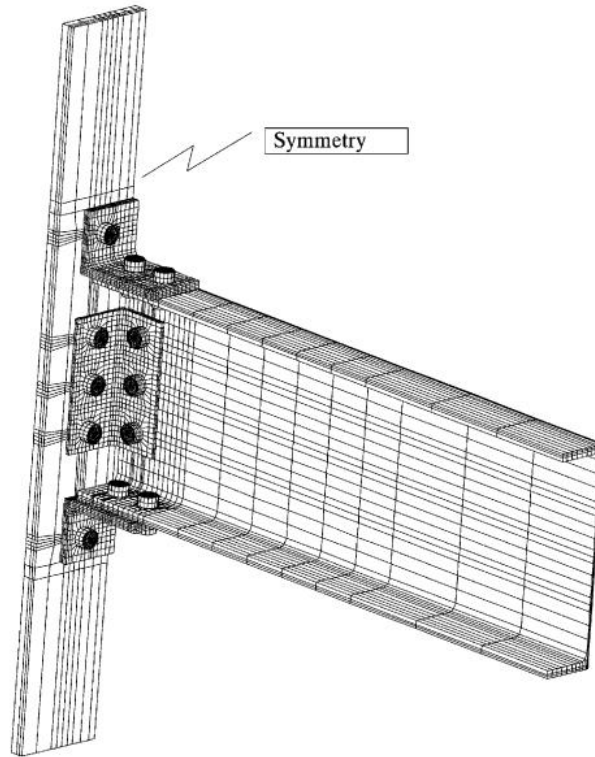


Figure 2-4 Three-dimensional FEM for top-and seat-angle with double web-angle connection (Citipitioglu, Haj-Ali et al. 2002)

Notwithstanding their effectiveness, 3D models are difficult to construct and are computationally intensive, thus their ability to conduct large parametric studies is limited. It is also worth noting that the available finite element models on top-and seat-angle with double web-angle connections have all been used and verified against experimental data under monotonic loading. Although it is not explicitly mentioned in the literature, it is believed that the evaluation of such models under cyclic loading has not been investigated since such assessment is computationally very demanding and the evaluation of one cyclic test results could take days to complete.

### **2.3 Analytical Investigation of Semi-rigid Frames**

Analyzing semi-rigid frames under dynamic loading requires a cyclic model of the connection behavior to be used in the analysis. The mathematical models discussed earlier in the chapter were developed for connections under monotonic loading and therefore are not suitable for cyclic or dynamic analysis of semi-rigid frames. Despite their effectiveness in representing the monotonic response of semi-rigid connections, the models cannot capture the inelastic characteristics of the connection.

The use of models developed for monotonic loading to predict cyclic behavior is based on the observation that the envelopes of cyclic tests match closely the envelope for static tests (Leon, Wan Hu et al. 2004). It is however known that cyclic tests of these types of connections show an increased strength with cycling due to hardening (Leon, Wan Hu et al. 2004). Therefore, it is inevitable that the curve-fitting models will always underestimate the capacity of the connection. The work by Leon et al. (2004) included a comparison between a cyclic test conducted by Azizinamini and Radzimirski (1989) and three curve-fitting models; Frye and Morris (1975), Ang and Morris (1984), and Kishi and Chen (1990). Only the model by Ang and Morris (1984) is capable of predicting the actual capacity of the connection. Comparison with other test results showed that in some cases the model by Ang and Morris failed to properly predict the moment capacity of the connection. It is important to point out that none of the curve-fitting models is capable of predicting the rotational capacity when the tension capacity of the bolts governs the behavior.



Early work on analyzing steel frames with semi-rigid connections was conducted by Frye and Morris (1975) where a static analysis technique was presented using a modified matrix analysis approach. The analysis highlighted the effect of including the flexibility of the connection on the redistribution of moments in the structure and increase in lateral displacements.

Work on modeling connection behavior under dynamic and cyclic loading included a trilinear model (Moncarz and Gerstle 1981) and a bilinear model (Sivakumaran 1988) representing the cyclic moment-rotation behavior of the connection. The models however do not represent the connection behavior accurately because of the abrupt changes in the connection stiffness in the transition from the elastic to the plastic region.

Recognizing the shortcomings of early models, Albermani et al. (1994) used a smooth connection model in a dynamic planar frame analysis. The model included the Bauschinger effect of the connection but disregarded the pinching and stiffness degradation characteristics of the moment-rotation diagram. The details of the model can be found in (Al-Bermani and Kitipornchai 1992) and (American Institute of Steel Construction (AISC) 1989).

A dynamic matrix analysis approach which incorporated geometric nonlinearity and a bilinear hysteresis model for semi-rigid connections was formulated by Lui and Lopes (1997). In the analysis, the frame was modeled as beam elements with nodal springs at the beam ends to simulate the semi-rigid connections. Geometric nonlinearity was accounted for through modification of the stiffness of the columns. The analysis

technique was applied to a portal frame, which was reduced from a six degree of freedom system to a single degree of freedom system, using static condensation while assuming no axial deformation in the beam.

The work by Lui and Lopes (1997) was extended by Awkar and Lui (1999) to multi-story structures. The model used matrix analysis that incorporated the connection flexibility and the effects of geometric nonlinearities to study the planar behavior of steel frames.

Salazar and Haldar (2001) performed a parametric study of the variation of energy dissipation, story drift, and base shear in steel frames when the rigidity of the beam-to-column connections is varied. An analytical finite element model was used, which utilized a discrete piecewise linear spring model for the semi-rigid beam-column connection. The spring model did not include asymmetry, strength degradation, stiffness reduction, or pinching.

Foutch and Yun (2002) performed static and dynamic analysis of a 9-story and a 20-story building. The frames were modeled using centerline dimensions. The behavior of the panel zone was included using a special arrangement of rigid links to simulate the panel region with nonlinear springs. In addition, the effect of the gravity frames in resisting the lateral load was included by modeling the connections between the gravity frames using nonlinear springs which accounted for the composite action of the slab. The models were also modified so that the effects of connection fracture could be investigated.

## **2.4 Code of Practice for the Seismic Design of Semi-rigid Connections**

### **2.4.1 American Institute of Steel Construction (2005)**

According to the American Institute of Steel construction (AISC) classifications, there are three types of moment frames: ordinary moment frames (OMF), intermediate moment frames (IMF), and special moment frames (SMF). The definition of the frames in accordance with the AISC Seismic Provisions for Structural Steel Buildings (ANSI/AISC 341-05) revolves around the degree of inelastic deformation the frames can sustain and the interstory drift accommodated during an earthquake. The OMF, IMF and SMF are assumed to be able to withstand total interstory drifts in the range of 0.01, 0.02, and 0.04 radians, respectively.

An OMF is used in low-seismic areas and is expected to undergo minimal inelastic deformations in its members during the seismic event (i.e. the frame is designed to remain essentially elastic). An IMF is used in low-to-mid seismic areas and is intended to withstand some permanent damage following an event. The frame is required to sustain a moderate interstory drift of 0.02 rad. An SMF is used in mid-to-high seismic areas and intended to withstand significant permanent damage following high inertial forces, while sustaining high level of interstory drift of 0.04 rad.

The provisions require beam-to-column connections to satisfy the requirements of Section 9.2 for SMF or 10.2 for IMF. These requirements include a minimum interstory drift angle each connection must be capable of sustaining, a minimum flexural resistance at that drift angle, and a minimum shear strength based on full yielding of the moment

connection at each end of the beam. The provisions allows for two different ways to demonstrate that these criteria have been met:

- 1) Testing of the connection in accordance with Appendix S of the Seismic Provisions
- 2) Using a prequalified connection in accordance with Appendix P of the Seismic Provisions including:
  - a) Reduced Beam Section (RBS) Moment Connection
  - b) Bolted Unstiffened and Stiffened Extended End-Plate Moment Connection
  - c) Bolted Flange Plate (PFB) Moment Connection (SMRF and IMF)

It is important to note that the three different types of frames are required to be designed according to the strong-column weak-beam provisions. That is, the columns are expected to remain elastic or experience small yielding while the beams are the main source of deformation and supply for the inelastic rotation of the joint.

It is clear from the above discussion that the AISC seismic design provisions call for testing if the connection to be used is not prequalified per Appendix P of the provisions. Despite the numerous tests conducted on angled connections, none of which have been qualified by AISC to be utilized in steel frames in seismic regions.

#### **2.4.2 Eurocode 3 (2005)**

The use of mechanical models in design codes of semi-rigid connections has been explored in EC3 (Eurocode 3 1998). The formulation described in Annex J of EC3 is developed such that the main component in the mechanical model is an equivalent T-stub positioned in the column-side and in the beam-side of an end-plate connection. The T-

stub model, by default, represents a top-and seat-angle connection and is described by linear elastic relationship if the applied moment  $M_{j,Sd}$  is lower than the elastic moment,  $M_e$  ( $M_e = 2/3M_{j,Rd}$ ), where  $M_{j,Rd}$  is the design or ultimate moment of the connection. The initial stiffness and the defined moments and rotations capacity are depicted in Figure 2-5.

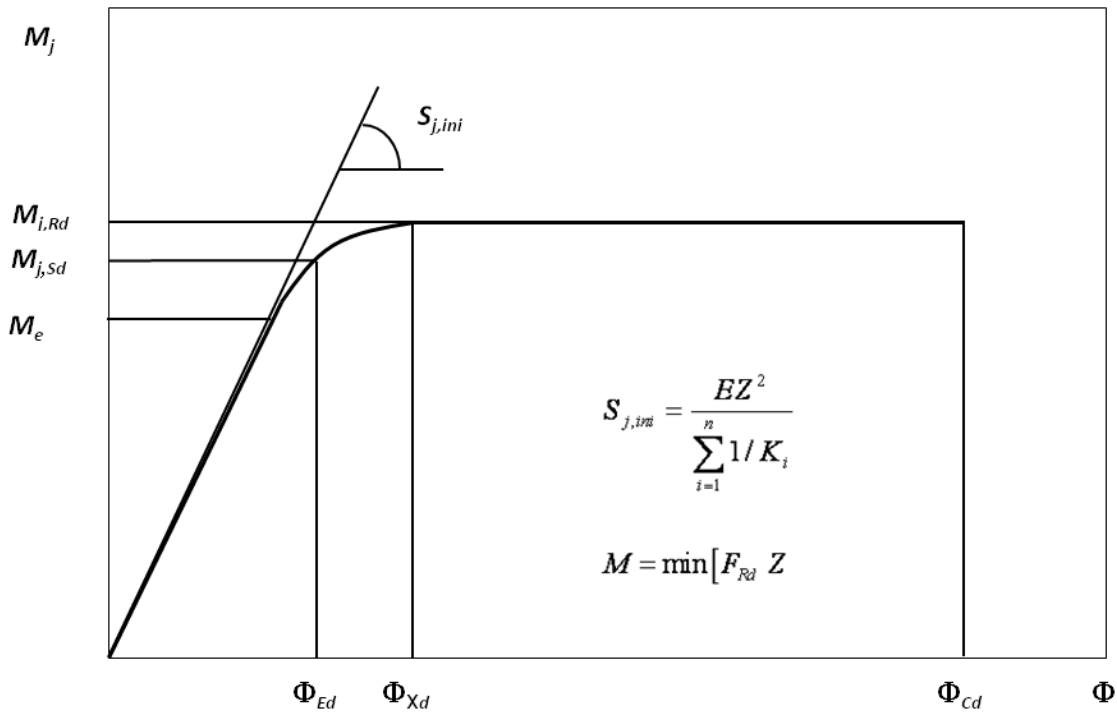


Figure 2-5 Moment-rotation curve defined in EC3 for top-and seat-angle connection, after: (Eurocode 3 1998)

The initial stiffness, the strength, and the rotational capacity are defined by the following equations:

$$S_{j,ini} = \frac{EZ^2}{\sum_{i=1}^n 1/K_i} \quad (2.15)$$

$$M_{j,Rd} = F_{Rd} Z \quad (2.16)$$

$$F_{Rd} = \min [F_{Rd1}, F_{Rd2}, \dots, F_{Rdn}] \quad (2.17)$$

Where;  $E$  is the Young's modulus;  $Z$  is the lever arm;  $K_i$  is the stiffness coefficient of the  $i^{\text{th}}$  component and  $n$  is the number of basic joint components.

The rotational capacity of the joint is deemed sufficient in accordance with EC3 if the following conditions are met:

- The moment resistance of the joint is governed by the resistance of either:
  - The column flange in bending; or,
  - The tension flange angle in bending
- The thickness,  $t$ , of either the column flange or the tension flange angle satisfies the following:

$$t \leq 0.36d \sqrt{f_{ub} / f_y} \quad (2.18)$$

Where,  $d$  is the nominal diameter of the bolts,  $f_{ub}$  is the ultimate tensile strength of the bolts, and  $f_y$  is the yield strength of the relevant basic component.

## 2.5 Summary and Conclusion

Various experimental and analytical studies on semi-rigid connections in beam-to-column subassemblies, including top-and seat-angle with double-web angle connections, have been conducted. The studies demonstrated the ability of the

connections to dissipate energy and withstand large seismic actions. Results of the studies were utilized in a number of frame analyses that included action-deformation relationships which are idealized and not well representative of the complex inelastic nature of the connection behavior. Such approach highlights the need for accurate and more refined system-level approach for the seismic assessment of steel frames with semi-rigid connections. With advancement in modeling techniques, computing power, and experimental facilities, a system-level hybrid simulation approach is the next logical step for conducting reliable seismic assessment of steel frames. In addition, the absence of top-and seat-angle with double web-angle connections from the ANSI/AISC list of prequalified connections calls for more research to be conducted on these connections to explore their full potential and prequalify them for seismic applications.

In the following chapters, a new approach for the seismic assessment of steel frames with semi-rigid connections is presented. The approach includes the development of experimental and analytical components and integrating them in a system-level hybrid simulation as well as conducting parametric studies of frames with varied design parameters.

## CHAPTER 3

### HYBRID SIMULATION ENVIRONMENT

#### 3.1 Introduction

Seismic evaluation of structural systems has traditionally been explored using either experimental methods or analytical models. Issues of scale, equipment capacity and availability of research funding continue to limit the full-scale testing of complete structures. Analytical platforms on the other hand are limited to solving specific type of problems and in many cases fail to capture complex behaviors or failure modes in structural systems (Kwon, Elnashai et al. 2007). Combining both tools in a single simulation, while taking advantage of what each tool has to offer, is referred to as hybrid simulation.

The concept of hybrid simulation was first developed by Japanese researchers where a single-degree-of-freedom system was analyzed under seismic loading (Hakuno et al. 1969). The work included using an analog computer for solving the equations of motion and an electromagnetic actuator to load the structure. Since then, simulation techniques has significantly evolved to include sub-structuring techniques with hybrid simulation making it possible to consider distributed hybrid simulation and real-time hybrid simulation (Nakashima, McCormick et al. 2008).



### 3.2 Overview of Pseudo Dynamic Testing

Different experimental approaches currently exist for dynamic experimental testing of structures and vary between shake table tests, pseudo dynamic tests, and cyclic tests. Shake table testing involves fixing structures at their bases on a table which is dynamically operated with hydraulic actuators. The input motion can be as simple as a sinusoidal function or an input resembling an actual ground motion. Dynamic testing using full-scale shake table is viewed as the most realistic method for the seismic evaluation of structural models. However, this testing method requires full-scale shake tables which are not readily available in structural labs due to the large space they typically occupy.

Cyclic loading is another alternative for the seismic evaluation of structures. It involves the application of increasingly repeated cycles using a predefined deformation history at different ductility levels. The drawback of using this approach is that applying large number of cycles at different ductility levels is likely to overestimates the seismic loads experienced by the structure during an event. In addition, since nonlinear problems are path dependent, the loading history imposed on the structure will cause the structure to experience stiffness and strength degradation which does not represent what it would have otherwise experienced during an actual earthquake.

Pseudo-Dynamic (PSD) testing is another testing technique that has been widely used by many researchers (Hakuno, Shidawara et al. 1969; Mahin and Shing 1985; Nakashima and Kato 1987; Elnashai, Elghazouli et al. 1990; Negro, Mola et al. 2004; Jeong and Elnashai 2005a). In this testing method, the use of a shake table is substituted

by hydraulic actuators connected to the structure. The problem associated with overestimating the loading during cycling testing is overcome by imposing realistic loading on the structure through numerical integration of the dynamic equation of motion while using an actual earthquake. The major shortcoming of using PSD testing is that it requires testing of the whole structure, which is not feasible in some cases due to limitations of the laboratory space and equipment capacity.

A more attractive approach is to use the concept sub-structuring PSD (SPSD) testing which is nothing but a derivative of PSD. In this method, the structure can be portioned into various components comprising of experimental or analytical modules or a combination of both. Combining analytical and experimental modules in a single simulation is known as hybrid simulation. This approach has been used by many researchers for the seismic evaluation of structures and has proven to be very valuable in overcoming the limitations of using conventional PSD (Watanabe, Kitada et al. 2001; Spencer, Elnashai et al. 2004; Kim, Elnashai et al. 2006; Stojadinovic, Mosqueda et al. 2006). The attractiveness of this option lies in the fact that it captures the complex interaction between the various modules while providing information on the global system behavior.

In this approach, the earthquake force is calculated numerically using time step-integration of the equation of motion. The corresponding displacements are then applied simultaneously to the test specimens and the analytical models. The resulting restoring forces are measured for each module and used in a feedback loop for the calculation of the next displacement command corresponding to the next step. A software called UI-SIMCOR, which is MATLAB based, is used to orchestrate the simulation. The software

is developed at UIUC which is capable of conducting the numerical integration as it steps through the seismic record. The numerical integration in UI-SIMCOR uses the OS method with a modified  $\alpha$ - parameter through the Newmark integration scheme ( $\alpha$ -OS method) which applies numerical damping to the undesired oscillations. A full description of UI-SIMCOR and its components can be found in (Kwon, Nakata et al. 2005).

### **3.3 The Must-SIM Facility**

The experimental component of the simulation utilizes the Multi-Axial Full-Scale Sub-Structured Testing and Simulation Facility (MUST-SIM) which is part of the 15 sites of the Network of Earthquake Engineering Simulations (NEES). The main testing components include a full-scale bolted beam-column subassembly. The beam comprises a portion of first-story beam in the first bay while the column includes portion of the first- and second-story columns in the same bay. The experiment utilizes two large load and boundary condition boxes (LBCBs), the L-shaped strong wall, and the advanced non-contact displacement measurement systems (Krypton). The main loading units (i.e., the LBCBs) are capable of providing deformations and actions in all 6 degrees of freedom at different contact points. Details on the advanced capabilities of the MUST-SIM facility are given in (Elnashai, Spencer et al. 2004).

### **3.4 Description of the Structure**

The structure under consideration is a 2-story, 4-bay (longitudinal) and 2-bay (transverse) steel frame, assumed to be located in Los Angeles, California. The height of the first and second story is 15 ft and 13.5 ft, respectively, and the bay width is 30 ft. The lateral load resisting system is special moment-resisting frame (SMRF) designed with the concept of strong-column weak-beam according to the International Building Code Structural Seismic Design Manual, Volume 3 (International Building Code 2006). The design of the SMRF resulted in a strong-column weak-beam design with W18 x 40 and W14 x 159 for the beams and columns, respectively.

Following sizing of the beams and columns, the assumed rigid connections in the frame are redesigned to reflect partial-strength and semi-rigidity. Three different frames are considered with the connections in each frame designed as top-and seat-angles with double web-angles according to the EC3 (Eurocode 3 1998). The sizes of the angles and the bolts are optimized such that the resulting connection capacity in frame 1, 2 and 3 is 70%, 50%, and 30%, respectively, of the plastic moment capacity of the beam. Plan view of the structure and an elevation of a typical SMRF are shown in Figure 3-1. Detailed description of the design procedure can be found in APPENDIX C.

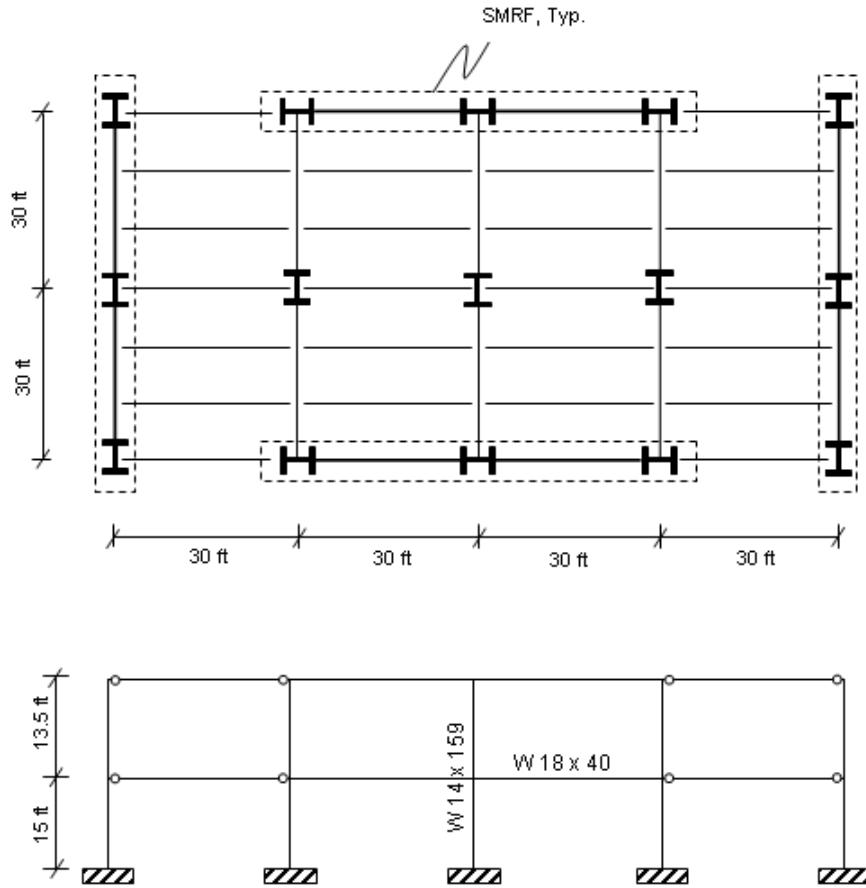


Figure 3-1 Plan view of the structure considered and an elevation of the SMRF

### 3.5 Analytical Module

Analytical models of frames have utilized line elements connected with springs representing the load deformation characteristics of the connection. Due to its minimal computational demands, this modeling approach has been viewed as the best alternative for hybrid simulation since the number of elements in this case is small and significant time is not required to complete a simulation step. However, the models typically represent idealized behavior and in many cases cannot capture the local response of the various connection components. Furthermore, the deformation and spread of yielding in the beam and the column are not well represented since the prying action and interaction

between the beam and column flanges and the various connection components is neither physically modeled nor accounted for.

In light of the above arguments, the use of 2D or 3D finite element models in hybrid simulations can pay significant dividends since the localized connection behavior and its interaction with the beam and column is physically represented. The decision to employ 2D or 3D models in hybrid simulations has been primarily driven by the notion that 2D models cannot properly capture the complex localized behavior of the connection. However, for planar problems or problems that could be idealized as planar, 2D models may be much more efficient when compared to 3D models. Moreover, the use of 3D models in a closed-loop hybrid simulation, where thousands of steps are executed, would be totally impractical.

### **3.5.1 Overview of the Model and Its Components**

An inelastic 2D finite element model is employed in the current investigation with 29203 nodes and 27617 elements. The model comprises a 2D generalized plane strain elements with reduced integration for the beam-to-column connections and 1D beam elements between subsequent connections. Bolts used to connect the various connection components are modeled using spring elements representing the desired load-deformation characteristics of the bolts. Spring elements are also used to represent the transverse behavior of the connection as explained below. The model is developed using ABAQUS which is a general purpose commercial package (Simula 2007) and includes various inelastic behavioral features namely; 1) hot-rolling residual stresses in the top and seat angles, 2) bolt preload, 3) friction between faying surfaces, 4) connection slip, 5) the

effect of bolt-hole ovalization, 6) transverse stiffness of the connections, and 7) idealization of the web angles.

The effect of the inner gravity frames on the stability of the moment-resisting frame (i.e. large P- $\Delta$  effect) is included in the model through a leaner column modeled as truss elements pinned at the base and at the first floor level. Tie multi-point constraints are used to provide rigid links between the SMRF and the leaner column. An overview of the analytical module with a zoom-in on the connection deformation is shown in Figure 3-2.

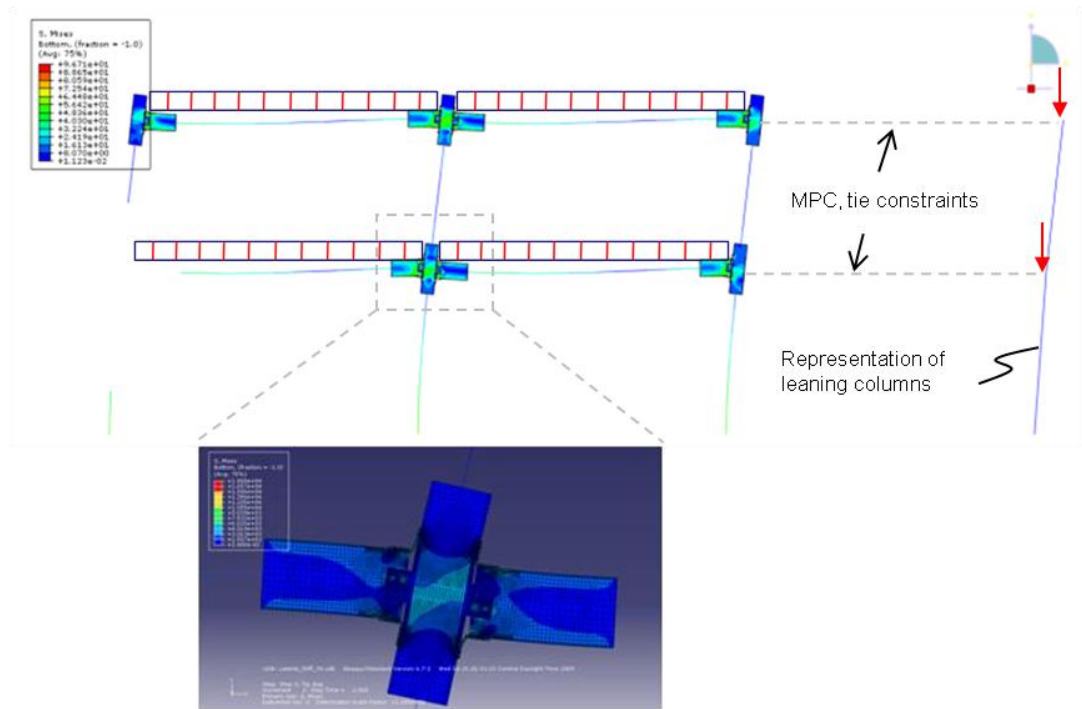


Figure 3-2 Overview of the analytical module

### 3.5.2 Approach for Modeling the Various Inelastic Features

#### 3.5.2.1 Hot Rolling Residual Stresses

The magnitude and distribution of longitudinal residual stresses arising from the hot-rolling process during fabrication of steel angles have been researched by others (O'Connor 1955; Beedle and Tall 1960; Nuttall and Adams 1970; Usami 1971; European Convention for Constructional Steelwork (ECCS) 1985; Elgaaly, Dagher et al. 1991). The work is motivated by the need for including residual stresses when assessing the flexure buckling capacity of steel angles. The results are highlighted by large scatter in the magnitude of measured stresses as shown in Figure 3-3. Linear stress distribution with an assumed peak value is recommended to account for the observed scatter. Peak values of  $0.30F_y$ ,  $0.25F_y$  and  $0.50F_y$  are assumed by ECCS, AISC, and Usami, respectively (Usami 1971; European Convention for Constructional Steelwork (ECCS) 1985; American Institute of Steel Construction (AISC) 1989).

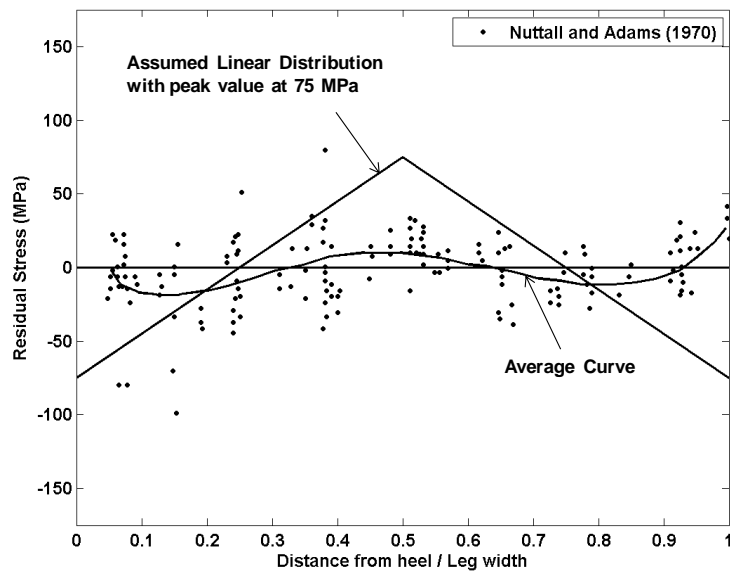


Figure 3-3 Measured hot-rolling residual stresses, *after*: (Nuttall and Adams 1970)



As mentioned above, the measured hot-rolling stresses are typically used to assess the ultimate capacity of a single angle in compression or tension when utilized as steel bracing or flexural member. On the other hand, the effect of hot-rolling residual stresses on the moment-rotation relationship; when the angle is used as a connecting element has never been investigated before.

In this study, hot-rolling residual stresses are included as per the ECCS (1985) recommendations assuming a linear distribution with a peak value of  $0.25F_y$  and  $0.22F_y$  at the heel and toe of the angle, respectively as shown in Figure 3-4. Because of the nature of the model, being a 2D model, residual stresses are only included in the top and seat angles and not in the web angles.

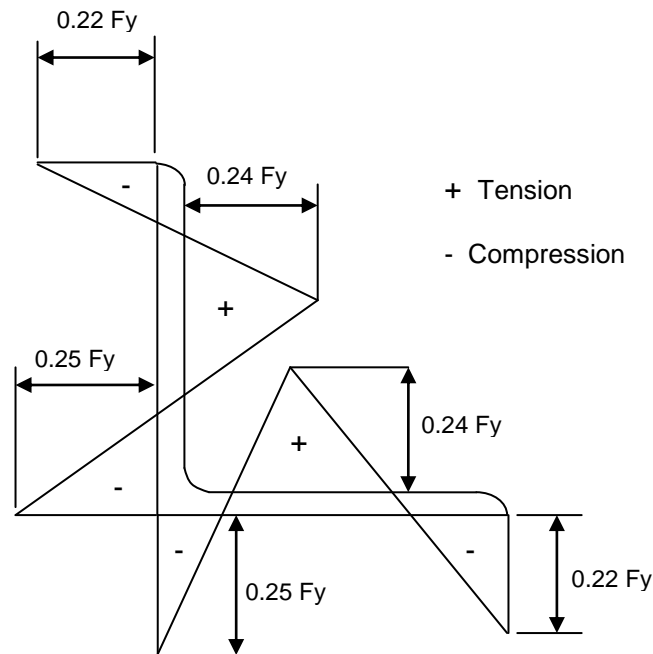


Figure 3-4 Recommended residual stress distribution per the Eurocode, *after*: (European Convention for Constructional Steelwork (ECCS) 1985)

The proposed residual stress distribution is introduced in the model by first applying the tension field in the desired local direction as initial stresses. The compressive stress field is then generated in the model through the redistribution of stresses to achieve equilibrium. This approach is based on trial and errors and requires the initial tensile field introduced to be higher than the target field since the redistribution of stresses results in reduction of the initially specified values. The approach has been used in the past to introduced residual stresses in welded stiffened steel panels (Mahmoud and Dexter 2005).

Prior to applying the above mentioned approach to the 2D model, a 3D model of a typical angle was developed using plate elements and used to validate the approach and visualize the resulting residual stress field. The angles are modeled using 4-nodal plate elements with reduced integrations. The resulting residual stress field is shown in Figure 3-5. After verifying the approach of introducing residual stresses through using a 3D model of the angle, the residual stress field is introduced in the 2D beam-column connection model using the same technique. The 2D model including the residual stresses field is shown in Figure 3-6.

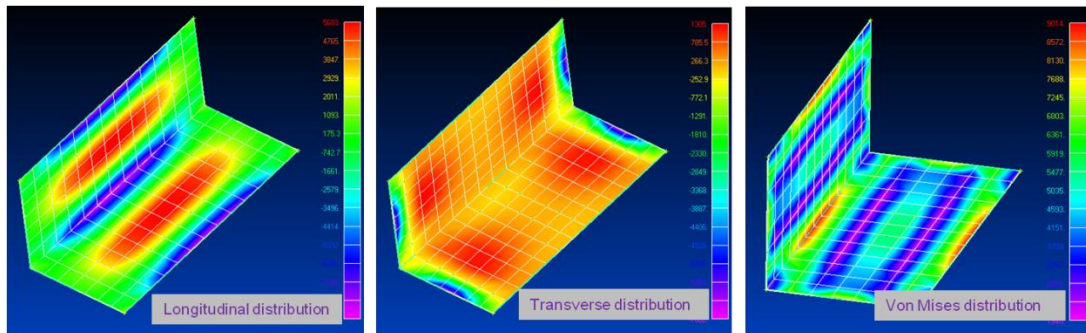


Figure 3-5 Simulated residual stresses in the top-and seat-angles

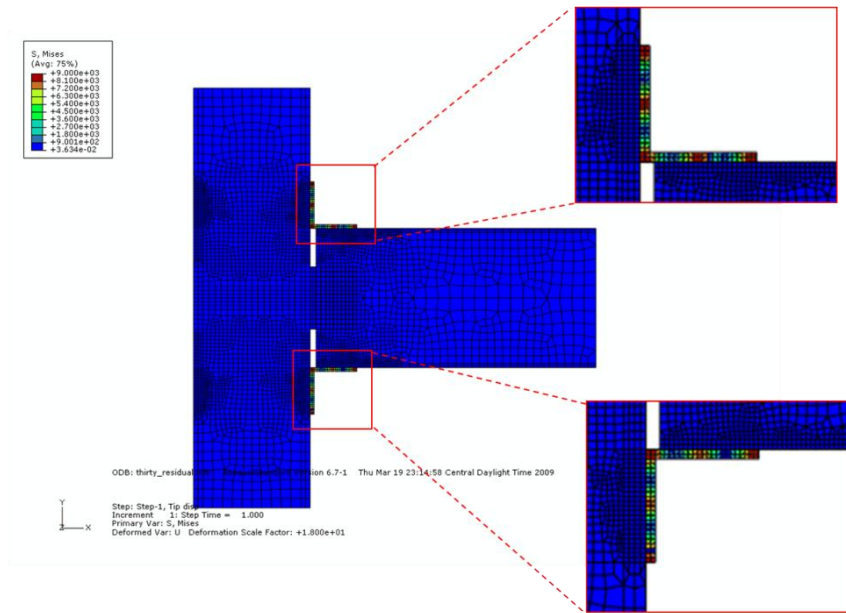


Figure 3-6 Two-dimensional model with residual stress distribution

### 3.5.2.2 Bolt Pretension

Depending on the model, 2D versus 3D, there exist multiple methods to represent typical bolt assemblies in finite element models (bolt head, bolt stud, washer, and nut) and introduce the pretension force resulting from bolt tightening. In 3D models, the most straight forward but computationally expensive approach is to model the actual bolt geometry. A more simplified approach, known as the coupled bolt simulation, includes using line elements to simulate the bolt stud and coupled nodes to simulate the head/nut. This approach allows for axial load transfer in the bolt without the need for using solid elements. Rigid body elements (RBE) is another way of including the bolt assembly where line elements are used to model the stud and rigid body elements are used to model the head and the nut, which are also connected with RBE. Spider bolt simulation is another approach for modeling bolts where line elements of the head and the nut in the RBE model are substituted with a series of line elements organized in a web-like fashion.

In this study each bolt was modeled using axial spring elements in parallel as shown in Figure 3-7. This approach takes into account the effect of the bolt action on the finite contact area. Its application for assessing the nonlinear behavior of single bolted T-stub connection was shown to yield significantly better results in comparison with a single spring representation (Coelho, Silva et al. 2004).

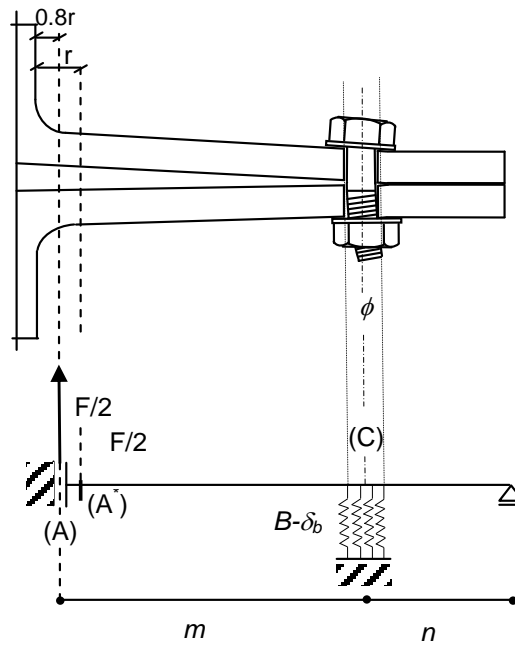


Figure 3-7 T-stub model accounting for the bolt action, *after*: (Coelho, Silva et al. 2004)

The application of bolt pretension is essential for maintaining the proper level of contact between the faying surfaces. The most common methods for simulating bolt preload include applying traction at the end of the bolt or applying the corresponding displacement to the end nodes. Other methods have been used to simulate the pretension load including using temperature fields, constraint equations, or initial strains.

In this analysis, bolt preload was modeled by shifting a load-deformation curve of a typical bolt so as to result in an initial axial load applied to the bolt. The axial load is chosen to be equal to 80% of the proof strength of the bolt material as recommended by AISC (American Institute of Steel Construction (AISC) 2005). Figure 3-8 (a), (b), and (c) show a typical axial load-deformation curve without bolt pretension, axial load-deformation curve with bolt pretension, and a zoom-in image of an exaggerated deformed shape of the top-angle connection showing the “cupping” effect resulting from introducing the preload, respectively.

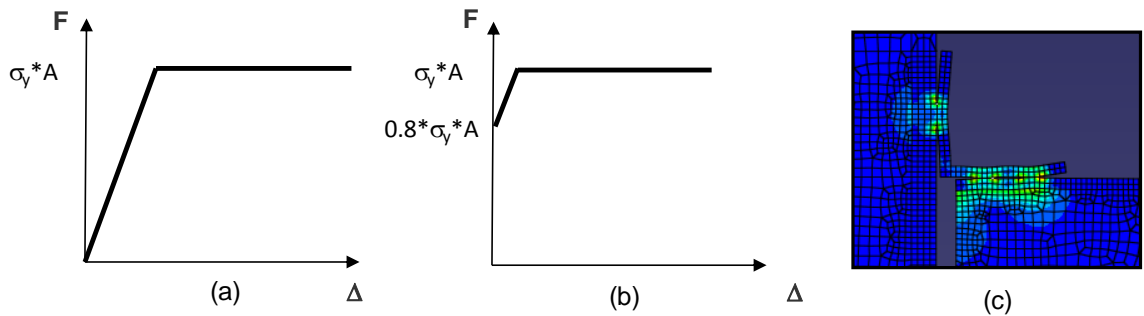


Figure 3-8 Simulating typical bolt preload (a) without pretension (b) with pretension

### 3.5.2.3 Friction and Slip

Contact pair with master-slave relationship and augmented Lagrange is used to model contact between the various surfaces. The friction coefficient used is 0.33 representing Class A surface (Kulak, Fisher et al. 1987; American Institute of Steel Construction (AISC) 2005).

A simplified slip model is used to characterize slip in the connection associated with the relative motion between the connecting elements. Spring elements are used to model the connection slip while accounting for the slip distance, which is half of the

difference between the bolt hole and the bolt-hole diameter. The reason for taking half of the distance is to account for the slip on each side of the bolt shank (1/32" slip distance for 1/16" oversized hole).

It is important to note that the shear resistance of the connection is characterized by four different stages; namely; 1) shear resistance due to friction, 2) bolt bearing, 3) bolt bending, and 4) bolt shearing through the plate. It is worth mentioning that shear resistance due to friction is a stage that is activated throughout the full loading stage of the connection and dynamically varies, depending the magnitude of pretension load present in the bolts. It is also important to note that the slip model in itself does not represent any shearing resistance of the connection. The shear resistance of the connection during the slipping stage is carried by friction between the top and seat angles and the beam and column flanges. In other words, within the slip distance, the load associated with the load-deformation curve of the springs is zero. Figure 3-9 (a), (b), and (c) show a plan view of a typical connection assembly prior to slippage, a plan view at the onset of contact between the bolt shank and the plate, and the associated load-deformation curve used to model slip, respectively.

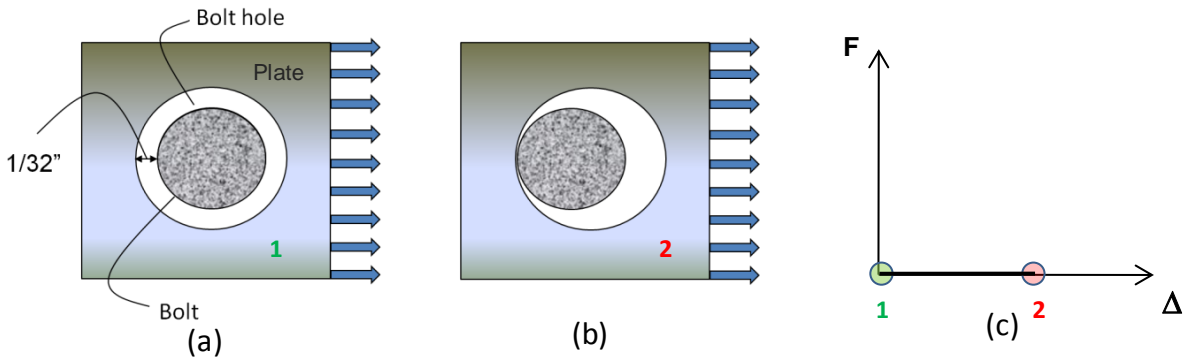


Figure 3-9 Simulating typical connection slip behavior (a) without slip (b) with slip (c) force deformation during slipping (friction excluded)

#### 3.5.2.4 Bearing, Bending, and Shearing Stiffness

As mentioned above, the initial transverse stiffness of the connection is characterized through friction between the top and seat angle and the beam and column flanges. Three other mechanisms contributing to the transverse stiffness of the connection have been defined as the bearing, bending, and shearing stiffness (Rex and Easterling 2003) and evaluated through finite element analysis; calibrated using experimental data. The test setup, shown in Figure 3-10, is aimed at evaluating the transverse stiffness of the connection through assessing the behavior of a single “loose” bolt interacting with a single plate. The bearing ( $k_{br}$ ), bending ( $k_b$ ), and shearing ( $k_v$ ) stiffness are evaluated through Equation (3.1), Equation (3.2), and Equation (3.3), respectively.

$$K_{br} = 120t_p F_y (d_b / 25.4)^{0.8} \quad (3.1)$$

$$K_b = 32Et_p (L_e / d_b - 1/2)^3 \quad (3.2)$$

$$K_v = 6.67Gt_p (L_e / d_b - 1/2) \quad (3.3)$$

Where  $t_p$ , and  $F_y$  are the plate thickness and yield strength, respectively,  $d_b$  is the bolt diameter,  $E$  is the elastic modulus of the plate,  $L_e$  is the plate edge distance, and  $G$  is the shear modulus of elasticity. It is important to note that the constant 25.4 in Equation (3.1) must be removed when working with USC units.

To simplify the derivation of the bearing stiffness equation, Rex and Easterling assumed that the problem is 2D and that the plate is at its yield strength once in contact with the bolt. For deriving the bending and shearing stiffness equations it is assumed that

the steel between the bolt and the end of the plate is modeled as a rectangular elastic fixed beam with length  $d_b$  and height  $L_e - d_b/2$ .

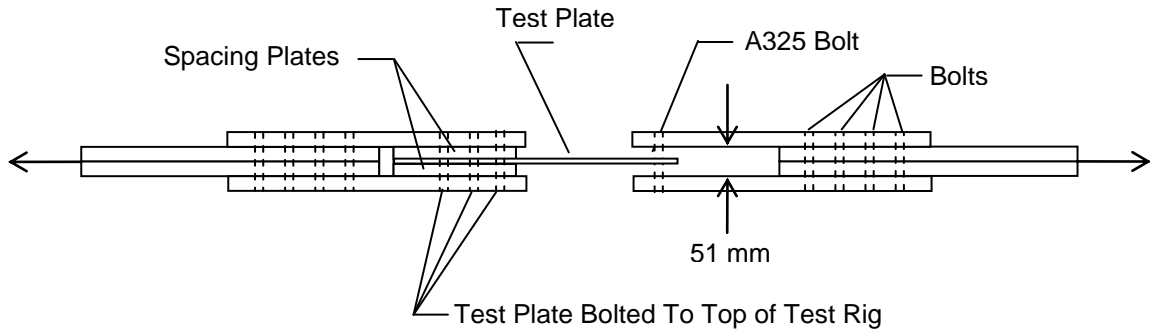


Figure 3-10 Test setup for a single bolt on a single plate, after: (Rex and Easterling 2003)

In this study, the above described model is modified to determine the three initial stiffness values ( $k_{br}$ ,  $k_b$ , and  $k_v$ ) while accounting for two deviations from the initial model. First, the bolts are interacting with two plates (beam or column flange plate and the angle) instead of one plate as in the case of Rex and Easterling's model. Secondly, when the connection is deformed, the contribution of each of the two plates to the shear resistance is in opposite directions. In other words, the top half of the bolt is interacting with one side of the angle hole while the bottom half of the bolt is interacting with the opposite side of the beam or column flange. This mechanism is schematically illustrated in Figure 3-11.



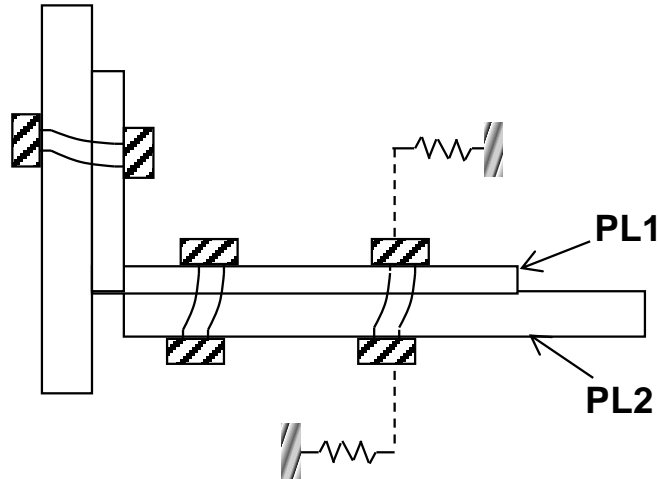


Figure 3-11 Illustrated arrangement of springs to account for the existence of two plates

In the study by Rex and Easterling, a single total initial stiffness value of the connection is determined by combining the three stiffness values assuming three springs in series as indicated in Equation (3.4). In this study, each shear resistant component is modeled separately to account for the order at which each spring/mechanism is activated in the model (i.e., bearing stiffness followed by bending stiffness then shearing stiffness). The resulting transverse stiffness model is shown in Figure 3-12. As shown in the figure, the transverse resistance is characterized by four stages; namely slipping where friction is the main contributor to the shear resistance, bearing or ovalization of the bolt-hole, bending, and shearing. Throughout all four stages, friction between the faying surfaces is activated in the finite element analysis through contact formulations.

$$K_i = \frac{1}{\frac{1}{K_{br}} + \frac{1}{K_b} + \frac{1}{K_v}} \quad (3.4)$$

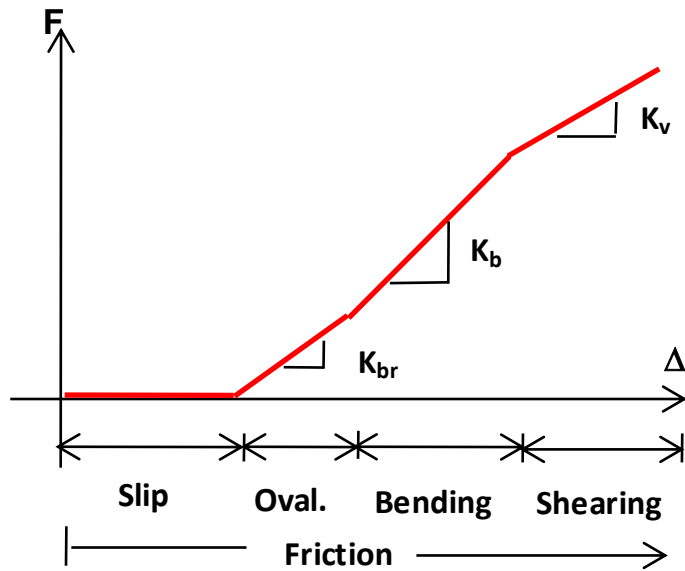


Figure 3-12 Transverse connection stiffness with all shear resistance mechanisms

### 3.5.2.5 Web Angle Idealization

The web angle leg connected to the column flange is modeled using planar 2D elements. Spring elements are used to represent the bolts connecting the angle leg to the column flange. The load-deformation relationship of the springs represents the axial stiffness of the bolt and bolt pretension while accounting for the complex 3D deformation of the angle leg. To account for such deformation, an equivalent angle strip model is developed and used to evaluate the bending stiffness of the angle leg as shown in Figure 3-13. The width and length of the equivalent strip are set equal to the width of the angle and half the length of the angle leg (accounting for tributary area on each side of the bolts), respectively. The initial step in evaluating the stiffness in each spring is setting proper boundary conditions to represent the actual physical behavior. To do so, the rotation at the end of the strip are set to zero to simulate prying action ( $\theta_1$  and  $\theta_2$  are set to zero), then a pretension force in the bolts, which is equal to  $0.8 \cdot f_y \cdot A_{\text{bolt}}$  is used as nodal

forces at the end of each strip. After formulating the boundary conditions, a unit displacement is applied at the middle of the strip to obtain stiffness coefficients for the springs. It is important to note that the flexibility of the column flange is accounted for in the finite element model through physical modeling of the column.

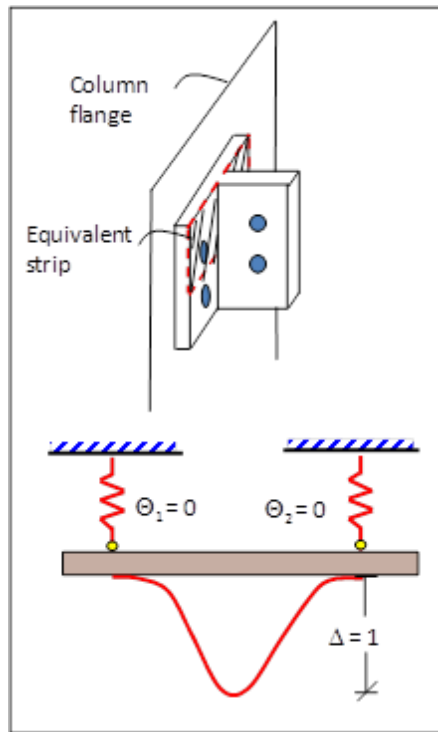


Figure 3-13 Idealization of the web angle including the equivalent strip model

### 3.5.3 Validation of the Analytical Model

The analytical model is verified against the first hybrid simulation results (frame with 30%  $M_{p_{beam}}$ ). Satisfactory agreement was observed between the experimental and analytical results as described in Chapter 4.

### 3.6 Experimental Module

The experimental component of the simulation utilizes the MUST-SIM facility at UIUC. The main testing components included a full-scale bolted beam-column subassembly. The beam comprised a portion of first-story beam in the first bay while the column included portion of the first-and second-story columns in the same bay. The experiment utilized two large LBCBs, the L-shaped strong wall, Krypton and other conventional instrumentations for measuring strain and displacement fields, and still cameras for collecting images.

#### 3.6.1 Test Specimen Configuration

As mentioned above, the column and beam are designed using strong-column-weak-beam provisions with the lateral load resisting system designed as a SMRF. The connections are designed as top-and seat-angle with double web-angle with capacity of 70%, 50%, and 30% of the beam's plastic moment capacity. Figure 3-14 shows an elevation of the frame with red dashed line representing the physical specimen to be tested.

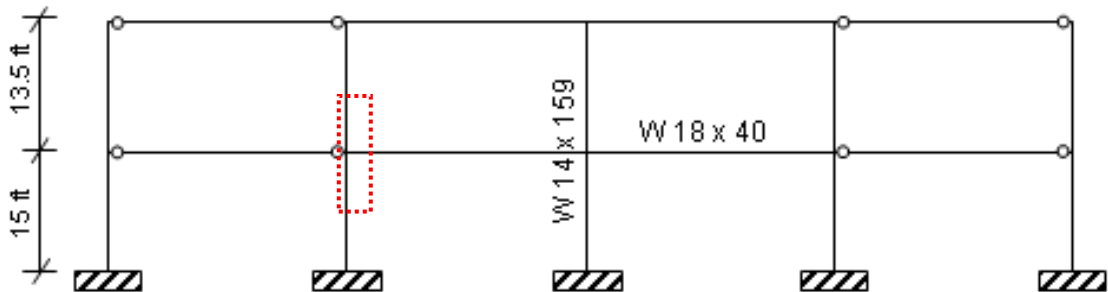


Figure 3-14 Elevation view of the SMRF with red-dashed line representing the physical specimen to be tested

### 3.6.2 Consideration for Column and Beam Length

Different factors are considered when selecting the length of the beam and column as well as the location at which the physical subassembly is extracted from the original frame (i.e. the interface points between the physical specimen and the analytical module). The plan at which the column is cut is selected such that the column remains elastic with no yielding or plastic hinge formation in the column specimen in any of the three simulations. In doing so, significant cost savings are achieved since the same column is used in all three simulations without the need for replacing the column specimen. Since W-sections are available in 20 ft length, the height of the column specimen is chosen such that enough steel is to remain for conducting material testing and quantify the material properties of the steel used. Similarly, for the beam portion of the specimen, a 20 ft long W-section is acquired for fabrication. Initial finite element results indicated local yielding of the beam web caused by load transfer resulting from the interaction between the top and seat angle with the beam flange. Therefore, it was decided to divide the beam into four different portions; three of which are used in the hybrid simulation while the fourth is used in material testing. With other constraints pertaining to the position of the LBCBs on the strong wall and the availability of steel used for the column base-plates and the end-plates connected to the end of the beam and column, the resulting final length of the column and beam is 17'-5/16" and 5'-1 5/8", respectively.

The beam and column are welded to 48" x 48" x 2 1/4" plates at their respective ends using 1 in full joint penetration welds. At the top end of the column and at the end of the beam, a positive bolted connection is used to attach the base plates to the LBCBs. At

the base of the column, additional plates and a load cell is used to fill-in the remaining gap between the column-end base plate and the strong floor such that a fully-fixed condition is achieved. Figure 3-15 shows an elevation view of the physical specimen with its final dimensions.

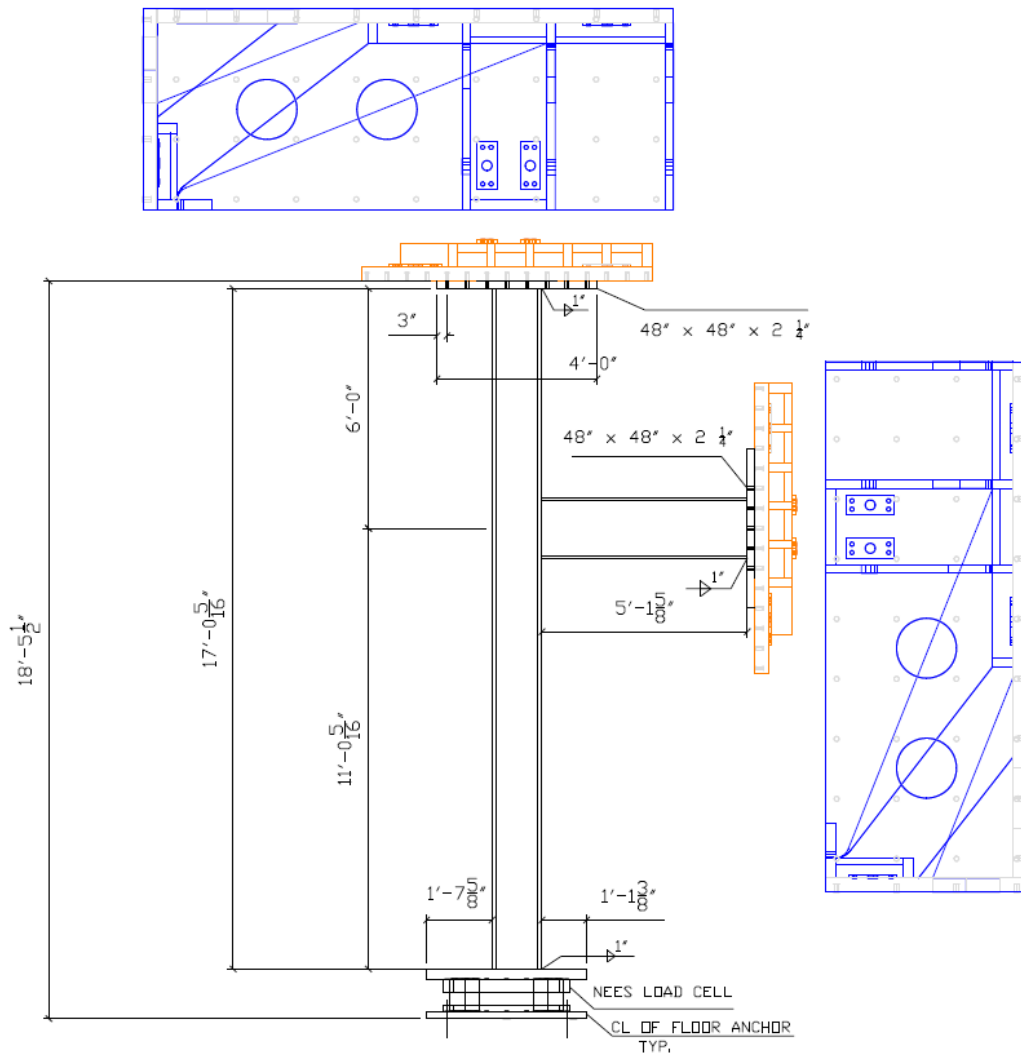
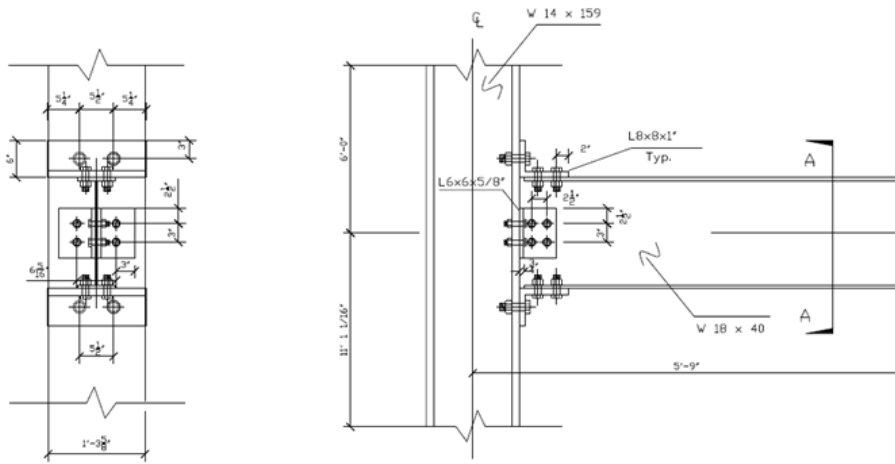


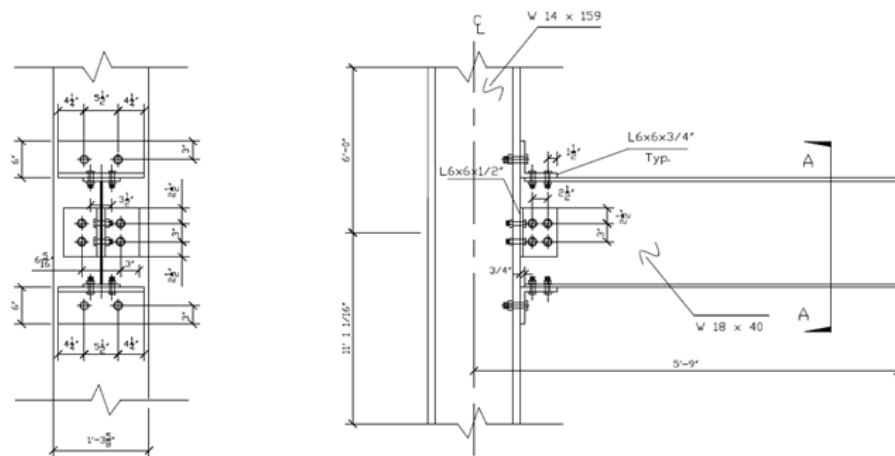
Figure 3-15 Elevation view of the physical specimen with its final dimensions

### 3.6.3 Connection Topology

As previously mentioned, the connection investigated in this study comprises top and seat-angle with double web-angle. The angle components of the connection are bolted to the beam and the column using A325 high strength structural bolts with turn-of-the-nut method. Figure 3-16 shows detailed geometry of the connections with capacity equal to 70%  $M_{pbeam}$ , 50%  $M_{pbeam}$ , and 30%  $M_{pbeam}$ .

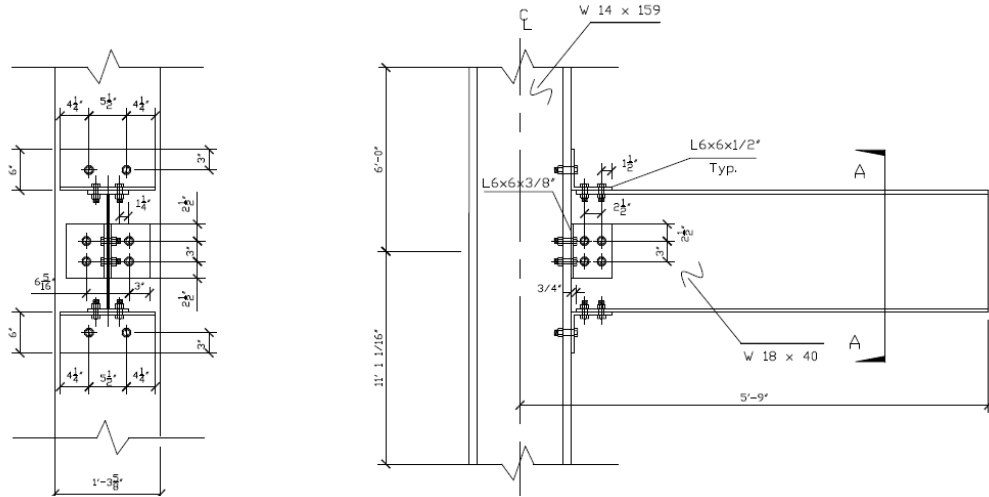


(a) 70%  $M_{pbeam}$  connection



(b) 50%  $M_{pbeam}$  connection

Figure 3 – 16 cont. at top of page 58



(c) 30%  $M_{pbeam}$  connection

Figure 3-16 Detailed geometry of the semi-rigid connections

The geometrical variation that constitutes the difference between all three specimens includes angle size, bolt size, and location of bolts (i.e. the beam and column sizes are kept the same throughout the investigation). The standardized parameters typically used for describing the geometry of these types of connections are shown in Figure 3-17. The geometrical parameters for all three connections are listed in Table 3-1.

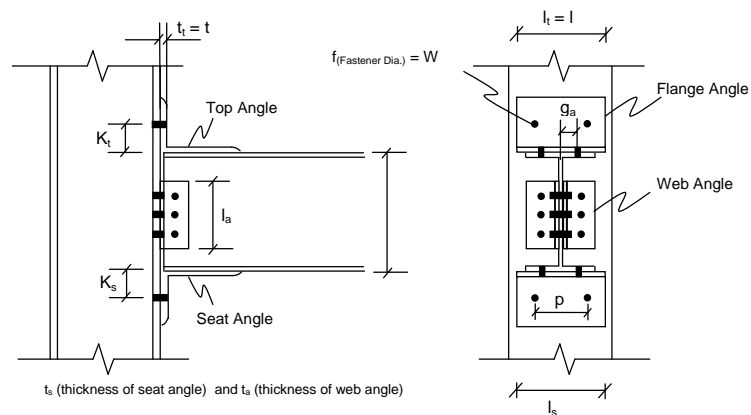


Figure 3-17 Geometrical parameters of the connection, after: (Leon, Wan Hu et al. 2004)



Table 3-1 Summary of the geometrical parameters of the connections

Connection Capacity	d (in)	T (in)	k (in)	La (in)	ts (in)	ta (in)	l (in)	ga (in)	p (in)	G (in)	W (in)
70% $M_{p_{beam}}$	17.9	1-3/16	3	8	1	5/8	16	2-3/4	5-1/2	3	1-1/4
50% $M_{p_{beam}}$	17.9	1-3/16	3	8	3/4	1/2	14	2-3/4	5-1/2	3	1
30% $M_{p_{beam}}$	17.9	1-3/16	3	8	1/2	3/8	14	2-3/4	5-1/2	3	1

### 3.6.4 Test Matrix

The tests are conducted on full-scale specimens representing a beam-column subassembly of the two-bay-two-story structure. The beam and column sections used are W18 x 40 and W14 x 159, respectively. For the purpose of preserving consistency with previously published test results, Table 3-2 summarizes the test matrix in the same format presented by Azizinamini and Radzinski (1989).

Table 3-2 Test matrix geometrical parameters

Specimen ID	Beam Section	Bolt Diameter* (in)	Top and Seat Angles			Web Angles		
			Angle	l (in)	g (in)	p (in)	Angle	la (in)
70% $M_{p_{beam}}$	W 18 x 40	1-1/4	L8 x 6 x 1	16	3	5-1/2	L6 x 6 x 5/8	8
50% $M_{p_{beam}}$	W 18 x 40	1	L6 x 6 x 3/4	14	3	5-1/2	L6 x 6 x 1/2	8
30% $M_{p_{beam}}$	W 18 x 40	1	L6 x 6 x 1/2	14	3	5-1/2	L6 x 6 x 3/8	8

\*Bolt diameter values are for the bolts connecting the top and seat angles to the column flange

Two different tests are conducted on each of the three specimens with the exception of the 70%  $M_{p_{beam}}$  specimen which was tested only once. The first test included subjecting the specimens to deformations resulting from stepping through a horizontal earthquake ground motion during the hybrid simulation. After the hybrid simulation is concluded, a post-earthquake cyclic test is initiated to assess the fundamental characteristic of the connection including its stiffness, residual capacity, and ductility. Due to technical problems associated with the LBCBs, cyclic testing of the 70%

$M_{p_{beam}}$  connection was not conducted. Table 3-3 lists a summary of the test matrix loading parameters. Detailed discussion of the ground motion scaling and the cyclic loading history is discussed below in this chapter.

Table 3-3 Test matrix loading parameters

Test ID*	Test Type	Input	Control Type
H70%	SPSD	Horizontal ground motion	Disp. control
--	--	--	--
H50%	SPSD	Horizontal ground motion	Disp. control
C50%	Cyclic	Cyclic arc motion	Disp. control
H30%	SPSD	Horizontal ground motion	Disp. control
C30%	Cyclic	Cyclic arc motion	Disp. control

\* "H" indicates hybrid testing whilst "C" indicates cyclic testing

### 3.6.5 Material Properties

To ensure the angles are the main energy dissipating elements when subjecting the frames to ground motion, the connections are designed with assumed material yield strength of 36 ksi for the angles and the beams and columns are designed with assumed yield strength of 50 ksi. Tensile coupon tests are conducted on specimens fabricated from material extracted from the beam, column and angles and the resulting stress-strain curves are used in the analytical model.

Two coupons are fabricated from the beam, the column, and the angles. Owing to their different heating and cooling rate during the hot-rolling process, the variation in the yield strength of the web and the flange is typically on the order of approximately 5%. Heavier W-sections with thick flanges, exceeding 2 inches, are expected to have larger variation in the flange and web yield strength due to the large difference in the cooling rates between the flange and the web during the manufacturing process. Since the sections used in this study are not classified as heavy sections according to AISC with

flange thickness of 1/2" and 1-3/16" for the beam and column, respectively, it was decided to fabricate the beam and column coupons from material extracted from the flanges only. Fabrication and testing of the coupons is in accordance with ASTM A370. A prototype coupon specimen, the 100 kip uniaxial universal testing machine used for testing, and the observed necking of the specimen during the tests are shown in . Summary of the material properties resulting from material testing is included in Table 3-4.

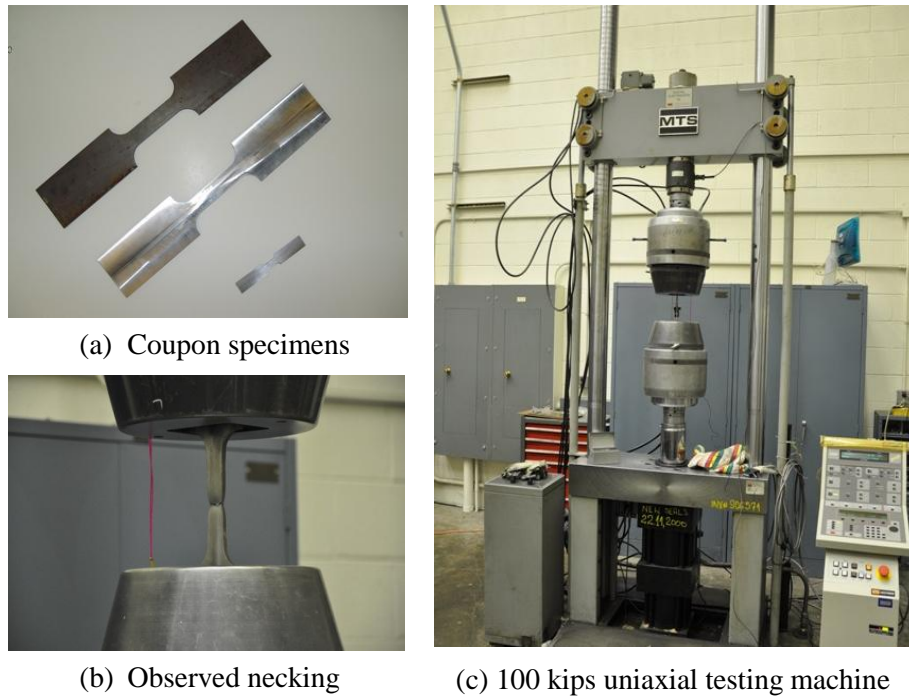


Figure 3-18 Tensile Testing of coupons specimens

Table 3-4 Material properties of beam, column, and angles

Component	$t_p$ (in)	* $\sigma_y$ (ksi)	* $\sigma_u$ (ksi)
Angles	3/8	46.1	69.6
	1/2	50.8	81.5
	3/4	52.2	75.3
	1	48.6	72.4
Beam flange	1/2	57.6	67.6
Column flange	1-3/16	54.66	71.2

\* Average of the two coupon tests is listed

### 3.6.6 Experimental Setup and Instrumentation

As illustrated in Figure 3-15, the experimental setup included a beam-column subassembly where the beam and column were welded to 48" x 48" x 2 1/4" plates at their respective ends using 1in full joint penetration welds. The base plates at the top end of the column and the right end of the beam are bolted to the LBCBs platforms which impose the required displacements and boundary conditions during testing. The base plate welded to the bottom end of the column is attached to different size steel plates which are tied to the strong floor. Several computer monitors are used during testing to provide an interactive visual analysis environment where all aspects of testing can be monitored. Figure 3-19 shows an overview of the display of each computer monitor used in the simulation, excluding the one associated with the Krypton camera. As shown in the figure, ten computers are utilized during the tests and included software needed for the experimental control and data collection. An overview of the experimental set up is shown in Figure 3-20.

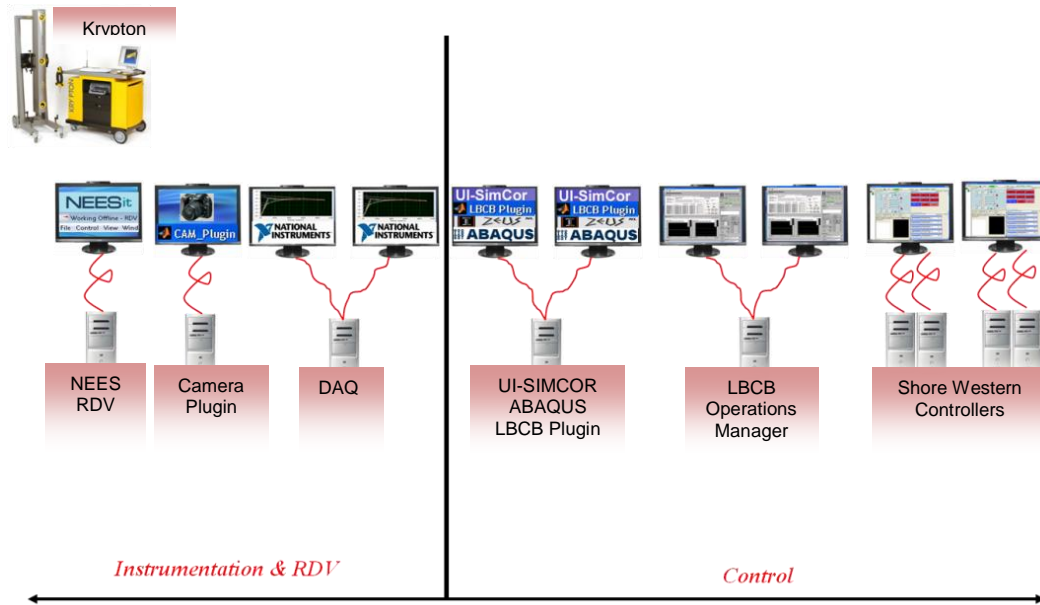


Figure 3-19 Display of computer monitors used during testing



Figure 3-20 Overview of the experimental setup

Each test included a total of 175 channels, which were installed on the specimen and recorded using a National Instrument Data Acquisition (NI-DAQ) system. In addition,

each LBCB houses 6 load cells and 6 LVDTs for displacement and load measurements, respectively, for each actuator.

The instrumentation plan is developed and installed to capture the global response of the beam-column subassembly as well as its local response. The global parameters measured during testing included displacement, rotations, forces, and moments. A dense instrumentation array is used to measure the localized deformation of the connection and included strain gauges, linear potentiometers (linear pots), inclinometers, and optical devices. The strain gauges are used to measure the strain distribution across the angles and the localized strain on the flange and web of the beam and column. The linear pots are used to measure slip of the bolts and bolt deformation, the relative deformation between the beam and column, and the panel zone deformation of the column web. The inclinometers are used to measure the relative rotation between the beam and column.

A breakdown of the sensors used to capture the local and global response of the specimens is listed in Table 3-5. Detailed description of the sensors and their locations can be found in APPENDIX B.

Table 3-5 Breakdown of the specimen and LBCBs sensors

	Sensor type	Count	Global response	Local response	Purpose
Specimen	String Pots	3	X	--	Displacement
	Linear pots	35	--	X	Displacement
	Strain gauges	134	X	X	Strain
	Inclinometers	3	X	--	Rotation
	Krypton	175	X	X	**Deformations
visual	Still cameras	6	X	X	Still images
	Video cameras	2	X	X	Video
LBCBs	LVDT	12	--	X	Displacement
	Load cells	12	--	X	***Actions
	String pots	6	X	--	Displacement

*\*XX LEDs were used*

*\*\*Deformations implies displacement and rotations*

*\*\*\*Actions implies loads and moments*

### 3.6.7 Control

#### 3.6.7.1 Elastic Deformations of the LBCBs

As previously mentioned, the actuators housed inside the LBCBs are connected at one of their end to a platen. The commands received by the LBCBs through UI-SIMCOR are specified in the Cartesian space and translated into actuator space commands. Mapping from Cartesian space to actuator space is done through a transformation matrix, resulting in motion of the platen to the desired position in space. It is important to point out that when the platen is not connected to a specimen, the resulting motion of the platen is exactly as desired. However, when a connection between the specimen and the platen is made, elastic deformation of the LBCBs could occur, leading to inaccurate motion of the platen.

Elastic deformations arise as a result of the interaction between the test specimen and the LBCBs during testing. Specifically, due to the finite stiffness of the specimen,

part of the executed motion by the actuators in their own space is consumed through the deformation of the LBCBs instead of the specimen. If no specimen is connected, the actuators are able to execute the commands with a very high accuracy on the order of 0.001 in.

To overcome the issue of elastic deformations, external sensors are used in a closed feedback loop to measure the physical displacement of the LBCBs in space, with reference to fixed external locations. The external transducers allowed for precise measurement of the in-plane rigid body displacements and rotation of the LBCB platform through the use of a variation of Newton's method with a Jacobian transformation matrix. A description and a verification of the used method can be found in (Bennier 2009)

Prior to employing the external sensor deformation approach in the large-scale facility, the small-scale (1/5<sup>th</sup>) MUST-SIM facility was used to verify the developed control protocol.

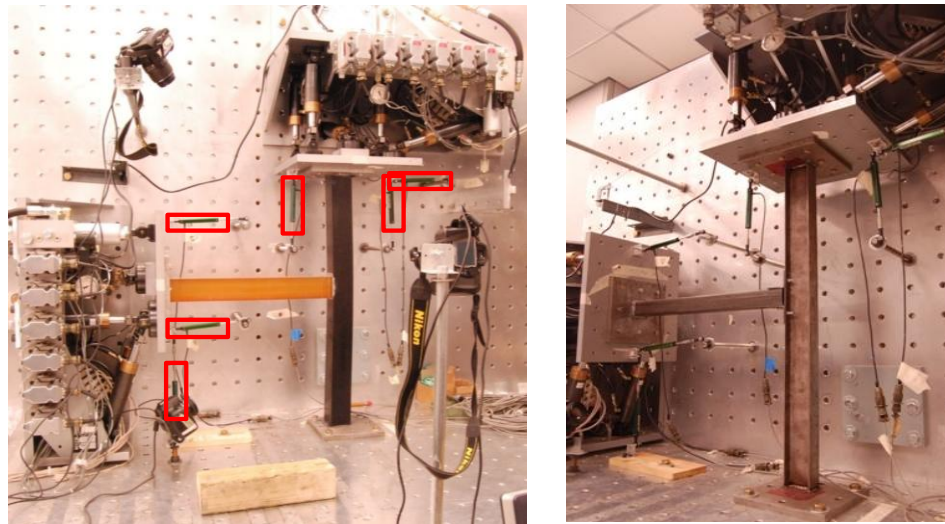


Figure 3-21 Small-scale testing facility including the rubber and steel specimens used for control verification



### 3.6.7.2 Relative Deformation Approach

As previously discussed, the physical component of the simulations comprised a beam-column subassembly in a two-story four-bay semi-rigid steel frames. Three locations are chosen for the interface between the experimental and the analytical component. The interface locations are nodes where force compatibility is enforced by UI-SIMCOR between the analytical and experimental modules. The plan at which the column is cut was selected such that the column specimen remains elastic with no yielding or plastic hinge formation in any of the three simulations. This resulted in cost savings associated with specimen fabrication since the same column can be used in all three simulations.

In each simulation step, all interface points (a total of three) received displacement commands from UI-SIMCOR and sent back their current executed displacement and the corresponding restoring forces. In the analytical module, all interface points are free to translate and rotate in planar motion based on the commands received from UI-SIMCOR. However, in the physical module, the column is fixed to the lab floor; allowing only for two points to freely move in planar space. These two points are the top end of the column and the right end of the beam, which are both connected to an LBCB, each of which is responsible for imposing the deformations received by UI-SIMCOR. The reason for physically controlling two points only in the laboratory is due to other testing commitments where a third LBCB was not readily available for usage. To overcome this issue, the concept of relative motions is used to impose deformations on the physical sub-structure by condensing the three nodal deformation values into two nodal values prior to sending the commands to the LBCBs. After the commands are

executed, the relative deformation approach is used once again to convert the two-nodal information into three-nodal information as required by UI-SIMCOR. The corresponding restoring force values at the base of the column are obtained using equilibrium since the force readings at the other two nodes are known. Prior to returning the displacement and force readings back to UI-SIMCOR, the relative displacements are inverted back into absolute displacements. The concept of relative deformation is shown schematically in Figure 3-22.

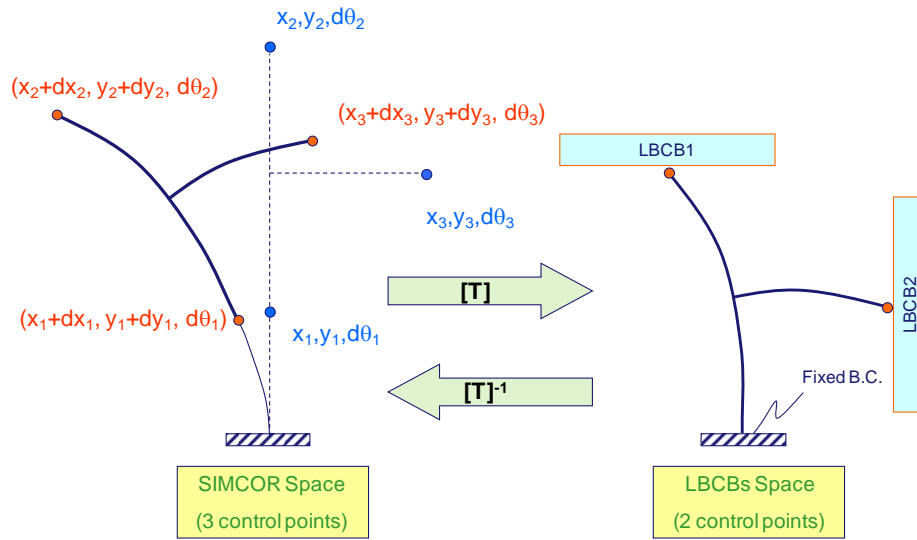


Figure 3-22 Concept of relative deformation used to map the three-point information to two-point information and vice-versa

The calculations associated with converting the three-point information to two-point information and vice versa are conducted using the LCB Plugin, which is a MATLAB-based GUI developed specifically for the tests and is shown in Figure 3-23. Verification of the used method can be found in (Bennier 2009). It is worth noting that using an LCB to control the bottom end of the column would have been a good

alternative as it eliminates the need for adopting the concept of relative deformation during testing.

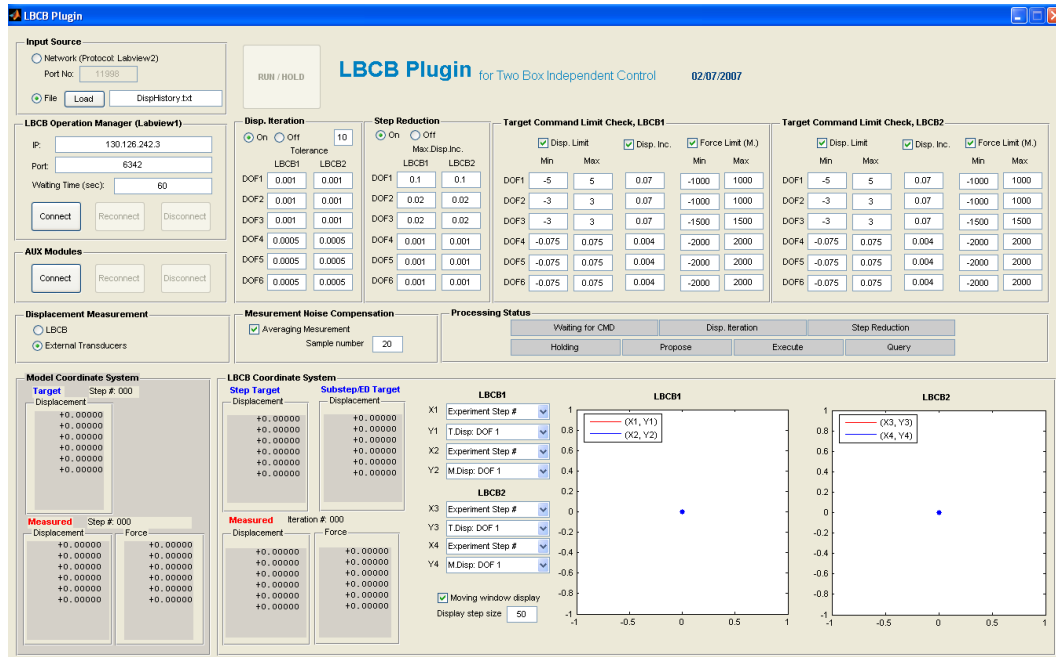


Figure 3-23 A snap shot of the LBCB plugin used during the simulation

It is worth noting that in addition to condensing the control points, the LBCB Plugin served various purposes during the simulations. For example, deformation commands sent by UI-SIMCOR to the LBCBs go through the Plugin first where they are checked against safety limits. Similarly, deformation and restoring actions measured by the LBCBs are returned to the Plugin for safety checks prior to being accepted by UI-SIMCOR. In addition, the elastic deformation calculations and the associated external control discussed above are also performed within the Plugin. Moreover, implementation of sub-stepping is also conducted within the plugin. As a safety precaution, the sub-stepping technique allowed for the reduction of the size of an experimental step into smaller steps based on a specific threshold value. The last functionality of the LBCB

Plugin is to trigger data collection once a simulation step is completed. Indeed, the Plugin is a vital component for successfully conducting the simulations.

### **3.7 Integration of the Analytical and Experimental Modules**

As previously mentioned, the integration of the experimental and analytical modules is conducted using UI-SIMCOR. The simulation starts with a stiffness evaluation step where predefined deformation values are sent to both the experimental and analytical modules for the evaluation of the system stiffness matrix. In the gravity load application step, following stiffness evaluation, gravity loads per tributary area of the moment-resisting frame are applied in the finite element model as distributed load on the beams. As a result of such, target deformation commands are sent to the LBCBs to enforce equilibrium of actions between the experimental and analytical modules, resulting in a desired deformation of the physical specimen in a way which corresponds to the application of distributed load on the specimen. In the dynamic step, time integration is conducted using the  $\alpha$ -Operator Splitting method. A schematic of the hybrid simulation approach is shown in Figure 3-24.

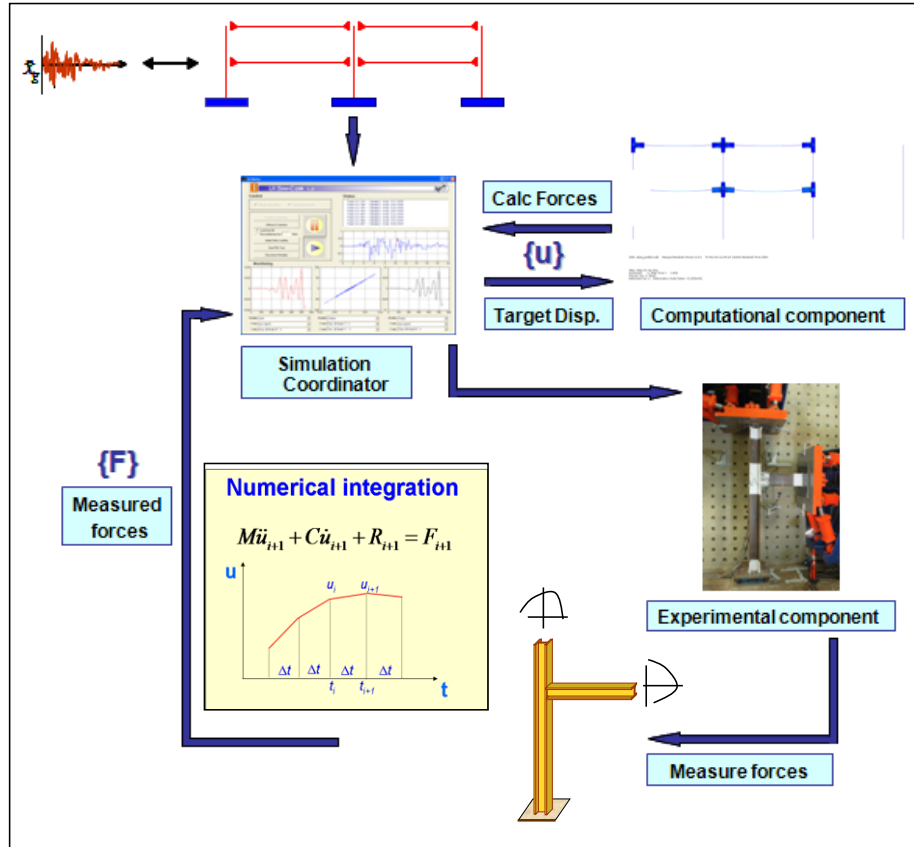


Figure 3-24 Schematic of the hybrid simulation approach

### 3.8 Selection of Ground Motion

As previously indicated, the building is designed assuming it is located in Los Angeles, California. Therefore, records collected during the Northridge and Loma Prieta earthquakes are considered as they fit the location criteria. A total of 40 records were selected with approximately 30 to 40 seconds of motion duration and 0.005 to 0.02 seconds of varied time steps. The number of records is further reduced to 20 based on epicentral distances of 5-10 km and 15-20 km such that both short-period and long-period structures would be excited. The records are further narrowed down based on the spectral acceleration to ensure that structures with periods between 0.5 sec and 1.2 sec would be

stimulated. The characteristics of the selected records are summarized in Table 3-6 and the acceleration elastic response spectra with 2% damping is shown in Figure 3-25.

Table 3-6 Characteristics of the selected ground motions for the hybrid simulation

Record	Recording Station	Recording Direction	Epicentral Distance (km)	PGA (g)
Loma Prieta (1989)	Corralitos	90	5.1	0.479
	LGPC	0	6.1	0.563
	Capitola	14.5	0.529	0
	Emeryville	260	67.7	0.25
Northridge (1994)	Sylmar	18	6.1	0.828
	Newhall FS	360	7.1	0.59
	Arleta FS	90	9.2	0.344
	Beverly Hills	9	19.6	0.416

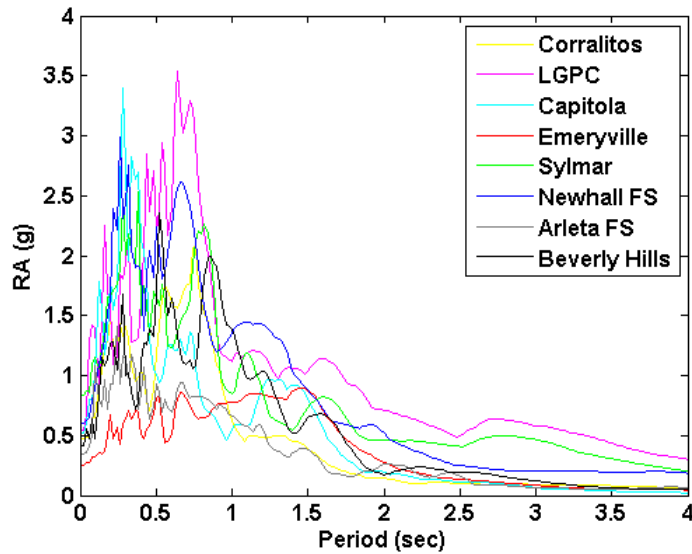


Figure 3-25 Acceleration elastic response spectra with 2% damping of the selected records

In order to select one of the eight records to be used in the hybrid simulation, an eigenvalue analysis is conducted to determine the natural period of the structure and ensure high demand on the frame in its elastic and inelastic ranges. Finite element models of the frames are developed and analyzed using ABAQUS software. The models are

discussed more in details in Chapter 4. The natural period of vibration calculated by UI-SIMCOR for the sub-structured models are 0.911 sec, 0.932 sec, and 0.971 sec for the 70%  $M_{p_{beam}}$ , 50%  $M_{p_{beam}}$ , and 30%  $M_{p_{beam}}$  frames, respectively. To ensure constant demand on the structure during its period elongation, the 1989 Loma Prieta earthquake is selected for the hybrid simulation. Specifically, the station used is USGS 1662 Emeryville, 77 km from the epicenter of the earthquake, on soft soil ( $V_s = 199$  m/s) with peak ground acceleration of 0.26 g. The record is shown in Figure 3-26.

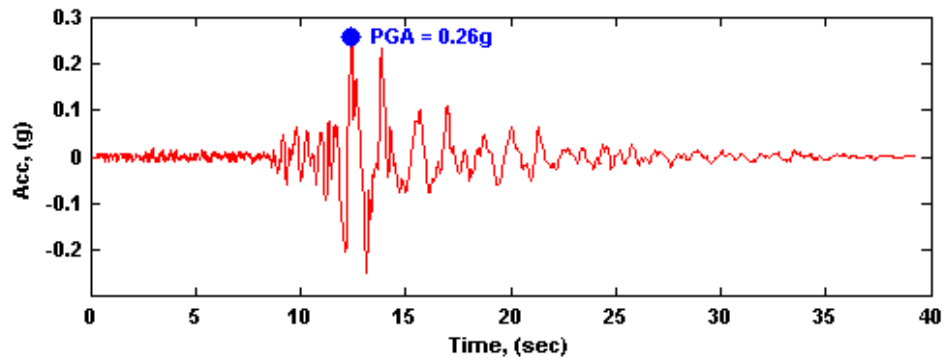


Figure 3-26 Loma Prieta acceleration time-history record with time step of 0.005 seconds

### 3.8.1 Duration of Motion and Time Step

To reduce the total time required to complete the simulation, the duration of motion and time step of the actual earthquake record are both modified. First, the duration of motion is reduced by removing the initial portion of the record, characterized by small acceleration amplitudes, while maintaining the same initial conditions of the record. Secondly, the time step is increased from 0.005 seconds to 0.02 seconds without missing any of the record peaks. The modified record is shown in Figure 3-27. Figure 3-28 shows excellent agreement between the elastic acceleration response spectrum of

the original and modified records which indicates that truncating the record and increasing the time step would not alter the impact of the earthquake on the structure.

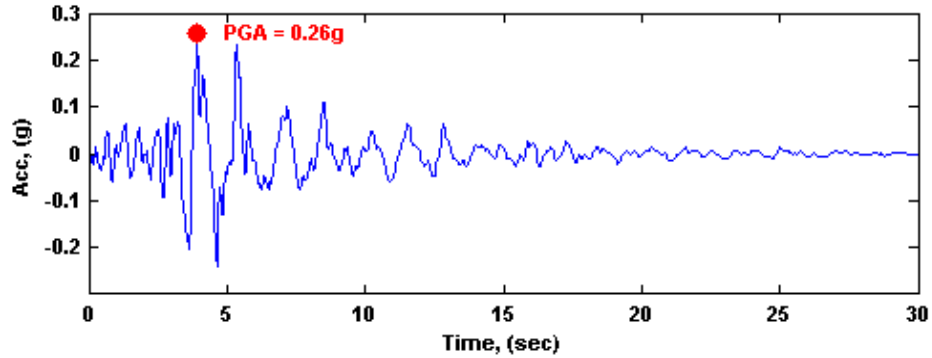


Figure 3-27 Loma Prieta acceleration time-history record with time step of 0.02 seconds

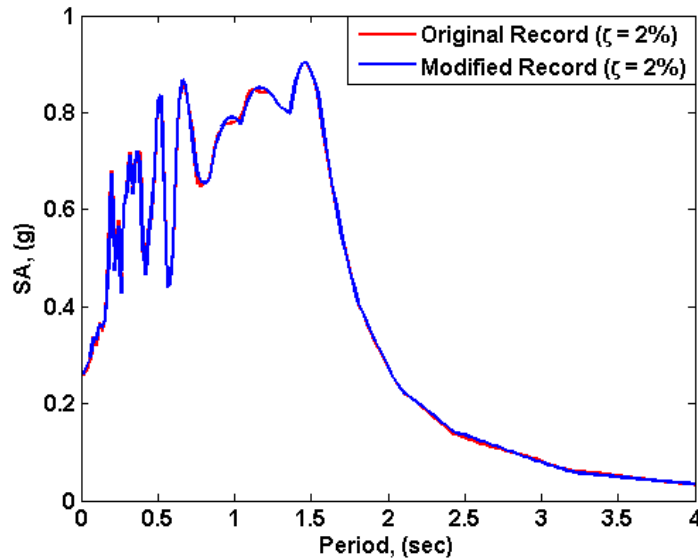


Figure 3-28 Elastic spectral acceleration of the original and modified records

### 3.8.2 Record Scaling

The record is scaled to ensure constant capacity-to-demand ratio for all three frames where the demand is chosen to be 5% higher than the capacity. The capacity is defined as the base shear value at which the base shear versus displacement curve starts



to flatten out. The curve is obtained from conventional pushover analysis of the structures as shown in Figure 3-29. The figure shows an example of how the capacity and demand are defined for the 30%  $M_{p_{beam}}$  frame. The resulting equation used for calculating the scaling factor used to scale the records is:

$$n = \frac{1.05 * V_{capacity}}{W * S_a} \quad (3.5)$$

Where;  $n$  is the scaling factor,  $V_{capacity}$  is the capacity of the structure (defined from pushover analysis),  $W$  is the weight of the structure, and  $S_a$  is the spectral acceleration. The scaling factor used in the simulations is calculated to be 0.830, 0.810, and 0.763 for the 70%  $M_{p_{beam}}$ , 50%  $M_{p_{beam}}$ , and 30%  $M_{p_{beam}}$  frames, respectively. It is important to point out that the pushover curves of all semi-rigid frames are characterized by a tri-linear curve which indicates early yielding of the frames. Such behavior is not observed through the pushover curve of the rigid frame.

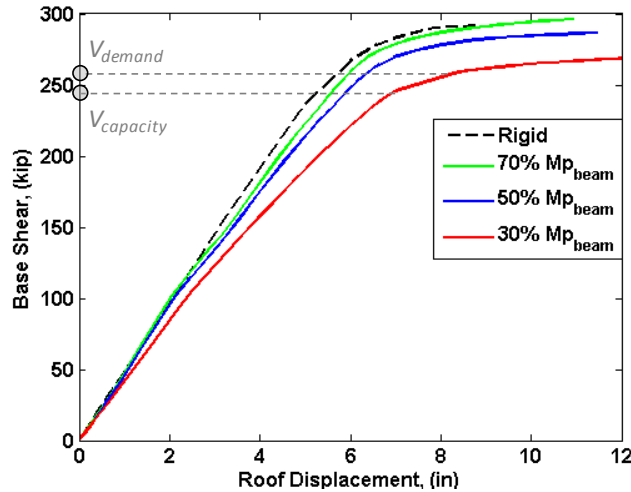


Figure 3-29 Pushover results for rigid and semi-rigid frames

The initial stiffness, yield base shear, and ultimate base shear for all three frames are listed in Table 3-7. The table also includes the corresponding values for a rigid frame of the same geometry, dimension, loading, and boundary conditions.

Table 3-7 Initial stiffness, yield, and ultimate base shear from pushover analysis

Frame ID	$k_i$ (kips/in)	$V_y$ (kips)	$V_u$ (kips)
70% $M_{p_{beam}}$	53.9	115.20	296.4
50% $M_{p_{beam}}$	43.3	107.52	286.6
30% $M_{p_{beam}}$	39.6	93.74	268.5
Rigid	48.6	266.9	291.2

It is worth noting that the 70%  $M_{p_{beam}}$  exhibit larger initial stiffness than the rigid frame. The frame although designed for semi-strength behavior, its response exceeds that of a fully rigid frame due to the size of the connection angles and bolts. According to AISC (American Institute of Steel Construction (AISC) 2005) a connection is defined as full strength once its capacity exceeds that of the beam as shown in Figure 3-30. A monotonic loading of an analytical model of a beam-column connection of the 70%  $M_{p_{beam}}$  frame indicated connection strength of 1.3 times that of the plastic moment of the beam. It is also worth mentioning that although during the hybrid simulation, the 70%  $M_{p_{beam}}$  specimen exhibited no visible permanent deformation; the maximum strength sustained by the connection during the simulation is approximately 86% of the beam plastic moment. Such value indicates the high inherent overstrength of the connection and the likelihood for the connection capacity to well exceed the plastic strength of the beam.

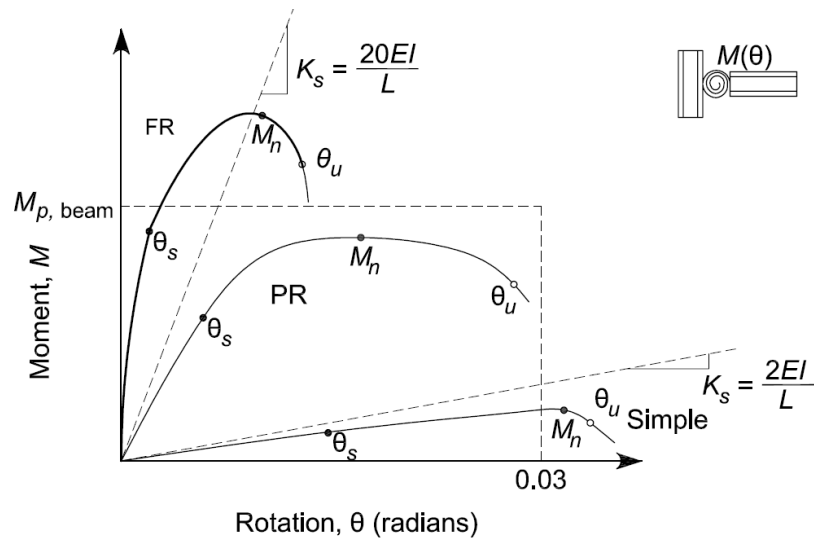


Figure 3-30 Relationship between the strength of the connection and the beam, after: (American Institute of Steel Construction (AISC) 2005)

### 3.9 Verification of the Sub-structuring Scheme

Prior to conducting the hybrid simulation using the analytical and experimental modules, a full analytical model of the 30%  $M_{p, \text{beam}}$  frame was sub-structured into two models and subjected to the ground motion using UI-SIMCOR to verify the sub-structuring technique and to ensure that the simulation yields similar results to that of a full model analyzed using ABAQUS alone. The SPSD simulation consisted of analytically dividing the whole frame into two models. The first model is a representation of the experimental module while the second model represents the analytical module as shown in Figure 3-31.

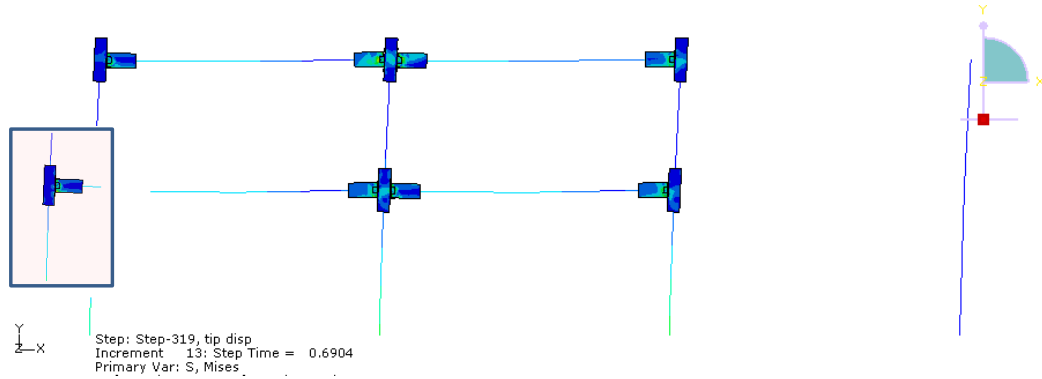


Figure 3-31 Sub-structured analytical models for the 30%  $M_{pbeam}$  frame with blue box enclosing the model representing the experimental component

The integration of both analytical models (analytical-analytical) in a PSD simulation was conducted using UI-SIMCOR. For the purpose of verifying the results of analytical sub-structured simulation, a full model is developed and nonlinear dynamic response-history analysis is carried out entirely within ABAQUS. The full model is shown in Figure 3-32.

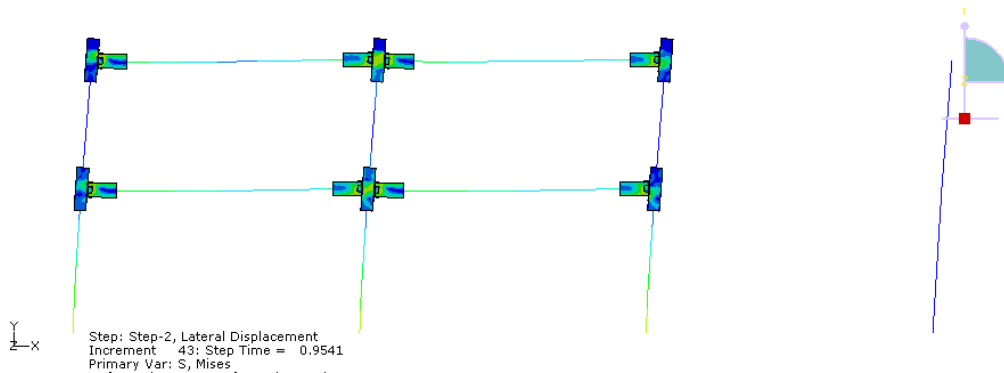


Figure 3-32 Complete analytical model of the 30%  $M_{pbeam}$  frame used for comparison against SPSD analytical simulation

The record selected for the verification is the same earthquake used in the hybrid simulation, which is the scaled 1989 Loma Prieta earthquake. The comparison is

conducted for the first 20 sec of the event since beyond the time of 20 seconds the record is characterized by very low acceleration amplitude. Figure 3-33 shows a comparison of the roof displacement resulting from the SPSS simulation and the full model. As shown in the figure, excellent match is observed in the linear range while some differences are observed in the nonlinear range of response. This could be due to many factors including for example the slight difference in the fundamental period of the structure calculated using UI-SIMCOR when compared with one calculated using the ABAQUS Eigen solver. For example, the fundamental period predicted by UI-SIMCOR is equal to 0.911 sec while ABAQUS determined the fundamental period to be 0.904 sec. In addition, differences exist between the time integration scheme used in UI-SIMCOR and ABAQUS. The observed difference in response is considered acceptable and therefore, investigation of the reasons for the inexact match will not be pursued.

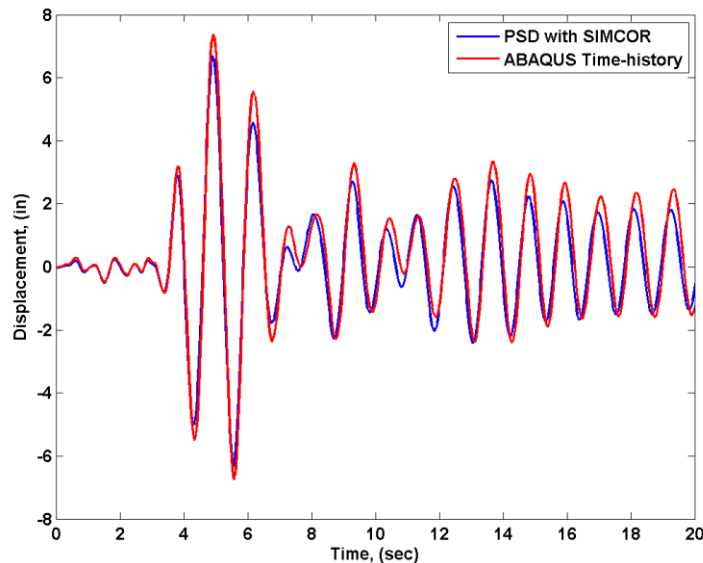


Figure 3-33 Roof displacement comparison between the sub-structured and full ABAQUS model

### **3.10 Summary and Conclusion**

In this chapter, different dynamic testing methods are highlighted and their pros and cons discussed. The concept of sub-structured PSD hybrid simulation is chosen in this study for the system-level evaluation of semi-rigid steel frames. The method requires the structure analyzed to be divided into various components; either experimental modules, analytical modules or a combination of both. In this investigation, an experimental and an analytical component of a 2-bay 2-story semi-rigid frame are used. The frame is designed as special moment-resisting frame (SMRF) with rigid connections according to IBC 2006. The rigid connections are then replaced by semi-rigid connections designed in accordance with EC3. Specifically, three connections with capacities equal to 30%, 50%, and 70% of the plastic moment capacity of the beam are employed in three different frames to investigate the response of the frames under seismic events.

The analytical component of the hybrid simulation is a multi-resolution model which comprised a 2D generalized plane strain element for the beam-to-column connections and 1D beam elements between subsequent connections. Many behavioral features are captured by the model including hot-rolling residual stresses in the angles, bolt preload, friction between faying surfaces, connection slip, and the effect of bolt-hole ovalization. The effect of the inner gravity frames on the stability of the moment-resisting frame is also accounted for in the model through a leaner column connected to the frame through tie multi-point constraint.

The experimental component of the simulation comprised a beam-column subassembly representing part of the column in the first-and second-stories and part of the beam framing into the column in the first left bay. The response of the physical specimen during the simulation is measured through the use of a very dense instrumentation array aimed at capturing the local and global behavior of the specimen. The instrumentation program utilized a noncontact measuring device (Krypton) for measuring the 3D deformation of the specimen as well as other conventional sensors for measuring strains and displacements. Stationary cameras are also used to collect images of the experiment during the simulation.

Prior to conducting the simulation, the 1/5<sup>th</sup>-scale was used for evaluating the control algorithm to be utilized in the simulation. External sensors are used in a feedback loop to account for the elastic deformation of the LBCBs and correct the position of the LBCB platens. In addition, relative deformation between the control points is used in the experimental module to account for the fact that the base of the column is fixed in the laboratory instead of being controlled by an LBCB. Accounting for elastic deformation and relative deformation is conducted using the LBCB Plugin, which is a MATLAB based software developed at UIUC. The whole simulation is orchestrated by UI-SIMCOR, which its primary responsibility is to perform the numerical integration and step through the acceleration history.

## CHAPTER 4

### SIMULATION RESULTS AND OBSERVATIONS

#### 4.1 Introduction

Pseudo-dynamic hybrid simulations are performed in order to investigate the effect of earthquake loading on the seismic performance of semi-rigid steel frames with top-and seat-angle with double web-angle connections. In addition, an assessment of the fundamental characteristics of the connection following an earthquake is conducted using cyclic tests with target rotational values which are multiples of the yield rotation of the 30%  $M_{p_{beam}}$  connection. In this chapter the experimental results, including visual description of the connection deformation, are discussed. It is important to note that dense instrumentation array was installed on the specimens to capture the behaviour. Additionally the array included sensors installed at redundant locations in case unexpected failure of any of the sensors occur during the tests. However, data collected by only a sample of the instruments are discussed in this chapter and are chosen such that the most important characteristics of the connections are highlighted.



## 4.2 Loading Scenario

### 4.2.1 Initial Stiffness Evaluation

The time integration scheme employed in UI-SIMCOR,  $\alpha$ -Operator Splitting time integration ( $\alpha$ -OS) method, requires the determination of the initial stiffness of the experimental module and the analytical module prior to conducting the simulation.

In determining the initial stiffness, UI-SIMCOR imposes a predefined target displacement on both modules for a given degree of freedom and records the restoring force needed to populate the stiffness matrix. For the experimental module, the predefined target displacement is imposed on the specimen using the LBCBs and the restoring forces are measured with load cells located at the end of the hydraulic actuators housed within the LBCBs.

### 4.2.2 Gravity Loading Stage

Prior to starting the simulations, gravity loads were applied to the system using the loading combination of:

$$1.0DL + 10psf + 0.25LL \quad (4.1)$$

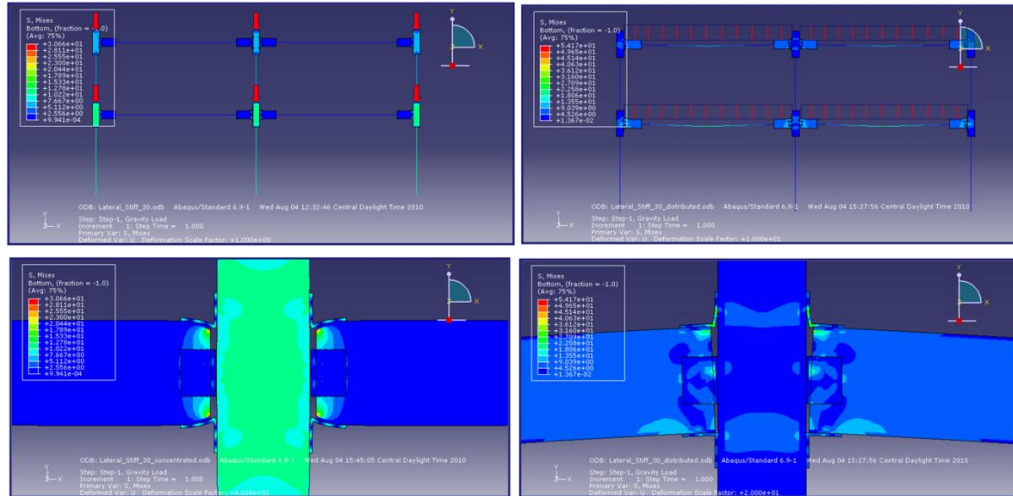
Where the *DL* indicates dead load, the 10 psf is used for partition walls, and *LL* indicates live load. The resulting distributed load is listed in Table 4-1.

Table 4-1 Distributed gravity loads applied to the frames during the simulations

Level	1.0 DL + Partitions (kips/in)	0.25 LL (kips/in)
Roof	0.0863	0.0013
1st	0.095	0.05

Gravity loads on the outer moment-resisting frames and the core gravity frames are calculated per their respective tributary areas and their effect is incorporated in the simulation. As previously discussed in Chapter 3, gravity loads carried by the core gravity frames are considered through the application of point loads on the leaner columns modeled as truss elements and connected to the frame through tie multi-point constraints. For the moment-resisting frames, gravity loads are applied as distributed load on the beam.

It is important to mention that in most of the analytical studies available in the literature, the gravity loads are applied as point loads on the columns at the beam-to-column joints instead of applying the load as distributed load on the beam. The approach is followed as some analytical software packages do not support the application of distributed loading and is justified by the fact that the  $P-\delta$  effect is taken into account regardless whether the load is applied as distributed load on the beam or as point load on the column. In spite the logic in following such approach, visual assessment of the local connection behavior indicates different localized connection deformation following the application of gravity loads as distributed load on the beam in comparison with the load being applied as point loads on column. Figure 4-1 shows the two different methods mentioned for applying gravity loads with the localized connection deformation resulting from each method. As the figure shows, applying the load as point loads at the column results in “opening” of the seat angle and “closing” of the top angle whereas the effect is reversed when the load is applied as distributed load. Such difference in angle deformation has an effect on determining the global drift value at which first yield is reached.



(a) Point load applied to the columns (b) Distributed load applied to the beam

Figure 4-1 Localized connection deformation due to gravity load application (deformation scale is set to 100x)

One approach for including the gravity load associated with the physical specimen is to include it as point loads in the analytical module at preferred locations/nodes. However, a new yet simple technique is utilized whereby gravity loads are indirectly applied to the specimen. To do so, distributed loads are applied only to the analytical model. As the case in all stages associated with testing, equilibrium has to be maintained during the initial loading stage between the experimental and analytical modules at their interface. Equilibrium is enforced as UI-SIMCOR sends target displacements to the LBCBs resulting in force and deformation compatibility between the two modules. The resulting physical deformation of the specimen is therefore representative of the gravity loading being applied. An exaggerated deformed shape of the analytical module due to gravity load is shown in Figure 4-2.

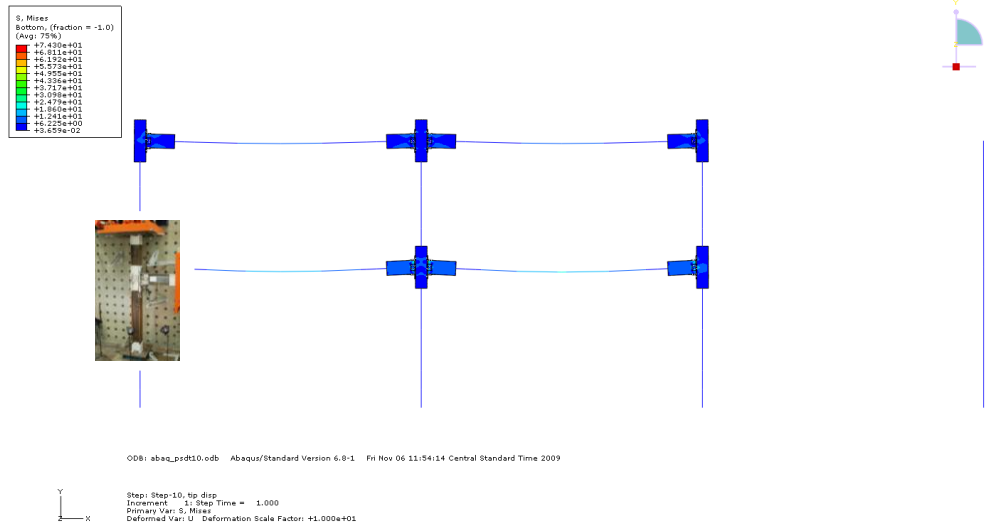


Figure 4-2 Deformed shape of the analytical module due to gravity loading (*deformation scale of the analytical module is set to 100x*)

### 4.2.3 SPSPD Tests with Selected Ground Motion

As previously discussed in Chapter 3, the 1989 Loma Prieta earthquake (record collected at the USGS 1662 Emeryville station) is used for all three hybrid simulations. For proper comparison of the seismic performance of all three frames, the record is scaled in each test with consistently defined capacity to demand ratios. Characteristics of the earthquake and the scale factor used in each simulation are shown in Table 4-2.

Table 4-2 Ground motion characteristics and scale factor

Earthquake	Mw	Station	Fault Distance		Hor. PGA (g)	Scale Factor		
			Epicentral (km)	Hypocentral (km)		30%	50%	70%
Loma Prieta (17/01/09)	7.1	Emeryville/Pacific Park Plaza Building	96	17.48	0.245	0.763	0.810	0.83

#### 4.2.4 Cyclic Tests with Different Rotation Levels

Cyclic tests are conducted to evaluate the post-earthquake connection characteristics. Due to technical problems with the LBCBs, only the 30%  $M_{p_{beam}}$  and 50%  $M_{p_{beam}}$  connections are cyclically tested. To ensure no participation of the beam end connected to the LBCB to the moment resistance during the simulation and that the LBCB motion remains tangent to the load path, the deformation path is applied such that the center of the connection is acting as the center of rotation. Figure 4-3 shows the motion path of LBCB2 during the cyclic tests. Equation (4.2) and (4.3) are used to derive the target cycling loading protocol.

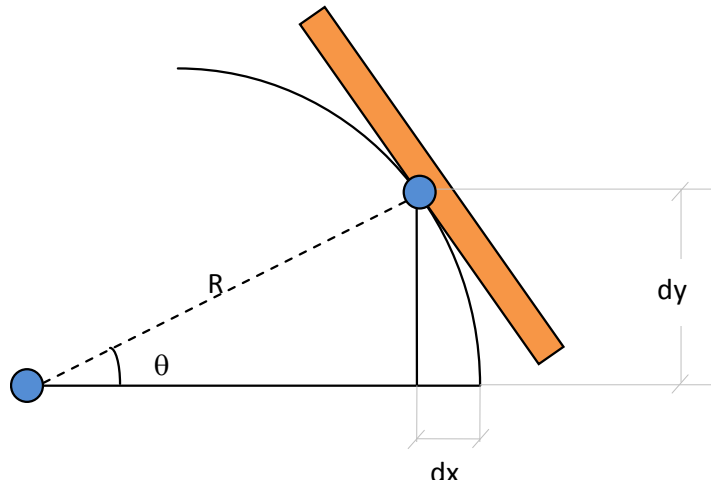


Figure 4-3 Motion path of LBCB2 during the cyclic tests

$$dx = 2R \sin^2\left(\frac{\theta}{2}\right) \quad (4.2)$$

$$dy = 2R \sin\left(\frac{\theta}{2}\right) \cos\left(\frac{\theta}{2}\right) \quad (4.3)$$

It is important to note that during cycling of the 30%  $M_{p_{beam}}$  connection a strut action developed at the compression flange of the beam. This is due to the fact that the center of rotation for the cyclic loads is taken at the mid-height of the beam. For the 50%  $M_{p_{beam}}$  connection, a traveling center of rotation is used to move the center of motion towards the compression flange as the rotations increased and allow the tension angle to freely open up.

The 30%  $M_{p_{beam}}$  cyclic test included two cycles through multiples of the yield rotation, which is determined from the hybrid simulation results to be 0.002 rad. Specifically, two cycles are applied at  $3\theta_y$ ,  $6\theta_y$ ,  $12\theta_y$  and  $24\theta_y$  for a total of 8 cycles. The increase in the target rotation is based on whether or not the connection sustained any damage. If no damage is observed at a given rotation, then the target rotation is increased. The imposed LBCB deformation history used to achieve the desired end rotation is shown in Figure 4-4. For proper comparison between the cyclic behaviors of the two tested connections, the same deformation demand is imposed on the 50%  $M_{p_{beam}}$  connection.

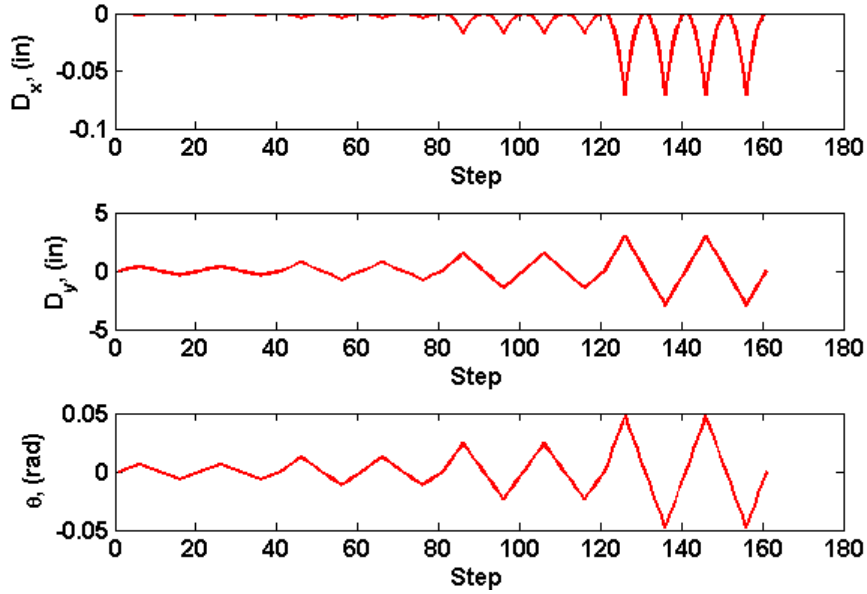


Figure 4-4 Deformation commands imposed at the LBCB connected to the beam end to achieve the desired connection rotation during the cyclic tests

### 4.3 Frame with 70% $M_{p_{beam}}$ under Earthquake Loading

#### 4.3.1 Comparison with Analytical Predictions

Comparison between the predicted and measured second-story displacement for the frame with connection capacity equal to 70%  $M_{p_{beam}}$  is shown in Figure 4-5. Acceptable correlation is observed between the analytical predictions and hybrid simulation except for the range of time between 8.92 sec and 10.34 sec. The predicted maximum absolute displacement of the second story is 6.16 in, while the maximum absolute second-story displacement resulting from the hybrid simulation is 6.48 in and occurred at time 5.02 sec. The resulting error associated with the difference between the hybrid simulation results and the analytical predictions for the second-story displacement is -4.94%. Small difference in the frame period elongation is noted between the analytical

predictions and the hybrid simulation with larger difference observed beyond the peak response.

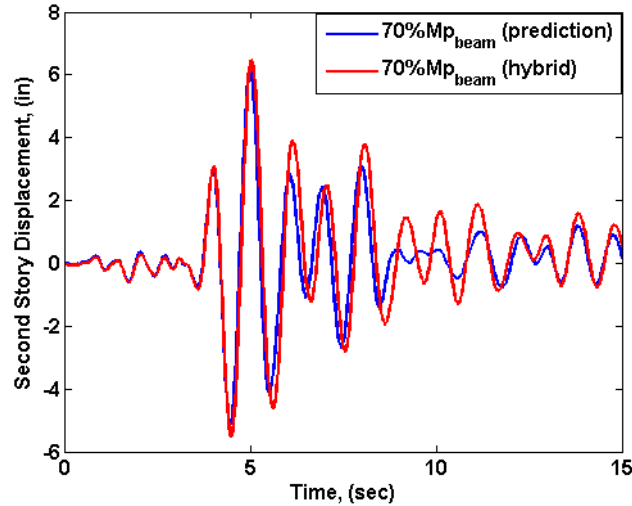


Figure 4-5 Second-story displacement comparison between the hybrid simulation and the analytical predictions for the 70%  $M_{p_{beam}}$  specimen

The overall comparison between the analytical predictions and hybrid simulation for the first-story displacement is similar to that of the second-story displacement where reasonable match is observed between both as shown in Figure 4-6. The predicted maximum absolute displacement of the first story is 2.67 in, while the maximum absolute first-story displacement resulted from the hybrid simulation is 2.89 in at time 5.02 sec. The corresponding error between the hybrid simulation results and the analytical predictions for the first-story displacement is -7.61%.



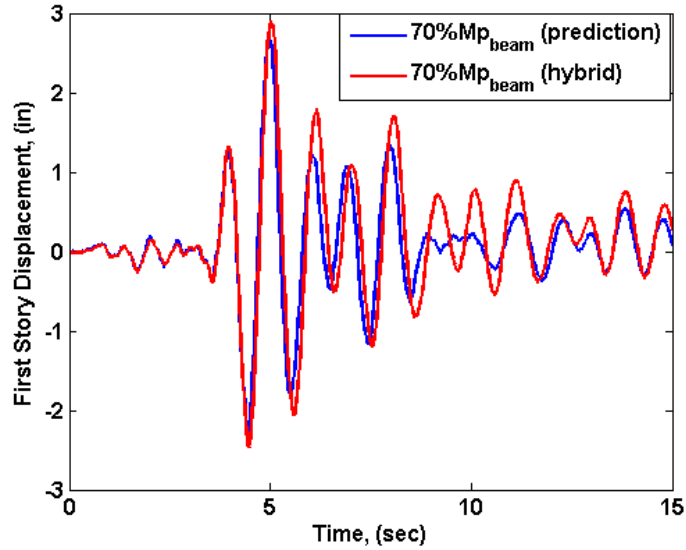


Figure 4-6 First-story displacement comparison between the hybrid simulation and the analytical predictions for the 70%  $M_{p_{beam}}$  specimen

Figure 4-7 shows comparison between the predicted and hybrid simulation base shear. Similar to previous comparisons, reasonable agreement is observed between the predicted and the actual response. The maximum absolute base shear predicted is equal to 280.4 kips, while the corresponding value resulting from the hybrid simulation is equal to 281.6 kips at time 5.06 sec. The resulting error between the hybrid simulation results and the analytical predictions for the base shear is -0.426%.

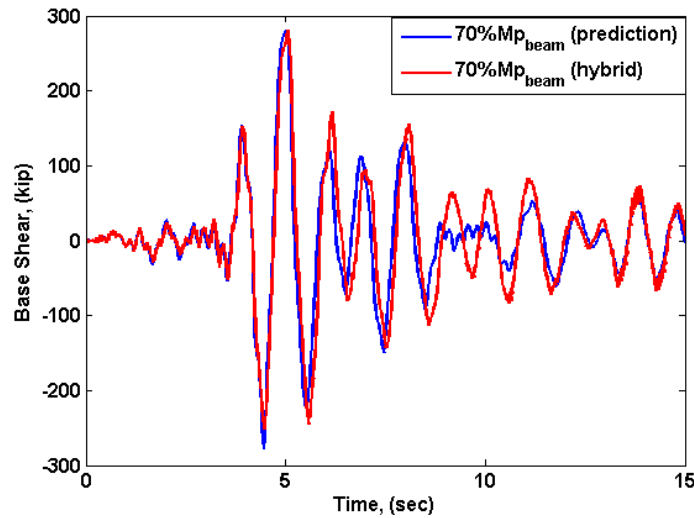


Figure 4-7 Base shear comparison between the hybrid simulation and the analytical predictions for the 70%  $M_{p_{beam}}$  specimen

In order to verify the analytical model and assess its capabilities in capturing the local moment-rotation relationship of the connection, a comparison is made between the analytical predictions and the physical specimen response during the hybrid simulation. Figure 4-8 shows a comparison of the rotation versus time between the predicted and the test value. Similarly, Figure 4-9 shows a comparison of the moment versus time between the predicted and the hybrid simulation results for the same specimen.

As shown in both figures, up to the first peak of moment response (time range between 0 sec and 3.72 sec) small difference is observed between the analytical prediction and the hybrid simulation results. The predicted moment and rotation values at the first peak response are 1077 kips.in and 0.0071 rad, respectively. The corresponding moment and rotation are measured to be 1288 kip.in and 0.0072 rad, respectively. The error between the predicted and measured response is therefore -16.38% for the moment and -1.39% for the rotation. It is worth noting that both the moment and rotation curves

start with an offset value which resulted from the gravity loading step. It is also important to note that these values correspond to yielding in the connection. In addition, the response of the connection is characterized by audible slip during the whole simulation time including the gravity loading stage. From evaluating the response up to time of 3.72 sec, one can conclude that the model captures the inelastic features of the connection with very reasonable accuracy.

The figures also show large unmatched response between the analytical predictions and the hybrid results, particularly for the three peak responses at time 4.20 sec, 4.76 sec, and 5.26. For the large positive peak response, the maximum predicted rotation at time 4.76 sec is 0.0143 rad while the measured response is 0.0197 rad, which corresponds to an error of -27.41%. The moment associated with the rotation at 4.76 sec is 3546 kips.in for the predicted response and 2454 kips.in for the measured response. The error between the predicted and measured large positive response is 44.50%.

The reason for the discrepancy is due to a very large and highly dynamic slip that occurred during the simulation. The slip is characterized by very loud noise and shaking of the specimen, causing some of the sensors to fall off during testing. When the very dynamic slip occurred, it resulted in large difference of the measured actions between the experimental module and the analytical module. As a result, rotational commands are sent to the LBCB connected to the beam to impose larger rotations on the beam as UI-SIMCOR attempts to maintain equilibrium at the interface of the modules. If equilibrium is not reached, larger rotations are imposed on the specimen in the next step in effort to increase the restoring forces to achieve equilibrium of actions. The process continues until the record reversed directions, and eventually equilibrium is reached at the same

load where slip occurred. It is rather surprising to note that all three connections experienced this dynamic slip at the exact same step in the simulation with the highest slip observed in the 30%  $M_{p_{beam}}$  followed by the 50%  $M_{p_{beam}}$ , then the 70%  $M_{p_{beam}}$  as shown in Figure 5-6, Figure 5-7, and Figure 5-8 for the 70%  $M_{p_{beam}}$ , 50%  $M_{p_{beam}}$  and 30%  $M_{p_{beam}}$ , respectively.

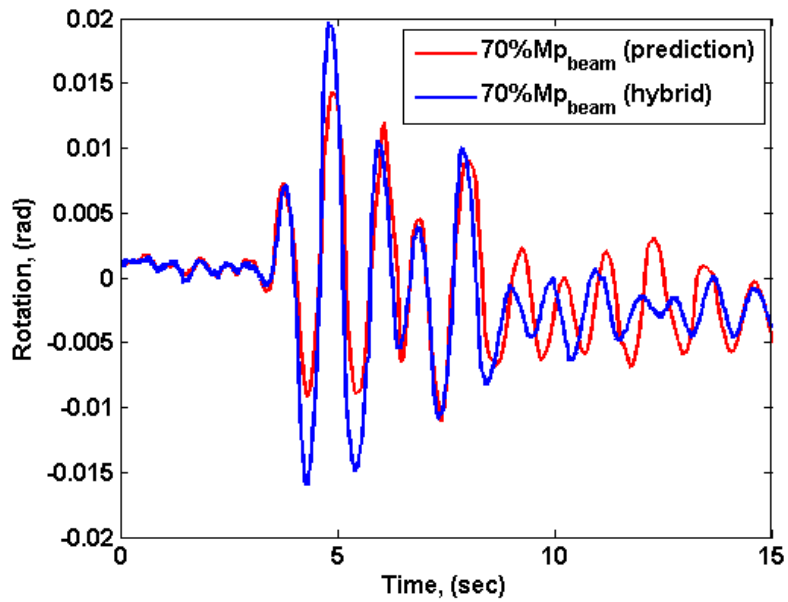


Figure 4-8 Rotation comparison between the hybrid simulation and the analytical predictions for the 70%  $M_{p_{beam}}$  specimen

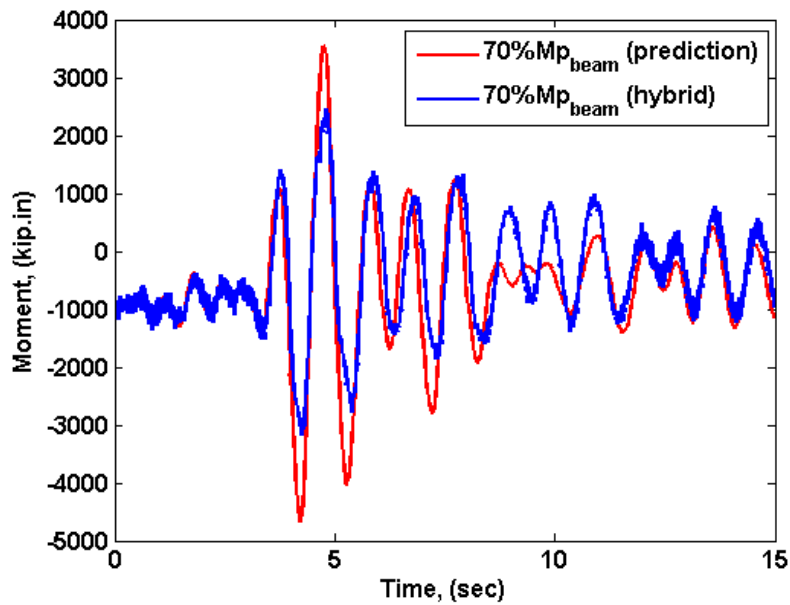


Figure 4-9 Moment comparison between the hybrid simulation and the analytical predictions for the 70%  $M_{p_{beam}}$  specimen

## 4.3.2 Experimental Observations

### 4.3.2.1 Connection Slip

Data on the relative motion between the bolts connecting the top and seat angle to the top and bottom flange of the beam, respectively, are collected. It is important to note that although such motion is referred to here as slip, the value represent slip of the bolts in the bolt hole as well as bolt deformation. Slip in both the top angle and the seat angle connection is shown in Figure 4-10 and Figure 4-11, respectively. The top left image of the figures shows the arrangement of the linear pots used for measuring the relative deformation between the connection components while the top right image includes the sensor ID with the bolts labeled as bolt 1 through bolt 4 as shown in the figures. Opposite signs for the measured slip between the top and seat angles are observed which is expected since the connection is asymmetric. During the simulation, slip is visually

observed and also heard throughout the whole test. The maximum absolute slip between the top angle and the top beam flange was measured in bolt 3 and is equal to 0.149 in. It is important to note that small amount of slip is observed in bolt 1. The maximum absolute slip between the seat angle and the bottom flange of the beam, measured in bolt 3, is equal to 0.162 in.

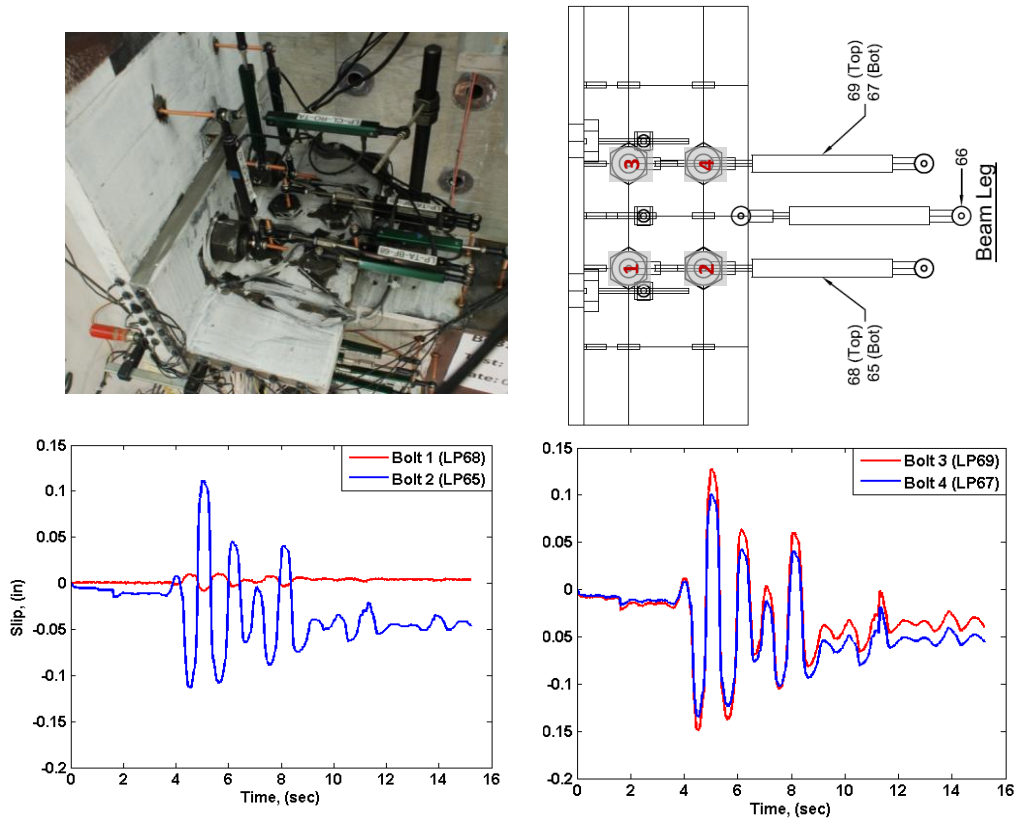


Figure 4-10 Slip of the top angle bolts relative to the top beam flange during the hybrid simulation of the 70%  $M_{p_{beam}}$  frame

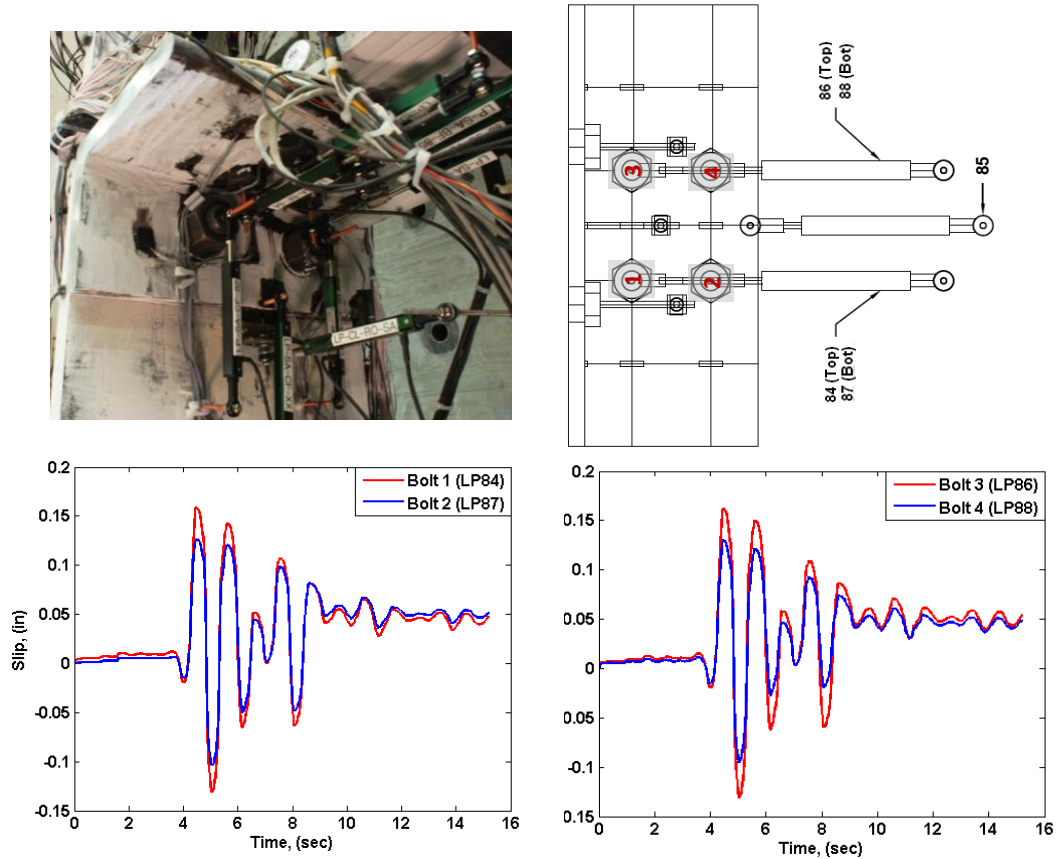


Figure 4-11 Slip of the bottom angle bolts relative to the bottom beam flange during the hybrid simulation of the 70%  $M_{p_{beam}}$  frame

#### 4.3.2.2 Localized Deformation

The deformation of the specimen is characterized mainly by yielding in the top and seat angles and in the beam flange and web. Very small deformation is visually observed at the end of the simulation in the top angle and seat angle as shown in Figure 4-12. Despite the low connection deformation, flaking of the whitewash, which was painted on the specimen prior to testing, is observed particularly on the top flange and beam web. The visual pattern resulting from flaking of the whitewash provides good indication of the localized deformation and yield line formation in the specimen. No failure of any of the connection components is observed during the test.

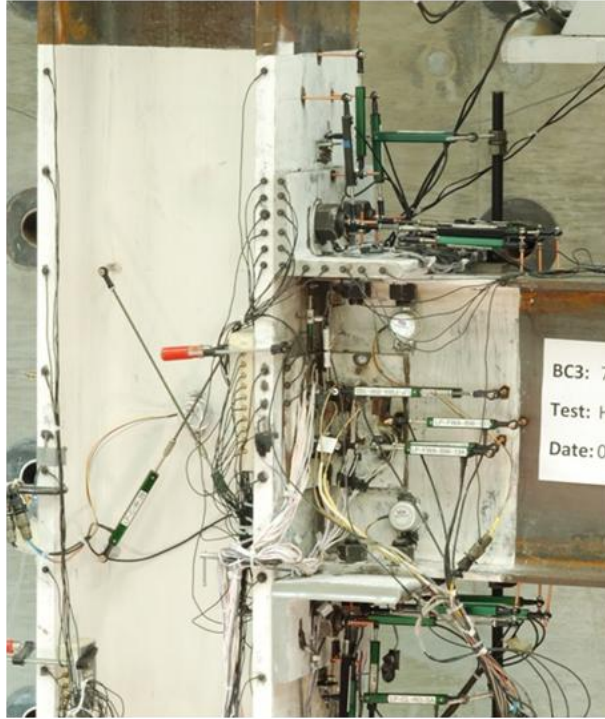


Figure 4-12 Deformation of the specimen during the hybrid simulation of the 70%  $M_{p_{beam}}$  frame

The localized yielding in the connection is measured using special strain gauges capable of measuring strain in excess of the yield strain. Uniaxial strain gauges are installed at various locations on the top and seat angle legs to characterize the distribution of stresses in the angles as influenced by stress raisers such as sharp re-entry corners and bolt holes. The left image of Figure 4-13 shows the layout of strain gauges installed on both legs of the top angle. The largest measured strain in the leg connected to the beam flange is equal to 0.0056 as shown in the figure, which is higher than the material yield strain. Similarly, large strain in the beam web resulting from the interaction between the angles and the beam, in addition to the nominal stress, is also captured through the installation of high yield strain gauges. The gauges are installed in a rectangular rosette configuration to allow for the determination of the principal strains and their orientation



with respect to the rosette gauge if needed. The maximum absolute strain is equal to 0.011 and is measured by the gauge oriented vertically on the web with the other two gauges exceeding the yield strain of the material as well.

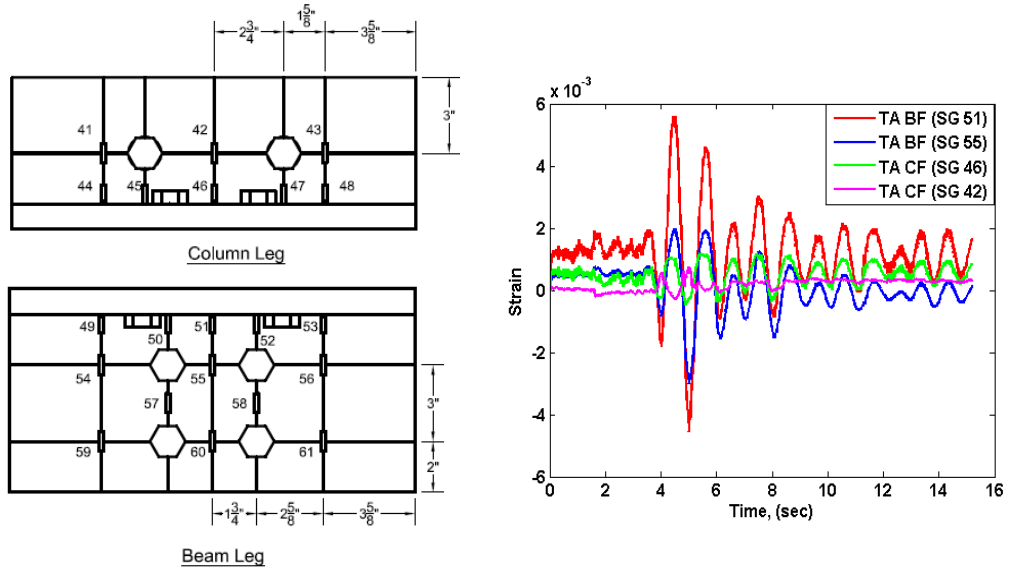


Figure 4-13 Strain measurements in the top angle legs connected to the beam flange and column flange during the hybrid simulation of the 70%  $M_{p,beam}$  frame

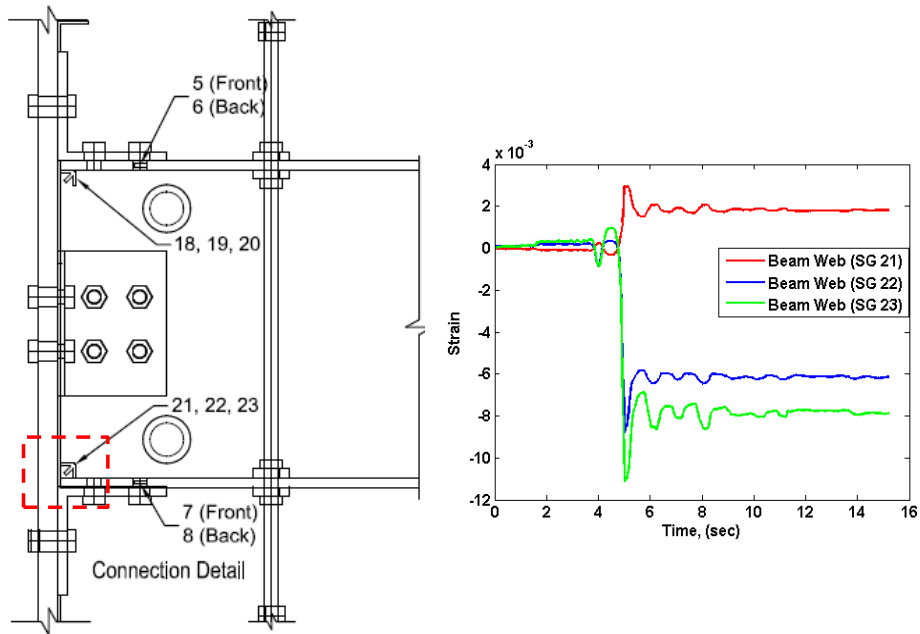


Figure 4-14      Localized strain in the beam web measured by the rectangular rosette gauges during the hybrid simulation of the 70% Mpbeam frame

#### **4.3.2.3 Relative Deformation of Beam with Respect to Column**

The deformation of the beam relative to the column is measured for the purpose of evaluating the connection relative rotation, which can be correlated with the moment at the column face. Since such information is of a very high importance as it characterizes the connection behavior, two different approaches are used to measure the deformation of the beam relative to the column. The main system utilized two linear potentiometers, with an accuracy of 0.001 in, which are perpendicularly mounted to the column and parallel to the beam (one above the top angle and one below the seat angle). With such arrangement, the relative displacement between the beam and column can be measured as the connection is cycled. The relative displacement between the top and bottom linear pots divided by the vertical distance between them is the corresponding rotation of the connection, which is presented in Chapter 5. The arrangement of the linear pots for measuring the relative displacement between the beam and column is shown in Figure 4-15. The maximum absolute relative displacement of the top of the beam with respect to the column is equal to 0.325 in while the maximum absolute relative displacement of the bottom of the beam with respect to the column is 0.303 in.

The second system used for measuring the relative rotation between the beam and column included three inclinometers (two mounted on the beam and one on the column). Specifically, one inclinometer is mounted at the center of the column panel zone, while the two other inclinometers are mounted on the beam web, directly above the bottom flange and directly below the top flange as shown in Figure 4-15. It is generally known

that inclinometers lack the level of accuracy needed for precise measurements. However, in using them, a level of redundancy in obtaining the moment-rotation relationship is ensured. It is important to note that it was expected that the two inclinometers on the beam, placed at two different locations, will not result in the same rotation values since the Euler-Beam theory assumption of “plane sections remain plane” will not be necessarily valid under large deformation. Therefore, the rotation of the beam is calculated as the average of the two inclinometers mounted on the beam. The difference between the beam and column rotation is taken as the relative rotation of the connection as discussed in Chapter 5. The maximum absolute rotation of the inclinometer installed near the top end of the beam web is measured to be  $0.471^\circ$  while the maximum absolute rotation of the bottom of the beam inclinometer is measured to be  $0.477^\circ$ . The maximum absolute rotation measured by the column inclinometer is  $0.821^\circ$ .

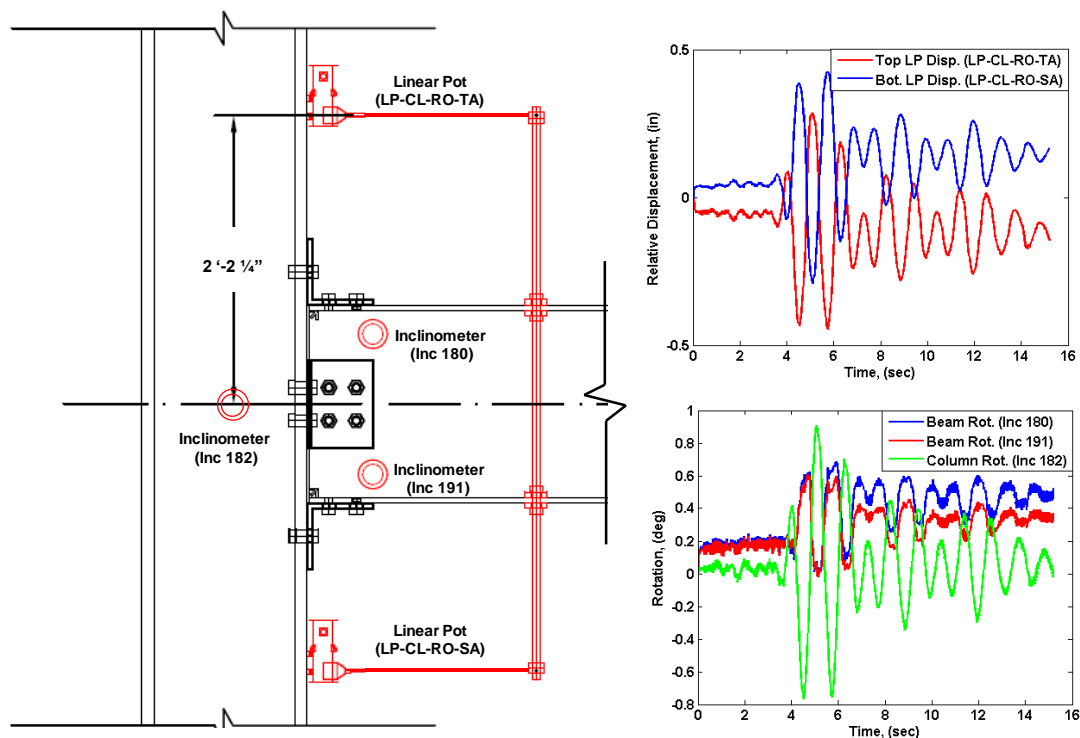


Figure 4-15      Rrelative rotation measurements between the beam and column during the hybrid simulation of the 70%  $M_{p_{beam}}$  frame

#### **4.4 Frame with 50% $M_{p_{beam}}$ under Earthquake Loading**

##### **4.4.1 Comparison with Analytical Predictions**

Comparison between the predicted and measured second-story displacement for the frame with connection capacity equal to 50%  $M_{p_{beam}}$  is shown in Figure 4-16. The figure shows good comparison between the analytical predictions and hybrid simulations. The predicted maximum absolute displacement of the second story is 6.73 in, while the maximum absolute second-story displacement resulting from the hybrid simulation is 7.17 in at time 5.08 sec. The resulting error associated with the difference between the hybrid simulation results and the analytical predictions for the second-story displacement is equal to -6.13%.

Larger period elongation is observed from the hybrid simulation in comparison with the analytical prediction, which implies that the analytical model is stiffer than the physical specimen. This is expected since stiffness and strength degradation of the material are not account for in the analytical model. The difference between the actual and predicted period elongation increase with increasing the number of cycles, which could be the reason for the larger difference observed towards the end of the simulation as shown in the figure.

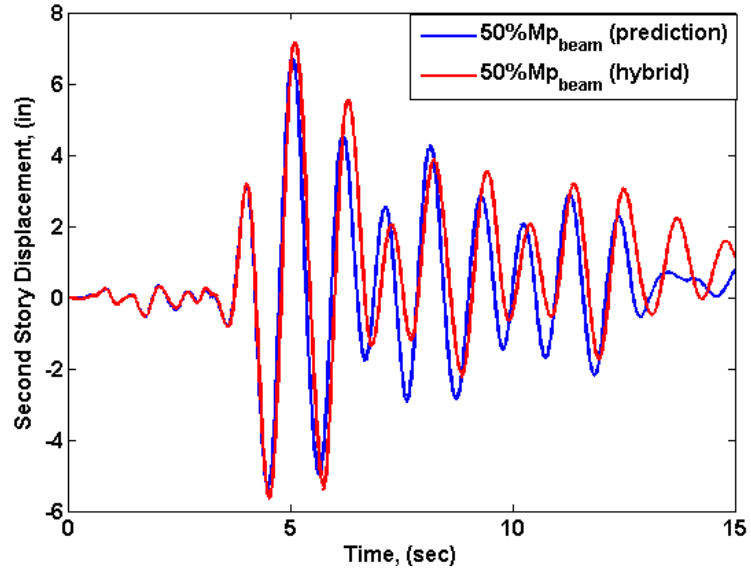


Figure 4-16 Second-story displacement comparison between the hybrid simulation and the analytical predictions for the 50%  $M_{p_{beam}}$  specimen

Reasonable agreement is also observed between the analytical prediction and the hybrid simulation for the first-story displacement as shown in Figure 4-17. The maximum absolute displacement of the first story is predicted to be equal to 2.87 in, while the maximum absolute first-story displacement resulting from the hybrid simulation is equal to 3.35 in at time 5.02 sec. The corresponding error between the hybrid simulation results and the analytical predictions for the first-story displacement is equal to -14.32%.

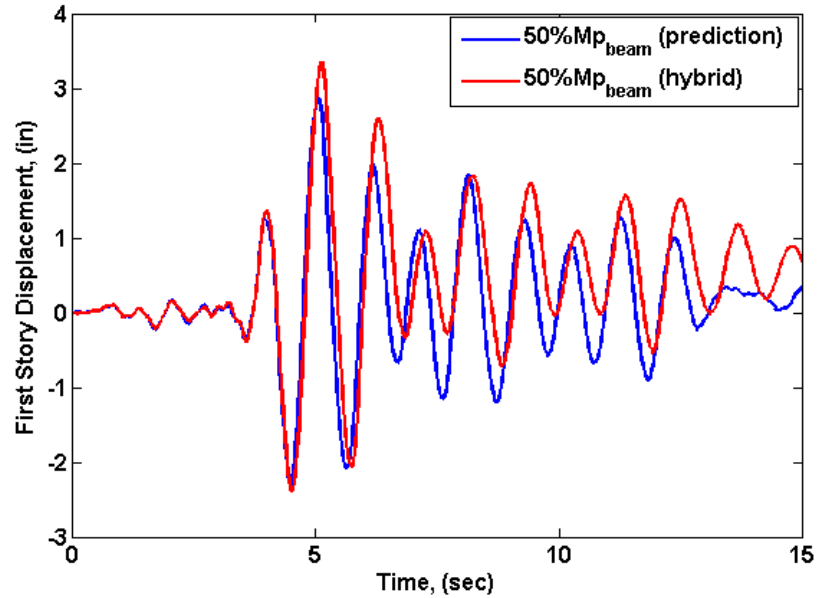


Figure 4-17 First-story displacement comparison between the hybrid simulation and the analytical predictions for the 50%  $M_{p_{beam}}$  specimen

Comparison between the predicted and hybrid simulation base shear is shown in Figure 4-18. Similar to previous comparisons, reasonable agreement is observed between the predicted and the actual response. The predicted maximum absolute base shear is equal to 273.3 kips, while the corresponding value resulting from the hybrid simulation is equal to 253.6 kips at time 5.14 sec. The resulting error between the hybrid simulation results and the analytical predictions for the base shear is equal to 7.77%.

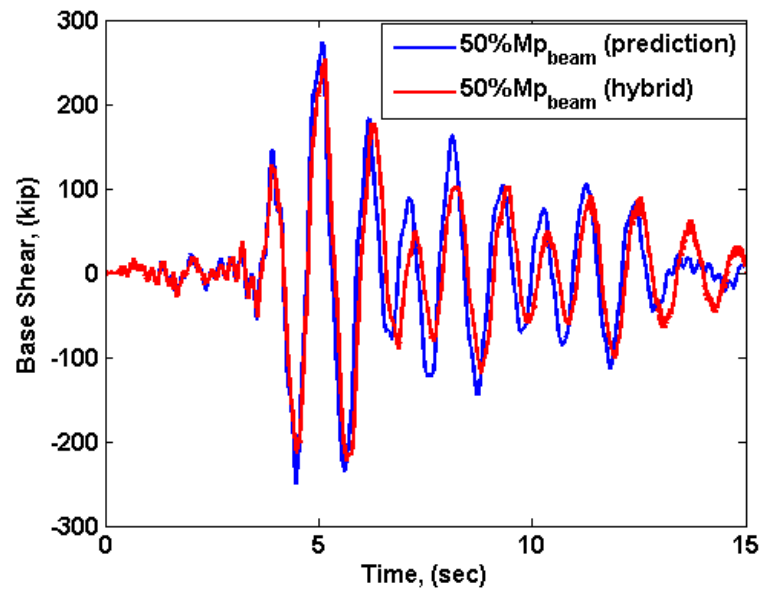


Figure 4-18 Base shear comparison between the hybrid simulation and the analytical predictions for the 50%  $M_{p_{beam}}$  specimen

The comparison between the predicted and the resulting moments and rotations are shown in Figure 4-19 and Figure 4-20, respectively. Similar observation is made with regard to the large discrepancy between the predicted and the measured values. The predicted rotation at time 4.94 sec is equal to 0.0087 rad while the measured value is 0.0176 rad, which corresponds to an error of -50.6 %. Similarly, the predicted moment at time 4.94 sec is equal to 2856 kips.in while the measure value is 1358 kips.in, which corresponds to an error of -110 %. It is also noted that there appears to be a drift in the results for the time range between 0 sec and 3.8 sec. This could primarily be due to slip of the specimen baseplate, which was welded to the bottom end of the column and bolted to the lab floor. Despite the sufficient pretension load applied to the threaded rods connecting the baseplate the lap floor, noticeable slip, of approximately 1 in, was observed in the base of the specimen after the data was processed. It is important to note

that this slip did not affect the global deformation of the system during the simulation since the deformation of the specimen is calculated using relative deformation not absolute.

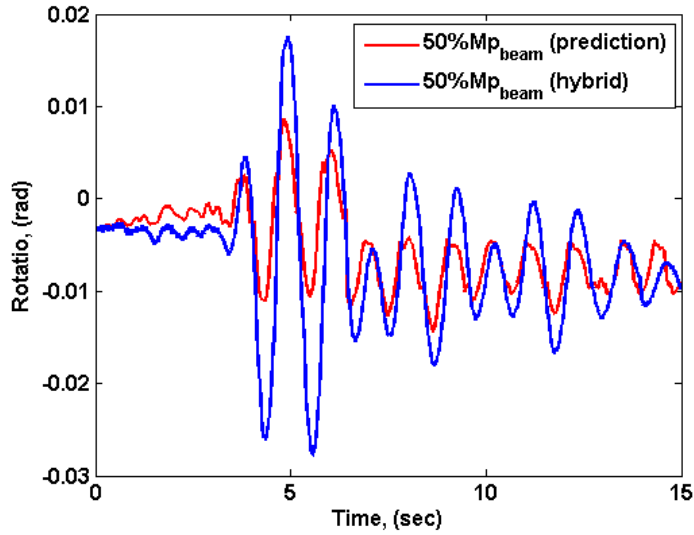


Figure 4-19 Rotation comparison between the hybrid simulation and the analytical predictions for the 50%  $M_{pbeam}$  specimen

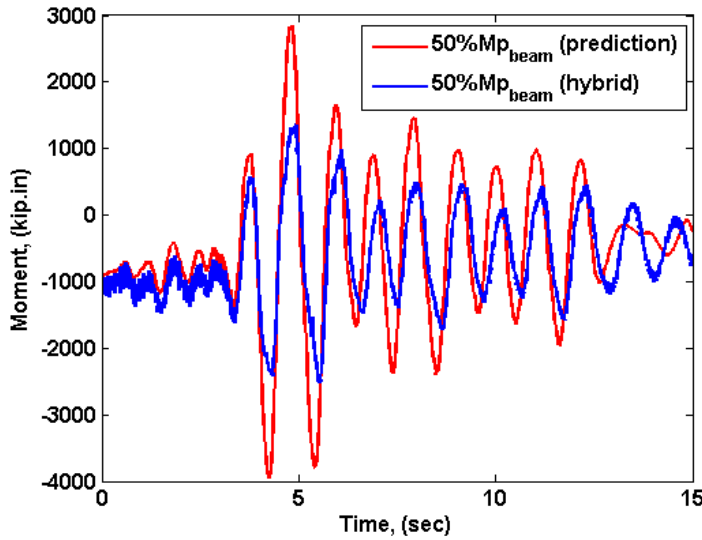


Figure 4-20 Moment comparison between the hybrid simulation and the analytical predictions for the 50%  $M_{pbeam}$  specimen



## 4.4.2 Experimental Observations

### 4.4.2.1 Connection Slip

Similar to the previous simulation, experimental slip measurements are collected to quantify the relative motion between the bolts and the beam and column flanges. Slip of the bolts connecting the top and seat angles to the top and bottom beam flanges, respectively is shown in Figure 4-21 and Figure 4-22, respectively.

The arrangement of the linear pots for measuring the relative deformation between the connection components is shown in the top left image of the figures while the top right image includes labeling of the bolts and the sensors number. Similar to the observation made in the first simulation, the slip is visually observed and heard throughout the test. The largest slip is measured and heard at time corresponding to the largest acceleration peaks. The expected opposite sign of slip shown in the figures is an indication of opening of one angle and closing of the other due to asymmetry of the connection. The figures also show that maximum slip in the top connection bolts and the seat connection bolts is observed in bolt 1 and bolt 3, which are the bolts closer to the column flange. The maximum absolute slip in the top angle is observed in bolt 3 to be 0.185 in while the maximum absolute slip in the seat angle is observed in bolt 1 to be 0.196 in. It is important to point out that although the largest slip value is observed in the seat angle, the top angle experienced larger slip at some locations along the record.

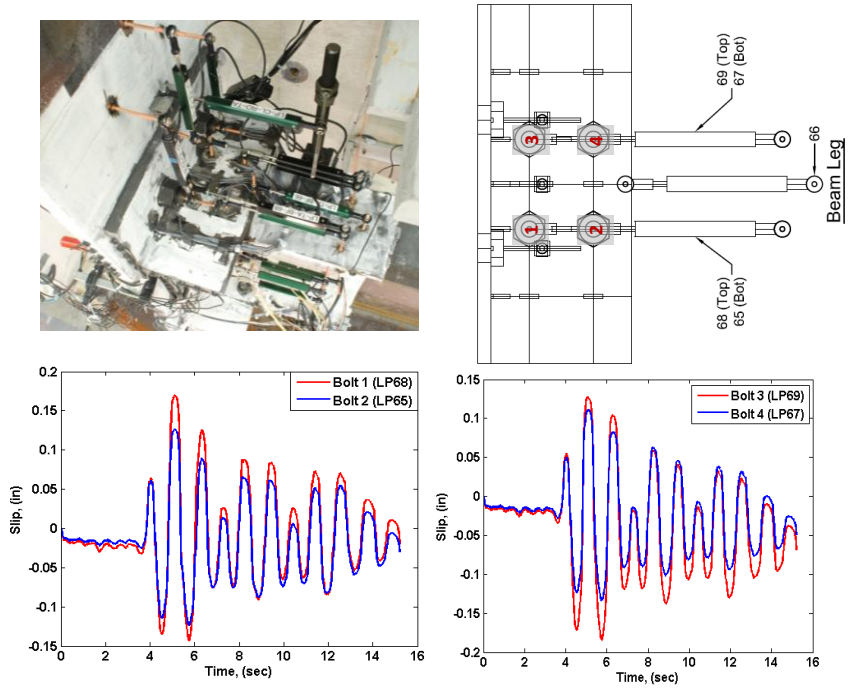


Figure 4-21 Slip of the top angle bolts relative to the top beam flange during the hybrid simulation of the 50%  $M_{pbeam}$  frame

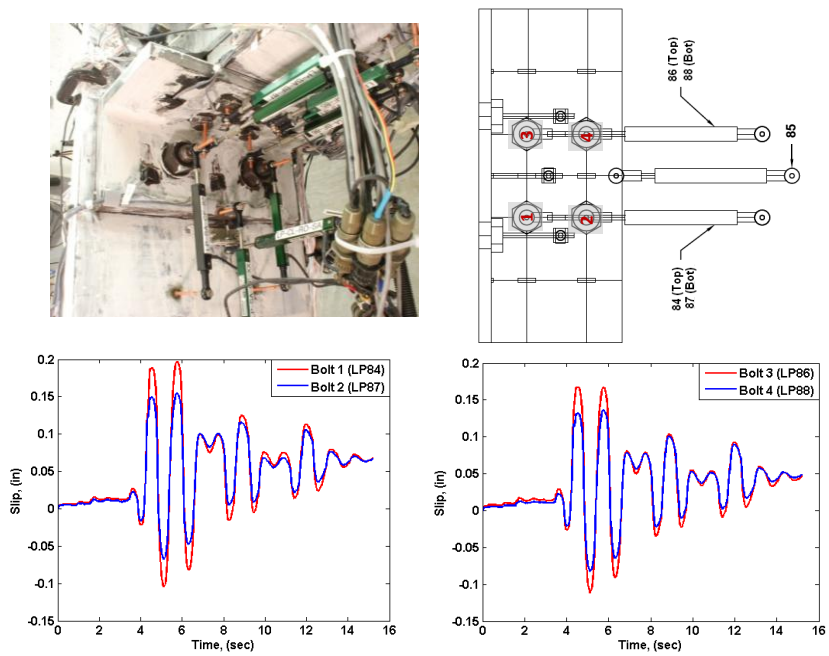


Figure 4-22 Slip of the seat angle bolts relative to the bottom beam flange during the hybrid simulation of the 50%  $M_{pbeam}$  frame

#### 4.4.2.2 Localized Deformation

The deformation of the specimen is characterized mainly by large yielding and plastic deformation in the top and seat angles and in the beam flange and web. As shown in Figure 4-23, gap opening between the top angle and the column flange is evident. Furthermore, large flaking of the whitewash on the bottom face of the top angle is observed, indicating the formation of yield lines and plastic hinges.

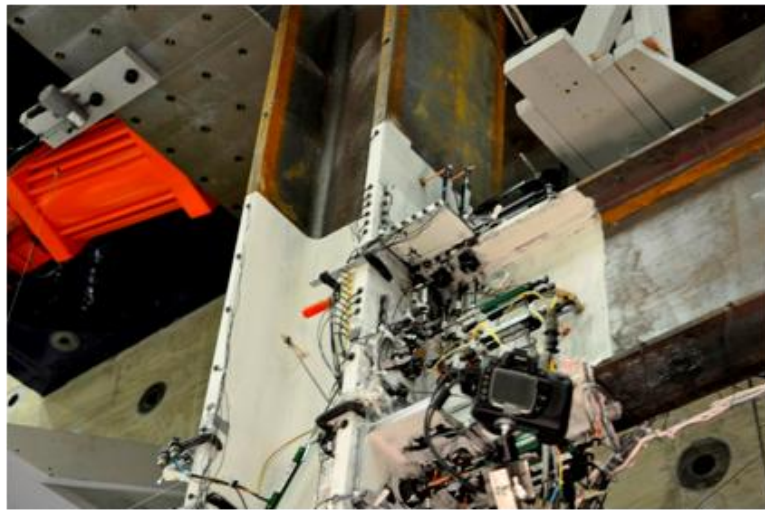


Figure 4-23 Deformation of the specimen during the hybrid simulation of the 50%  $M_{p_{beam}}$  frame

Uniaxial strain gauges are used to measure the distribution of the localized strain in the top and seat angle legs. The layout of strain gauges in both legs of the top angle used is shown in the left image of Figure 4-24. The largest measured strain is measured in the leg connected to the beam flange to be 0.023 as shown in the figure, which is significantly higher than the yield strain. Rectangular rosette gauges are installed on the beam web to measure the localized yielding in the web as shown in Figure 4-25. The

highest absolute strain is measured to be 0.0026 by the gauge oriented longitudinally on the web.

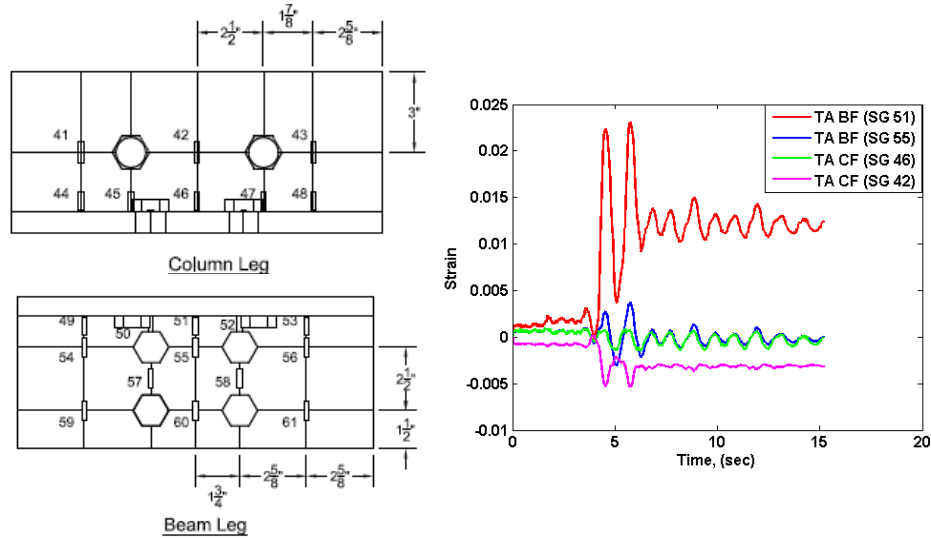


Figure 4-24 Strain measurements in the top angle legs connected to the beam flange and column flange during the hybrid simulation of the 50%  $M_{p\text{beam}}$  frame

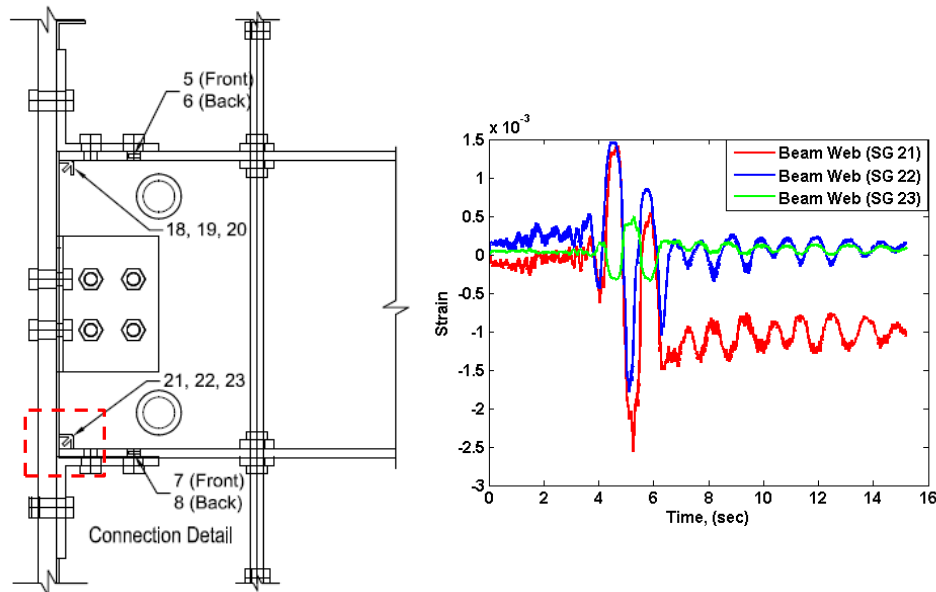


Figure 4-25 Localized strain in the beam web measured by the rectangular rosette gauges during the hybrid simulation of the 50%  $M_{p\text{beam}}$  frame

#### 4.4.2.3 Relative Deformation of Beam with Respect to Column

The sensor layout arrangement used for measuring the relative deformation of the beam with respect to the column is the same used for the 70%  $M_{p_{beam}}$  simulation as shown in Figure 4-26. As previously mentioned, both linear pots and inclinometers are used to obtain the relative deformation to ensure redundancy in the measurements in case any of the sensors malfunctions during the simulation. The two sets of measurements are later used to derive the moment-rotation relationship of the connection as discussed in Chapter 5.

With the linear pots arrangement, the maximum absolute relative displacement of the top of the beam with respect to the column is 0.446 in while the maximum absolute relative displacement of the bottom of the beam with respect to the column is 0.425 in.

The measured inclinometer rotations are also recorded during the simulation. The maximum absolute rotation of the top beam inclinometer is  $0.686^\circ$  while the maximum absolute rotation of the bottom beam inclinometer is  $0.597^\circ$ . The maximum absolute rotation measured by the column inclinometer is equal to  $0.908^\circ$ .

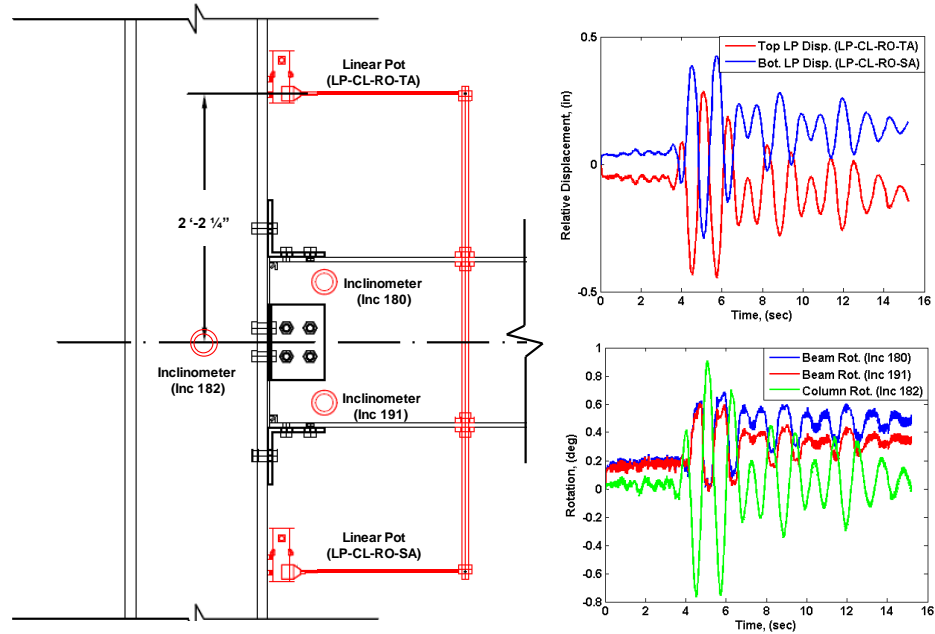


Figure 4-26 Relative rotation measurements between the beam and column during the hybrid simulation of the 50%  $M_{p_{beam}}$  frame

## 4.5 Frame with 30% $M_{p_{beam}}$ under Earthquake Loading

### 4.5.1 Comparison with Analytical Predictions

Figure 4-27 shows comparison of the second-story displacement between the analytical predictions and the sub-structured pseudo-dynamic test for the frame with connection capacity equal to 30%  $M_{p_{beam}}$ . It is important to note that the simulation was not completed and stopped after time 6.42 sec of the earthquake motion due to convergence problems associated with the analytical model. A closer look at the issue indicated contact convergence problems in the FEM. Interestingly, all sub-structured analytical simulations conducted prior to executing the actual hybrid test, demonstrated superior convergence which gave a false sense of confidence, prior to testing, in terms of

the ability to complete the hybrid simulation. The contact formulation was revisited and modified to increase the stability of the solution.

The figure shows very good comparison between the analytical predictions and hybrid simulations. The predicted maximum absolute displacement of the second story is equal to 6.34 in, while the maximum absolute second-story displacement resulting from the hybrid simulation is equal to 7.13 in at time 5.80 sec. The resulting error associated with the difference between the hybrid simulation results and the analytical predictions for the second-story displacement is equal to -11.08%.

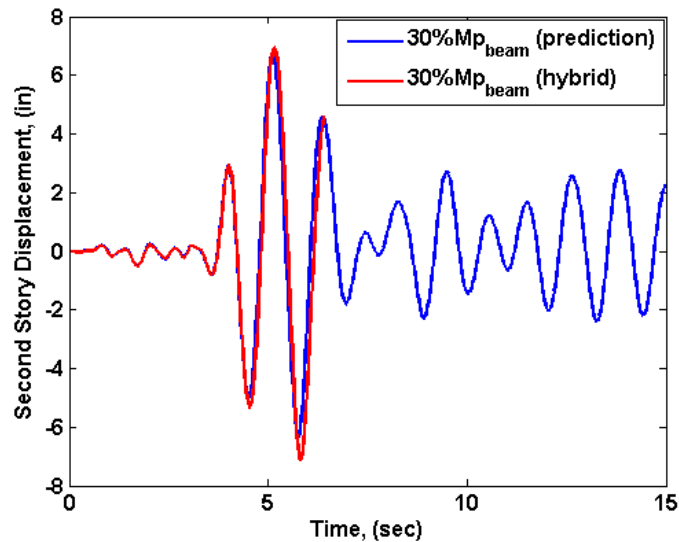


Figure 4-27 Second-story displacement comparison between the hybrid simulation and the analytical predictions for the 30%  $M_{p_{beam}}$  specimen

A similar comparison is made between the analytical predictions and the hybrid simulation results for the first-story displacement as shown in Figure 4-28. Acceptable agreement between the analytical prediction and the hybrid simulation is observed. The maximum absolute displacement of the first story is predicted to be equal to 2.41 in,

while the maximum absolute first-story displacement resulting from the hybrid simulation is equal to 2.77 in. The corresponding error between the hybrid simulation results and the analytical predictions for the first-story displacement is equal to -13%.

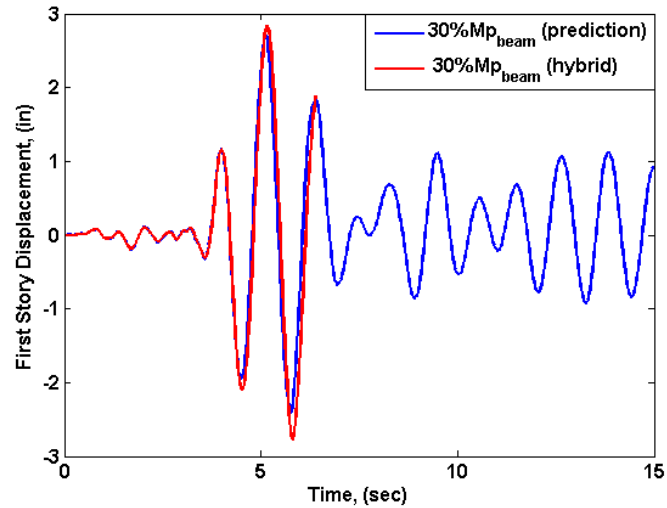


Figure 4-28 First-story displacement comparison between the hybrid simulation and the analytical predictions for the 30%  $M_{p_{beam}}$  specimen

A comparison between the predicted and hybrid simulation base shear is shown in Figure 4-29. Similar to the previous comparisons, reasonable agreement is observed. The maximum absolute base shear is predicted to be 219.7 kips, while the corresponding value resulting from the hybrid simulation is 202.8 kips at time 5.16 sec. The resulting error between the hybrid simulation results and the analytical predictions for the base shear is 8.3%.



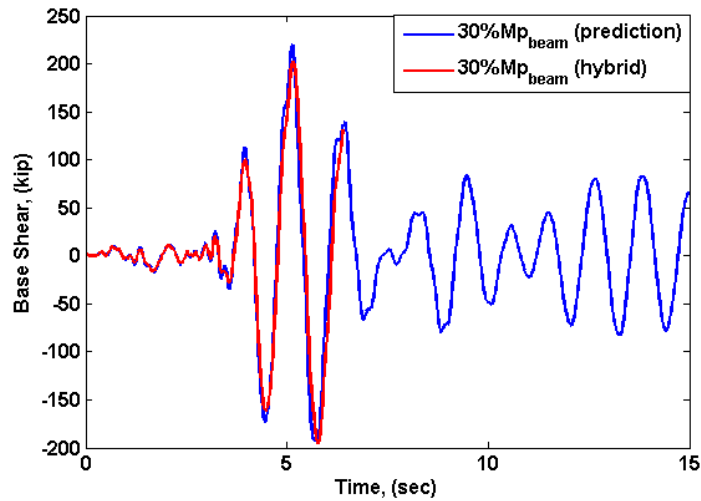


Figure 4-29 Base shear comparison between the hybrid simulation and the analytical predictions for the 30%  $M_{p_{beam}}$  specimen

Figure 4-30 shows a comparison of the rotation versus time between the predicted and that of the hybrid simulation. Similarly, Figure 4-31 shows a comparison of the moment versus time between the predicted and the hybrid simulation results for the same specimen. As shown in both figures, the analytical model is capable of capturing the response very well with the exception of two peaks at time 4.36 sec and 5.62 sec, which are not properly predicted. For the large positive peak response, the maximum predicted rotation at time 5.0 sec is 0.0138 rad while the measured response is 0.0154 rad, which corresponds to an error of -10.39%. The moment associated with the rotation at 5.0 sec is 1723 kips.in for the predicted response and 1421 kips.in for the measured response. The error between the predicted and measured large positive response is -10.39% and 21.25%, respectively. As previously discussed, the reason for the discrepancy is due to the large dynamic slip in the connection as the case for the 50%  $M_{p_{beam}}$  and 70%  $M_{p_{beam}}$  specimens.

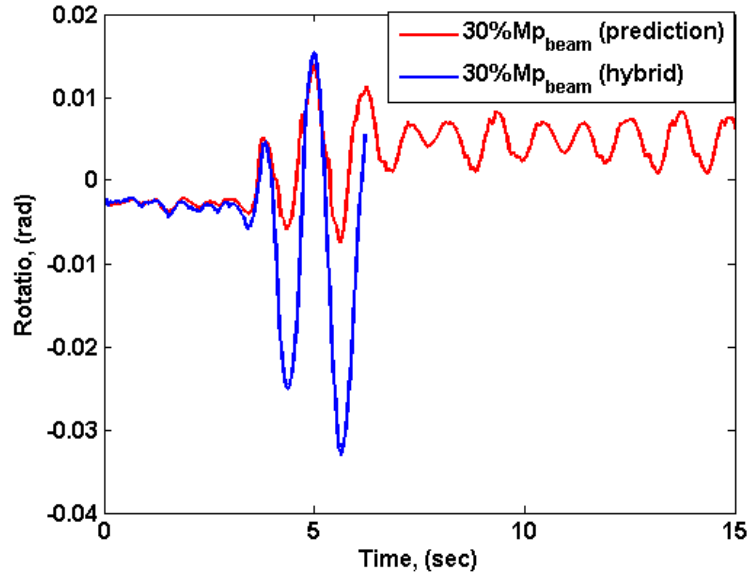


Figure 4-30 Rotation comparison between the hybrid simulation and the analytical predictions for the 30%  $M_{p_{beam}}$  specimen

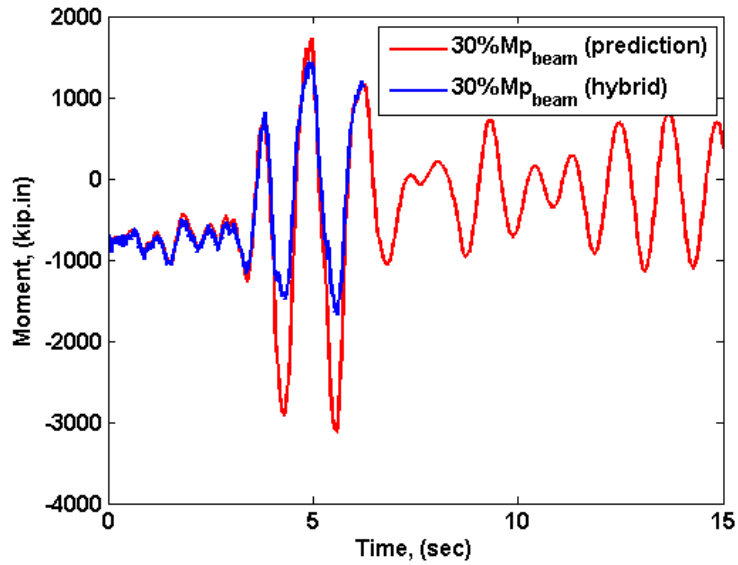


Figure 4-31 Moment comparison between the hybrid simulation and the analytical predictions for the 30%  $M_{p_{beam}}$  specimen

## 4.5.2 Experimental Observations

### 4.5.2.1 Connection Slip

One of the main observations during the simulation is the large slip in the connection caused by the relative motion between the top and seat angles and the beam flanges. Figure 4-32 and Figure 4-33 show the linear pots arrangement and detailed description of sensor layout in the top left and right images of the figures, respectively. The slip is observed visually and also heard throughout the tests with very large audible sound characterizing large dynamic slip in the connection corresponding to the large peaks of the earthquake motion. The top and seat angle bolts connected to the beam flange are labeled as bolt 1 through bolt 4. Opposite sign of the measured slip values between the top and seat angles is shown in the figures, which is in agreement with the expected physical deformation of the angles.

The figures also show scatter in the measured slip values with obvious difference in the slip of bolt 4 of the top angle. The maximum absolute slip value is observed to be in bolt 3 of the top angle and is equal to 0.0645 in. The maximum absolute slip in the seat angle is measured in bolt 1 and is equal to 0.165 in.

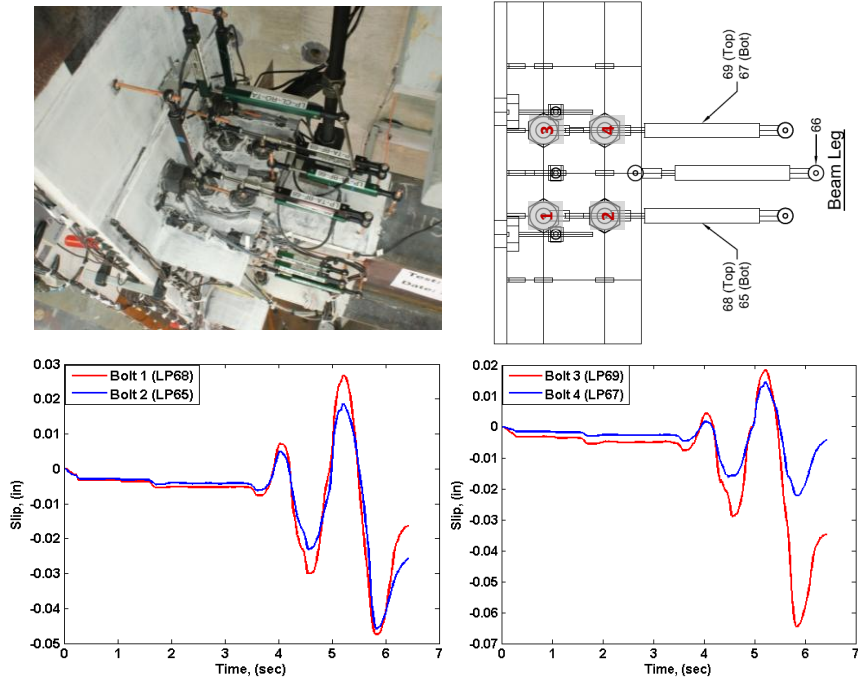


Figure 4-32 Slip of the top angle bolts relative to the top beam flange during the hybrid simulation of the 30%  $M_{p,beam}$  frame

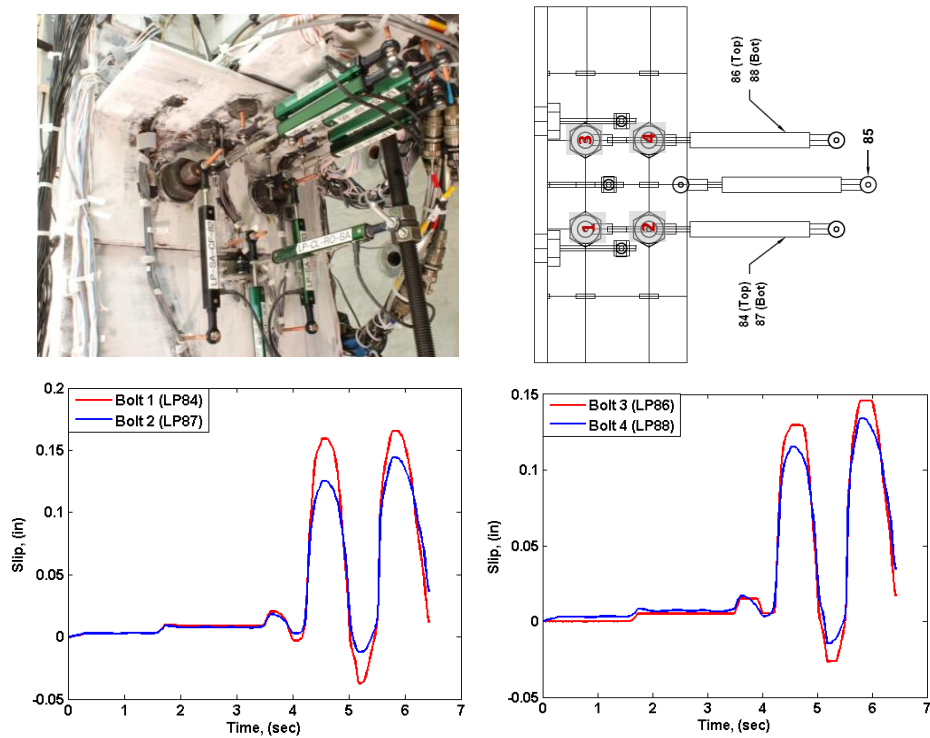


Figure 4-33 Slip of the seat angle bolts relative to the bottom beam flange during the hybrid simulation of the 30%  $M_{p,beam}$  frame

#### 4.5.2.2 Localized Deformation

Another main observation during the simulation is the significant yielding and plastic deformation noted in the top and seat angles as well as the beam flange and web. As shown in Figure 4-34, the deformation of the specimen is characterized by large gap opening between the top angle and the column flange as well as flaking of the whitewash which was installed on the specimen prior to testing. The visual pattern resulting from flaking of the whitewash provides excellent visualization of the localized deformation and yield line formation in the specimen.

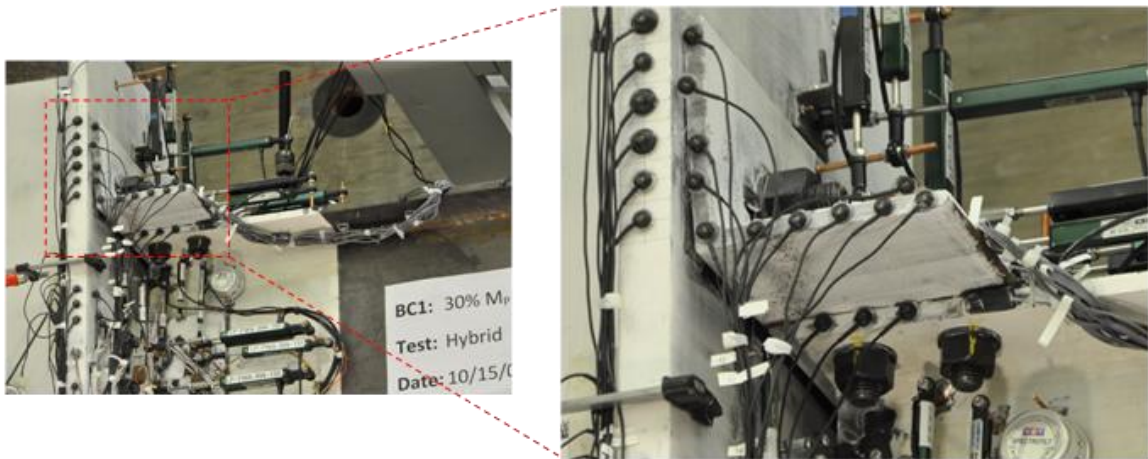


Figure 4-34 Deformation of the specimen during the hybrid simulation of the 30%  $M_{p_{beam}}$  frame

As noted previously, uniaxial strain gauges are installed at various locations on the top and seat angle legs to characterize the distribution of stresses in the angles. The layout of strain gauges in both legs of the angles is shown in the top left image of Figure 4-35. The maximum absolute strain is measured in the leg connected to the beam flange and is equal to 0.037 as shown in the figure, which is significantly larger than the yield strain. The strain gauges installed on the beam in a rectangular rosette gauges

configuration measured a maximum absolute strain of 0.007 by the gauge oriented at 45° on the beam web.

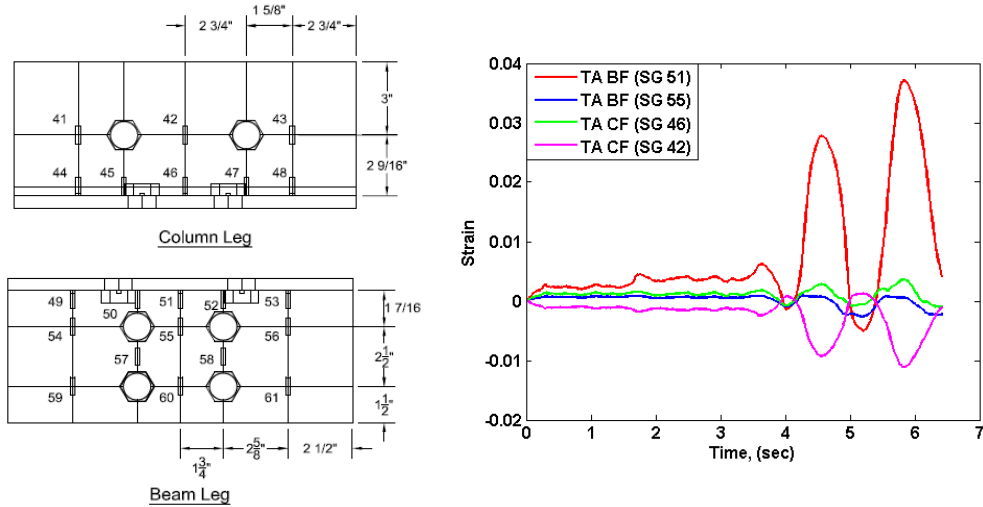


Figure 4-35 Strain measurements in the top angle legs connected to the beam flange and column flange during the hybrid simulation of the 30%  $M_{p\text{beam}}$  frame

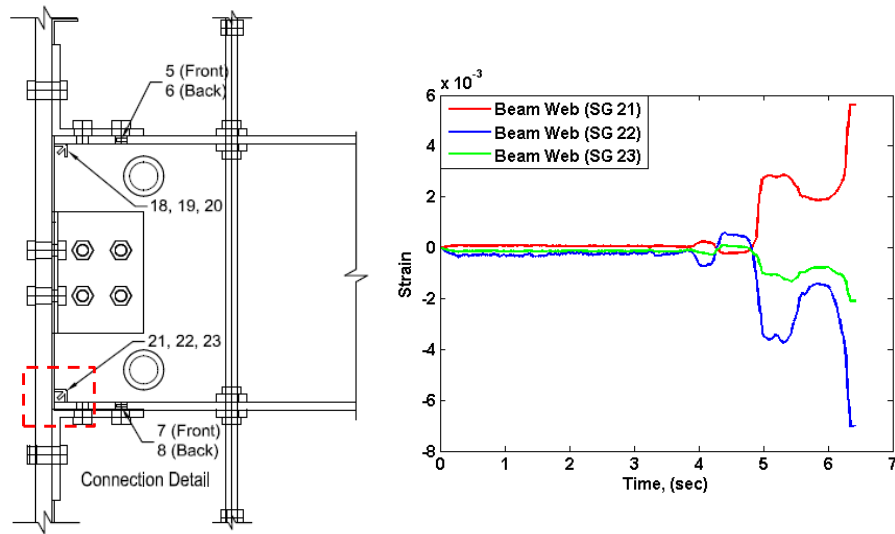


Figure 4-36 Localized strain in the beam web measured by the rectangular rosette gauges during the hybrid simulation of the 30%  $M_{p\text{beam}}$  frame

#### **4.5.2.3 Relative Deformation of Beam with Respect to Column**

Similar to the previous simulations, redundant set of measuring systems are installed to collect information on the relative deformation of the beam with respect to the column. The arrangement of the linear pots for measuring the relative displacement between the beam and column and the inclinometers used to measure their relative rotation is shown in Figure 4-37. The collected data showing the relative displacement between the beam and column are shown in the figure. The maximum absolute relative displacement of the top face of the beam flange with respect to the column is 0.663 in while the maximum absolute relative displacement of the bottom face of the beam flange with respect to the column is 0.419 in.

The measurements collected using the inclinometers are shown in Figure 4-37. The maximum absolute rotation of the top beam inclinometer is equal to be  $0.908^\circ$  while the maximum absolute rotation of the bottom beam inclinometer is equal to  $0.796^\circ$ . The maximum absolute rotation measured by the column inclinometer is equal to  $1.039^\circ$ .

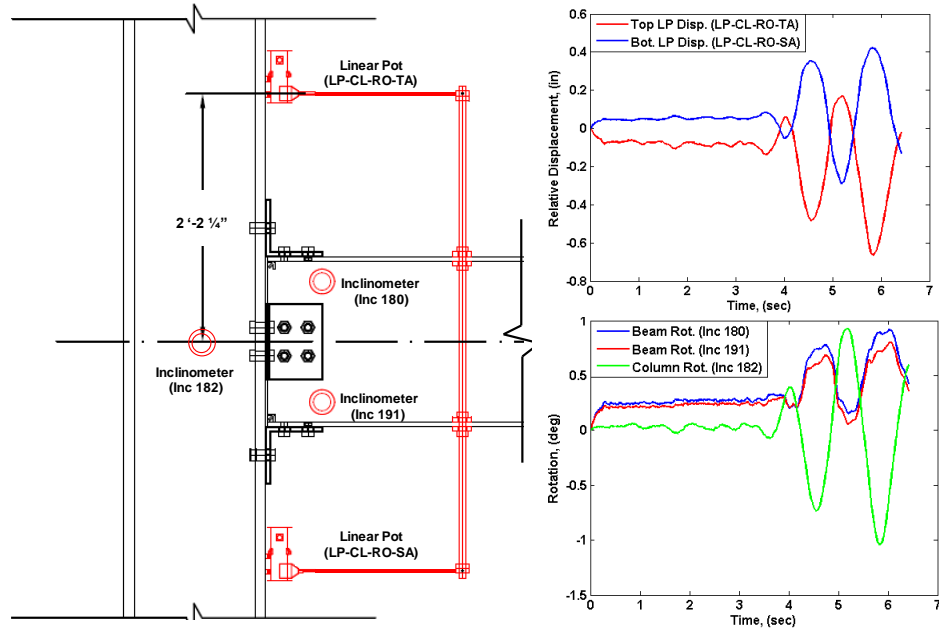


Figure 4-37 Relative deformation measurements between the beam and column during the hybrid simulation of the 30%  $M_{p_{beam}}$  frame

## 4.6 Cyclic Tests

As previously mentioned, cyclic tests are conducted to evaluate the post-earthquake behavior of the connection and its residual characteristics including stiffness, strength, and ductility. Since the specimens are used in the hybrid simulations prior to conducting the cyclic tests, the experimental observations will not include discussion on any of the strain measurements. Connection slip and deformation are the only two observations highlighted in this section. As indicated in the previous chapter, cyclic tests on the 70%  $M_{p_{beam}}$  connection was not conducted due to required maintenance of the LBCBs.



## 4.6.1 Experimental Observations (50% $M_{p_{beam}}$ )

### 4.6.1.1 Connection Slip

Slip in the bolts used to connect the top angle to the top beam flange is shown in Figure 4-38. As shown in the figure, similar magnitude of slip is observed between the set of bolts close to the column flange (bolt 1 and bolt 3) when compared to the set of bolts further away from the column flange (bolt 2 and bolt 4). Such observation also resulted from the hybrid simulation. The maximum absolute slip is observed in bolt 3 of the top angle connection to be 0.579 in while the maximum absolute value measured in the seat angle connection is 0.380 in bolt 1.

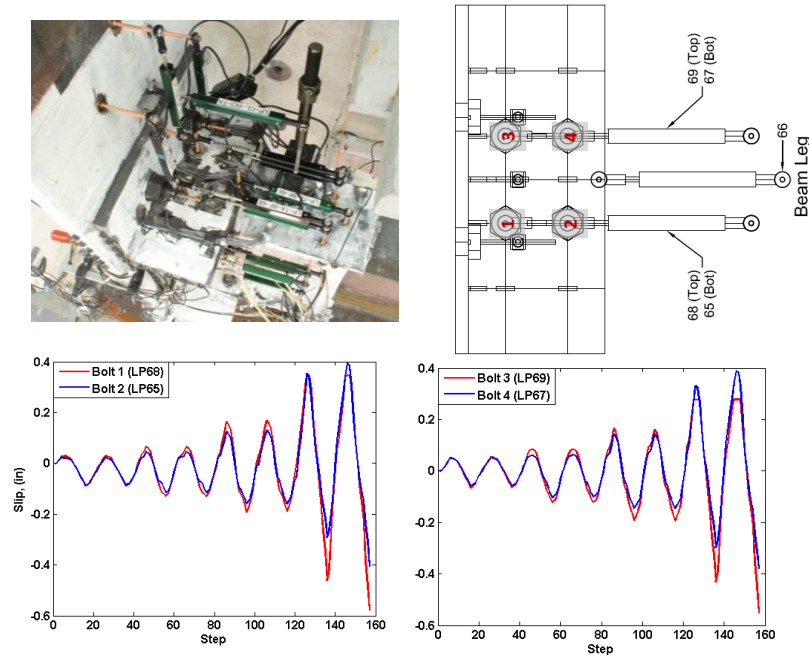


Figure 4-38 Slip of the top angle bolts relative to the top beam flange during the post-earthquake cyclic testing of the 50%  $M_{p_{beam}}$  connection

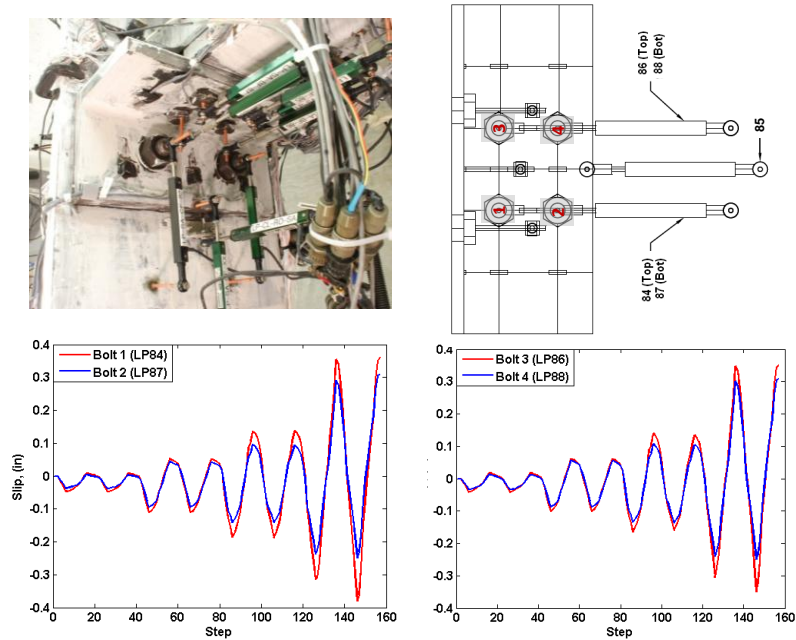


Figure 4-39 Slip of the seat angle bolts relative to the bottom beam flange during the post-earthquake cyclic testing of the 50%  $M_{p_{beam}}$  connection

#### 4.6.1.2 Connection Deformation

Significant deformation is noted in the connection components which progressed with increase in the magnitude and number of cycles. Figure 4-40 shows very notable yield lines forming in the beam flange and web as well as the top angle. The figure also shows one of the bolts connecting the top angle to the beam flange to be missing. This is due to failure of the bolt at the last cycle of loading. It is important to note the corresponding bolt on the opposite side of the connection also failed at the same cycle. Failure of bolts is characterized by shear failure and formation of shear lips on the failed surface as shown in Figure 4-41 and Figure 4-42.

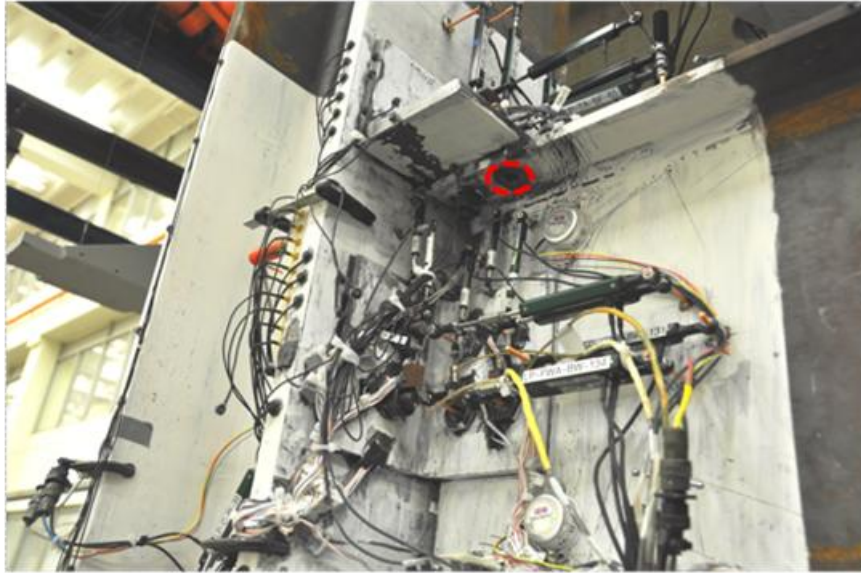


Figure 4-40 Deformation of the specimen during the post-earthquake cyclic testing of the 50%  $M_{p_{beam}}$  connection



Figure 4-41 Shear failure of bolt 2 including failure surface characterized by shear lips during cyclic testing of the 50%  $M_{p_{beam}}$  connection



Figure 4-42 Shear failure of bolt 4 including failure surface characterized by shear lips during cyclic testing of the 50%  $M_{p_{beam}}$  connection

#### 4.6.1.3 Relative Deformation of Beam with Respect to Column

The collected data showing the relative displacement between the beam and column are shown in Figure 4-43. The maximum absolute relative displacement of the top of the beam with respect to the column is 0.871 in while the maximum absolute relative displacement of the bottom of the beam with respect to the column is 0.852 in. The figure also shows the collected data characterizing the relative rotation of the beam and column. The maximum absolute rotation of the top beam inclinometer is  $2.820^{\circ}$  while the maximum absolute rotation of the bottom beam inclinometer is  $2.767^{\circ}$ . The maximum absolute rotation measured by the column inclinometer is  $0.147^{\circ}$ . The reason for the low rotation value measured by the inclinometer installed on the column web is due to the fact only the LBCB connected to the beam end is used to impose rotation on the specimen while the LBCB connected to the top end of the column remained stationary. The small rotation value measure by the inclinometer installed on the column web is caused by the deformation of the column as it interacted with the beam.

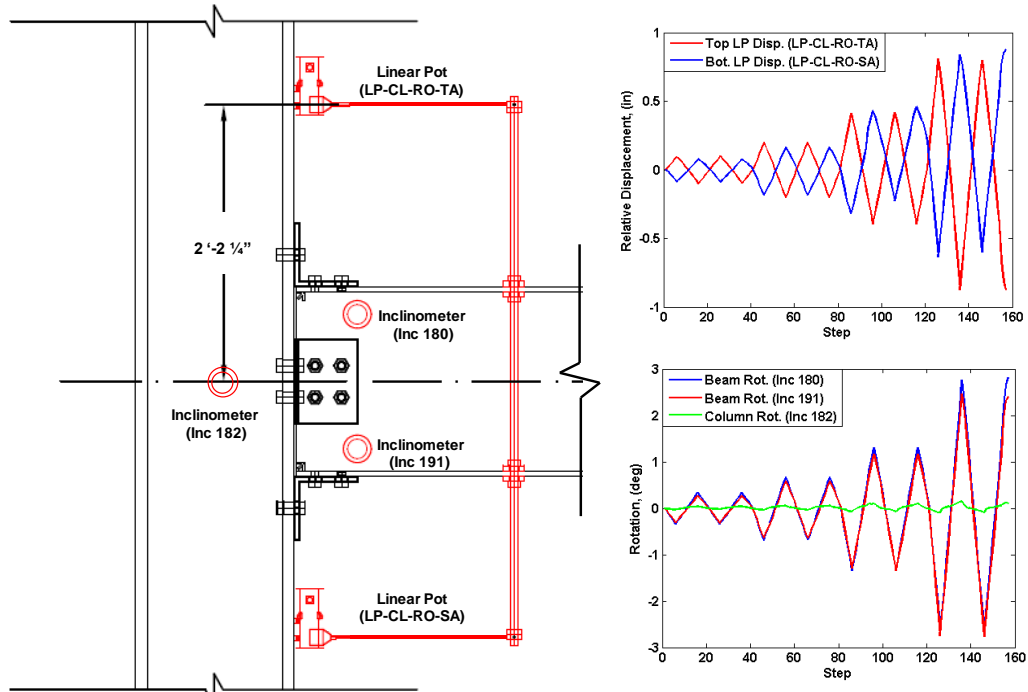


Figure 4-43 Relative deformation measurements between the beam and column during the post-earthquake cyclic testing of the 50%  $M_{p_{beam}}$  connection

## 4.6.2 Experimental Observations (30% $M_{p_{beam}}$ )

### 4.6.2.1 Connection Slip

Slip in the bolts used to connect the top angle to the top beam flange is shown in Figure 4-44 while the measured slip in the bolts connecting the seat angle to the bottom beam flange is shown in Figure 4-45.

Similar to the observation made for the 50%  $M_{p_{beam}}$  cyclic test, similar amount of slip is observed between the set of bolts close to the column flange (bolt 1 and bolt 3) when compared to the set of bolts further away from the column flange (bolt 2 and bolt 4) with higher slip measured in bolt 1 and bolt 3. However, the slip seems to be concentrated in one direction. In other words, significantly larger slip is observed as the connection is loaded in one direction versus the other. The maximum absolute slip is

measured in bolt 1 of the top angle connection to be 0.316 in while the maximum absolute slip measured in the seat angle connection is 0.228 in bolt 4.

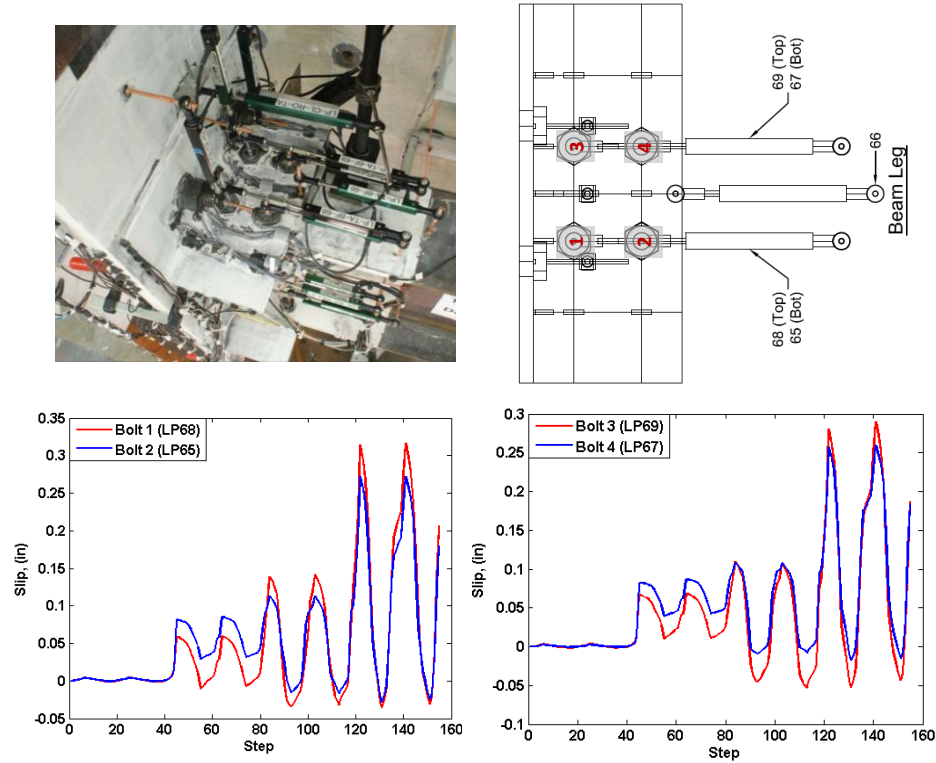


Figure 4-44 Slip of the top angle bolts relative to the top beam flange during the post-earthquake cyclic testing of the 30%  $M_{p_{beam}}$  connection

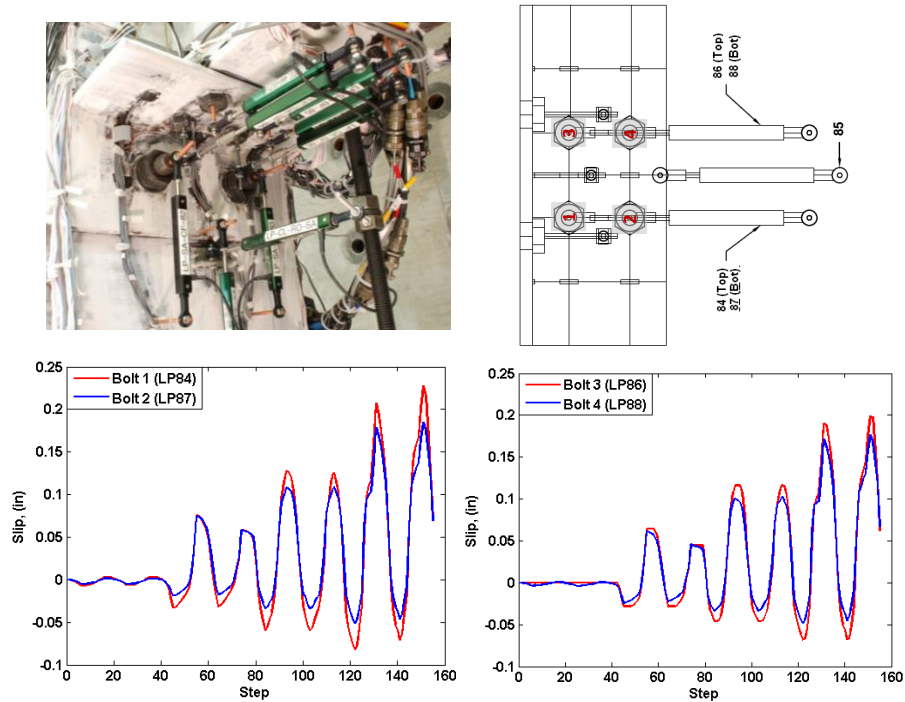


Figure 4-45 Slip of the seat angle bolts relative to the bottom beam flange during the post-earthquake cyclic testing of the 30%  $M_{p\text{beam}}$  connection

#### 4.6.2.2 Connection Deformation

Figure 4-46 shows large yielding and gap opening between the top and seat angle and the column flange during the cyclic test. The deformation is highlighted as the whitewash flaked off the connection, revealing the yield line formation in the angles and the beam web and flange including around the bolt hole as shown in the figure. No failure in any of the connection components is observed upon the completion of the test.





Figure 4-46 Deformation of the specimen during the post-earthquake cyclic testing of the 30%  $M_{p_{beam}}$  connection

#### 4.6.2.3 Relative Deformation of Beam with Respect to Column

Figure 4-47 shows the measured data of the relative displacement between the beam and column. The maximum absolute relative displacement of the top of the beam with respect to the column is measured to be 0.838 in. The maximum absolute relative displacement of the bottom of the beam with respect to the column is measured to be 0.748 in. The figure also shows the rotation of the beam and column with the maximum absolute rotation of the top beam inclinometer to be  $2.714^{\circ}$  and the maximum absolute rotation of the bottom beam inclinometer to be  $2.652^{\circ}$ . The maximum absolute rotation measured by the column inclinometer is found to be  $0.114^{\circ}$ . As previously mentioned, small rotation values are measured by the inclinometer installed on the column since the column remained stationary and only the beam was cycled. The small measured values are imposed on the column as it interacts with the beam during the beam rotation.



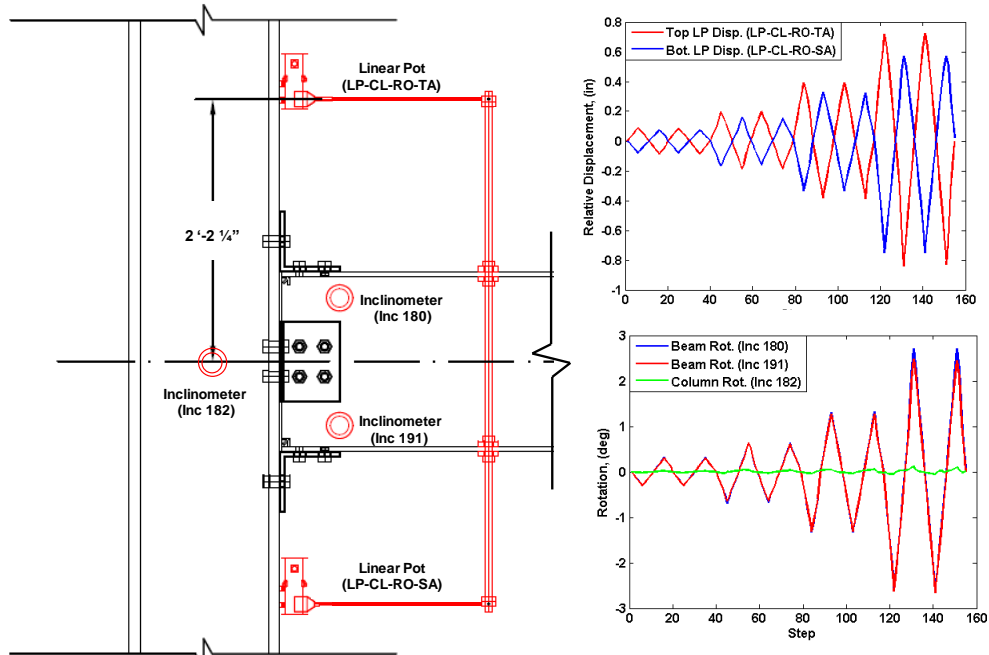


Figure 4-47 Relative deformation measurements between the beam and column during the post-earthquake cyclic testing of the 30%  $M_{p_{beam}}$  connection

## 4.7 Summary and Conclusion

In this chapter, observations made during the hybrid simulation and cyclic testing are discussed. In total three hybrid tests and two cyclic tests are conducted. Specifically, three hybrid simulations of semi-rigid frames with three different connection capacities of 70%  $M_{p_{beam}}$ , 50%  $M_{p_{beam}}$ , and 30%  $M_{p_{beam}}$  are completed.

Upon the completion of a hybrid simulation, cyclic tests are conducted to quantify the post-earthquake fundamental characteristic of the connection. The response of the physical specimen is assessed using data collected through instrumentations installed at various key locations to capture the local response of the connection as well as the global response. In addition to assessing the specimen response, the results of the hybrid simulations are compared to that of the analytical predictions. reasonable agreement

between the hybrid simulation and the analytical predictions are observed. The main response features observed during the hybrid simulation and laboratory testing are summarized below:

***Hybrid testing of the 70%  $M_{p_{beam}}$  frame***

- The simulation is successfully completed for a period of 15 sec of the earthquake.
- No failure is observed in any of the connection components.
- The maximum absolute roof displacement occurred at time 5.02 sec and is equal to 6.48 in.
- The corresponding maximum base shear is equal to 281.6 kips at time 5.06 sec.
- Within reasonable scatter and with the exception of bolt 1 in the top angle connection, similar slip is observed in the bolts used for connecting the top angle to the top beam flange when compared with the bolts used for connecting the seat angle to the bottom beam flange.
- The maximum absolute slip between the top angle and the top beam flange is measured in bolt 3 to be 0.149 in while the maximum absolute slip between the seat angle and the bottom flange of the beam is measured in bolt 3 to be 0.162 in.
- Very small deformation is visually observed in the connection components during the simulation.
- Strain in excess of the yield strain is measured in the top angle and is equal to 0.0056.
- Large strain is also measured by all three rectangular rosette gauges installed on the beam web with the highest strain measured as 0.011 by the gauge oriented vertically.

- Relative deformation between the beam and column is measured by employing linear pots to measure the relative displacement of the beam with respect to the column and by using inclinometers installed on the beam and column to measure their rotations.
- The maximum relative displacement of the top of the beam with respect to the column is 0.325 in while the maximum absolute relative displacement of the bottom of the beam with respect to the column is 0.303 in.
- The inclinometers recorded maximum absolute rotation of  $0.471^\circ$  for the instrument installed near the top end of the beam flange while the maximum absolute rotation near the bottom of the beam is  $0.477^\circ$ . The maximum absolute rotation measured by the column inclinometer is  $0.821^\circ$ .

#### ***Hybrid testing of the 50% $M_{p_{beam}}$ frame***

- The simulation is successfully completed for a period of 15 sec of the earthquake.
- No failure is observed in any of the connection components.
- The maximum absolute roof displacement occurred at time 5.08 sec and is equal to 7.17 in.
- The maximum base shear is equal to 253.6 kips and occurred at time 5.14 sec.
- Scatter in the measured slip data is observed with the largest slip in the top angle measured at 0.185 in by bolt 3 while the maximum absolute slip in the seat angle is 0.196 in by bolt 1.
- Large deformation of the connection is observed and is characterized by flaking of the whitewash installed on the specimen and large gap opening between the top angle and the column flange.

- Large magnitude of strain is measured in the top angle leg connected to the beam flange to be equal to 0.023.
- The largest strain measured by the rectangular rosette gauge arrangement on the beam web is measured by the gauge oriented longitudinally on the web and is equal to 0.0026.
- Large strain is also measured by all three rectangular rosette gauges installed on the beam web with the highest strain measured at 0.011 by the gauge oriented vertically on the web.
- The relative displacement between the beam flange and the column is 0.446 in at the top of the beam and 0.452 in at the bottom of the beam.
- The maximum absolute rotation is  $0.686^\circ$  and is measured by the inclinometer installed near the top end of the beam,  $0.597^\circ$  by the inclinometer installed near the bottom end of the beam, and  $0.908^\circ$  by the inclinometer installed on the column.

***Hybrid testing of the 30%  $M_{p_{beam}}$  frame***

- The simulation stopped at time 6.42 sec of the ground motion due to convergence problems associated with contact formulation in the analytical model.
- No failure is observed in any of the connection components.
- The maximum absolute roof displacement occurred at time 5.08 sec and is equal to 7.13 in.
- The maximum base shear is equal to 202.8 kips and occurred at time 5.14 sec.

- Large scatter in the measured slip is observed with the largest maximum absolute slip in the top angle measured to be 0.0645 in by bolt 3 while the maximum absolute slip in the seat angle is measured to be 0.165 in by bolt 1.
- Significant connection deformation is observed with yield lines forming in the beam and in the angle and highlighted by flaking of the whitewash installed on the specimen prior to testing.
- The maximum absolute strain value measured in the top angle leg connected to the beam flange is equal to 0.037.
- The maximum absolute strain measured by the rectangular rosette gauge arrangement is 0.007 and is measured by the gauge oriented at  $45^\circ$  on the web.
- The maximum absolute relative displacement between the beam flange and the column is 0.663 in at the top of the beam and 0.419 in at the bottom of the beam.
- The maximum absolute rotation measured is  $0.908^\circ$ , which is measured by the inclinometer installed near the top end of the beam,  $0.796^\circ$  by the inclinometer installed near the bottom end of the beam, and  $1.039^\circ$  by the inclinometer installed on the column.

***Cyclic testing of the 50%  $M_{p_{beam}}$  connection***

- Only 7.75 cycles out of the eight cycles imposed on the specimen are completed.
- Shear failure in two of the top angle bolts are observed and highlighted by the formation of shear lips on the failure surfaces.
- The largest maximum absolute slip in the top angle is 0.579 in by bolt 3 while the maximum absolute slip in the seat angle is 0.380 in by bolt 1.

- Significant deformation is noted in the connection components which progressed as the number and magnitude of cycles increased.
- The maximum absolute relative displacement between the beam flange and the column is measured to be 0.871 in at the top of the beam and 0.852 in at the bottom of the beam.
- The maximum absolute rotation measured is  $2.820^\circ$  by the inclinometer installed near the top end of the beam,  $2.767^\circ$  by the inclinometer installed near the bottom end of the beam, and  $0.147^\circ$  by the inclinometer installed on the column.

***Cyclic testing of the 30%  $M_{p_{beam}}$  connection***

- All 8 cycles of loading are completed.
- The largest maximum absolute slip in the top angle is 0.316 in by bolt 1 while the maximum absolute slip in the seat angle is by bolt 4.
- The slip is concentrated in one direction where more slip is observed with positive cycles and significantly less slip observed with negative applied cycles.
- Significant deformation is noted in the connection components which progressed as the number and the magnitude of the cycles increased.
- No failure is observed in any of the connecting components.
- The maximum absolute relative displacement between the beam flange and the column is 0.838 in at the top of the beam and 0.748 at the bottom of the beam.
- The maximum absolute rotation measured is  $2.714^\circ$  by the inclinometers installed near the top end of the beam,  $2.652^\circ$  by the inclinometer installed near the bottom end of the beam, and  $0.114^\circ$  by the inclinometer installed on the column.

## **CHAPTER 5**

### **INTERPRETATION OF RESULTS**

#### **5.1 Introduction**

This chapter provides detailed assessment of the global response of the frames as well as the local behavior of the connections during the simulations. The base shear and global drift resulting from all three hybrid simulations are compared. The interstory drift ratios are evaluated against the ASCE 41-06 (ASCE/SEI 41-06 2007) drift requirements corresponding to the design basis earthquake (DBE) and the maximum considered earthquake (MCE). After evaluating the global response of the frames, the local behavior of the physical specimens is compared in terms of connection slip, local deformation, and the level of strain in the top angle and beam web. In addition, data collected on the relative deformation between the beam and the column is used to drive the moment-rotation relationship of all three connections. The fundamental cyclic characteristics of the connections including stiffness, strength, and ductility along with stiffness degradation and strength degradation are compared. The post-earthquake cyclic tests are also discussed in terms of connection capacity and ductility.

## 5.2 Comparison of Hybrid Simulation Results

### 5.2.1 Global Drift and Base Shear

Figure 5-1 shows a comparison of the second-story displacement and the first-story displacement for all three frames during the hybrid simulations. The largest absolute second-story peak displacement is equal to 6.48 in, 7.17 in, and 7.13 in and the largest absolute first-story peak displacement is 2.89 in, 3.35 in, and 2.84 in for the 70%  $M_{p_{beam}}$  frame, 50%  $M_{p_{beam}}$  frame 30%  $M_{p_{beam}}$ , respectively.

Similarly, Figure 5-3 shows the base shear comparison between all three frames during the simulations. The maximum absolute base shear developed is equal to 281.6 kips, 253.6 kips, and 202.8 kips for the 70%  $M_{p_{beam}}$ , 50%  $M_{p_{beam}}$ , and 30%  $M_{p_{beam}}$  frame, respectively. It is also noted in the figure that the fundamental period of the frames are very similar up to time 5 sec. In the time range of 5 sec to 6.42 sec, the 30%  $M_{p_{beam}}$  frame starts to show signs of larger period elongation when compared to the other frames. This is a result of the larger nonlinearity experienced by the 30%  $M_{p_{beam}}$  frame at lower displacement. The difference in period elongation of the frames is more evident for the time range between 6 sec to 15 sec of the ground motion.



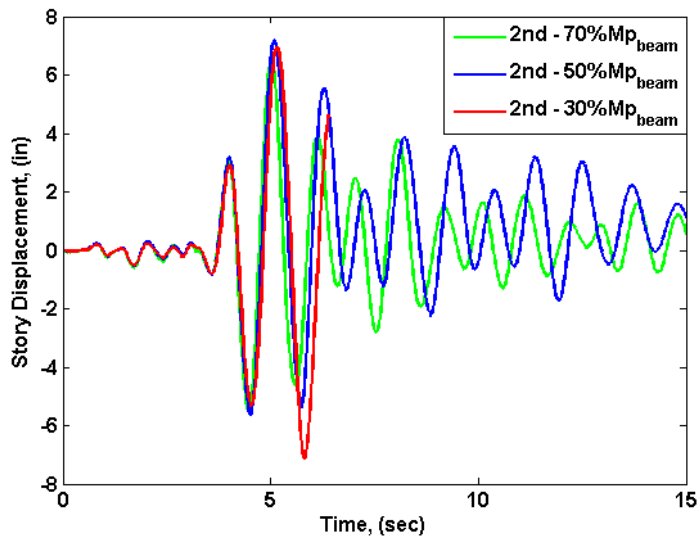


Figure 5-1 Comparison of the second-story displacement between all three frames during the hybrid simulations

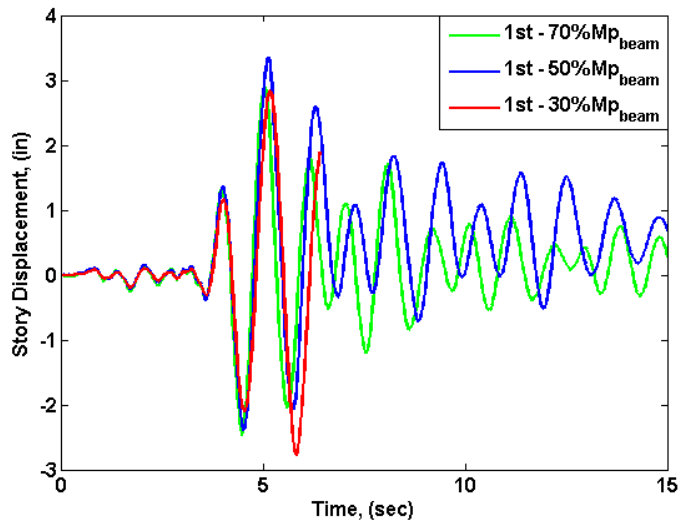


Figure 5-2 Comparison of the first-story displacement between all three frames during the hybrid simulations

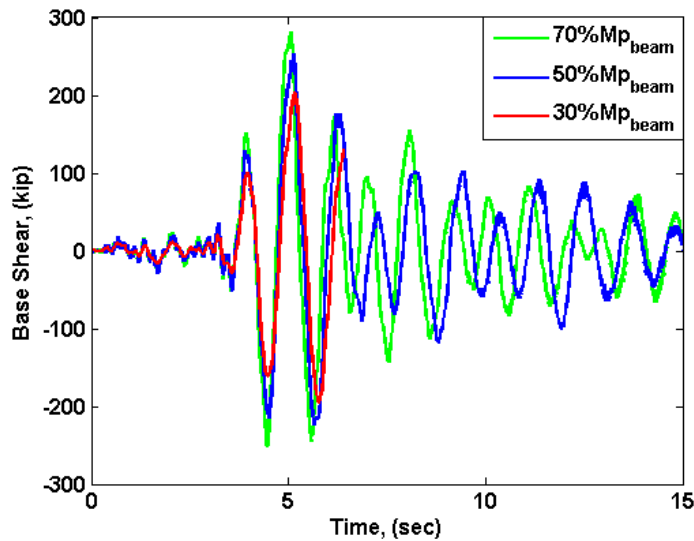


Figure 5-3 Comparison of the base shear between all three frames during the hybrid simulations

The above mentioned maximum absolute displacement and base shear values are listed below in Table 5-1. It is important to note that the values listed in the table correspond to different time of the earthquake ground motion. This is expected since the frames have different fundamental periods and will respond differently when excited by the earthquake.

Table 5-1 Maximum absolute bolt slip in the top angles during the simulations

	$ \Delta^{2nd} _{Max}$ (in)	$ \Delta^{1st} _{Max}$ (in)	Base Shear  <sub>Max</sub> (kips)
70% $M_{p_{beam}}$	6.48	2.89	281.6
50% $M_{p_{beam}}$	7.17	3.35	253.6
30% $M_{p_{beam}}$	7.13	2.84	202.8

### 5.2.2 Interstory Drift Ratio and Compliance with ASCE 41-06

The interstory drift ratio (IDR) of all three frames is shown in Figure 5-4. As shown in the figure, the 50%  $M_{p_{beam}}$  sustained the highest IDR for the first story while the 30%  $M_{p_{beam}}$  sustained the highest IDR for the second story. Specifically, the maximum IDR was found to be equal to 1.61%, 1.86%, and 1.58% for the first story and 2.32%, 2.42%, and 2.70% for the second story for the 70%  $M_{p_{beam}}$ , 50%  $M_{p_{beam}}$ , and 30%  $M_{p_{beam}}$ , respectively.

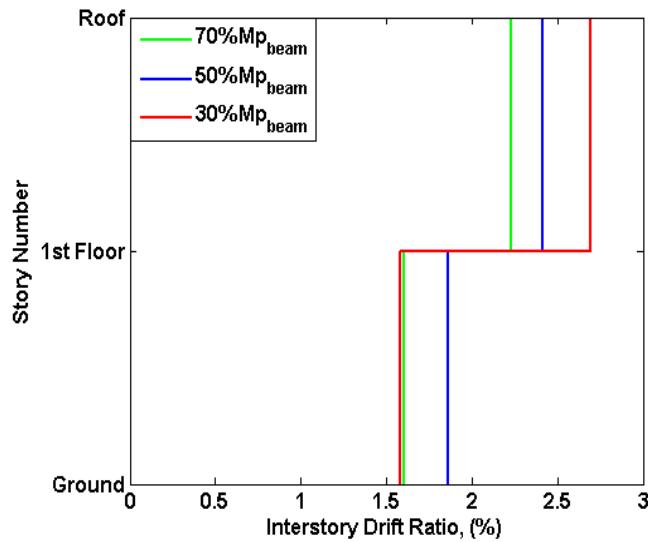


Figure 5-4 Comparison of the maximum interstory drift ratios between all three frames during the hybrid simulations

In addition to calculating the maximum IDR, the frames are assessed using two different performance levels, namely Life Safety (LS) or Design Basis Earthquake (DBE) and Collapse Prevention (CP) or Maximum Considered Earthquakes (MCE). The acceptance criteria used in this study is limiting the interstory drift ratio to 2.5% and 5% for DBE and MCE as defined by ASCE 41-06 (ASCE/SEI 41-06 2007). Even though the

criteria defined by ASCE 41-06 is used for assessing steel moment-resisting frames, it is felt that the same criteria should be used for assessing the semi-rigid frames to fully evaluate their performance in high seismic regions.

It is important to note, that the procedure used to scale the records during the simulations (i.e. constant capacity-to-demand ratio) does not allow for direct comparison with the interstory drift limits of ASCE 41-06. Therefore, the response spectra for the scaled records are compared with that of the DBE and MCE at the period range of 1 sec to 1.5 sec. The first period value selected corresponds to the average fundamental period of the frames while the second period value is a conservative upper bound corresponding to the maximum expected period elongation and is based on the analytical investigation of period elongation discussed in Chapter 6.

Figure 5-5 below shows the DBE, MCE, and the response spectra for the three frames. The DBE spectrum intercepts the response spectrum of the 70%  $M_{p_{beam}}$  frame and the 50%  $M_{p_{beam}}$  frame at periods of 0.90 sec, sec 0.94 and 0.98 sec, respectively. Coincidentally, the values are approximately equal to the calculated elastic fundamental periods of 0.911 sec, and 0.932 sec and 0.971 sec for the 70%  $M_{p_{beam}}$ , 50%  $M_{p_{beam}}$ , and 30%  $M_{p_{beam}}$ , respectively. As such, one can conclude that the 70%  $M_{p_{beam}}$  and the 50%  $M_{p_{beam}}$  frames are deemed acceptable for LS limit state (DBE) while the 30%  $M_{p_{beam}}$  violates the ASCE 41-06 LS requirement as its roof drift ratio is 2.70%, which is slightly higher than the limit of 2.5%.

It is important to note that the response spectra of the records are higher than that of the DBE spectrum until a period of 1.88, 1.80, and 1.78 sec for the 70%  $M_{p_{beam}}$ , 50%

$M_{p_{beam}}$ , and 30%  $M_{p_{beam}}$ , respectively. This implies that within the expected period elongation of the structure, the demand on the structures is always higher than the DBE and in some cases even higher than the MCE. In other words, all three frames comply with the drift requirements for DBE and in some cases even with that of MCE.

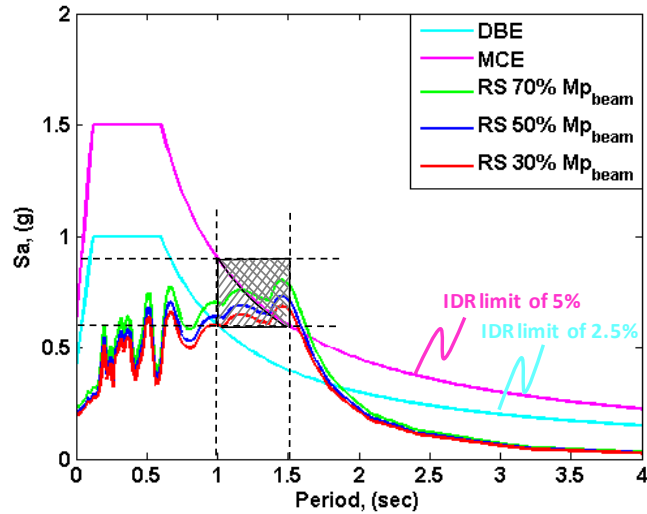


Figure 5-5 Comparison between the response spectrum of all three frames and the DBE and MCE spectrum of ASCE 41-06

The calculated IDR for the first and second story and their normalized values with respect to ASCE 41-06 requirements are listed in Table 5-2. As shown in the table, the second-story IDR normalized to that of MCE approaches 1 for the 70%  $M_{p_{beam}}$  and 50%  $M_{p_{beam}}$  frames and exceeds 1 for the 30%  $M_{p_{beam}}$  frame while the value is well below 1 for the DBE. The first-story IDR normalized to that of MCE and DBE is always well below 1.

Table 5-2 Maximum and normalized IDR

	$IDR_{Max}^{1st}$ (%)	$IDR_{Max}^{1st} / IDR_{ASCE41}^{DBE}$	$ IDR_{Max}^{1st}  / IDR_{ASCE41}^{MCE}$	$IDR_{Max}^{2nd}$ (%)	$ IDR_{Max}^{2nd}  / IDR_{ASCE41}^{DBE}$	$ IDR_{Max}^{2nd}  / IDR_{ASCE41}^{MCE}$
70% $M_{p_{beam}}$	1.61	0.322	0.644	2.32	0.464	0.928
50% $M_{p_{beam}}$	1.86	0.372	0.744	2.42	0.484	0.968
30% $M_{p_{beam}}$	1.58	0.316	0.632	2.70	0.540	1.080

### 5.2.3 Connection Slip

The maximum absolute bolt slip measured during the three simulations is listed in Table 5-3. As shown in the table, the largest slip value in all four bolts connecting the top angle leg to the beam flange is measured by the 50%  $M_{p_{beam}}$  specimen. The mean slip value for the connection is 0.1538 in with a standard deviation of 0.0277. The lowest amount of slip is measured by the 30%  $M_{p_{beam}}$  connection with mean and standard deviation values of 0.0450 in and 0.1654, respectively. The higher standard deviation is an indication of larger scatter in the measured slip. The slip in the top angle bolts of the 70%  $M_{p_{beam}}$  connection falls between that of the other two specimens with mean value of 0.1017 in and standard deviation of 0.0628. The scatter in the slip data is related to the inherent randomness in the pretension force applied when bolting the connection as well as how the connection was fitted during construction.

Table 5-3 Maximum absolute bolt slip in the top angles during the simulations

Connection ID	Top Angle					
	Bolt 1 Slip (in)	Bolt 2 Slip (in)	Bolt 3 Slip (in)	Bolt 4 Slip (in)	Mean Slip (in)	Std Dev.
70% $M_{p_{beam}}$	0.0100	0.1132	0.1492	0.1342	0.1017	0.0628
50% $M_{p_{beam}}$	0.1697	0.1266	0.1845	0.1344	0.1538	0.0277
30% $M_{p_{beam}}$	0.0474	0.0457	0.0645	0.0222	0.0450	0.1654

Similar to the observation made with the top angle, the seat angle of the 50%  $M_{p_{beam}}$  connection experienced the largest amount of slip during testing with mean value of 0.1474 in and standard deviation of 0.0253. However, unlike the top angle, the seat angle of the 30%  $M_{p_{beam}}$  connection appear to have experienced more slip than that of the 70%  $M_{p_{beam}}$  connection. The mean and standard deviation slip values for the 30%  $M_{p_{beam}}$  connection are 0.1474 in and 0.0131, respectively, while the mean and standard deviation slip values for 70%  $M_{p_{beam}}$  connection are 0.1429 in and 0.0186, respectively.

Table 5-4 Maximum absolute bolt slip in the seat angles during the simulations

Connection ID	Seat Angle				Mean Slip (in)	Std Dev.
	Bolt 1 Slip (in)	Bolt 2 Slip (in)	Bolt 3 Slip (in)	Bolt 4 Slip (in)		
70% $M_{p_{beam}}$	0.1581	0.1258	0.1298	0.1617	0.1439	0.0186
50% $M_{p_{beam}}$	0.1962	0.1542	0.1362	0.1677	0.1636	0.0253
30% $M_{p_{beam}}$	0.1654	0.1442	0.1342	0.1459	0.1474	0.0131

Although the turn of the nut method was specified for pretensioning the bolts, the torque applied on the bolt is not exact. Furthermore, another source of the randomness in the measured slip values could be due to the existence of locked up stresses, which arise when assembling the specimen together as drilled holes do not necessarily line up exactly as intended during fabrication.

#### 5.2.4 Connection Deformation

As mentioned in the previous chapter, large strain is measured by the strain gauges installed on the top angle connected to the beam flange and column flange. Summary of the recorded strains at the four strain gauges discussed in the previous chapter is listed below in Table 5-5. As shown in the table, the largest strains are measured in the top angle of the 30%  $M_{p_{beam}}$  specimen followed by the 50%  $M_{p_{beam}}$  and

the 70%  $M_{p_{beam}}$ . This is expected since the size of the angles used in the tests are proportioned to the connection capacity (i.e., the thickness of the top and seat angles used are 1/2 in, 3/4 in, and 1 for the 30%  $M_{p_{beam}}$ , 50%  $M_{p_{beam}}$ , and 70%  $M_{p_{beam}}$  specimens, respectively). The highest magnitude of strain is measured by strain gauge SG51 in all three tests. This is the gauge located on the angle leg connected to the beam and butted against the angle leg connected to the beam flange.

Table 5-5 Maximum absolute strain in the top angle during the simulations

Connection ID	Top Angles			
	TA BF (SG51)	TA BF (SG55)	TA CF (SG46)	TA CF (SG42)
	Max. Abs. Strain ( $\epsilon$ )	Max. Abs. Strain ( $\epsilon$ )	Max. Abs. Strain ( $\epsilon$ )	Max. Abs. Strain ( $\epsilon$ )
70% $M_{p_{beam}}$	0.0056	0.0030	0.0012	0.000745
50% $M_{p_{beam}}$	0.0231	0.0037	0.0015	0.0054
30% $M_{p_{beam}}$	0.0371	0.0026	0.0036	0.0111

Table 5-6 includes the measured strain normalized to the yield strain obtained from material testing. As shown in the table, the angle leg connected to the beam flange experienced strain higher than the yield strain in all three specimens. The highest magnitude of strain is measured by strain gauge SG 51 installed in the top angle leg connected to the beam flange.

Table 5-6 Normalized maximum absolute strain in the top angle during the simulations

Connection ID	Top Angles			
	TA BF (SG51)	TA BF (SG55)	TA CF (SG46)	TA CF (SG42)
	Normalized Strain ( $\epsilon/\epsilon_y$ )	Normalized Strain ( $\epsilon/\epsilon_y$ )	Normalized Strain ( $\epsilon/\epsilon_y$ )	Normalized Strain ( $\epsilon/\epsilon_y$ )
70% $M_{p_{beam}}$	3.3797	1.8081	0.7126	0.4489
50% $M_{p_{beam}}$	13.9245	2.2469	0.9070	3.2725
30% $M_{p_{beam}}$	22.3403	1.5958	2.1707	6.7033



The magnitude of strain measured by the gauges located on the beam web showed variation in the measurements with respect to the three beams used during the simulations. For example and as shown in Table 5-7, higher strain is measured by strain gauge SG21 installed longitudinally on the beam web in the 30%  $M_{p_{beam}}$  specimen followed by the 70%  $M_{p_{beam}}$ , and the 50%  $M_{p_{beam}}$ . The table shows that for strain gauge SG22 installed at a 45° angle on the beam web, the largest magnitude of strain is measured in the 70%  $M_{p_{beam}}$  specimen, followed by the 30%  $M_{p_{beam}}$  then the 50%  $M_{p_{beam}}$ . The largest strain measured by SG23, which was installed transversely on the beam web is measured in the 70%  $M_{p_{beam}}$  specimen followed by the 30%  $M_{p_{beam}}$  specimen then the 50%  $M_{p_{beam}}$  specimen.

Table 5-7 Maximum absolute strain in the beam web during the simulations

Connection ID	Beam Web		
	Beam Web (SG21)	Beam Web (SG22)	Beam Web (SG23)
	Max. Abs. Strain ( $\epsilon$ )	Max. Abs. Strain ( $\epsilon$ )	Max. Abs. Strain ( $\epsilon$ )
70% $M_{p_{beam}}$	0.0030	0.0088	0.0111
50% $M_{p_{beam}}$	0.0026	0.0018	0.000513
30% $M_{p_{beam}}$	0.0056	0.0071	0.0021

The normalized values for the strain measured on the beam web are shown in Table 5-8 below. As shown in the table, all three strain gauges measured values in excess of the yield strain on the beam web of the 70%  $M_{p_{beam}}$  specimen. The gauges installed longitudinally and diagonally on the beam web of the 30%  $M_{p_{beam}}$  specimen measured strain larger than the yield strain. For the 50%  $M_{p_{beam}}$  specimen, the strain gauge installed longitudinally was the only gauge that reached the yield strain of the material.

Table 5-8 Normalized maximum absolute strain in the beam web during the simulations

Connection ID	Beam Web		
	Beam Web (SG21)	Beam Web (SG22)	Beam Web (SG23)
	Normalized Strain ( $\epsilon/\epsilon_y$ )	Normalized Strain ( $\epsilon/\epsilon_y$ )	Normalized Strain ( $\epsilon/\epsilon_y$ )
70% $M_{p_{beam}}$	1.1786	3.4807	4.4192
50% $M_{p_{beam}}$	1.0148	0.7095	0.2040
30% $M_{p_{beam}}$	2.2420	2.8057	0.8367

### 5.2.5 Moment-rotation Relationship

As previously discussed, instrumentations are installed on the specimens to collect information related to the relative deformation between the beam and the column, which can be used to drive the moment-rotation relationship of the connections. Two different sets of instrumentations are installed for that purpose. The first set of instrumentations included two linear pots perpendicularly mounted to the column and parallel to the beam (one above the top angle and one below the seat angle). The corresponding rotation obtained from the linear pots is found by dividing the relative displacement between the two linear pots by the vertical distance between them. The second set of instrumentations included three inclinometers, two of which installed on the beam web directly below the top flange and directly above the bottom flange while the third inclinometer is installed on the column web at the center line of the connection. The rotation of the beam is calculated as the average rotation of the two inclinometers mounted on the beam. The connection rotation is derived by calculating the difference between the beam and column inclinometer rotations.

The derived moment-rotation relationships from all three simulations are shown in Figure 5-6, Figure 5-7, and Figure 5-8 for the 70%  $M_{p_{beam}}$ , 50%  $M_{p_{beam}}$  and 30%

$M_{p_{beam}}$ , respectively. As shown in the figures, higher level of agreement between the derived relationships using the inclinometers versus the linear pots is observed for the positive rotation. Less agreement between the two methods is observed when the connections are characterized by negative moment and rotation.

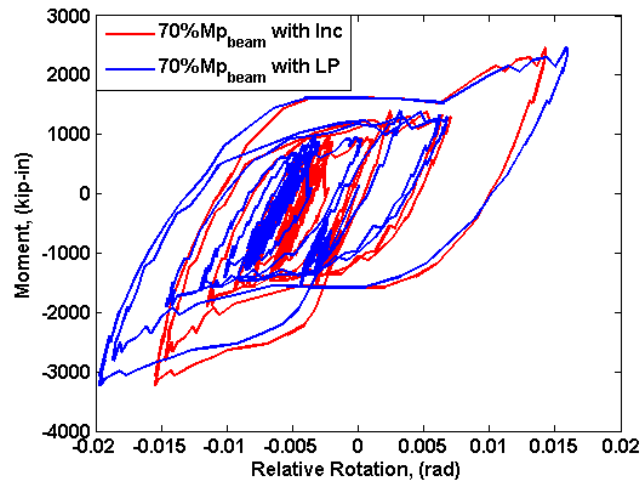


Figure 5-6 Comparison between the moment-rotation relationships derived using the linear pots and the inclinometers resulting from the hybrid simulation of the 70%  $M_{p_{beam}}$  frame

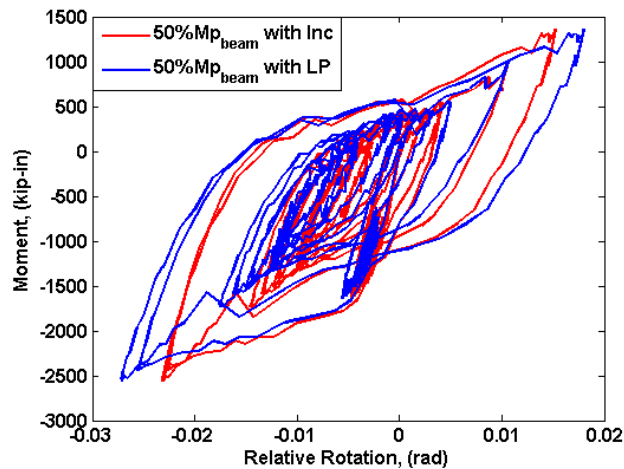


Figure 5-7 Comparison between the moment-rotation relationships derived using the linear pots and the inclinometers resulting from the hybrid simulation of the 50%  $M_{p_{beam}}$  frame

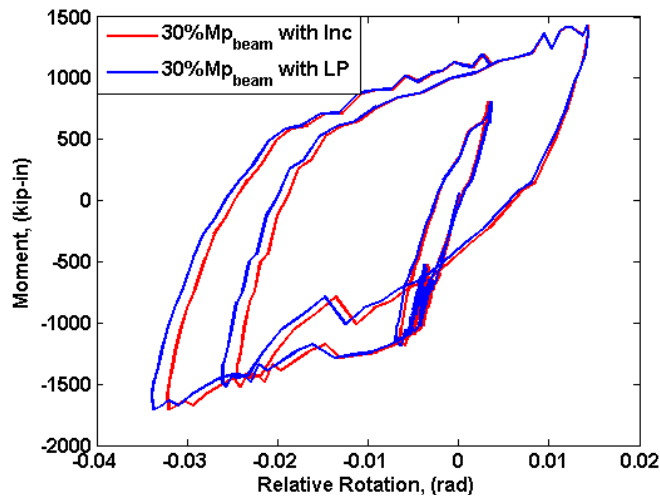


Figure 5-8 Comparison between the moment-rotation relationships derived using the linear pots and the inclinometers resulting from the hybrid simulation of the 30%  $M_{p_{beam}}$  frame

The moment-rotation relationships derived using the linear pots are used for the purpose of comparing the behavior of all three connections. The reason for choosing the linear pots results for the purpose of comparison is because the displacement resolution achieved using the linear pots is 0.001 in while the inclinometer measurements are known to be less reliable. Furthermore, evaluation of the of the sensor measurements prior to conducting the hybrid simulation showed low level of repeatability in the measurements (Bennier 2009). In addition, using the linear posts in representing the moment-rotation relationship ensures consistency between the current study and previous studies conducted by others, which facilitates comparison of results if needed.

A comparison of the derived moment-rotation relationships for all three connections is shown in Figure 5-9. As shown in the figure, large pinching and hardening is observed in the response of the 70%  $M_{p_{beam}}$  connection when compared to the other

two connections. The highest stiffness degradation is observed in the 50%  $M_{p_{beam}}$  specimen, which is 46.05% of the original stiffness, followed by the 30%  $M_{p_{beam}}$  specimen, which experienced degradation in its stiffness of 33.59%, and finally the 70%  $M_{p_{beam}}$  specimen with stiffness degradation of 23.47%. It is important to note that the high percent degradation in the 50%  $M_{p_{beam}}$  specimen does not imply that the connection experienced the lowest unloading stiffness. In fact that lowest unloading stiffness is experienced by the 30%  $M_{p_{beam}}$  due to the high level of inelasticity in the top and seat angles of the connection during the simulation as shown by the strain gauge data discussed previously and listed in Table 5-6. As shown in the table, the strain in the top angle is 22.34 times higher, 13.92 times higher, and 3.38 times higher than the yield strain of the material for the 30%  $M_{p_{beam}}$ , 50%  $M_{p_{beam}}$  and 70%  $M_{p_{beam}}$  connections, respectively.

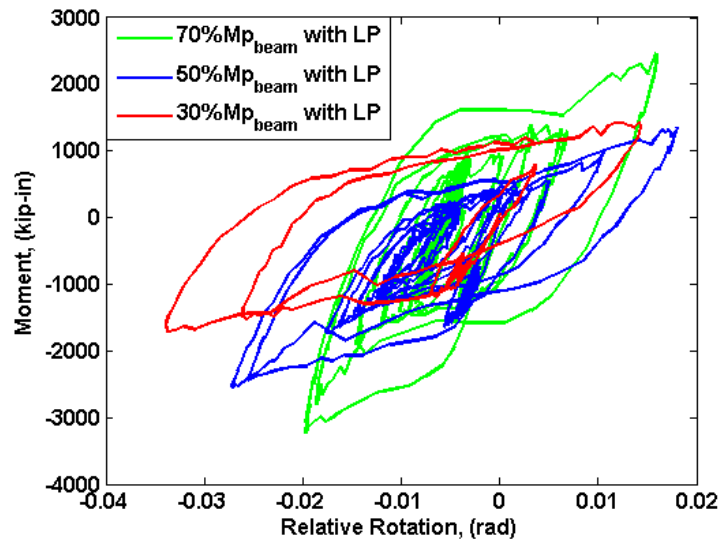


Figure 5-9 Comparison between the moment-rotation relationships derived using the linear pots resulting from the hybrid simulation of all three frames

The characteristics of the connections during the simulations are listed in Table 5-9. The table includes values for the initial stiffness ( $k_i$ ), the unloading stiffness ( $k_u$ ), the percent of stiffness degradation ( $k_{deg}$ ), the maximum moment and rotations experienced by the connections, and the energy dissipated by each connection during the simulations.

Table 5-9 Characteristics of the connections during the simulations

	$k_i$ (kips.in/rad)	$k_u$ (kips.in/rad)	$k_{deg}$ (%)	$ M _{Max}$ (kips.in)	$\%M_{p_{beam}}$	$ \theta _{Max}$ (rad)	Energy Dissipated (kips.in.rad)
70% $M_{p_{beam}}$	510,683	390,827	23.47	3,222	82.0	0.0196	195.18
50% $M_{p_{beam}}$	494,314	266,718	46.04	2,556	65.2	0.0271	177.45
30% $M_{p_{beam}}$	306,521	203,565	33.59	1,708	43.6	0.034	109.56

As mentioned previously, the connections used are not considered one of the prequalified connections per AISC 358 for special and intermediate moment-resisting frames. The prequalified connections include reduced beam section (RBS), bolted unstiffened extended end plate (BUEEP), and bolted stiffened extended end plate (BSEEP). According to AISC, the connection must be fully restrained (FR) to be considered to exhibit sufficient stiffness for seismic applications. Furthermore, it is required that the connection be able to sustain an interstory drift angle of 0.04 rad which is equivalent to a plastic rotation of 0.03 rad. It is important to point out that the maximum rotation sustained by the specimens are not the rotation capacity of the connection since none of the connections are shown to exhibit flattening of its capacity curves to indicate that capacity is reached. The maximum rotations achieved during the simulations are 0.0196 rad, 0.0271 rad, and 0.034 rad for the 70%  $M_{p_{beam}}$ , 50%  $M_{p_{beam}}$ , and 30%  $M_{p_{beam}}$  connections, respectively.

### 5.3 Comparison of Cyclic Test Results

Cyclic tests are conducted to investigate the post-earthquake behavior of the connections. Due to some technical difficulties with the loading units, cyclic tests are conducted only on the 50%  $M_{p_{beam}}$  and 30%  $M_{p_{beam}}$  specimens. Bolt slip and the derived moment-rotation relationships of the connections is discussed in the sections below.

#### 5.3.1 Connection Slip

The maximum absolute bolt slip in the top and seat angle bolts measured during the three simulations is listed in Table 5-10 and Table 5-11. As shown in Table 5-10, larger slip in the top angle bolts is observed in the 50%  $M_{p_{beam}}$  connection with mean slip of 0.4808 in when compared to the 30%  $M_{p_{beam}}$  with mean slip value of 0.2846 in. Similar to the hybrid simulation results, bolt 1 and bolt 3 located closer to the column flange experienced the largest amount of slip.

Table 5-10 Maximum absolute bolt slip in the top angles during the cyclic tests

Connection ID	Top Angle					Std Dev.
	Bolt 1 Slip (in)	Bolt 2 Slip (in)	Bolt 3 Slip (in)	Bolt 4 Slip (in)	Mean Slip (in)	
50% $M_{p_{beam}}$	0.5786	0.4048	0.5512	0.3887	0.4808	0.0979
30% $M_{p_{beam}}$	0.3161	0.2725	0.2897	0.2601	0.2846	0.0242

The seat angle connection of the 50%  $M_{p_{beam}}$  specimen experienced larger slip than its 30%  $M_{p_{beam}}$  counterpart with mean slip of 0.3367 in while the mean slip in the 30%  $M_{p_{beam}}$  specimen is equal to 0.2846 in. Summary of the measured slip values for the seat angle bolts during cyclic testing is shown Table 5-11.

Table 5-11 Maximum absolute bolt slip in the seat angles during the cyclic tests

Connection ID	Seat Angle					Std Dev.
	Bolt 1 Slip (in)	Bolt 2 Slip (in)	Bolt 3 Slip (in)	Bolt 4 Slip (in)	Mean Slip (in)	
50% $M_{p_{beam}}$	0.3800	0.3087	0.3086	0.3492	0.3367	0.0347
30% $M_{p_{beam}}$	0.2279	0.1853	0.1767	0.1990	0.1972	0.0224

The observed slip in the top and seat angle bolts during cyclic testing is higher than that observed during the hybrid simulation as shown in Table 5-12. The table shows that the largest absolute mean maximum slip is observed in the top angle of the 50%  $M_{p_{beam}}$  connection during cyclic testing.

Table 5-12 Absolute mean maximum bolt slip in the top-and seat-angles for all tests

Connection ID	Top Angle		Seat Angle	
	Hybrid Mean Slip (in)	Cyclic Mean Slip (in)	Hybrid Mean Slip (in)	Cyclic Mean Slip (in)
50% $M_{p_{beam}}$	0.1538	0.4808	0.1636	0.3367
30% $M_{p_{beam}}$	0.1474	0.2846	0.1474	0.1972

### 5.3.2 Moment-rotation Relationship

The derived moment-rotation relationships from the two cyclic tests using the inclinometers and the linear pots are shown in Figure 5-10 and Figure 5-11 for the 50%  $M_{p_{beam}}$  and 30%  $M_{p_{beam}}$ , respectively. As shown in the figures, for the 50%  $M_{p_{beam}}$  connection, higher level of agreement between the derived relationships using the inclinometers versus the linear pots is observed for the positive rotation region while less agreement is observed for the negative moment region. For the 30%  $M_{p_{beam}}$  connection, very high level of agreement is observed between the derived relationships for both the negative and positive regions.



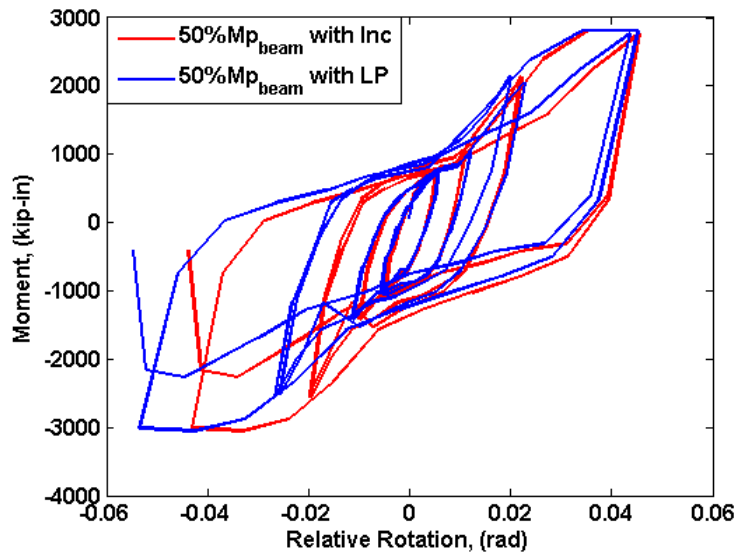


Figure 5-10 Comparison between the moment-rotation relationships derived using the linear pots and the inclinometers resulting from cyclic testing of the 50%  $M_{p_{beam}}$  connection

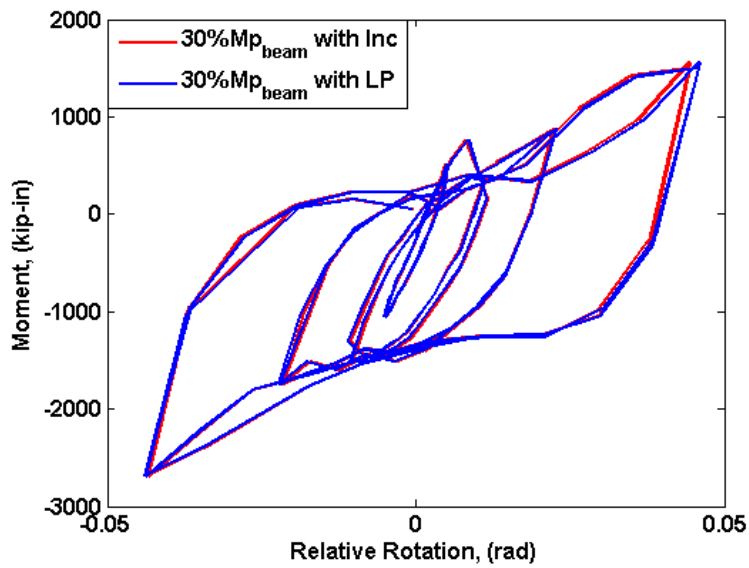


Figure 5-11 Comparison between the moment-rotation relationships derived using the linear pots and the inclinometers resulting from cyclic testing of the 30%  $M_{p_{beam}}$  connection

A comparison of the derived moment-rotation relationships between the two connections is shown in Figure 5-12. The behavior of the connections is highlighted by stable hysteretic behavior and large pinching. Furthermore, the 50%  $M_{p_{beam}}$  connection appear to have reached its positive and negative moment capacity as indicated by the flattening of the moment-rotation curve at the maximum rotation sustained while the 30%  $M_{p_{beam}}$  connection reached its positive moment capacity but not its negative moment capacity. As mentioned in the previous chapter, two bolts connecting the top angle to the beam flange of the 50%  $M_{p_{beam}}$  connection failed at the peak of the very last cycle during the test as indicated in the figure by the sharp drop in the capacity curve.

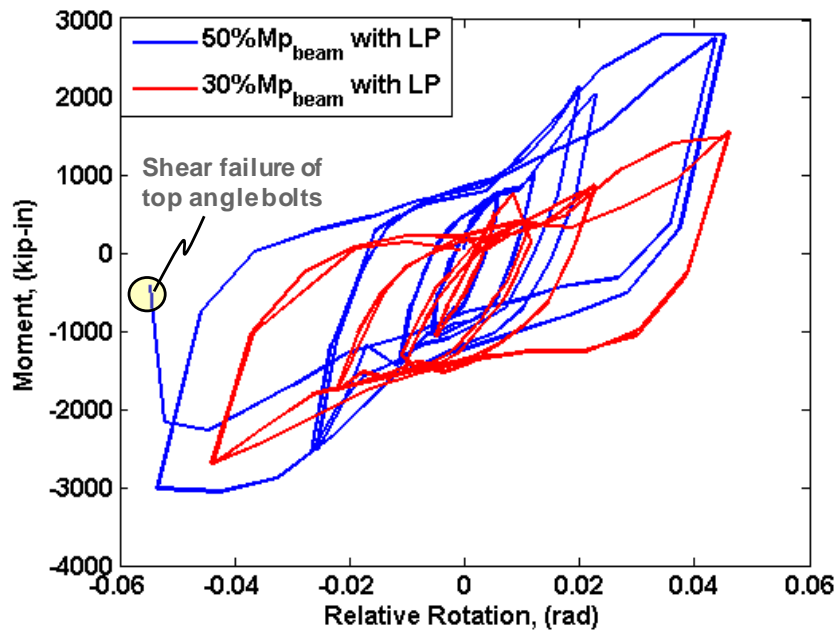


Figure 5-12 Comparison between the moment-rotation relationships derived using the linear pots resulting from the hybrid simulation of all 50%  $M_{p_{beam}}$  and 30%  $M_{p_{beam}}$  connections

The characteristics of the connections during the cyclic tests are listed Table 5-13 including the maximum moment and rotations experienced by the connections, the energy dissipated by each connection during the tests, the percent of connection capacity with respect to the moment, and the connection capacity normalized to its design capacity. As shown in the table large moment and rotation was experienced by the connections. In fact the moment sustained by the connections was approximately 76%  $M_{p_{beam}}$  and 68.41%  $M_{p_{beam}}$  for the 50%  $M_{p_{beam}}$  and 30%  $M_{p_{beam}}$  connection, respectively. The results are a clear indication for the need to reevaluating the Eurocode design guidelines since it was used to design the connection.

Table 5-13 Characteristics of the connections during the cyclic tests

	$ M _{Max}$ (kips.in)	$ \theta _{Max}$ (rad)	Energy Dissipated (kips.in.rad)	$(\%M_{p_{beam}})_{Actual}$	$(\%M_{p_{beam}})_{Actual} / (\%M_{p_{beam}})_{Design}$
50% $M_{p_{beam}}$	3,002	0.0534	569.82	76.58	1.53
30% $M_{p_{beam}}$	2,682	0.0440	407.36	68.41	2.28

It is important to note that the rotations sustained by both connections during the tests are measured as 0.053 rad and 0.0440 rad for the 50%  $M_{p_{beam}}$  and 30%  $M_{p_{beam}}$ , respectively. The measured rotations exceeded the required rotation of 0.04 rad per the 2005 seismic provisions of AISC, section 9.2a. The specification calls for flexural resistance of the connection, determined at the column face, to be at least equal to 0.80Mp of the connected beam at an interstory drift angle of 0.04 radians. As shown in Table 5-13 above, the flexural resistance of the connections is equal to 76.58% and 68.41% for the 50%  $M_{p_{beam}}$  and 30%  $M_{p_{beam}}$  connection, respectively. Although the capacity of the connection does not meet the seismic specifications requirements, it is unclear as to why a connection capacity of 0.80 Mp of the connected beam is needed. The connections

appear to be penalized by these provisions despite the fact that their rotations exceed the required rotation according to the specification.

#### **5.4 Summary and Conclusion**

In this chapter, the results of the hybrid simulation and the cyclic tests are discussed. Specifically, the results of the hybrid simulation are compared and the global behavior of the frames evaluated against the ASCE 41-06 requirements. In addition, the local characteristics of the connections are compared including the initial stiffness, the unloading stiffness, the moment and rotation sustained, and the amount of energy dissipated in the connections. Comparison between the moment and rotation sustained by the connections and the 2005 seismic provisions of AISC is made. The main findings are summarized below.

- **Hybrid testing of the 70%  $M_{p_{beam}}$ , 50%  $M_{p_{beam}}$ , 30%  $M_{p_{beam}}$**

When comparing the results of all three hybrid simulations, it is observed that the maximum base shear is developed in the 70%  $M_{p_{beam}}$  frame followed by the 50%  $M_{p_{beam}}$  frame then the 30%  $M_{p_{beam}}$  frame. Difference in period elongation is observed as a result of the large inelasticity imposed on the frames beyond time equal to 5 sec. The interstorey drift ratio of all three frames differed by very small amount. The maximum IDR is equal to 2.7% in the second story of the 30%  $M_{p_{beam}}$  frame. The record used during the simulation is scaled to a constant capacity-to-demand ratio, and hence the results cannot be directly compared to the requirements set by ASCE 41-06. However, a quick comparison for a period range between 1.0 sec and 1.5 sec showed the response

spectra resulting from scaling the record to be bounded by the DBE and MCE spectra given within ASCE 41-06 and in some cases exceeded MCE spectrum for the period range of interest. Therefore, it is conservative to conclude that the 70%  $M_{p_{beam}}$  and 50%  $M_{p_{beam}}$  frames satisfy the DBE drift requirements of 2.5% while the requirement is slightly violated by the 30%  $M_{p_{beam}}$  frame. The period range mentioned above is chosen to reflect the approximate initial period of the structures and the maximum expected period elongation based on the results of Chapter 6.

Comparison of the local behavior of the connection revealed that the lowest amount of slip in the top angle bolts is measured by the 30%  $M_{p_{beam}}$  connection with a mean and standard deviation values of 0.0450 in and 0.1654, respectively. The mean slip in the top angle of the 70%  $M_{p_{beam}}$  connection is 0.1017 in while the standard deviation is 0.0628, respectively. The top angle of the 50%  $M_{p_{beam}}$  connection measured a mean slip and standard deviation of 0.1538 in and 0.0277, respectively.

The mean slip of the seat angle bolts is 0.1439 in, 0.1636 in, and 0.1474 in for the 70%  $M_{p_{beam}}$ , 50%  $M_{p_{beam}}$ , and 30%  $M_{p_{beam}}$ , respectively. Less variation is observed for the mean slip of the seat angle bolts as reflected by the calculated standard deviations of 0.0186, 0.0253, and 0.0131 for all three connections, respectively. Therefore, it can be concluded that the largest scatter in the slip results is associated with the top angles of the connections.

In addition to the observed slip, the largest strain is measured in the top angle connected to beam flange and is equal to 3.38, 13.92, and 22.34 times the yield strain of the material for the 70%  $M_{p_{beam}}$ , 50%  $M_{p_{beam}}$ , and 30%  $M_{p_{beam}}$  connections, respectively.

Strain at other locations on the angles exceeded the yield strain of the material as well. Similarly large strain, in excess of the yield strain, is measured on the beam web by all three gauges in the rectangular rosette arrangement.

The moment-rotation relationships of the connections are derived using two different set of measurement including liner pots installed above the top angle and below the seat angle to measure the relative displacement between the beam and column as well as inclinometers installed on the beam web and column web. Very reasonable agreement in the derived moment-rotation relationships using both sets of measurements is observed. Large pinching and hardening is observed in the 70%  $M_{p_{beam}}$  connection when compared to the other two connections. The highest stiffness degradation of the original stiffness is observed by the 50%  $M_{p_{beam}}$  specimen to be 46.049%, followed by the 30%  $M_{p_{beam}}$  specimen with stiffness degradation of 33.59%, and finally the 70%  $M_{p_{beam}}$  specimen with stiffness degradation of 23.47%. The maximum moment sustained by the 70%  $M_{p_{beam}}$ , 50%  $M_{p_{beam}}$ , and 30%  $M_{p_{beam}}$  connections is equal to 3,222 kips.in, 2,556 kips.in, and 1,708 kips.in, respectively, with corresponding rotations of 0.0196 rad, 0.0271 rad, and 0.3400 rad, respectively. The behavior of all three connections is highlighted by stable hysteretic behavior and high energy dissipation.

- **Cyclic testing of the 50%  $M_{p_{beam}}$  and the 30%  $M_{p_{beam}}$**

Due to some technical problems with the LBCBs, cyclic testing of the 70%  $M_{p_{beam}}$  was not conducted. As expected, larger slip is observed when comparing the cyclic test results to that of the hybrid simulation due to the large magnitude of cycles imposed on the connection. The mean slip in the top angle bolts is equal to 0.4808 in and 0.2846 in with standard deviation of 0.0979 and 0.0242, respectively, for the 50%  $M_{p_{beam}}$

connection and the 30%  $M_{p_{beam}}$  connection, respectively. The mean slip in the seat angle bolts is equal to 0.3367 in and 0.1972 in with standard deviation of 0.0347 and 0.0224, respectively, for the 50%  $M_{p_{beam}}$  connection and the 30%  $M_{p_{beam}}$  connection, respectively.

The moment sustained by the connections is approximately 76% and 68.41% of the plastic moment of the beam for the 50%  $M_{p_{beam}}$  and 30%  $M_{p_{beam}}$  connections, respectively. The rotations sustained by both connections during the tests are 0.053 rad and 0.0440 rad for the 50%  $M_{p_{beam}}$  and 30%  $M_{p_{beam}}$ , respectively. The measured rotations exceeded the required rotation of 0.04 rad as per the 2005 seismic provisions of AISC, section 9.2a. The achieved moments do not meet the seismic specification of  $0.80M_p$  of the connected beam at an interstory drift angle of 0.04 radians for the SMRF. The requirement for complying with IMRF of 0.02 rad of interstory rotation is satisfied.

## CHAPTER 6

### ANALYTICAL INVESTIGATION AND DESIGN IMPLICATIONS

#### 6.1 Introduction

In this chapter, nonlinear dynamic response-history analyses are carried out using a suite of 10 records to investigate the seismic performance of semi-rigid frames. The goal of the parametric studies is to assess the effect of varying various connection design parameters on the global behavior of the frames. The design parameters include strength of the connection, yield strength of the angles, coefficient of friction used between faying surfaces, and the magnitude of slip allowed in the top and seat angles. In addition, a rigid frame of the same geometry is modeled and analyzed to be used as a reference for evaluating the performance of the semi-rigid frames. The varied design parameters and their magnitude are listed in Table 6-1.

Table 6-1 Varied design parameters used in the parametric studies

Connection Strength (% $M_{p_{beam}}$ )	Angle Yield Strength (ksi)	Friction Coefficient	Bolt Slip (in)
70			
50	36	0.25	1/16
30	50	0.33	NA

The semi-rigid frame models include the same element formulation and mathematical representation of the various inelastic features of the connection as the ones used in the hybrid simulation. The difference between the models used in the parametric studies and the hybrid simulations is in the material model employed in the analyses. In



this study, a simplified linear kinematic hardening model, used in design, is utilized since the motive behind the study is to investigate frame response as influenced by design parameters. The model, shown in Figure 6-1, is a bilinear model with an initial stiffness  $k_1$  representing the young's modulus of the material and a hardening stiffness,  $k_2 = 0.01k_1$  as suggested by (Elnashai and Elghazouli 1994).

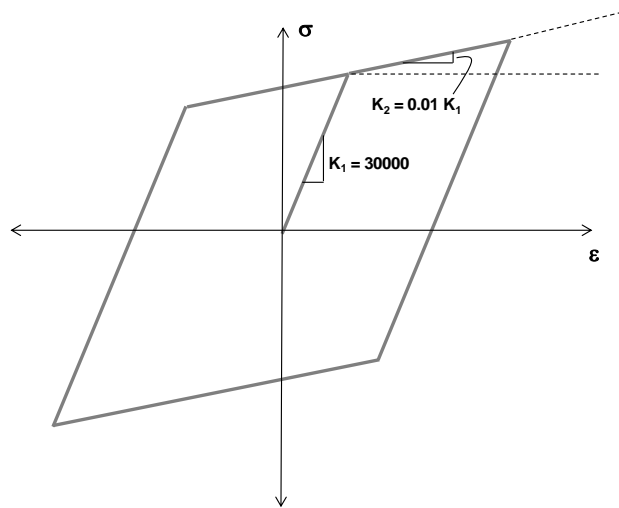


Figure 6-1 Linear kinematic hardening material model used in the parametric study

Various studies have been aimed at developing design guidelines for this type of connections with focus on connection detailing including size of angles and bolts, among other parameters. However, the effect of connection geometry and the design parameters on the global frame response and the implication on seismic design is yet to be conducted. Analysis of the frame is carried out to evaluate the period elongation of the structures and assign a realistic demand-based force reduction factor for each frame. Particularly, three main fundamental design parameters, including, the equivalent damping ratio,  $\zeta_{eq}$ , the inelastic period of the frames,  $T_{inelastic}$ , and the response modification factor,  $R_{demand}$ , are

investigated. The parameters are needed for constructing the inelastic response spectrum and estimating the inelastic base shear.

Naming of the models used in the analyses is assigned to reflect the earthquake the model is subjected to as well as the design parameters varied in each model. When naming the models a dash symbol, “-”, is used to separate the earthquake names and each of the design parameters. Specifically, each model name reflects the following; “the earthquake - earthquake station - connection strength - angle yield strength - coefficient of friction - amount of slip used in the model”. For example, a model named “LP-CLS-50%-36-0.33-0.0625” indicates that the Loma Prieta earthquake recorded at Corralitos station (CLS) is used to analyze a frame with connection capacity of 50%  $M_{p_{beam}}$  where the yield strength of the angles is 36 ksi, the coefficient of friction between surfaces is 0.33, and the bolt is allowed to slip for a distance of 0.0625 in (1/16 in). More detailed descriptions of the earthquakes used, the recorded stations, and the reference names used to describe the records are listed in Table 6-3.

## **6.2 Description of the Selected Building Structure**

The building layout used for the analysis is the same used in the hybrid simulation and is described in Chapter 3. The structure is a 2-story, 4-bay (longitudinal) and 2-bay (transverse) steel frame located in Los Angeles, California. The outer frames are designed as special moment-resisting frames to resist the earthquake loads using the International Building Code (International Building Code 2006). The height of the first and second

story is 15 ft and 13.5 ft, respectively and the bay width is 30 ft. The sizes of the beams and columns are W18 x 40 and W14 x 159, respectively.

### 6.3 Eigen Value Analysis and Fundamental Periods

Eigen value analyses are conducted to investigate the modes of vibrations and the fundamental period of the structures. A typical first three modes of vibrations for all frames are shown in Figure 6-2.

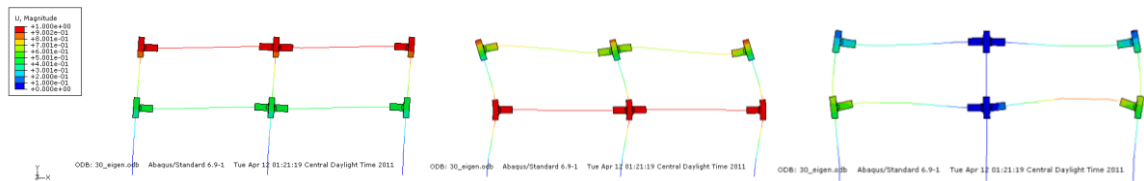


Figure 6-2 First three mode shape of vibrations for the 30%  $M_{p_{beam}}$  frame (typical for the other two frames)

The first three natural periods of the structures, including that of a rigid frame are listed in Table 6-2. As shown in the table, the periods of vibration for all frames are almost the same. This is due to the similarity in the initial stiffness of all three frames as shown in Figure 3-29 and listed in Table 3-7. Furthermore, the initial period of the 70%  $M_{p_{beam}}$  frame is higher than that of the rigid frame which is in correlation with the fact that the initial stiffness of the 70%  $M_{p_{beam}}$  frame is higher than that of its rigid frame counterpart as discussed in Chapter 3.

Table 6-2 First three natural periods of the structures

Frame ID	T <sub>1</sub> (sec)	T <sub>2</sub> (sec)	T <sub>3</sub> (sec)
Rigid	0.879	0.230	0.093
70% Mp <sub>beam</sub>	0.864	0.229	0.094
50% Mp <sub>beam</sub>	0.882	0.231	0.097
30% Mp <sub>beam</sub>	0.904	0.237	0.098

#### 6.4 Selection of Ground Motion Records

Ten horizontal ground motion records are selected for the dynamic response-history analysis. The records are a subset of an ensemble of 40 records (22 far-field and 28 near-field), recommended for the collapse assessment of building structures in Appendix-A of ATC 63 (Applied Technology Council (ATC) 2009). It is important to note that the records listed in ATC 63 are recommended on the basis of distance to fault rupture and not on either site condition or source mechanism. Selection of ground motions based on distance to fault rupture ensures the inclusion of directivity and pulse effect.

The appendix describes several criteria used for selecting the 40 records including; 1) very strong ground motion, 2) large number of records, 3) structure-type independent, and 4) site-hazard independent. According to ATC 63, the very strong motion criterion corresponds to MCE, which is a characteristic of shaking of buildings in high seismic regions with  $M_w \geq 6.5$ . Including large number of records is to ensure that a statistically sufficient number of earthquakes are used whereby the inherent variability in the ground motions is sufficiently represented. Finally, the importance of including records that are structure-type independent and site-hazard independent is to guarantee

that the records are applicable to evaluating a wide range of structural systems and can be used in the collapse evaluation of structures located at different sites.

Two criteria are used for determining the subset records, selected from the 40 records, to be used in the response-history analyses of the frames. First, the number of records to be used is such that the time required to complete all analyses is at minimum. The reason for such requirement is because on average, 10 hours of computational time is required to complete an analysis when subjecting any of the semi-rigid frames to 20 seconds of earthquake duration. On the other hand, it is important to include sufficient number of ground motions that well represent the hazard. A study conducted by Wen and Wu (2001) indicates that suites of 10 selected ground motions yield median response spectra that closely match the uniform hazard spectra in the elastic and inelastic ranges with coefficient of variation of less than 10%. In addition, the uniform hazard spectra developed are comparable to those corresponding to the USGS hazard map. Based on the results by Wen and Wu, it was decided to employ ten ground motion records in the parametric studies.

Upon deciding to use ten records in the analyses, selection of the ground motions is made such that large variation in the distance from the fault is represented as recommended by ATC 63. This is achieved through the selection of 5 earthquakes from the 22 far field set and 5 earthquakes from the 28 near field set of ATC63 with distance from fault ranging between approximately 2 km to 25 km.

The characteristics of the selected ground motions are shown in Table 6-3. The table includes the magnitude of the events, the year of occurrence, the earthquake name,

the station at which the record is measured, the closest distance to the fault, the PGA of the record, and the scale factor used to scale the records.

Table 6-3 Characteristics of the ground motion records used in the parametric study

Mw	Year	Earthquake Name	Station ID	Reference Name	Distance (km)	PGA	Scale Factor
6.5	1979	Imperial Valley	Bonds Corner (HBCR230)	IV-HBCR	2.7	0.775	1.002
6.9	1989	Loma Prieta	Corralitos (CLS000)	LP-CLS	3.9	0.644	1.339
6.7	1992	Erzincan	Erzincan (ERZEW)	EZ-ERZ	4.4	0.496	0.997
7.5	1999	Kocaeli	Izmit (IZT090)	KC-IZT	7.2	0.220	2.347
6.7	1994	Northridge	Arleta (ARL360)	NR-ARL	8.7	0.308	1.989
7.1	1999	Duzce	Bolu (BOL000)	DZ-BOL	12.0	0.728	0.929
6.7	1994	Northridge	Canyon County WLC (LOS000)	NR-LOS	12.4	0.410	1.636
6.9	1989	Loma Prieta	Capitola (CAP090)	LP-CAP	15.2	0.443	1.542
6.9	1995	Kobe	Shin Osaka (SHI090)	KB-SHI	19.2	0.212	1.731
6.7	1994	Northridge	Century City CC North (CCN360)	NR-CCN	25.7	0.222	1.225

The records are scaled to the MCE spectrum per ASCE07 (American Society of Civil Engineers (ASCE 7-05) and Structural Engineering Institute (SEI) 2005) where the response spectrum of the record is anchored at the spectral acceleration of the MCE design spectrum corresponding to the period of the structure. The MCE design spectrum is developed assuming the structures are founded on an area with soil classification D with occupancy category of II and an importance factor of 1.0. The response acceleration for short period and one second period are taken as 1.50g and 0.60g, respectively. The frames are designed as special moment-resisting frames with seismic response modification factor ( $R$ ), overstrength factor ( $\Omega_d$ ) and deflection amplification factor ( $C_d$ ) of 8, 3, and 5.5 respectively. The scaled records and the resulting PGA are shown in Figure 6-3. The corresponding response spectra are shown in Figure 6-4.

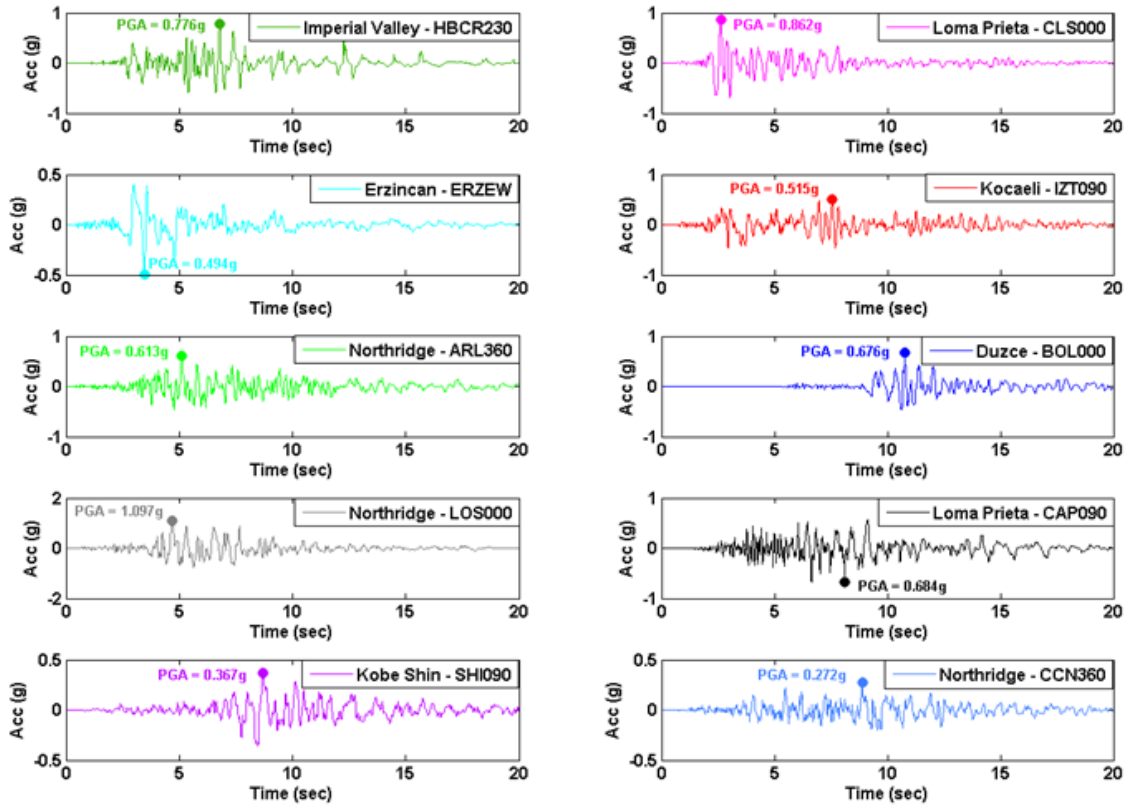


Figure 6-3 Scaled records used in the parametric studies

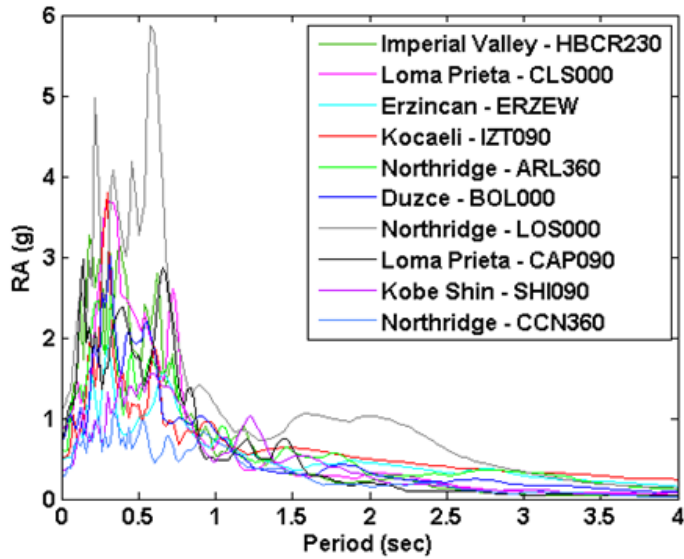


Figure 6-4 Response spectra of the scaled records

## 6.5 Investigation of Frame Response

To evaluate the seismic response of the frames, different parameters are investigated including global drift, base shear, and interstory drift ratio. Comparison of the results is summarized in tables to reflect the following:

- Average response for a given connection strength and design parameters under all earthquakes (i.e., average response of the first model of the 30%  $M_{p_{beam}}$  frame under all earthquakes).
- Average response for a given connection strength with all different design parameters under a given earthquake (i.e., comparison of average of all 30%  $M_{p_{beam}}$ , 50%  $M_{p_{beam}}$  and the 70%  $M_{p_{beam}}$  models under individual earthquakes).

### 6.5.1 Global Drift and Base Shear

With the exception of connection strength, varying the design parameters appear not to significantly influence the behavior except in the nonlinear range (i.e., after the peak response). This is expected since for low rise frames, the columns are the primary contributors to the resistance of lateral forces. Figure 6-5 shows the influence of connection flexibility on the fundamental period of vibrations for frames with varying heights. As shown in the figure, for low-rise frames the ratio of the fundamental period of a semi rigid frame to that of a rigid frame is smaller than the ratio for taller frames. In other words, the lateral stiffness of semi-rigid frames approaches that of rigid frames as the height of the frames decreases. Furthermore, the figure shows the ratio to approach one as the connection stiffness reaches that of a rigid frame as indicated by the nondimensional connection stiffness parameter,  $m$ .



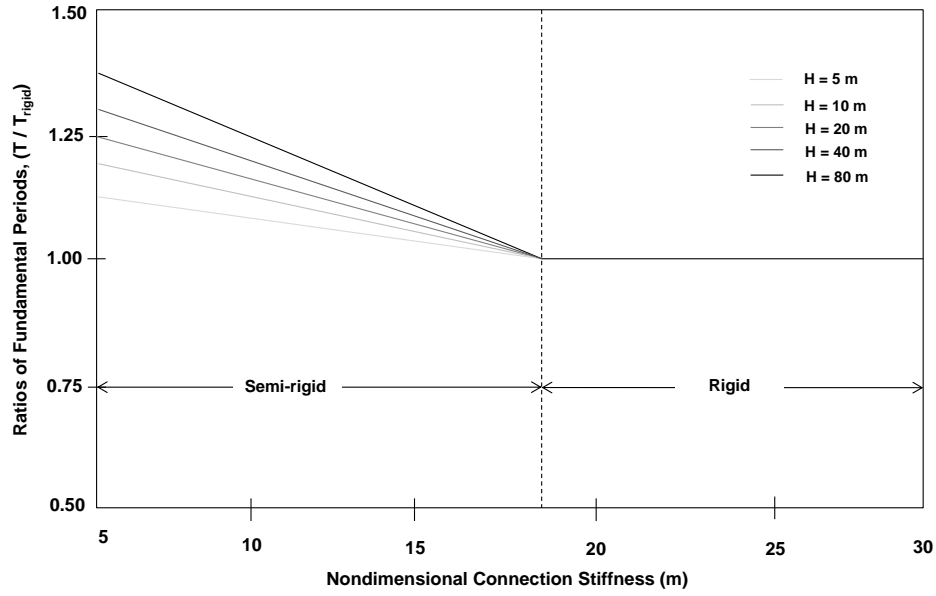


Figure 6-5 Influence of connection flexibility on the fundamental period of vibration for frames with varying heights (Elnashai and Di Sarno 2008)

Figure 6-6 shows an example of the effect of varying the angle yield strength, coefficient of friction, and slip on the roof displacement response of the 50%  $M_{p_{beam}}$  frame under the Loma Prieta earthquake (LP-CLS). As shown in the figure, variation in the response, as a result of varying the design parameters, is evident after time of approximately 3.1 sec.

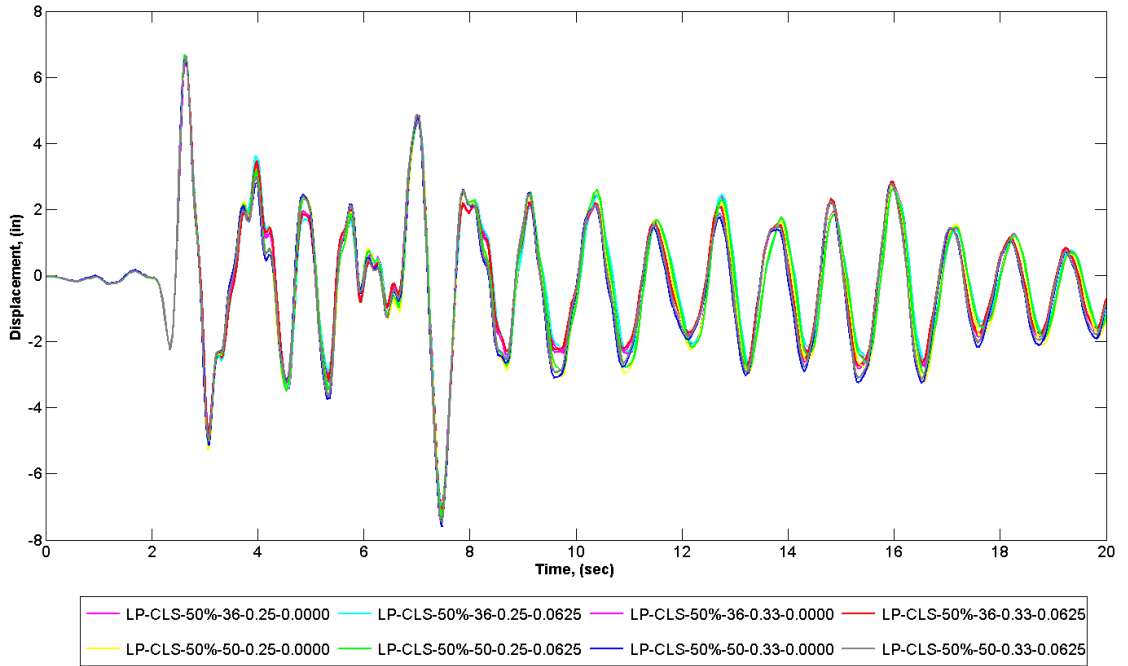


Figure 6-6 Roof displacement response of the 50%  $M_{p_{beam}}$  frame to the 1989 Loma Prieta earthquake (LP-CLS)

As shown in Table 6-4, as the connection strength decreases, the average maximum absolute response of the frames is characterized by an increase in roof displacement and a decrease in base shear. This is expected since the stiffness of the frames decreases with reduction in connection strength, causing higher displacement and lower base shear demand on the frames. Specifically, the roof displacement of the 50%  $M_{p_{beam}}$  and 30%  $M_{p_{beam}}$  is 2.86% and 4.29% higher than that of the 70%  $M_{p_{beam}}$  frame, respectively, while the base shear of the 50%  $M_{p_{beam}}$  and 30%  $M_{p_{beam}}$  frames is 5.04% and 21.07% lower than that of the 70%  $M_{p_{beam}}$  frame, respectively.

The dispersion in the results as influenced by the variation in the angle yield strength, the coefficient of friction, and the magnitude of slip is quantified with the

calculated standard deviation. Lower standard deviation is observed for the roof displacement results while higher standard deviation is observed with the base shear results. The maximum percent difference between the highest and lowest values is equal to 3.43%, 5.89%, and 4.99% for roof displacement and 6.52%, 8.55%, and 19.21% for the base shear for the 70%  $M_{p_{beam}}$ , 50%  $M_{p_{beam}}$ , and 30%  $M_{p_{beam}}$  frames, respectively. Variation in the response is better visualized through the bar graphs shown in Figure 6-7.

Table 6-4 Average maximum absolute response for a model under all ground motions

Model Parameters	70% $M_{p_{beam}}$		50% $M_{p_{beam}}$		30% $M_{p_{beam}}$	
	$\Delta_{Roof}$ (in)	$V_{Base}$ (kips)	$\Delta_{Roof}$ (in)	$V_{Base}$ (kips)	$\Delta_{Roof}$ (in)	$V_{Base}$ (kips)
36-0.25-0.000	6.39	266.82	6.57	242.89	6.41	198.82
36-0.25-0.0625	6.29	264.51	6.48	244.68	6.44	189.94
36-0.33-0.000	6.27	265.71	6.36	242.44	6.44	198.37
36-0.33-0.0625	6.19	251.57	6.28	238.10	6.42	198.75
50-0.25-0.000	6.41	267.98	6.65	258.47	6.66	220.64
50-0.25-0.0625	6.30	265.70	6.58	258.01	6.69	211.78
50-0.33-0.000	6.25	263.94	6.45	256.36	6.73	226.43
50-0.33-0.0625	6.21	252.48	6.40	251.85	6.70	211.75
Mean	6.29	262.34	6.47	249.10	6.56	207.06
STD Dev.	0.078	6.49	0.124	8.03	0.145	12.59

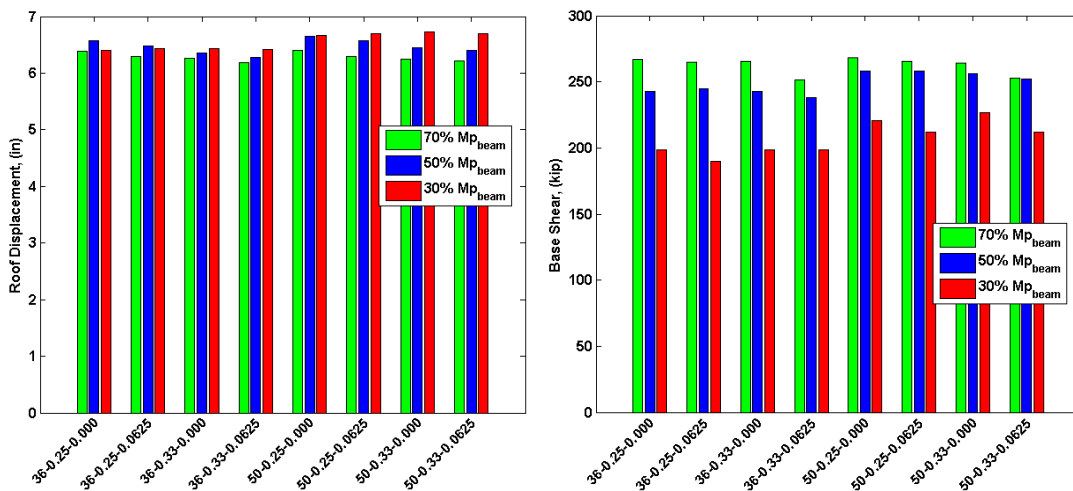


Figure 6-7 Average maximum absolute response with varying design parameters under all ground motions

Table 6-5 shows the average maximum absolute response of all models under a given earthquake. In addition to the average response shown in the table for the semi-rigid frames, analyses are also conducted on rigid frames so that reference comparison can be established. As shown in the table, the resulting roof displacement and base shear of the rigid frame are significantly higher than that of the semi-rigid frames with the exception of the performance under the Northridge earthquake (NR-CCN). This might be due to the fact that the semi-rigid frames have significantly higher energy dissipation characteristic when compared to the rigid frame since their pushover curves is characterized by early yielding of the frames, unlike the rigid frame. It is important to note that the rigid frame model is developed to represent a typical pre-Northridge structure which has shown poor performance during the earthquake.

A number of design strategies to improve the beam-to-column connection behavior of steel structures were proposed after the Northridge earthquakes and have shown satisfactory results. It is possible that if one of such strategies is employed in the rigid frame model (ex. reduced beam section), the results could be more satisfactory than shown in Table 6-5 below. The average maximum response results listed in the table are superimposed on the pushover curves of the semi-rigid frames as shown in Figure 6-8. As expected, scatter in the results of the dynamic-response analyses is shown when compared to that of the pushover curves.

Table 6-5 Average maximum absolute response of all models under a given earthquake

EQ- Station ID	Rigid		70% $M_{p_{beam}}$		50% $M_{p_{beam}}$		30% $M_{p_{beam}}$	
	$\Delta_{Roof}$ (in)	$V_{Base}$ (kips)	$\Delta_{Roof}$ (in)	$V_{Base}$ (kips)	$\Delta_{Roof}$ (in)	$V_{Base}$ (kips)	$\Delta_{Roof}$ (in)	$V_{Base}$ (kips)
IV-HBCR	9.13	638.06	5.20	319.10	4.98	329.67	5.48	298.11
LP-CLS	9.16	382.50	6.72	382.50	6.62	379.17	6.46	412.49
EZ-ERZ	9.93	467.51	3.69	281.52	3.85	274.85	4.14	252.43
KC-IZT	18.05	464.50	6.04	327.99	6.60	286.61	9.35	328.22
NR-ARL	12.07	473.11	4.61	384.18	5.31	341.36	6.37	285.54
DZ-BOL	10.78	560.95	7.77	281.13	6.53	285.89	5.38	275.98
NR-LOS	18.82	640.89	3.85	305.94	4.17	282.58	6.28	236.82
LP-CAP	8.00	594.12	5.79	230.36	6.43	228.05	8.24	204.86
KB-SHI	8.19	474.86	5.38	209.45	7.10	229.7	7.62	212.67
NR-CCN	6.15	354.56	6.18	262.34	6.22	249.05	5.90	180.07
Mean	11.03	505.11	5.52	298.45	5.78	288.69	6.52	268.72
STD Dev.	4.22	99.92	1.26	57.94	1.13	12.59	1.52	8.13

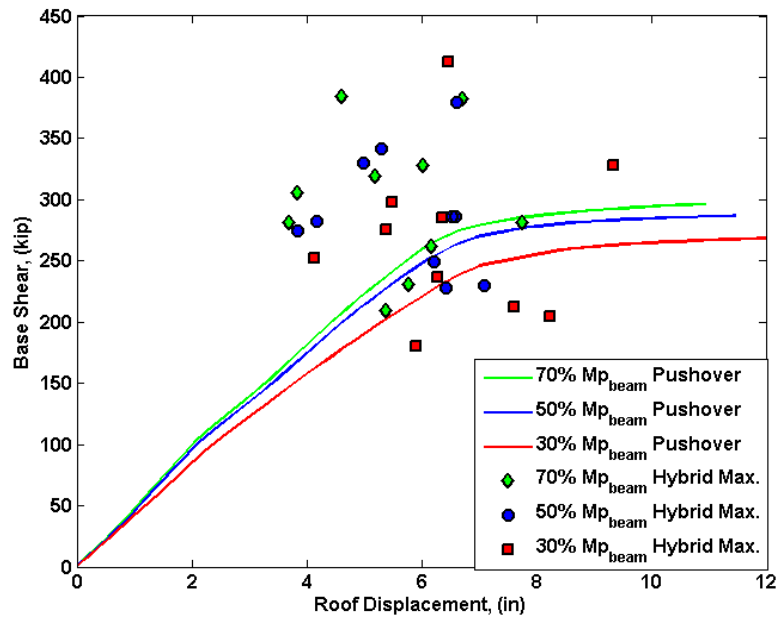


Figure 6-8 Average maximum absolute base shear and displacement from the dynamic analyses superimposed on the pushover results

## 6.5.2 Interstory Drift Ratio

Table 6-6 below shows the average maximum absolute IDR for all models under all ground motions. As shown in the table, all models satisfied the ASCE 41-06 requirement of 5% IDR for MCE. The table also shows the calculated average IDR to be larger for the first story than the second story. This is due to the mass of the first story being larger than that of the second story which causes higher IDR between the first story and the ground when compared to that of the second story and the first story.

Table 6-6 Average maximum absolute IDR for a model under all ground motions

Model Parameters	70% $M_{p_{beam}}$		50% $M_{p_{beam}}$		30% $M_{p_{beam}}$	
	IDR <sub>1st</sub> (%)	IDR <sub>2nd</sub> (%)	IDR <sub>1st</sub> (%)	IDR <sub>2nd</sub> (%)	IDR <sub>1st</sub> (%)	IDR <sub>2nd</sub> (%)
36-0.25-0.000	2.66	1.76	2.70	1.78	2.91	1.72
36-0.25-0.0625	2.60	1.73	2.70	1.77	2.91	1.71
36-0.33-0.000	2.62	1.73	2.66	1.74	2.91	1.72
36-0.33-0.0625	2.58	1.69	2.65	1.73	2.91	1.73
50-0.25-0.000	2.67	1.77	2.70	1.81	2.92	1.78
50-0.25-0.0625	2.62	1.73	2.69	1.80	2.91	1.77
50-0.33-0.000	2.63	1.75	2.67	1.76	2.91	1.78
50-0.33-0.0625	2.57	1.70	2.63	1.75	2.91	1.76
Average	2.62	1.73	2.67	1.77	2.91	1.75
STD Dev.	0.035	0.028	0.027	0.028	0.004	0.029

The results listed in Table 6-6 are shown with a bar chart in Figure 6-9. The figure shows that for a given combination of design parameters, the largest calculated average maximum IDR of the first story resulted in the 30%  $M_{p_{beam}}$  frame, followed by the 50%  $M_{p_{beam}}$  frame, then the 70%  $M_{p_{beam}}$ . A strong conclusion cannot be made regarding the IDR response of the second story since the results of all three semi-rigid frames lay within a very narrow range. However, it appears from the figure that the largest

calculated average maximum absolute IDR of the second story is experienced by the 50%  $M_{p_{beam}}$ .

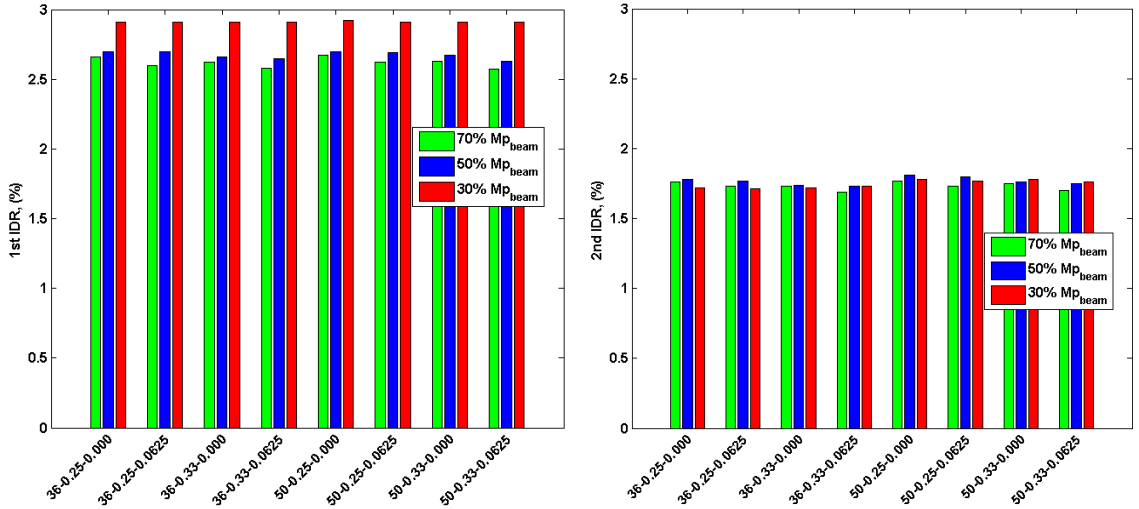


Figure 6-9 Average maximum absolute IDR ratios with varying design parameters under all ground motions

The average maximum absolute IDR for all models under a given earthquake are shown in Table 6-7. Despite the rigid frame experiencing large roof displacement when excited by the earthquakes (Table 6-5), the average first-and second-story IDR of the rigid frame is still below the 5% limit of ASCE 41-06 for MCE except when the frame is subjected to the NR-LOS record.

Table 6-7 Average maximum absolute IDR of all models under a given earthquake

EQ- Station ID	Rigid		70% $M_{p_{beam}}$		50% $M_{p_{beam}}$		30% $M_{p_{beam}}$	
	IDR <sub>1st</sub> (%)	IDR <sub>2nd</sub> (%)	IDR <sub>1st</sub> (%)	IDR <sub>2nd</sub> (%)	IDR <sub>1st</sub> (%)	IDR <sub>2nd</sub> (%)	IDR <sub>1st</sub> (%)	IDR <sub>2nd</sub> (%)
IV-HBCR	3.13	2.25	3.05	2.38	2.92	1.73	2.43	1.78
LP-CLS	3.87	1.72	2.94	1.50	2.84	1.50	3.14	1.80
EZ-ERZ	3.65	2.94	3.08	2.16	3.53	2.11	2.90	2.17
KC-IZT	5.56	5.10	2.47	1.71	3.27	2.36	2.74	1.50
NR-ARL	3.96	3.24	2.62	1.82	2.54	1.54	2.83	2.11
DZ-BOL	4.00	2.75	2.73	1.49	2.66	1.47	3.18	1.68
NR-LOS	6.49	5.22	2.60	1.97	2.82	1.74	2.69	2.13
LP-CAP	2.96	1.78	2.32	1.48	3.07	1.83	2.09	1.37
KB-SHI	2.93	2.40	2.56	1.65	3.00	1.77	1.93	1.32
NR-CCN	2.44	1.51	2.36	1.51	2.48	1.42	2.26	1.49
Average	3.90	2.89	2.67	1.77	2.91	1.75	2.62	1.73
STD Dev.	1.25	1.32	0.272	0.314	0.324	0.299	0.428	0.319

The interstory drift ratios for 70%  $M_{p_{beam}}$ , 50%  $M_{p_{beam}}$ , and 30%  $M_{p_{beam}}$  are shown in Figure 6-10, Figure 6-11, and Figure 6-12, respectively. The figures combine the IDRs of the first and second stories to give a more physical sense of the deformation of the frame as a whole. In addition, the figures illustrates the effect of varying the design parameters under a given earthquake on the IDRs (i.e., average values are not used). As shown in the figures, the effect of varying the design parameters on the IDR increases as the connection strength degrades. Such observation suggests that there is coupling between yielding of the angles and the increase in the effect of the design parameters on the system behavior.



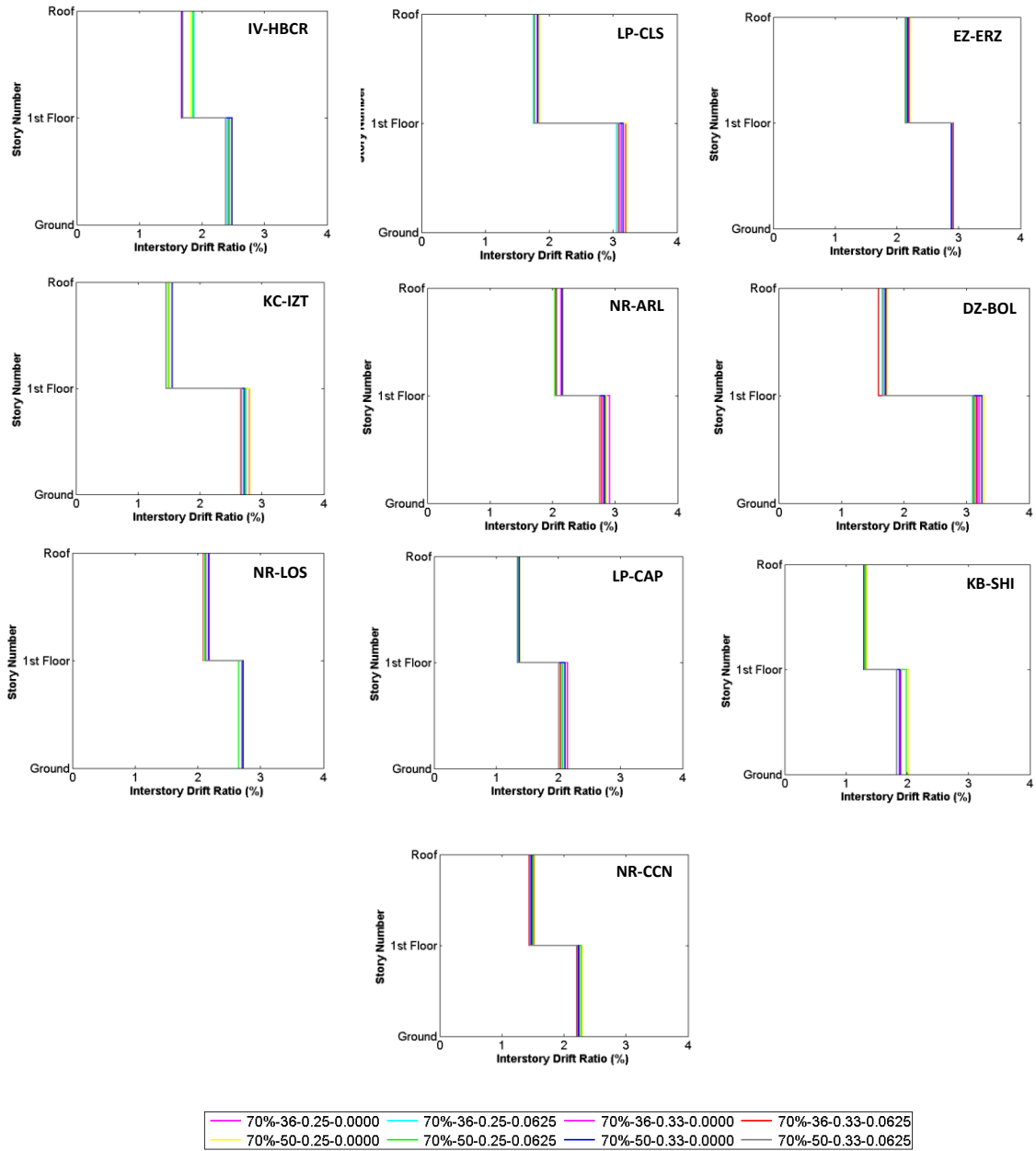


Figure 6-10 IDR for the 70%  $M_{p,beam}$  frame

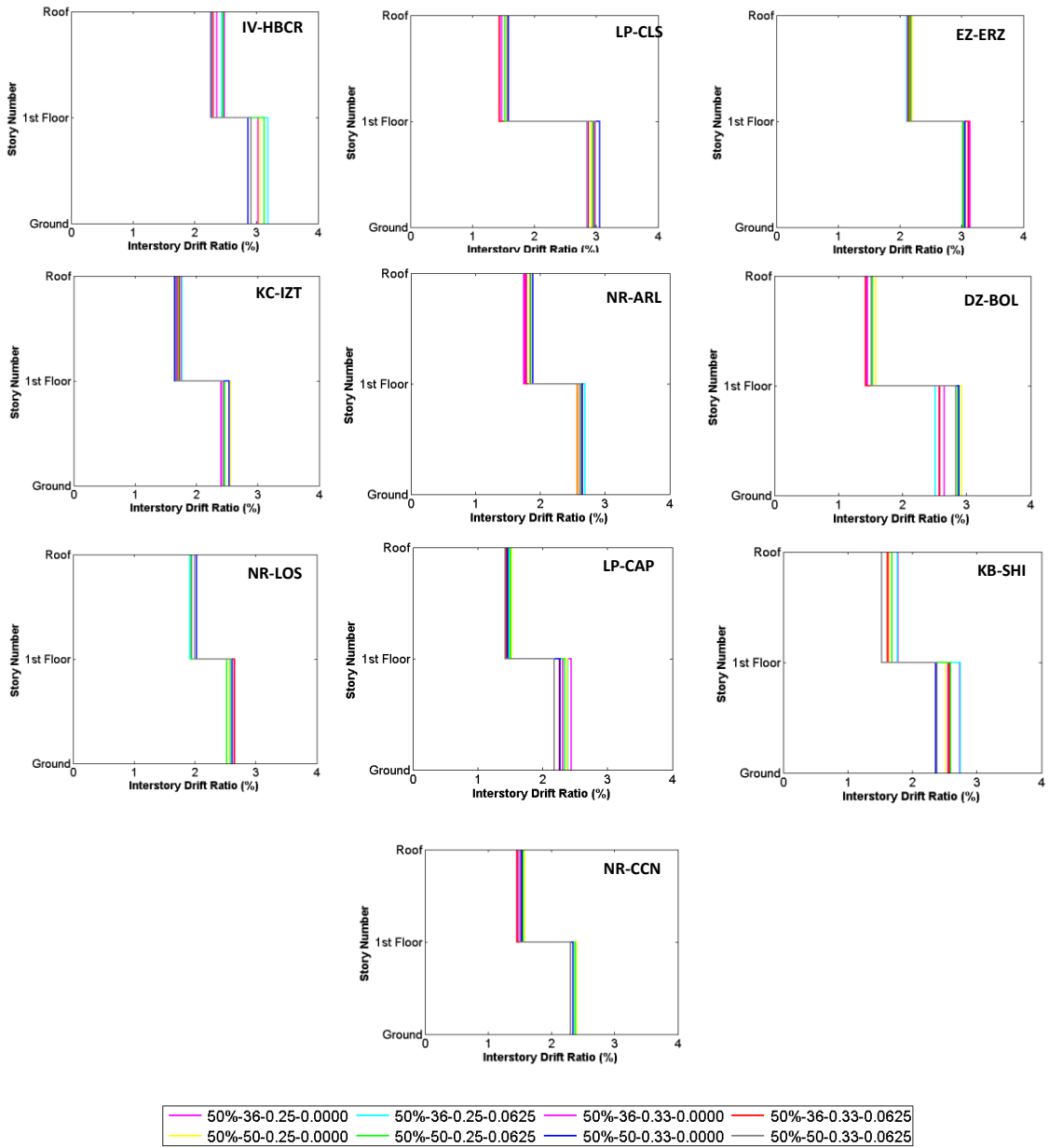


Figure 6-11 IDR for the 50%  $M_{p,beam}$  frame

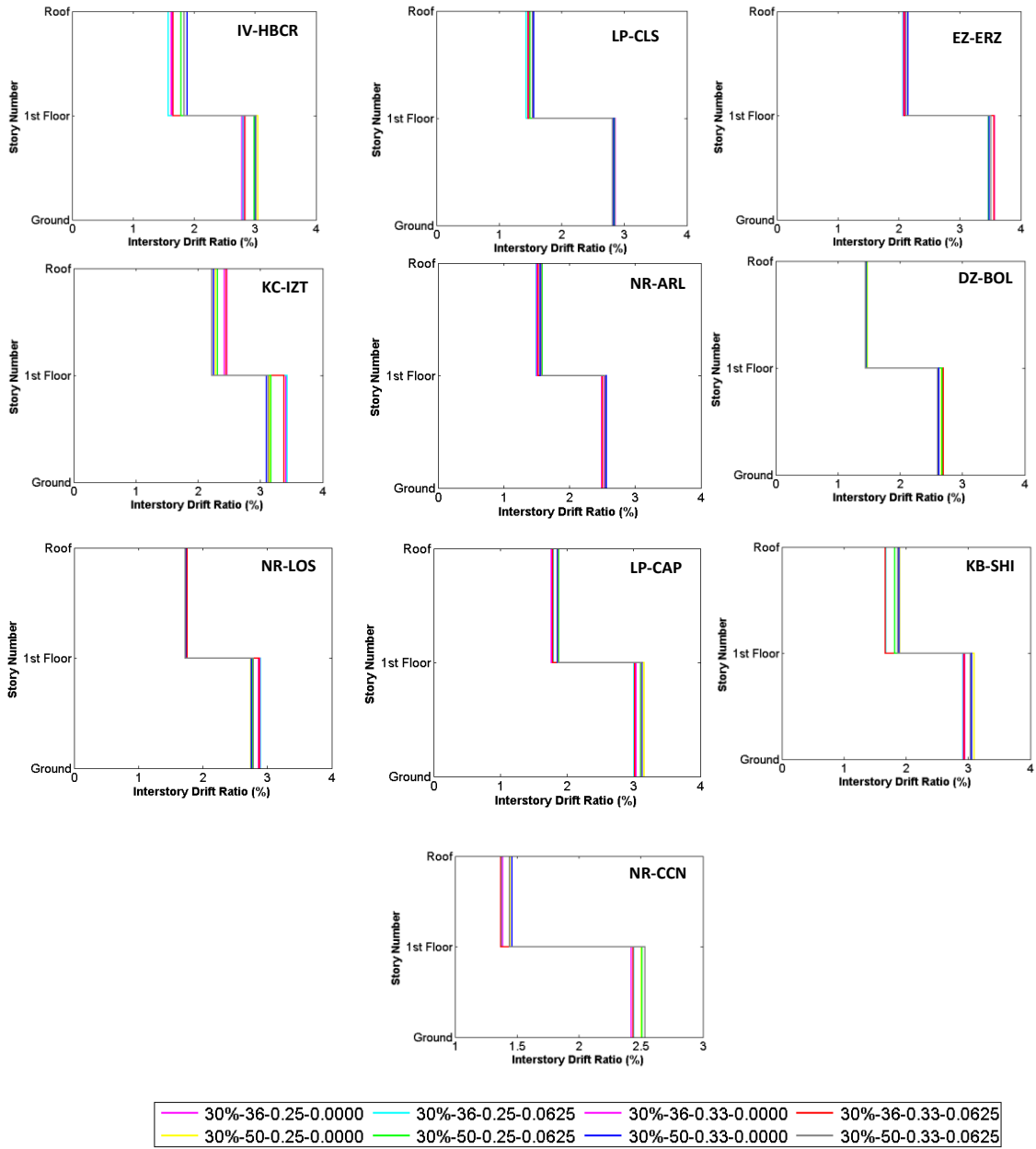


Figure 6-12 IDR for the 30%  $M_{p\text{beam}}$  frame

## 6.6 Design Approach and Methodology

The code approach for the seismic design of structures is based on constructing a simplified response spectrum from which the base shear is estimated (American Society of Civil Engineers (ASCE 7-05) and Structural Engineering Institute (SEI) 2005; International Building Code 2006). In a general term, the spectrum is used to determine the spectral acceleration corresponding to the period of the structure, which is then multiplied by the mass of the structure to determine the base shear. The parameters used for constructing the response spectrum ( $S_{D1}$  and  $S_{DS}$ ), shown in Figure 6-13, are simply the coefficients for the MCE spectral response acceleration, adjusted for site class effects.

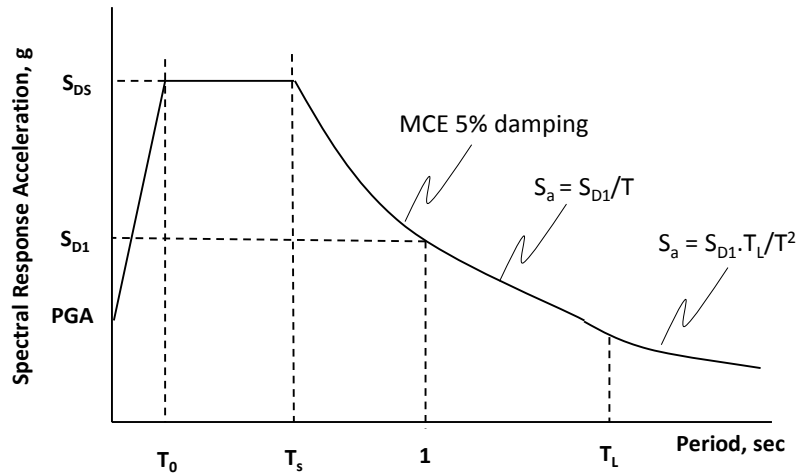


Figure 6-13 Design elastic response spectrum, *after*: (American Society of Civil Engineers (ASCE 7-05) and Structural Engineering Institute (SEI) 2005)

Three major fundamental design parameters are required for constructing the response spectrum and estimating the inelastic base shear, which is used to determine actions on the various components and elements of the structure considered. The main design parameters include, the equivalent damping ratio,  $\zeta_{eq}$ , the period of the structure,

$T_{elastic}$  (known as  $T_a$  in codes), and the response modification factor,  $R$ . First, the equivalent damping ratio is used in the construction of the elastic response spectra where the peak of the spectrum is determined for the MCE mapped spectral acceleration 5% critical damping. It is important to note that the 5% damping value is fixed regardless of frame type and height. A mapped MCE spectral acceleration that is adjusted to account for the actual equivalent damping of the structure will lead to more accurate estimates of the base shear. Once the elastic response spectrum is constructed, the elastic spectral acceleration corresponding to the approximated structural period,  $T_a$ , can be estimated. The elastic base shear is then determined by multiplying the elastic spectral acceleration by the mass. The approximated period is calculated using the following equation.

$$T_a = C_t h_n^x \quad (6.1)$$

Where  $C_t$  is a coefficient equal to 0.028 for steel,  $h_n$  is the height of the structure in feet, and  $x$  is a constant equal to 0.8. The code imposes an upper limit on estimating the period for strength determination,  $T_s$ , to ensure that an unreasonably low design base shear is not calculated by using a long period based on an unrealistic frame stiffness assumption.

Following the calculation of the elastic spectral response acceleration, the inelastic seismic response coefficient is then calculated using equation (6.2). Where,  $I$  is the importance factor and  $R$  is the response modification factor.

$$C_s = \frac{S_{Ds}}{R/I} \quad (6.2)$$

The current code design approach is conservative in that it uses the elastic period of the structure for estimating the inelastic seismic response coefficient. This results in estimating higher base shear than what is likely to be experienced by the structure. An improvement to the code design approach can be achieved if the inelastic period of the structure can be estimated and used to determine the inelastic seismic response coefficient. A modified code-based seismic design approach can be as follows:

- Construct the elastic response spectrum using the conventional code approach with damping coefficient value representing the actual damping in the structure instead of that assumed by the code
- Construct the inelastic response spectrum by dividing the elastic spectrum by (R/I) where a realistic R value, which accounts for the actual period elongation of the system is used
- Use an estimated inelastic period of the structure,  $T_{inelastic}$  to estimate the seismic response coefficient,  $C_s$ , from the inelastic response spectrum
- Estimate the base shear by multiplying the seismic response coefficient with the mass of the structure

From the above discussion, it is clear that calculating the inelastic base shear for the seismic design of frames requires the determination of the following design parameters:

- The equivalent damping ratio,  $\zeta_{eq}$

- The initial period and elongated period of the structure  $T_{inelastic}$
- The response modification factor,  $R$

The sections below are aimed towards assessing the three design parameters indicated above.

### 6.7 Determination of the Equivalent Damping Ratio, $\zeta_{eq}$

The equivalent damping ratio of a structure,  $\zeta_{eq}$ , is simply an equivalent viscous damping that is based on the measured response of a structure at a particular frequency, which is equal to the natural frequency of the system. Such value should be representative of all damping mechanism present in the structure. The value could be determined by equating the energy dissipated in a vibration cycle of the actual structure,  $E_D$ , to that of an equivalent viscous system using the following equation.

$$4\pi\zeta_{eq} \frac{\omega}{\omega_n} E_{So} = E_D \quad (6.3)$$

Where,  $E_{So} = ku_o^2 / 2$  and  $u_o$  is the maximum displacement. It is important to note that  $E_D$  is defined at  $\omega = \omega_n$ , resulting in  $\zeta_{eq}$  defined as:

$$\zeta_{eq} = \frac{1}{4\pi} \frac{E_D}{E_{So}} \quad (6.4)$$

A schematic of the energy dissipated in the actual structure,  $E_D$ , and the strain energy,  $E_{So}$ , is shown in Figure 6-14.

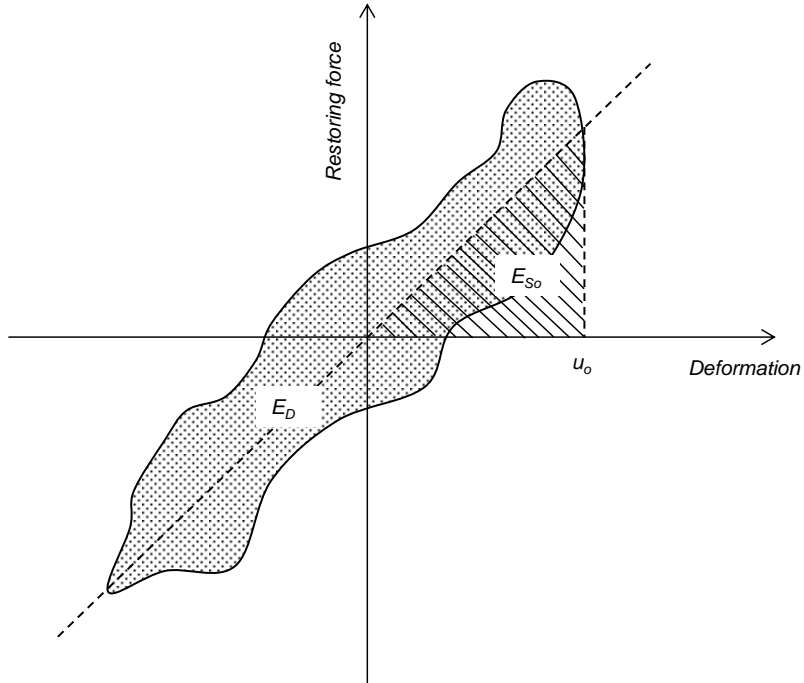


Figure 6-14 Schematic of the dissipated energy,  $E_D$ , in a cycle of harmonic vibration and the strain energy,  $E_{S_0}$ , after: (Chopra 2006)

A distributed inverted triangle load is used to develop a force-displacement curve for the frames similar to the one shown in the figure. The distributed load used corresponds to the base shear value developed as a result of imposing a peak displacement on the frame, which is equal to the force reduction factor multiplied by yield displacement. In other words, an inverted load triangle is assumed along the frame height and a pushover analysis is conducted. If the peak displacement resulting from the analysis is equal to the ultimate displacement calculated by  $(\Delta_u = R * \Delta_y)$ , where  $R$  and  $\Delta_y$  are given, then the pushover analysis is deemed acceptable and the resulting force-displacement cycle is used in calculating the equivalent damping. The reason for using such approach instead of applying the ultimate displacement directly to the frame is due to the fact that using displacement control in pushover analysis results in an excessively



stiffer behavior of the frame and deformation that does not correspond to mode one deformation, which will result in inaccurate representation of the energy dissipated by the frame. To use displacement control in a pushover analysis, one should employ an algorithm such that one node at a floor level is being pushed while the magnitude of the displacement of the other node, at the other floor level, is adjusted so that the restoring forces are maintained as a constant ratio of each other.

It is important to note that the force reduction factor used to calculate the ultimate displacement is derived in Section 6.9. The target ultimate displacement is calculated to be equal to 15.57 in, 15.68 in, and 15.05 in for the 70%  $M_{p_{beam}}$ , 50%  $M_{p_{beam}}$ , and the 30%  $M_{p_{beam}}$  frame, respectively. That is,  $\Delta_u = R * \Delta_y$ , which is equal to  $6.55 * 2.377$  for the 70%  $M_{p_{beam}}$  frame,  $6.79 * 2.31$  for the 50%  $M_{p_{beam}}$  frame, and  $6.81 * 2.21$  for the 30%  $M_{p_{beam}}$  frame.

The hysteretic loops used for calculating the dissipated energies and the equivalent damping for all models are shown in Figure 6-15. It is noted that the larger hysteretic loop is developed by the 70%  $M_{p_{beam}}$  and 50%  $M_{p_{beam}}$  frames when compared to the 30%  $M_{p_{beam}}$  frame. This is due to the fact that as the connection strength increases, so is the angle size used in constructing the connection (i.e., there is more material that can yield and dissipate energy).

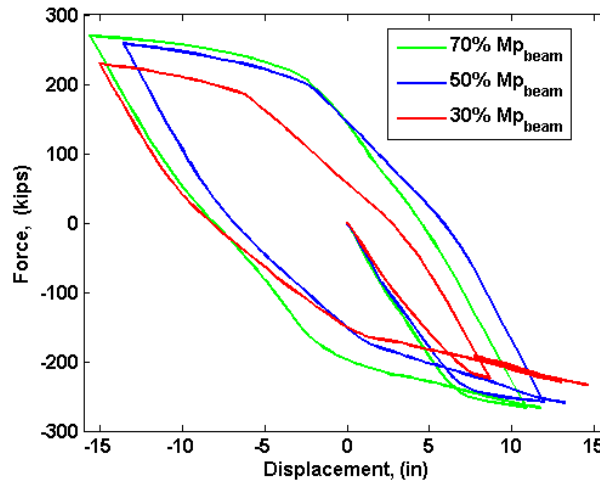


Figure 6-15 Cyclic response of the semi-rigid frames

It is worth noting that in a multi-degree of freedom system, an equivalent damping can be assigned to each natural vibration mode. The equivalent damping ratios calculated are, however, associated with the first mode response. This is because the lateral load applied to the frames is distributed along the height per each floor weight to represent mode one deformation shape. The resulting equivalent damping is 7.78%, 7.23%, and 5.13% for the 70%  $M_{p_{beam}}$ , 50%  $M_{p_{beam}}$  and 30%  $M_{p_{beam}}$  frame, respectively, as listed in Table 6-8.

Table 6-8 Equivalent damping for all three semi-rigid frames

Frame ID	$\zeta_{eq}$ (%)
70% $M_{p_{beam}}$	7.78
50% $M_{p_{beam}}$	7.23
30% $M_{p_{beam}}$	5.13

It is important to note that the IBC or ASCE 07-2005 design codes assume 5% damping when the spectral response acceleration associated with MCE is constructed.

The same damping value is assumed for steel structures by other design codes including for example EC 8 (Eurocode 8 2003). Analytical studies of steel frames have shown very large variation in the damping ratio employed by researchers in the analysis, ranging from 2% to 5% (Pong 2002; Murat Diclelia and Anshu Mehtab 2006; Monica D. Kohler, Thomas H. Heaton et al. 2007). An analytical investigation was conducted to evaluate the magnitude of the equivalent damping ratio of rigid 1-bay steel frames, with varying number of stories, as a function of the ductility ratio and the peak ground acceleration (Parulekar, Vaity et al. 2004). The number of stories used in the investigations is 5, 10, and 20. Similar to this study, the equivalent damping ratio is determined by equating the energy dissipated in a vibration cycle of the actual structure,  $E_D$ , to that of an equivalent viscous system. The results show large magnitudes of equivalent damping ratio associated with large ductility ratio and peak ground acceleration as shown in Figure 6-16.

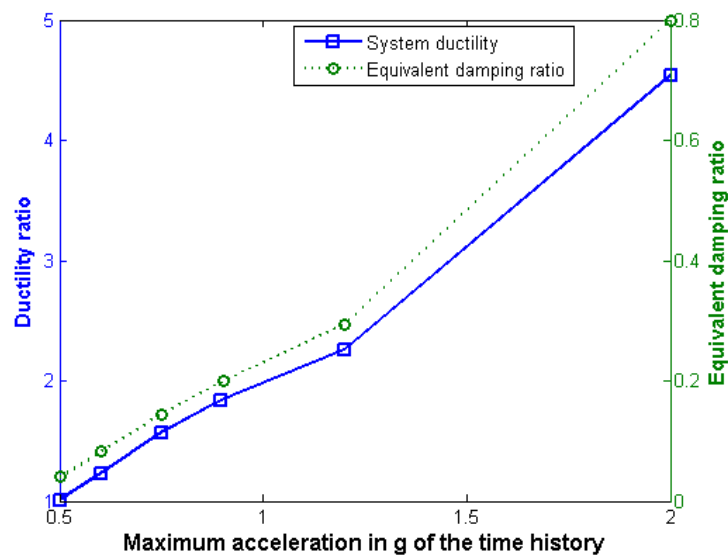


Figure 6-16 Variation of ductility and damping ratio with peak ground acceleration, *after*: (Parulekar, Vaity et al. 2004)

## 6.8 Investigation of Period Elongation

### 6.8.1 Fourier Transformation

Traditionally, studies have focused on evaluating the inelastic period of structures using Fourier transformation. The Fourier transformation is a mathematical representation of the amplitudes of the signal by decomposing a function into oscillatory function. The discrete Fourier transformation is a periodic sequence of sampled values  $\{x_n\}_{n=0}^{N-1}$  of period  $N$  (or number of sample  $N$ ) transformed into  $X_p$  values using the following equation:

$$X_p = \sum_{n=0}^{N-1} x_n e^{-j \frac{2\pi}{N} np}, p \in \{0, 1, \dots, N-1\} \quad (6.5)$$

Where  $e$  denotes the natural exponent and  $j = \sqrt{-1}$ , and  $x_n$  is a complex number equal to  $x_{real} + j x_{imag}$ . Similar to the DFT, the fast Fourier transform (FFT) of a periodic function is an extraction of the series of the sines and cosines for which the function is made up of (i.e., the superposition of the sines and cosines reproduces the function). In fact, FFT is nothing but an efficient algorithm used to compute the DFT and its inverse. A real periodic function  $x(t)$  can be expressed as sum of trigonometric series ( $-L < t < L$ ) as:

$$x(t) = \frac{1}{2} a_0 + \sum_{n=1}^{\infty} \left( a_n \cos \frac{\pi n}{L} t + b_n \sin \frac{\pi n}{L} t \right) \quad (6.6)$$

For which the coefficients can be computed by:

$$a_n = \frac{1}{L} \int_{-L}^L x(t) \cos \frac{\pi n}{L} t dt \quad (6.7)$$

$$b_n = \frac{1}{L} \int_{-L}^L x(t) \sin \frac{\pi n}{L} t dt \quad (6.8)$$

The generalization of the continuous Fourier series for infinite domains can be expressed by:

$$x(t) = \int_{-\infty}^{\infty} F(f) e^{-2\pi i f t} df \quad (6.9)$$

When fast Fourier transformation (FFT) is carried out on the function above, the result is the real and imaginary terms for  $F(f)$  defined at all frequencies that indicates how big the amplitude of the sin wave has to be to make the function  $x(t)$  for all frequencies. The resulting  $F(f)$  is defined as:

$$F(f) = \int_{-\infty}^{\infty} x(t) e^{-2\pi i f t} dt \quad (6.10)$$

The FFT algorithm within MATLAB, which is a high-level technical computing language, was used to conduct an FFT on the relative roof acceleration with respect to the ground acceleration to provide an insight on the predominant frequency response of the structure. This proves to be helpful when the response is predominantly mode one and the natural frequency of the structure are well spaced. For example, as shown in Figure 6-17, the predominant period of the structure is 1.177 sec. Since the fundamental period of the

structure is 0.904 sec, the 1.177 sec value must correspond to the inelastic period of the structure (period elongation).

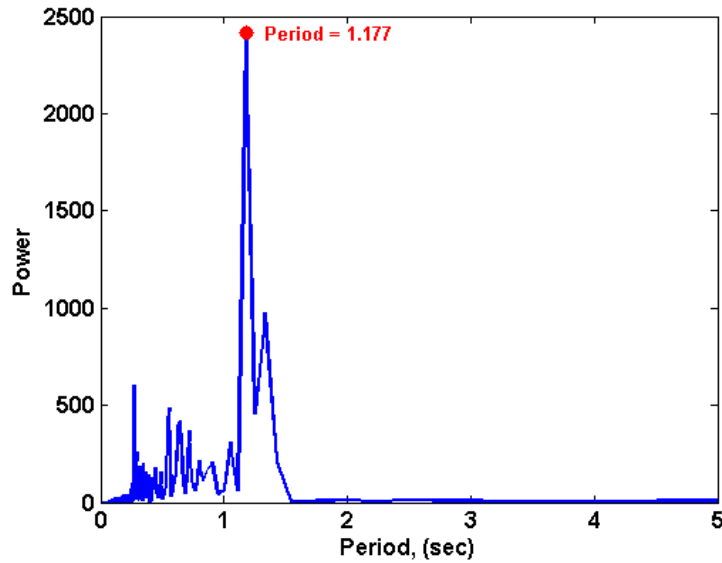


Figure 6-17 FFT of the roof acceleration response of the 30%  $M_{p_{beam}}$  frame under the 1979 Imperial Valley earthquake (IV-HBCR)

When the response of the structure is governed by various modes, conducting FFT on the acceleration response reveals that multiple modes are highly participating in the response of the structure as shown in Figure 6-18. In this case, the predominate period of 0.714 sec must correspond to an elongation of the second mode since the fundamental period of the structure is 0.904 sec.

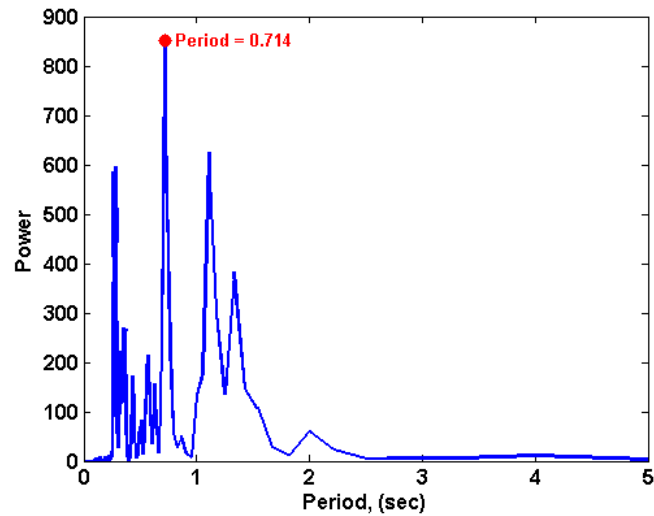


Figure 6-18 FFT of the roof acceleration response of the 30%  $M_{p_{beam}}$  frame under the 1989 Loma Prieta earthquake (LP-CLS)

Fourier transform is considered the primary tool for signal processing and interpretation of system response. It provides an insight on the inelastic period of the structure corresponding to period elongation when the response of the system is governed by the first mode. However, for higher modal participation, the information gathered from conducting an FFT appears to be washed away by the complexity of the response. The inability of the FFT to capture the time-varying response of the system motivated the use of time-frequency transformation for analyzing the high transient events such as structural response due to earthquakes.

### 6.8.2 Short-time Fourier Transformation

Another alternative to FFT is short-time Fourier transform (STFT) which is a powerful tool for signal processing specifying complex amplitude versus time and frequency for any signal. Introducing the time scale into the Fourier transformation

analysis enables for the quantification of the modal participation at a given time of interest. Similar to FFT, both discrete and continuous forms of the STFT are used for signal analysis. In the discrete time case, used in this study, the data is divided into chunks of overlapping frames where each chunk is transformed and the complex results are added to a matrix recording the magnitude and phase of each point in time and frequency.

$$STFT \{x[n]\} \equiv X(m, \omega) = \sum_{n=-\infty}^{\infty} x[n] \omega[n - mR] e^{-j\omega n} \quad (6.11)$$

Where  $x[n]$  represents the signal input at time  $n$ ,  $\omega[n]$  represents the length  $m$  window functions (e.g., hamming), and  $R$  is the hop size in samples between successive discrete time Fourier transformation.

A time-varying spectral representation showing the variation of the spectral density with time is called a spectrogram. In its most common format, a spectrogram has two geometric dimensions with the vertical axis representing frequency while the horizontal axis represents time. A third dimension is added to the graph by representing the amplitude of the frequency through a color bars or intensity. A spectrogram of a signal is developed by calculating the squared magnitude of the STFT of the signal as:

$$spectrogram(t, \omega) \equiv |STFT \{x[n]\}|^2 \quad (6.12)$$

As mentioned above, the FFT of the roof acceleration of the 30%  $Mp_{beam}$  resulting from subjecting the structure to the Loma Prieta earthquake is shown in Figure 6-18. The



FFT gives an insight on the predominate period of the structure with no reference to the time at which the period was dominating. Such information is needed particularly when determining period elongation as a function of time is needed.

Figure 6-21 below shows a spectrogram of the roof acceleration response of the 30%  $M_{p_{beam}}$  frame to the Loma Prieta earthquake (LPCLS). As shown in the figure, the STFT is characterized by distinct high participation of various modes at two different time ranges. The first high modal participation approximately corresponds to time range between 2 sec to 4 sec while the second high modal participation approximately corresponds to time range between 6 sec to 8 sec.

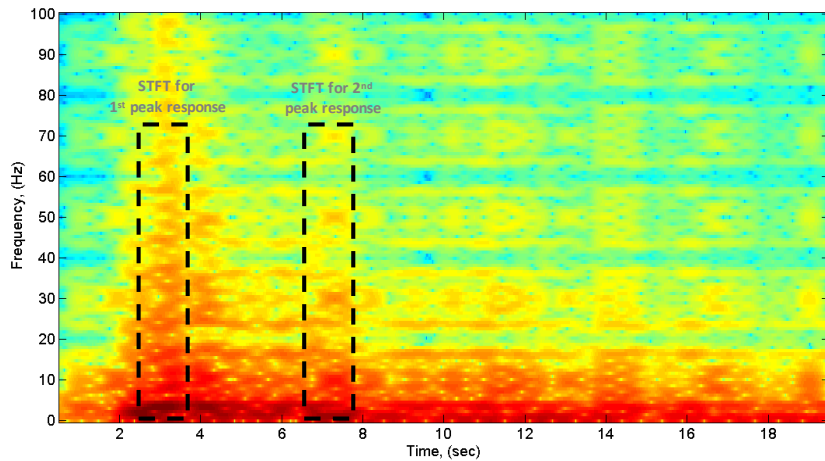


Figure 6-19 Spectrogram of the roof acceleration response of the 30%  $M_{p_{beam}}$  frame under the 1989 Loma Prieta earthquake (LP-CLS)

A visual evaluation of the roof displacement response of the frame under the same ground motion clearly shows the highest displacement response of the frame to be associated with the same time range corresponding to high modal participation (i.e., 2 sec to 4 sec and 6 sec to 8 sec).

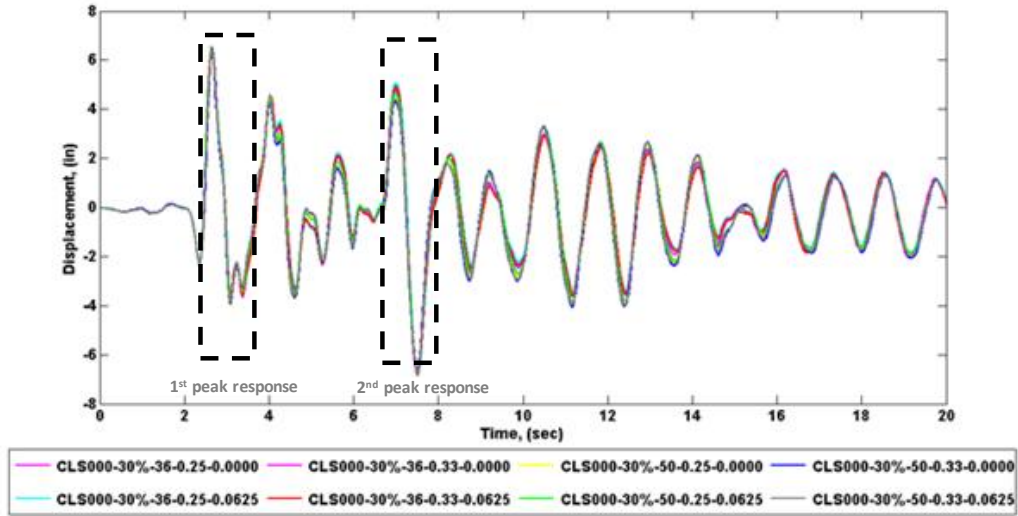


Figure 6-20 Roof displacement response of the 30%  $M_{p_{beam}}$  frame under the 1989 Loma Prieta earthquake (LP-CLS)

The correlation between the roof displacement response and the spectrogram of the roof acceleration response proves to be useful in providing an insight on characterizing the structural response with the progression of time. The drawback of using STFT in signal analysis is that it has a fixed resolution where the width of the windowing function is related to how the signal is presented. The resolution of the analysis is controlled by either obtaining a good frequency resolution at the expense of the time resolution (wideband) or obtaining the desired time resolution at the expense of frequency resolution (narrowband). The selection of the widow size must be such that sharp peaks or low frequency features can be captured. This is because of the inverse relationship between the window length and the corresponding frequency bandwidth.

Figure 6-21 shows a zoom in image of the spectrogram of the roof acceleration response shown in Figure 6-19. The maximum frequency included in figure is 5 Hz. As the figure shows, it is difficult to obtain a clear idea regarding period elongation of the

frame with the progression of time. Furthermore, the resolution obtained on the time axis is quite high at the expense of a low resolution of the frequency axis. The result of achieving higher resolution on the frequency axis is lower resolution on the time axis.

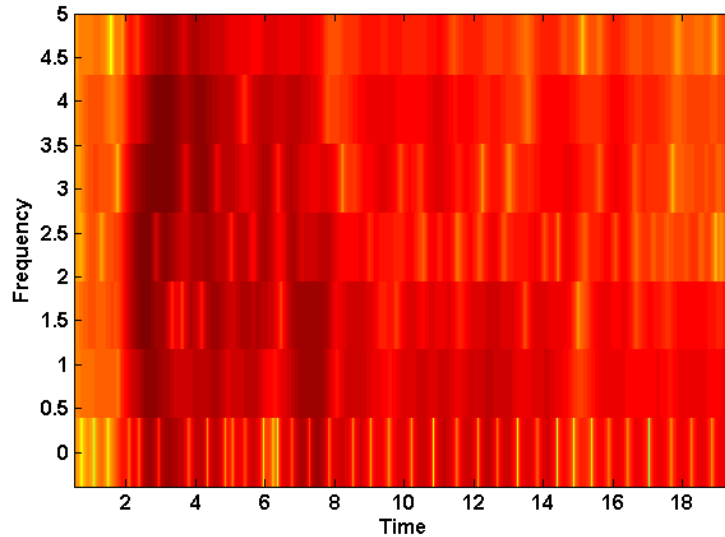


Figure 6-21 A Zoom in image of the Spectrogram of the roof acceleration response of the 30%  $M_{p_{beam}}$  frame under the 1989 Loma Prieta earthquake (LP-CLS)

In some cases it might be useful to obtain a 3D snazzy spectrogram which includes peaks and valleys characterizing the amplitude of a given frequency in addition to the color map intensity. Figure 6-22 shows a 3D spectrogram of the roof acceleration response. The figure shows peaks and valleys characterizing the frequency response of the system. However, the 3D spectrogram still lacks the needed resolution for quantifying the period elongation of the system.

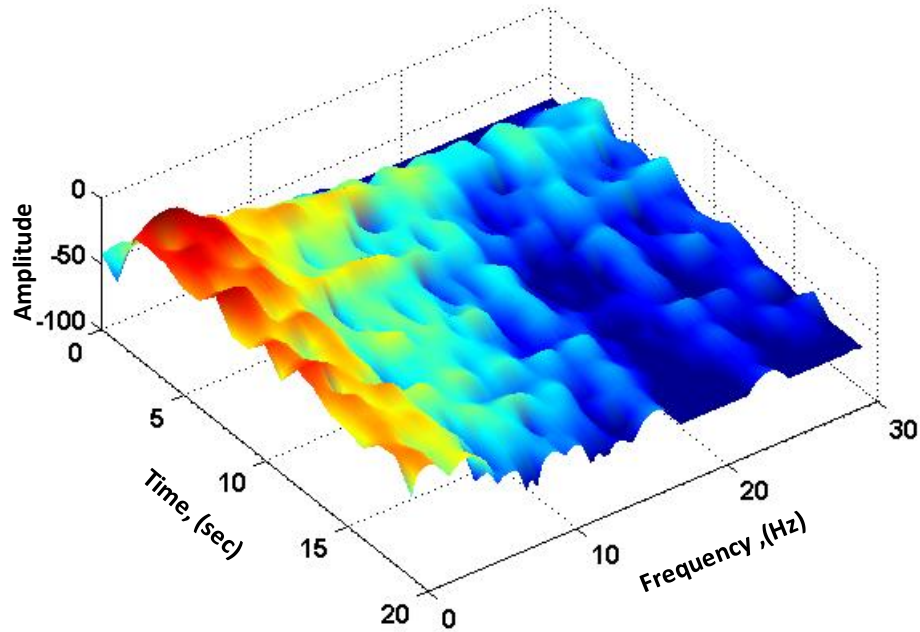


Figure 6-22 Three-dimensional spectrogram of the roof acceleration response of the 30%  $M_{p_{beam}}$  frame under the 1989 Loma Prieta earthquake

An alternative to overcome the issue of resolution tradeoff between the frequency and time domains is to conduct a discrete wavelet transformation (DWT). In DWT the resolution in time and frequency can be controlled independently as desired.

### 6.8.3 Wavelet Transformation

The wavelet transform is used to decompose random non-stationary signals into localized orthogonal basis functions. Time-frequency maps of the time-varying signals can be formulated with desired resolution to provide insight into the characteristics of the signal. The method allows for an automated change of the window size to observe high and low frequency content of the signal. The process starts by formulating a single parent wavelet which is then decomposed into a series of basis functions characterized by

different scales and positions in time or space, which are related based on power of two.

A continuous wavelet transform is presented by:

$$W(a, t) = \frac{1}{\sqrt{a}} \int_{-\infty}^{\infty} x(\tau) g^* \left( \frac{\tau - t}{a} \right) dt \quad (6.13)$$

Which represents the decomposition of a signal  $x(t)$  through basis functions that are a subset of the complex conjugate parent wavelet  $g(t)$ , and  $a$  represents the scale or the frequency of the basis functions. This study utilized Morlet wavelet for the continuous wavelet transform which is a Gaussian-windowed Fourier transform, with sines and cosines oscillating at the central frequency,  $f_0$  ( $\omega_0 = 2\pi f_0$ ) (Correa and Kareem 2004).

The square magnitude of the wavelet coefficient of Equation (6.13) is referred to as wavelet scalogram, which is a color contours representing the energy of the signal in scale and time  $SG(a, t)$ . The contours are more apparent at the dominate frequency of the signal and when combined they form a time-evolving curves called ridges where the frequency of the scaled wavelet coincides with that of the signal. Defined as the instantaneous frequency (IF) or the wavelet instantaneous frequency (WIFS), the isolated ridges provide very useful information on the evolution of the signal with time.

$$WIFS(a, t) = \begin{cases} SG(a, t) & |_{a=a_r(t)} \\ 0 & |_{a \neq a_r(t)} \end{cases} \quad (6.14)$$

The wavelet scalogram and the instantaneous frequency corresponding to the roof acceleration response with respect to the ground of the 30%  $M_{p_{beam}}$  frame when subjected to the 1989 Loma Prieta earthquake are shown in left and right part of Figure 6-23, respectively. The figure clearly shows the predominate response modes with resolution higher than that provided by the spectrogram.

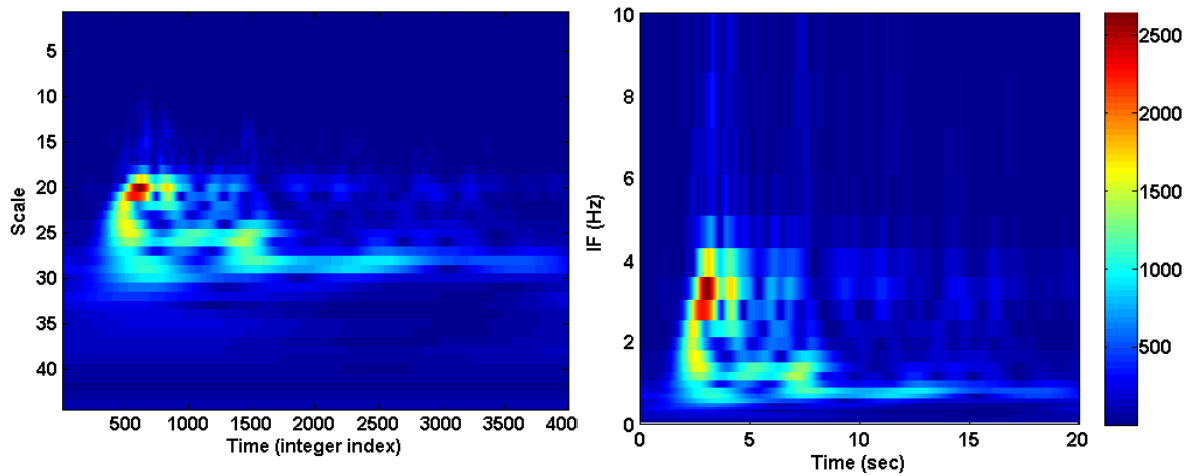


Figure 6-23 Wavelet scalograms (left) and instantaneous frequency (right) of the roof acceleration response of the 30%  $M_{p_{beam}}$  frame under the 1989 Loma Prieta earthquake

An inverse of the IF values represents the evolution of the period of the structure as it responds to the seismic event. As shown in Figure 6-24 the dominate response of the structure is between the period of 0 sec and 2 sec with most of the activities dominated by lower period response. Such information correlates very well with the FFT analysis shown in Figure 6-18 where the dominate response is also mainly governed by lower modes.

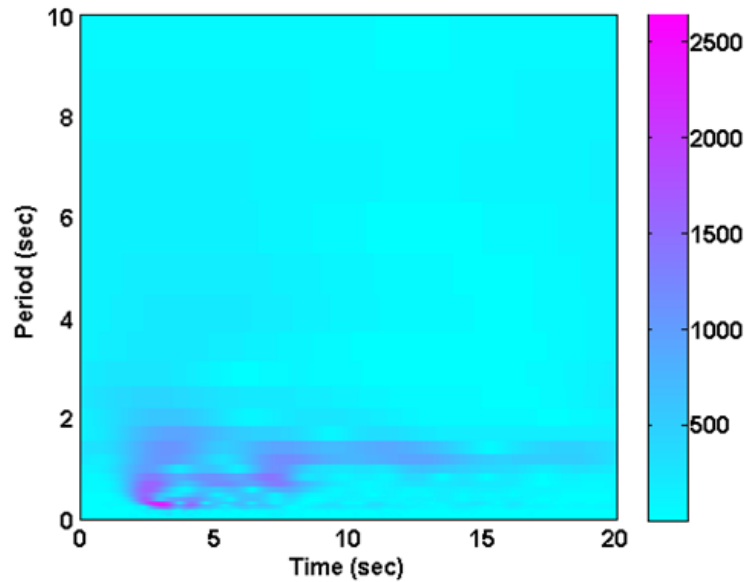


Figure 6-24 Instantaneous period of the structural response of the 30%  $M_{p_{beam}}$  frame under the 1989 Loma Prieta earthquake

As previously discussed, the instantaneous frequency (IF) or ridges provide an insight on the evolution of the structural period with time. Although the first mode of vibration is not the primary contributor to response in this case, one way to extract the ridges corresponding to the first mode is to use a weighted average only on frequencies corresponding to mode one and lower (i.e., low frequencies corresponding to low-frequency response and period elongation). The weighted average is with respect to the absolute of the wavelet transformation (i.e. how intense each frequency is participating in the response). This is done while excluding any frequency higher than that of the fundamental mode. It is important to note that the resulting frequency (or period) profile with time does not imply higher participation of the first mode. Instead, it is simply an indication of the most predominate period of mode one at a given point in time.

The extracted period from the above scalogram is shown in Figure 6-25. It is important to note that the first period shown in the figure at time of zero sec is 1.2 sec. This value neither represents the fundamental period of the structure nor any period elongation since it is shown at time of zero seconds where the structure is under very small to no excitation. In another words, the calculated period is the most predominate period of response at time when there is no response and is simply the outcome of conducting the weighted average on the scalogram at a point in time.

The scalogram of Figure 6-24 clearly shows no predominate period of response for the time and up to approximately 2.5 sec. However, when taking a closer visual inspection of the scalogram, one can see higher intensity “purple” color for period up to 2 sec. Therefore, when a weighted average is conducted up to the time of 2.5 sec, it results in a higher period than the elastic one. From the figure below one can clearly see that indeed the maximum period elongation of 1.22 sec corresponds to the maximum response of the frame. The value corresponds very well to the average of mode one period elongation that could be estimated using FFT as shown below in Figure 6-26. The method used for extracting the fundamental mode of vibration and its elongation is further highlighted below as shown in Figure 6-27 and Figure 6-28. It is also important to point out that the oscillation of the period with time is expected since a simplified material model was used in the analysis with an unloading stiffness taken to be the same as the initial stiffness.



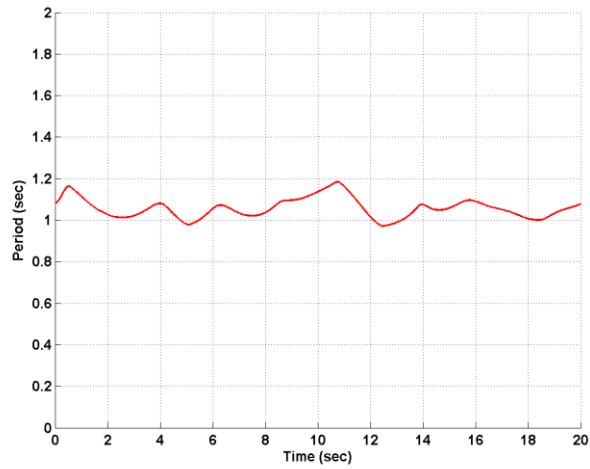


Figure 6-25      Extracted instantaneous fundamental period of the structural response of the 30%  $M_{p_{beam}}$  frame under the 1989 Loma Prieta earthquake (LP-CLS)

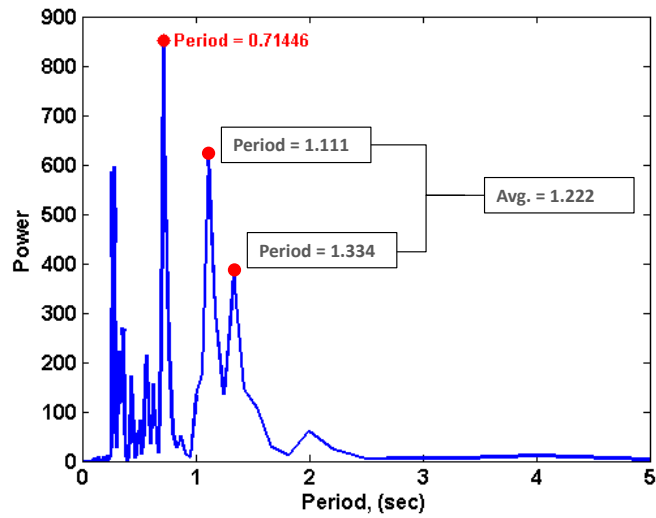


Figure 6-26      FFT of the roof acceleration response of the 30%  $M_{p_{beam}}$  frame under the 1989 Loma Prieta earthquake (LP-CLS) showing the predominate mode two response and the average of the elongated first mode period

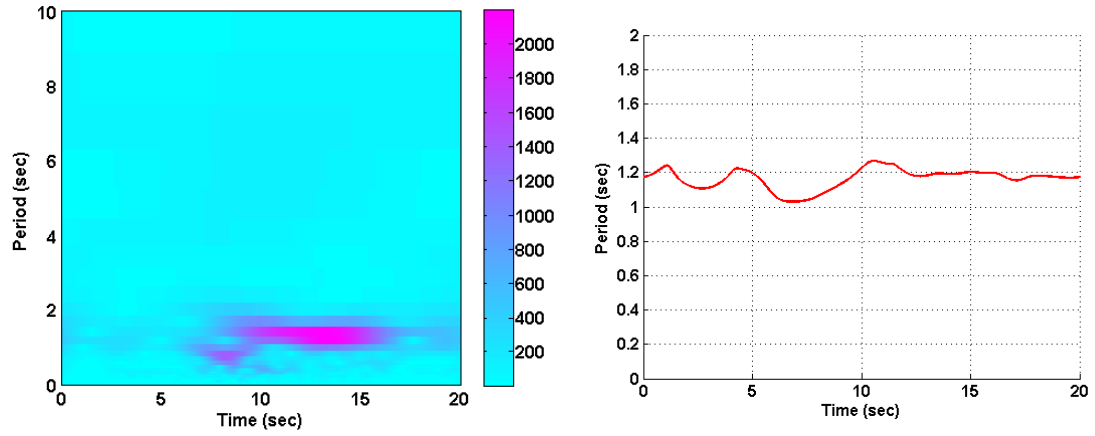


Figure 6-27 Scalogram (left) and instantaneous period of the structural response (right) of the 30%  $M_{p_{beam}}$  frame under the 1994 Northridge earthquake (NR-LOS)

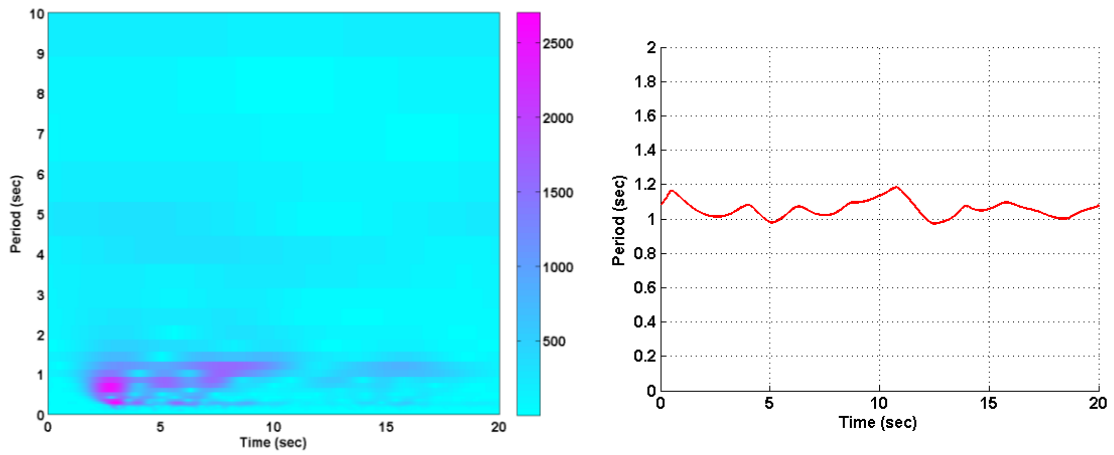


Figure 6-28 Scalogram (left) and instantaneous period of the structural response (right) of the 70%  $M_{p_{beam}}$  frame under the 1995 Kobe earthquake (KB-SHI)

Table 6-9 list a summary of the average inelastic period and percent period elongation for the 70%  $M_{p_{beam}}$ , 50%  $M_{p_{beam}}$  and the 30%  $M_{p_{beam}}$  frames under all ground motions. As shown in the tables, the average period elongation of the three frames is equal to 1.16 sec (34.48%), 1.20 sec (35.92%), and 1.25 sec (38.24%) for the 70%  $M_{p_{beam}}$ , 50%  $M_{p_{beam}}$  and 30%  $M_{p_{beam}}$  frames, respectively.

Table 6-9 Average inelastic period and percent period elongation for all frames

EQ-Station ID	70% $M_{p_{beam}}$		50% $M_{p_{beam}}$		30% $M_{p_{beam}}$	
	$T_{inelastic}$ (sec)	$T_{elongation}$ (%)	$T_{elongation}$ (%)	$T_{elongation}$ (%)	$T_{inelastic}$ (sec)	$T_{elongation}$ (%)
IV-HBCR	1.170	35.417	1.18	33.787	1.201	32.854
LP-CLS	1.184	37.037	1.177	33.447	1.221	35.066
EZ-ERZ	1.132	31.019	1.245	41.156	1.274	40.929
KC-IZT	1.141	32.060	1.194	35.374	1.218	34.735
NR-ARL	1.214	40.509	1.22	38.322	1.291	42.810
DZ-BOL	1.19	37.731	1.18	33.787	1.212	34.071
NR-LOS	1.156	33.796	1.18	33.787	1.315	45.465
LP-CAP	1.156	33.796	1.217	37.982	1.269	40.376
KB-SHI	1.176	36.111	1.213	37.528	1.267	40.155
NR-CCN	1.1	27.315	1.182	34.014	1.229	35.951
Mean	1.16	34.48	1.20	35.92	1.25	38.24
STD Dev.	0.03	3.76	0.02	2.66	0.04	4.25

It is important to note that very limited research has been conducted on evaluating the evolution of period elongation in structures. Furthermore, research on quantifying period elongation to be used in seismic design is lacking. One paper is found in the literature where ground intensity parameters are used to develop a relationship between expected structural damage and the seismic forces experienced by the structure (Kadas, Uakut et al. 2011). To achieve this goal an equation is developed describing the final period elongation as a function of the spectral acceleration normalized to yield spectral acceleration. It important to note, however, that although the ground motions used in the

current analyses are all scaled with different scaling factors, one could argue that the intensity of the records are the same since all records are scaled to the MCE (i.e., intensity of the records are not varied).

One approach to describe period elongation of the structures investigated is through describing a relationship between the ratio of the inelastic to the elastic period as a function of connection strength as shown in Figure 6-29. The inelastic period used in the plot are listed in Table 6-9. Although the figure shows large scatter in the measured period elongation, there is a clear trend pointing towards an increase of the ratio of the inelastic to the elastic period with reduction in connection strength. The reason for choosing connection strength as a parameter for describing period elongation is because connection strength is the main parameter used in the design of the connections. A linear regression line of the plotted data and an equation describing the period elongation is shown in the figure.

As the figure shows, large scatter is observed in the calculated period elongation of the frames. Further research should be carried out to investigate the effect of the yield median response spectra of the records used in the dynamic response-history analyses on the dispersion of the calculated elongated period. Furthermore, the proposed equation for period elongation requires further investigation to incorporate the effect of various parameters, including for example building height, intensity of the record, and site conditions on the resulting inelastic period.

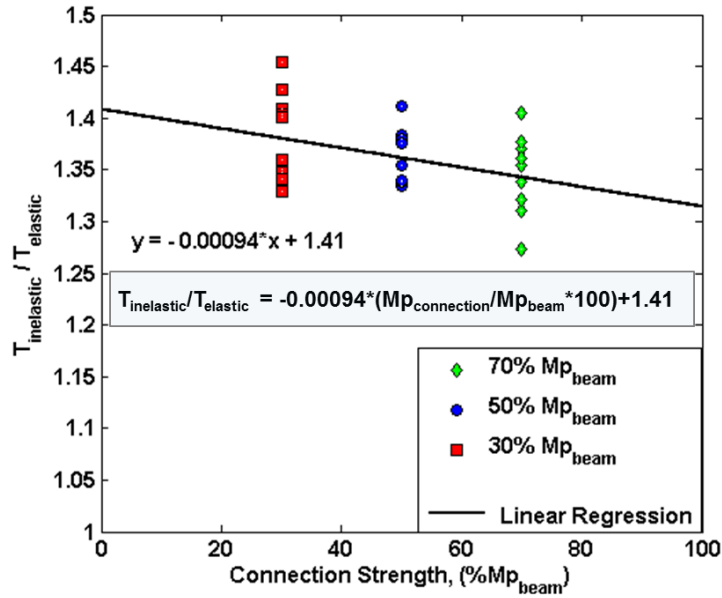


Figure 6-29 Ratio of the elastic to the inelastic period as a function of connection strength

## 6.9 Proposed Response Modification Factor (demand)

Inelastic energy absorption is key to the seismic design of structures to ensure proper energy absorption capacity needed to reduce the seismic demand. Such behavior is accounted for in building codes through the use of force reduction factors “R” used to reduce the elastic seismic demand to an inelastic demand.

The demand R value represents a minimum reduction of forces corresponding to a specific level of ductility. The R factor, known as the behavior factor (q) in EC8 (Eurocode 8 2003) is the ratio between the elastic and inelastic design spectra, that is:

$$q = R = \frac{S a_{elastic}}{S a_{inelastic}} \quad (6.15)$$

The determination of  $S_{a_{\text{inelastic}}}$  requires knowledge of the expected inelastic period of the structure. Among other factors, such value depends on various parameters including structural type and material used. Eurocode 8 includes a maximum allowable behavior factor, accounting for difference in structural type, material type, and desired ductility. Similarly, US codes provide R factors for different structural types (International Building Code 2006). The recommended R factors implemented in US seismic codes and reports are frequency dependent and are a result of much extensive work on relating the nonlinear behavior of multi-degree of freedom systems to that of single-degree of freedom systems.

As previously discussed, the use of wavelet transformation is the most accurate tool for quantifying elongation of the period as the structure exhibit large nonlinear defamations. By using such tool, the average period elongation of all models for a given period strength is calculated. With the calculated  $T_{\text{elastic}}$  and  $T_{\text{inelastic}}$ , the corresponding  $S_{a_{\text{elastic}}}$  and  $S_{a_{\text{inelastic}}}$  are determined for all ten records used in the analyses. The ratio of both values is defined as the demand force reduction factor  $R_{\text{demand}}$ . When determining the elastic and inelastic spectral accelerations, a damping ratio of 2% and a ductility demand of 4 are used. Table 6-10 lists a summary of  $S_{a_{\text{elastic}}}$ ,  $S_{a_{\text{inelastic}}}$ , and the proposed average R factor for each connection type.

Table 6-10 Proposed average force reduction factor,  $R_{demand}$

EQ-Station ID	70% $M_{p_{beam}}$			50% $M_{p_{beam}}$			30% $M_{p_{beam}}$		
	$S_{a_{elastic}}$ (g)	$S_{a_{inelastic}}$ (g)	$R_{demand}$	$S_{a_{elastic}}$ (g)	$S_{a_{inelastic}}$ (g)	$R_{demand}$	$S_{a_{elastic}}$ (g)	$S_{a_{inelastic}}$ (g)	$R_{demand}$
IV-HBCR	0.944	0.105	8.994	0.749	0.108	6.933	0.757	0.116	6.545
LP-CLS	0.814	0.159	5.105	0.786	0.159	4.950	0.748	0.160	4.676
EZ-ERZ	0.777	0.222	3.495	0.735	0.137	5.385	0.703	0.129	5.474
KC-IZT	0.810	0.216	3.749	0.810	0.218	3.709	0.901	0.221	4.082
NR-ARL	0.895	0.091	9.835	0.873	0.091	9.591	0.849	0.090	9.433
DZ-BOL	0.976	0.150	6.527	1.013	0.152	6.663	1.027	0.145	7.105
NR-LOS	0.832	0.216	3.857	0.854	0.147	5.812	0.856	0.140	6.133
LP-CAP	1.151	0.096	12.036	0.883	0.094	9.374	0.625	0.088	7.099
KB-SHI	0.811	0.163	4.972	0.724	0.171	4.226	0.669	0.146	4.572
NR-CCN	0.66	0.094	6.97	0.717	0.064	11.216	0.795	0.061	13.030
Mean	0.87	0.15	6.55	0.81	0.13	6.79	0.79	0.13	6.81
STD Dev.	0.13	0.05	2.91	0.09	0.05	2.51	0.12	0.04	2.69

The demand force reduction factor is found as the ratio between the elastic to the inelastic spectral accelerations. The calculated average demand force reduction factor is 6.55, 6.79, and 6.81 for the 70%  $M_{p_{beam}}$ , 50%  $M_{p_{beam}}$  and 30%  $M_{p_{beam}}$ , respectively. The small dispersion in the values is somewhat expected since the fundamental period of all three frames are closely spaced with very comparable period elongation. *A supply force reduction value of 7 can be specified for all three frames.*

## 6.10 Summary and Conclusion

In this chapter, the response of semi-rigid frames with varying design parameters is studied. The parameters included connection strength as a function of the plastic moment capacity of the beam, yield strength of the angles, coefficient of friction between faying surfaces, and the magnitude of slip allowed in the connection.

The results of the analyses indicated that all frames, including the rigid frame (except for one analysis), met the requirement of ASCE 41-06 for interstory drift ratio of 5% for the MCE. It is worth noting that the semi-rigid frames outperformed the rigid frame with lower base shear and lower IDR. On average, ranking of the behavior of the semi-rigid frames is as expected where the frame with the highest stiffness (70%  $M_{p_{beam}}$ ) developed the highest base shear and the lowest displacement and the frame with the lowest initial stiffness (30%  $M_{p_{beam}}$ ) developed the lowest base shear and the highest displacement. Measurable, but not drastic, differences are noted in the response of the frames when changing the design parameters.

The implication of the behavior of the structures on design is assessed through quantifying various code-based design parameters including the equivalent damping ratio ( $\zeta_{eq}$ ), the inelastic period of the structure ( $T_{inelastic}$ ), and the force reduction factor (R).

Equating the hysteretic energy dissipated in one cycle of loading to that of an equivalent viscous system resulted in equivalent damping ratios of 7.78%, 7.23%, and 5.13% for the 70%  $M_{p_{beam}}$ , 50%  $M_{p_{beam}}$  and 30%  $M_{p_{beam}}$  frame, respectively. Wavelet transformation analysis is used to characterize the response of the structures as a function of time. Instantaneous frequency scalograms are developed to highlight the dominate period of the structure. The evolution of period elongation with time is characterized through the extraction of ridges from the scalogram using a weighted average. The corresponding average percent period elongation is equal to 34.48%, 35.92%, and 38.24% for the 70%  $M_{p_{beam}}$ , 50%  $M_{p_{beam}}$ , and 30%  $M_{p_{beam}}$ , respectively. Based on the results, an equation describing the period elongation as a function of connection strength is presented.



The elastic and inelastic periods of the frames are used in response spectrum analysis, with damping ratio of 2% and ductility demand of 4, to determine the elastic and inelastic spectral acceleration. The spectral acceleration values are then used to calculate the demand force reduction factor for the frames. The average R value for the frames is 6.55, 6.79, and 6.81 for the 70%  $M_{p_{beam}}$ , 50%  $M_{p_{beam}}$  and 30%  $M_{p_{beam}}$ , respectively. Based on this result, a supply force reduction of 7 could be specified for these types of frames that are 2-story high.

The advanced tools utilized for determining the equivalent damping ratio, the inelastic period, and the force reduction factor results in more accurate quantification of such parameters. The implication on design of semi-rigid frames is that, more realistic estimate of the seismic forces is achieved while using the simplified code-based design response spectrum.

## CHAPTER 7

### CONCLUSIONS AND FUTURE RESEARCH REQUIREMENTS

#### 7.1 Summary of Current Work

In this thesis, a new methodology for the seismic evaluation of semi-rigid steel frames is proposed and executed. The methodology includes conducting system-level PSD hybrid simulations, performing nonlinear response-history analyses, and evaluating code-based design parameters used for constructing the elastic and inelastic response spectrum to accurately estimate the design base shear.

The hybrid simulation methodology consists of integrating a 2D analytical model with an experimental setup to conduct a system-level assessment of the frames. Three nodes are used to define the interface between the analytical and experimental modules during the simulations. At each node, lateral, transverse, and rotational degrees of freedoms are controlled. Both modules are successfully integrated in three independent full-scale hybrid simulations.

The analytical module includes generalized plane strain elements with reduced integration to model the beam-to-column connections and 1D beam elements for portions of the beams between subsequent connections. The model represents many behavioral features of the connection including; 1) hot-rolling residual stresses in the top and seat angles, 2) bolt preload, 3) friction between faying surfaces, 4) connection slip, 5) the effect of bolt-hole ovalization, 6) transverse stiffness of the connections, and 7) idealization of the web angles.

The experimental module comprises a beam-column subassembly representing portion of the first and second floor columns and portion of the first floor beam of the left bay. The experimental control included various advanced techniques to ensure that the target commands are accurately reached. In addition, to account for the fact that only two LBCBs are available during the simulations, the concept of relative motion is used to condense the three nodal deformation values into two nodal values prior to sending the commands to the LBCBs.

Upon the completion of a hybrid simulation, cyclic tests were conducted to quantify the post-earthquake fundamental characteristic of the connection (only for the 50%  $M_{p_{beam}}$  and 30%  $M_{p_{beam}}$ ). The response of the physical specimen is assessed using data collected through instrumentations installed at various key locations to capture the local response of the connection as well as the global response.

Furthermore, the seismic performance of semi-rigid frames with varying design parameters is assessed using nonlinear dynamic response-history analyses. The design parameters investigated included connection capacity, yield strength of the angles, friction coefficient, and the amount of bolt slip allowed in the connection. Analysis of rigid frames is also conducted and compared to that of the semi-rigid frames. The results of the hybrid simulations and the parametric studies are used to quantify various fundamental code-parameters needed for the seismic design of structures including equivalent damping ratio, the inelastic period, and the force reduction factor. In addition, an equation is proposed for the prediction of the inelastic period of the frames, under maximum considered earthquake, as a function of the connection strength.

## 7.2 Summary of Findings

### 7.2.1 Hybrid Simulation

The simulations were completed for a period of 15 sec for the 70%  $M_{p_{beam}}$  and 50%  $M_{p_{beam}}$  frames and 6.48 sec for the 30%  $M_{p_{beam}}$  frame (due to convergence problems). The behavior of the connections during the simulations is characterized by large slip and deformation of the bolts and high localized yielding of the top-and seat-angle. Similarly, large deformation and localized yielding is noted in the beams as a result of the interaction between the beams and angles. It is important to note that no failure is observed in any of the specimen components during the simulations.

The behavior of the connections during the simulations is characterized by large hysteretic loops with no failure in any of the connection components. The maximum moment sustained by the 70%  $M_{p_{beam}}$ , 50%  $M_{p_{beam}}$ , and 30%  $M_{p_{beam}}$  connections is 3,222 kips.in, 2,556 kips.in, and 1,708 kips.in, respectively, with corresponding rotations of 0.0196 rad, 0.0271 rad, and 0.34 rad, respectively.

When comparing the global frame behavior during the simulations, it is observed that the maximum base shear is developed in the 70%  $M_{p_{beam}}$  frame followed by the 50%  $M_{p_{beam}}$  frame then the 30%  $M_{p_{beam}}$  frame. A small difference in the magnitude of the IDRs is noted in all three frames with maximum value of 2.32%, 2.42, and 2.70% in the second story of the 70%  $M_{p_{beam}}$  frame, 50%  $M_{p_{beam}}$  frame, and 30%  $M_{p_{beam}}$  frame, respectively. It could be concluded that the 70%  $M_{p_{beam}}$  and 50%  $M_{p_{beam}}$  frames satisfy the DBE drift requirements of 2.5% while the requirement is slightly violated by the 30%  $M_{p_{beam}}$  frame.

### **7.2.2 Cyclic Tests**

Cyclic tests on the 30%  $M_{pbeam}$  and 50%  $M_{pbeam}$  connections are conducted. Due to technical issues associated with the LBCBs. Due to some technical problems associated with one of the LBCBs, cyclic testing of the 70%  $M_{pbeam}$  was not conducted.

Larger slip and deformation of the connections is observed when compared to the hybrid simulation as a result of the large magnitude of rotational cycles imposed on the connections. The moment sustained by the connections is approximately 76% and 68.41% of the plastic moment of the beam for the 50%  $M_{pbeam}$  and 30%  $M_{pbeam}$  connections, respectively, which is larger than what the connections are designed for. A rotation of 0.053 rad and 0.0440 rad are sustained by the 50%  $M_{pbeam}$  and 30%  $M_{pbeam}$  connections, respectively. When compared to the 2005 seismic provisions of AISC, section 9.2a, the resulting rotations exceed the minimum specified code value of 0.04 rad. The achieved moments, however, do not meet the seismic specification of 0.80 $M_p$  of the connected beam at an interstory drift angle of 0.04 radians for the SMRF. The requirement for complying with IMRF of 0.02 rad of interstory rotation is satisfied.

### **7.2.3 Analytical Study of Semi-rigid and Rigid Frames**

The analytical nonlinear response-history analyses of semi-rigid and rigid frames with varying design parameters indicated that all frames, including the rigid frame (except for one analysis), satisfied the ASCE 41-06 requirement for interstory drift ratio of 5% for the MCE. With the exception of the connection strength, the influence of varying the design parameters on the frame response influenced the results but not in a

significant way. Furthermore, the semi-rigid frames outperformed the rigid frame with lower base shear and Interstory drift ratios.

#### **7.2.4 Design Implications**

The implication of the behavior of the structures on design is assessed through evaluating various code-based design parameters; namely the equivalent damping ratio, the inelastic period of the structure, and the force reduction factor.

The equivalent damping ratio is 7.78%, 7.23%, and 5.13% for the 70%  $M_{p_{beam}}$ , 50%  $M_{p_{beam}}$  and 30%  $M_{p_{beam}}$  frame, respectively. The values although larger than the 5% value adopted by the code for MCE, they are much lower than some values listed in the literature for steel frames. In addition to calculating the equivalent damping, the evolution of period elongation with respect to the earthquake time is investigated. The corresponding average percent period elongation is equal to 34.48%, 35.92%, and 38.24% for the 70%  $M_{p_{beam}}$ , 50%  $M_{p_{beam}}$ , and 30%  $M_{p_{beam}}$ , respectively. Moreover, an equation relating the inelastic to the elastic period ratio to connection strength is proposed to facilitate the determination of period elongation of any frame for a given connection strength.

The resulting inelastic period is used with the elastic period in a response spectrum analysis to determine the elastic and inelastic spectral acceleration, which are used to calculate the demand force reduction factor,  $R$ . The average  $R$  value for the frames is 6.55, 6.79, and 6.81 for the 70%  $M_{p_{beam}}$ , 50%  $M_{p_{beam}}$  and 30%  $M_{p_{beam}}$ , respectively. Based on this result, a supply force reduction of 7 could be specified for these types of frames.

The advanced techniques used resulted in an accurate determination of the equivalent damping ratio, the inelastic period, and the force reduction factor of the frames. Such parameters can be utilized in current seismic codes for more realistic estimate of the seismic forces imposed on the semi-rigid structures. The outcome of such is frames that are designed to resist earthquake forces in a controlled and economical manner.

### **7.3 Future Research Requirements**

In this study experimental and analytical investigations are carried out to evaluate the seismic performance of steel frames under high seismic loads. Advanced tools utilized in the studies for an accurate evaluation of frame behavior. The results of the study highlight the significant potential for using frames with top-and seat angles with double web angles in high seismic regions. However, future research directions can include the following:

- The frames investigated included only bare steel with no concrete slab utilized in the experimental testing or the analytical studies. The effect of the concrete slab on the behavior of the frames should be investigated since the slab will affect the location of the neutral axis in the connection; hence, the onset of yielding in the connection will not be the same. Furthermore, the effect of changing various design hypotheses on the connection behavior and frame response can be investigated including the density of the reinforcement used in constructing the slab and the effectiveness of the stress transfer mechanisms from the slab to the columns (Plumier, Doneux et al. 1998). A slab that is fully

isolated from the column will have no effect on the semi-rigidity of the connection and is likely not to affect the global response of the frame. On the other hand, a slab that is rigidly connected to the column flange will increase the rigidity of the connection, resulting in frame behavior similar to that of a rigid frame.

- In this study two-story structures are investigated under horizontal ground motions. Due to their low height, the initial stiffness of all three frames is very similar which makes it difficult to highlight the effect of connection strength on the performance of the frames. This is also evident in how similar the calculated R factors and equivalent damping are for all three frames. Therefore, it is suggested that a study is conducted on frames with varying heights so that the effect of connection flexibility and strength on the behavior can be fully explored. In doing so, acceptance criteria for semi-rigid frames with various heights can be established.
- The absence of top-and seat-angle with double web-angle connections from the ANSI/AISC list of prequalified connections calls for more research to be conducted on this type of connections to explore their full potential and prequalify them for seismic applications.
- The large dynamic slip which occurred in the physical connections during the hybrid simulations was not captured by the analytical module. Developing an algorithm for real-time model updating could increase the accuracy of the



simulation as the analytical module is updated during the simulation to reflect more realistic behavior of the connections.

- Large scatter is observed in the calculated percent period elongation of the frames. The effect of the yield median response spectra of the records used in the dynamic-response history analyses on the dispersion of the calculated elongated period should be investigated further. Moreover, the proposed period elongation equation requires further investigation to include the effect of various parameters are incorporated in the analysis including for example, building height, intensity of the record, and site conditions.
- In constructing the code-based response spectrum, the peak of the spectrum is determined from the MCE mapped spectral acceleration for 5% critical damping. The 5% damping value is used regardless of frame type and height. Therefore, a mapped MCE spectral acceleration, which is adjusted to account for the actual equivalent damping of the frames, should be investigated as it will lead to more accurate estimates of the base shear.
- The conducted research included only the effect of horizontal ground motions. The effect of vertical ground motions on the response of semi-rigid frames might be of significant importance since the flexibility of the connections can result in large vertical vibration of the beams when subjected to vertical earthquakes.
- Research on semi-rigid frames should include the effect of soil-structure interaction, which could amplify or reduce the response of the frames.

In general, the experimental and analytical evidence presented in this thesis highlight the potential construction of steel frames with top- and seat-angle with double web-angle connections in high seismic regions.

## REFERENCES

- Ahmed, A., N. Kishi, et al. (2001). "Nonlinear Analysis on Prying of Top- and Seat-Angle Connections." Journal of Applied Mechanics **4**: 227-236.
- Al-Bermani, F. G. A. and S. Kitipornchai (1992). "Elastoplastic Nonlinear Analysis of Flexibly Jointed Space Frames." Journal of Structural Engineering **118**(1): 108-127.
- Albermani, F. G. A., B. Li, et al. (1994). "Cyclic and Seismic Response of Flexibly Jointed Frames." Engineering Structures **16**(4): 249-255.
- American Institute of Steel Construction (AISC) (1989). Specifications for Allowable Stress Design of Single Angle Members. Chicago, IL, American Institute of Steel Construction (AISC), Inc.
- American Institute of Steel Construction (AISC) (2005). Specification for Structural Steel Buildings. Chicago, IL, American Institute of Steel Construction (AISC), Inc.
- American Society of Civil Engineers (ASCE 7-05) and Structural Engineering Institute (SEI) (2005). Minimum Design Loads for Buildings and Other Structures. Reston, VA, American Society of Civil Engineers/Structural Engineering Institute.
- Ang, K. M. and G. A. Morris (1984). "Analysis of Three-Dimensional Frames with Flexible Beam-Column Connections." Canadian Journal of Civil Engineering **CSCE**(11): 245-254.
- Applied Technology Council (ATC) (2009). ATC-63 (FEMA P695): Quantification of Building System Performance and Response Parameters. Redwood City, CA, Applied Technology Center.
- ASCE/SEI 41-06 (2007). Seismic rehabilitation of existing buildings, ASCE.
- Awkar, J. C. and E. M. Lui (1999). "Seismic analysis and response of multistory semirigid frames." Engineering Structures **21**(5): 425-442.
- Azizinamini, A. and J. B. Radzinski (1989). "Static and cyclic performance of semi-rigid steel beam-to-column connections." Journal of Structural Engineering **115**(12): 2979-2998.
- Barry, J. (2004). structural Performance and Economics of Buildings with Semi-rigid Connections Under Seismic Loading. Civil and Environmental Engineering. Urbana, University of Illinois. **Masters of Science**.
- Beedle, L. S. and L. Tall (1960). "Basic Column Strength." Journal of Structural Division **127**(II): 138-179.
- Bennier, D. (2009). Hybrid Simulation of Steel Frames with Semi-rigid Connections. Department of Civil and Environmental Engineering. Urbana, University of Illinois at Urbana-Champaign. **Masters of Science**: 158.
- Bursi, O. S. and J. P. Jaspart (1997). "Benchmarks for finite element modeling of bolted steel connections." Journal of Constructional Steel Research **43**(1-3): 17-42.
- Chen, W. F. (2000). Practical Analysis for Semi-Rigid Frame Design., World Scientific Publishing.
- Chmielowiec, M. and R. M. Richard (1987). Moment rotation curves for partially restrained steel connections., Report to AISC, University of Arizona: 127.
- Chopra, A. (2006). Dynamics of Structures: Theory and Applications of Earthquake Engineering. Englewood Cliffs, NJ, Prentice Hall.

- Citipitioglu, A. M., R. M. Haj-Ali, et al. (2002). "Refined 3D finite element modeling of partially-restrained connections including slip." Journal of Constructional Steel Research **58**(5-8): 995-1013.
- Coelho, A., L. Silva, et al. (2004). Characterization of the Nonlinear Behavior of Single Bolted T-Stub Connections. Connections in Steel Structures V Amsterdam
- Correa, T. and A. Kareem (2004). Time-frequency Perspectives in the Analysis and Interpretation of Ground Motions and Structural Response. 13th World Conference on Earthquake Engineering, Vancouver, B.C., Canada.
- De Stefano, M., A. De Luca, et al. (1994). "Modeling of cyclic moment-rotation response of double-angle connections." Journal of Structural Engineering **120**(1): 212-229.
- Elgaaly, M., H. Dagher, et al. (1991). "Behavior of Single Angle Compression Members." Journal of Structural Engineering **117**(12).
- Elnashai, A. and L. Di Sarno (2008). Introduction to Earthquake Engineering., Wiley.
- Elnashai, A., B. K. Spencer, D., et al. (2004). Multi-Axial Full-Scale Sub-Structured Testing and Simulation (MUST-SIM) facility at the University of Illinois at Urbana-Champaign. 13th World Conference on Earthquake Engineering. Vancouver, B.C., Canada.
- Elnashai, A. S. and A. Y. Elghazouli (1994). "Seismic behavior of semi-rigid steel frames." Journal of Constructional Steel Research **29**(Special issue on seismic response of steel structures ): 149-174.
- Elnashai, A. S., A. Y. Elghazouli, et al. (1990). "Verification of Pseudo-dynamic Testing of Steel Members." Journal of Constructional Steel Research **16**: 153-161.
- Eurocode 3 (1998). Design of steel structures. Annex J, Joint in building frames, ENV 1993-1-1. Brussels.
- Eurocode 8 (2003). Eurocode No. 8: Design of structures for earthquake resistance, Part 1: General rules, seismic actions and rules for buildings. Brussels.
- European Convention for Constructional Steelwork (ECCS) (1985). Recommendations for Angles in Lattice Transmission Towers. Brussels.
- Foutch, D. A. and S.-Y. Yun (2002). "Modeling of steel moment frames for seismic loads." Journal of Constructional Steel Research **58**(5-8): 529-564.
- Frye, M. J. and G. A. Morris (1975). "Analysis of flexibly connected steel frames." Canadian Journal of Civil Engineering **2**(3): 291-380.
- Gendron, G., D. Beaulieu, et al. (1989). "Finite element modeling of bolted connections." Can. J. Civ. Engng **16**: 172-181.
- Hakuno, M., M. Shidawara, et al. (1969). "Dynamic Destructive Test of a Cantilever Beam, Controlled by an Analog-computer." Transactions of Japan Society of Civil Engineering **171**: 1-9.
- International Building Code (2006). Structural/Seismic Design, Volume 3: Building Design Examples for Steel and Concrete.
- Jeong, S. H. and A. S. Elnashai (2005a). "Analytical Assessment of an Irregular RC Frame for Full-scale 3D Pseudo-dynamic Testing:Part I: Analytical model verification." Journal of Earthquake Engineering **9**(1): 95-128.
- Johnson, B. and L. Green (1940). "Flexible welded angle connections." AWS. Weld Journal **19**(10): 402-408.
- Kadas, K., A. Uakut, et al. (2011). "Spectral Ground Motion Intensity Based on Capacity and Period Elongation." Journal of Structural Engineering **137**(3): 401-409.

- Kim, J., J. Ghaboussi, et al. (2010). "Mechanical and informational modeling of steel beam-to-column connections." Engineering Structures **32**(2): 449-458.
- Kim, S.-J., A. S. Elnashai, et al. (2006). Seismic Assessment of RC Bridge Pier Behavior by Complementary Large and Small-Scale Hybrid Simulation. Fifth National Seismic Conference on Bridges & Highways. San Francisco, CA.
- Kishi, N., A. Ahmed, et al. (2001). "Nonlinear finite element analysis of top-and-seat angle with double web angle connections." Structural Engineering and Mechanics **12**(2): 201-214.
- Kishi, N. and W.-F. Chen (1990). "Moment-Rotation Relations of Semirigid Connections with Angles." Journal of Structural Engineering **116**(7): 1813-1834.
- Kishi, N. and W. F. Chen (1986a). Data base of steel beam-to-column connections. West Lafayette, Purdue University.
- Kishi, N. and W. F. Chen (1986b). Steel connection data bank program. West Lafayette, Purdue University.
- Kishi, N., W. F. Chen, et al. (1988). Moment-rotation relation of top and seat angle with double web angle connections. Connection in steel structures, behavior strength and design. E. A. S. Publishers. London, England: 121-134.
- Krishnamurthy, N. (1980). "Modeling and prediction of steel bolted connection behavior." Computers & Structures **11**(1-2): 75-82.
- Kukreti, A. R., T. M. Murray, et al. (1987). "End plate connection moment-rotation relationship." Journal of Constructional Steel Research **8**: 137-157.
- Kulak, G., J. Fisher, et al. (1987). Guide to design criteria for bolted and riveted joints. Wiley. New York.
- Kwon, O., A. Elnashai, et al. (2007). UI-SIMCOR: A global platform for hybrid distributed simulation. 9th Canadian Conference on Earthquake Engineering (9CCEE). Ottawa, Canada.
- Kwon, O. S., N. Nakata, et al. (2005). "A Framework for Multi-site Distributed Simulation and Application to Complex Structural Systems." Journal of Earthquake Engineering **9**(5): 741-753.
- Leon, R., J. Wan Hu, et al. (2004). Rotational Capacity and Demand in Top-and-Seat Angle Connections Subjected to Seismic Loading. Connections in Steel Structures V, Amsterdam.
- Lui, E. M. and W. F. Chen (1986). "Analysis and behaviour of flexibly-jointed frames." Engineering Structures **8**(2): 107-118.
- Lui, E. M. and A. Lopes (1997). "Dynamic analysis and response of semirigid frames." Engineering Structures **19**(8): 644-654.
- Mahin, S. A. and P. B. Shing (1985). "Pseudodynamic Method for Seismic Testing." Journal of Structural Engineering **111**(7): 1482-1503.
- Mahmoud, H. N. and R. J. Dexter (2005). "Propagation Rate of Large Cracks in Stiffened Panels under Tension Loading." Journal of Marine Structures **18**(3): 265-288.
- Moncarz, P. D. and K. H. Gerstle (1981). "Steel frames with nonlinear connections." Journal of Structural Division **107**(8): 1427-1441.
- Monica D. Kohler, Thomas H. Heaton, et al. (2007). "Propagating Waves in the Steel, Moment-Frame Factor Building Recorded during Earthquakes." Bulletin of the Seismological Society of America **97**(4): 1334-1345.

- Murat Diclelia and Anshu Mehtab (2006). "Seismic performance of chevron braced steel frames with and without viscous fluid dampers as a function of ground motion and damper characteristics." Journal of Constructional Steel Research **63**: 1102-1115.
- Nader, N. and A. Astaneh-Asl (1996). " Shaking table tests of rigid, semirigid, and flexible steel frames." Journal of Structural Engineeirng **122**(6): 589-596.
- Nakashima, M. and H. Kato (1987). Experimental Error Growth Behavior and Error Growth Control in On-line Computer Test Control Method. BRIReport. M. o. Construction. Tsukuba, Japan, Building Research Institute. **No. 123**.
- Nakashima, M., J. McCormick, et al. (2008). Hybrid Simulation: Theory, Implementation and Applications., Taylor and Francis.
- Negro, P., E. Mola, et al. (2004). Full Scale Bi-directional PSD Testing of a Torsionally Imbalanced Three Storey Non-seismic RC Frame. 13th World Conference on Earthquake Engineering, Vancouver, Canada.
- Nuttall, N. J. and P. F. Adams (1970). "Flexural and Lateral-torsional Buckling Strength of Double Angle Struts." Structural Engineering Representative **30**.
- O'Connor, C. (1955). "Residual Stresses and Their Influence on Structural Design." Journal of the Institution of Engineers, Australia **27**(12).
- Parulekar, Y. M., K. N. Vaity, et al. (2004). "Earthquake response of inelastic structures." Nuclear Engineering and Design **227**: 185-193.
- Plumier, A., C. Doneux, et al. (1998). Slab design in connection zone of composite frames. 11th European Conference on Earthquake Engineering Balkema, Rotterdam.
- Pong, W. (2002). "Performance-Based Design Examples for Steel Moment-Resisting Frames with Supplemental Damping." Electronic Journal of Structural Engineering **2**: 44-58.
- Popov, P. and P. Bertero (1973). "Cyclic loading of steel beams and connections." ASCE Journal of Structural Division **99**(6): 1189-1204.
- Pucinotti, R. (2001). "Top-and-seat and web angle connections: prediction via mechanical model." Journal of Constructional Steel Research **57**(6): 663-696.
- Rex, C. and S. Easterling (2003). "Behavior and Modeling of a Bolt Bearing on a Single Plate." Journal of Structural Engineering **129**(6): 729 - 800.
- Richard, R. M. and B. J. Abbott (1975). "Versatile Elastic-Plastic Stress-Strain Formula." Journal of Engineering Mechanics **101**(EM4): 511-515.
- SAC (2000). Recommended Seismic Evaluation and Upgrade Criteria for Existing Welded Steel Moment-Frame Structures. SAC Joint Venture. FEMA-351. Washington D.C.
- Salazar, A. R. and A. Haldar (2001). "Energy Dissipation at PR Frames under Seismic Loading." Journal of Structural Engineering **127**(5): 588-592.
- Sarraf, M. and M. Bruneau (1996). "Cyclic testing of existing and retrofitted riveted stiffened seat angle connections." Journal of Structural Engineeirng **122**(7): 762-775.
- Shen, J. and A. Astaneh-Asl (2000). "Hysteresis model of bolted-angle connections." Journal of Constructional Steel Research **54**(3): 317-343.
- Sherbourne, A. N. and M. R. Bahaari (1994). "3D Simulation of End-Plate Bolted Connections." Journal of Structural Engineering **120**(11): 3122-3136.

- Sherbourne, A. N. and M. R. Bahaari (1996). "3D simulation of bolted connections to unstiffened columns--I. T-stub connections." Journal of Constructional Steel Research **40**(3): 169-187.
- Simula (2007). Abaqus/Standard Users' Manual, Hibbit, Karlsson and Sorenson 2007.
- Sivakumaran, K. S. (1988). "Response of multi-storey steel buildings with flexible connections." Engineering Structures **10**: 239-248.
- Spencer, B. F., A. S. Elnashai, et al. (2004). The MOST Experiment: Earthquake Engineering on the Grid. Technical Report NEESgrid-2004-41, <http://it.nees.org/>.
- Stojadinovic, B., G. Mosqueda, et al. (2006). "Event-driven Control System for Geographically Distributed Hybrid Simulation." Journal of Structural Engineering **132**(1): 68–77.
- Usami, T. (1971). Restrained Single Angle Columns Under Biaxial Bending. Civil and Environmental Engineering. St. Louis, MO., Washington University. **Ph.D.**
- Wales, M. and E. Rossow (1983). "Coupled moment-axial force behavior in bolted joints." Structural Division **109**(ST5): 1250–1266.
- Watanabe, E., T. Kitada, et al. (2001). Parallel Pseudodynamic Seismic Loading Test on Elevated Bridge System through the Internet. The Eight East Asia-Pacific Conference on Structural Engineering and Construction. Singapore.
- Wen, Y. K. and C. L. Wu (2001). "Uniform Hazard Ground Motions for Mid-America Cities." Earthquake Spectra **17**(2): 359-384.
- Yang, J. G., T. M. Murray, et al. (2000). "Three-dimensional finite element analysis of double angle connections under tension and shear." Journal of Constructional Steel Research **54**(2): 227-244.

## APPENDIX A.

### SPECIMEN DESIGN AND CONSTRUCTION

#### A.1 Building Configuration

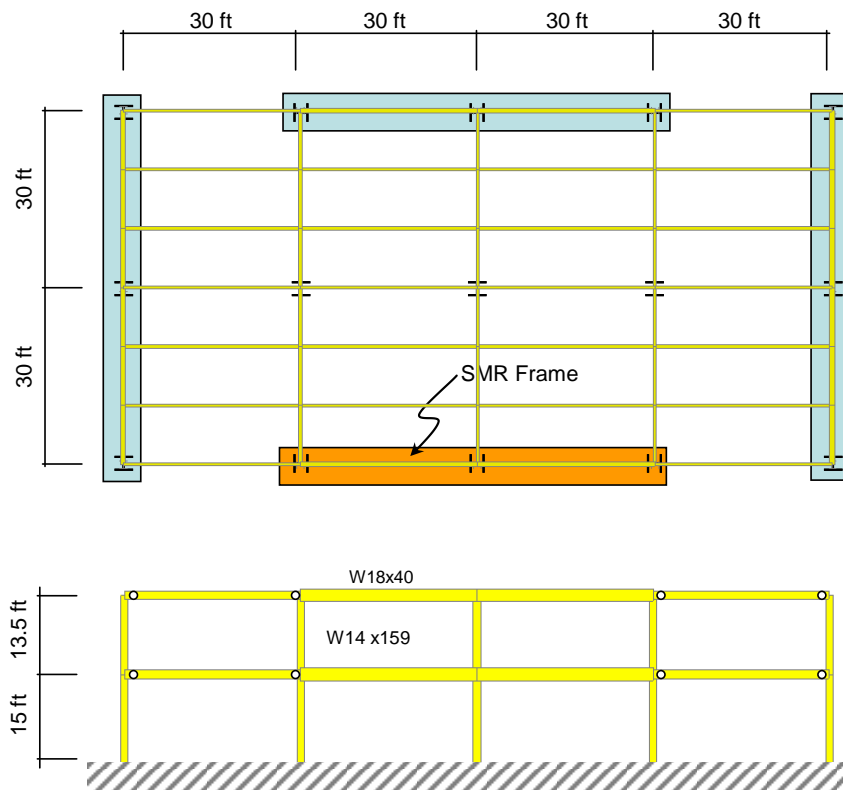


Figure A-1 Plan and side view of the building including the SMRF



## A.2 Frame Strength and Drift per ASCE 7-02

The maximum considered earthquake (MCE) spectral response acceleration (9.4.1) & (9.4.1.1)

$$S_s = 1.5g \text{ @ } T = 0.2 \text{ sec} \quad (\text{for short period}) \quad (\text{Eq. 9.4.1.1(a)})$$

$$S_1 = 0.6g \text{ @ } T = 1.0 \text{ sec} \quad (\text{for long period}) \quad (\text{Eq. 9.4.1.1(b)})$$

Note: using the USGS website, the  $S_s$  and  $S_1$  values can be obtained for LA area:

For 0.2 sec horizontal ground motion and 2% probability of exceedence in 50 yrs

$$S_s = 234.79\%g = 2.35g$$

For 1 sec horizontal ground motion and 2% probability of exceedence in 50 yrs

$$S_1 = 10\%g = 0.1g$$

The values of  $S_s$  and  $S_1$  are used to produce the coefficient  $S_{DS}$  and  $S_{D1}$ , which are then used to construct the response spectra. The strength is determined using the  $S_{DS}$  value since it is higher than the  $S_{D1}$ . It is important to note that one could use the  $S_{DS}$  and  $S_{D1}$  that are based on actual values of  $S_s$  and  $S_1$  as oppose to the values of 1.5g and 0.6g.

Site coefficients to adjust the MCE spectral response (Table 9.4.1.2.4a and b)

Assume stiff soil, (Site class D)

$$F_a = 1.0 \quad (\text{Table 9.4.1.2.4a})$$

$$F_s = 1.5 \quad (\text{Table 9.4.1.2.4b})$$

Site Coefficient and Adjusted Maximum Considered Earthquake Spectral Response Acceleration Parameters (9.4.1.2.4)

The site coefficient is the Maximum Considered Earthquake (MCE) spectral response acceleration, adjusted for site class effects:

$$S_{MS} = F_a * S_s = 1.0 * 1.5g = 1.5g \quad (\text{Eq. 9.4.1.2-1})$$

$$S_{M1} = F_v * S_1 = 1.0 * 0.6g = 0.9g \quad (\text{Eq. 9.4.1.2-1})$$

Design spectral response acceleration

$$S_{DS} = (2/3) * S_{MS} = 2/3 * 1.5g = 1.0g \quad (\text{Eq. 9.4.1.2.5-1})$$

$$S_{DS} = (2/3) * S_{M1} = 2/3 * 0.9g = 0.6g \quad (\text{Eq. 9.4.1.2.5-2})$$

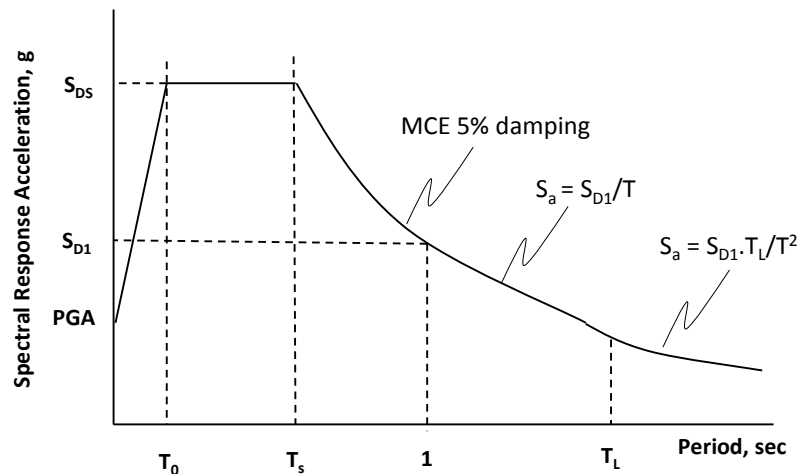


Figure A-2 Design elastic response spectrum

Seismic use Group (Table 9.1.3)

Is based on the occupancy category (Table 1.1)

Occupancy category is II

Therefore, Seismic Use Group = I

Importance factor = I		(Table 9.1.4)
Response modification factor	R = 8	(Table 9.5.2.2)
System overstrength factor	$\Omega = 3$	(Table 9.5.2.2)
Deflection amplification factor	$C_d = 5.5$	(Table 9.5.2.2)
Coefficient for upper limit on calculated period $C_u = 1.4$		(Table 9.5.5.3.1)

Approximate Fundamental period (9.5.5.3.2)

$$T_a = C_t h_n^x \quad (\text{Eq. 9.5.5.3.2-1})$$

$C_t = 0.028$  for steel moment-resisting frames

$h_n =$  height in ft above the base to the highest level = 28.5 ft

$x = 0.8$

$$T_a = 0.028 * (28.5)^{0.8} = 0.408 \text{ sec}$$

Maximum allowable period (T) (9.5.5.3.1)

$$T_s = T_a * C_u$$

$$T_s = T_x = T_y = 0.408 \text{ sec} * 1.4 = 0.571 \text{ sec}$$

This upper limit on estimating the period for strength determination is to ensure that an unreasonably low design base shear is not calculated by using a long period based on an unrealistic frame stiffness assumption.

## ***Strength Requirement***

---

From eigen value analysis

$$T = 0.963 \text{ sec} > 0.571 \text{ sec}$$

Therefore, need to use 0.571 sec for strength determination. Note that this restriction does not hold for drift determination. When checking for drift use actual period (T = 0.963 sec)

### *Seismic response coefficient for strength check (9.5.5.2.1)*

$$\begin{aligned} C_s &= \frac{S_{Ds}}{R/I} \\ &= \frac{1.0g}{8/1.0} = 0.125g \end{aligned} \quad (\text{Eq 9.5.5.2.1-1})$$

### *Upper limit on the seismic response coefficient (9.5.5.2.1)*

$$\begin{aligned} C_s &= \frac{S_{D1}}{T(R/I)} \\ &= \frac{0.6g}{0.571*(8/1.0)} = 0.131g \end{aligned} \quad (\text{Eq 9.5.5.2.1-2})$$

### *Lower limit on the seismic response coefficient (9.5.5.2.1)*

$$\begin{aligned} C_s &= 0.044 * S_{DS} * I \\ &= 0.044 * 1.0g * 1 = 0.044g \end{aligned} \quad (\text{Eq 9.5.5.2.1-3})$$

Therefore; use 0.125g

Calculate Design Seismic Base Shear (9.5.5.2)

$$V = C_s * W$$

W = the total dead load and applicable portions of other loads as indicated in Section 9.5.3

$$W = 1.0DL + 0.5LL = (3 * 0.236 \text{ kips} \cdot \text{sec}^2 / \text{in} * 386 \text{ in} / \text{sec}^2) + (3 * 0.3132 \text{ kips} \cdot \text{sec}^2 / \text{in} * 386 \text{ in} / \text{sec}^2) = 635.97 \text{ kips}$$

$$0.125g * 635.97 \text{ kips} = 79.5 \approx 80 \text{ kips.}$$

Accounting for accidental eccentricity, (details not presented here)

$$80 + 130 (0.05) = 86.5 \text{ kips} \approx 87 \text{ kips.}$$

This is the design base shear that all three columns need to withstand.

Therefore, the next step needed it distribute the base shear over the height to check yielding in the columns and connections.

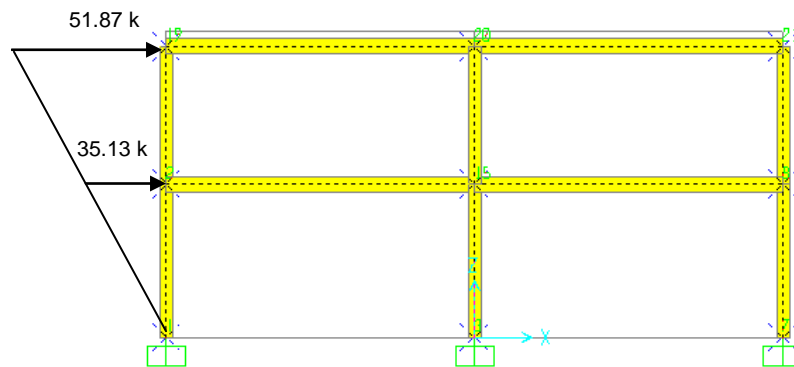


Figure A-3 Distribution of base shear along the height to check columns and connections yielding using SAP2000

Resulting reactions

The resulting frame reactions are shown in Table A-1.

Table A-1 Reactions resulting from ELF analysis

Connection ID	Rx	Rz	My
Left column	-28.46	-15.73	-4304.99
Middle column	-32.80	0.22	-4419.81
Right column	-26.74	15.51	-4091.67

$$\text{Shear Capacity of the column} = 0.577 * F_y * A_w$$

$$= 0.577 * 50 \text{ ksi} * (0.745 \text{ in} * 14 \text{ in}) = 300 \text{ kips}$$

$$V_y = 300 \text{ kips} > V = 32 \text{ kips}$$

Therefore,

**OK**

$$\text{Moment capacity of the column} = M * Y / I$$

$$= 4305 \text{ kips.in} * 7 \text{ in} / 1900 \text{ in}^4 = 15.86 \text{ ksi} < 50 \text{ ksi}$$

$$\sigma = 15.86 \text{ ksi} < \sigma_y = 50 \text{ ksi}$$

Therefore,

**OK**

***Drift Requirements***

---

Seismic response coefficient for drift check (9.5.5.2.1)

$$C_s = \frac{S_{D1}}{T(R/I)} \quad (\text{Eq 9.5.5.2.1-1})$$

$$= \frac{0.6g}{0.963*(8/1.0)} = 0.0779g$$

Note that for drift check, the actual frame period can be used when calculating  $C_s$ .

$$\text{Total base shear} = m_{\text{total}} * S_A$$

For 1.0DL + 0.50 LL

$$\begin{aligned} \text{Total base shear} &= m_{\text{total}} * 0.0779g * 386 \text{ kips.in/sec}^2 \\ &= (0.236*3) + (0.3132*3) * 0.0779g * 386 \text{ kips.in/sec}^2 = 49.54 \\ &\text{ kips} \end{aligned}$$

Therefore, need to distribute the 49.54 kips over the height and use the calculated the drift values to check for drift.

$$F_i = \frac{h_x \cdot W_x}{\sum_{i=1}^n W_i \cdot h_i}$$

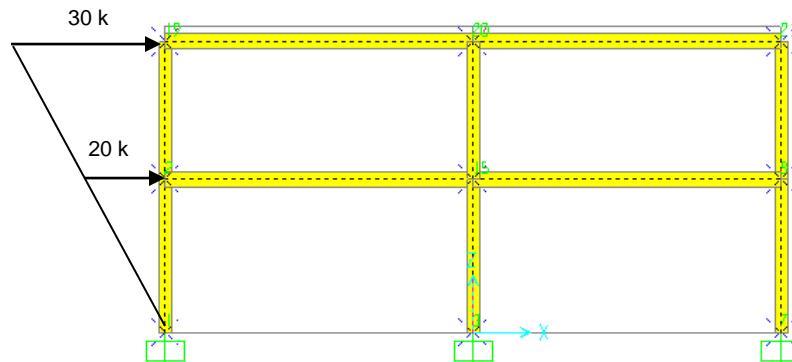


Figure A-4 Distribution of base shear along the height to check drift using SAP2000

**Resulting drift**

First floor = 0.501 in

Top floor = 1.097 in

Check Drift (9.5.2.8) & (9.5.5.7):

$$\delta_x < \Delta a \quad (\text{Eq.9.5.2.8})$$

$\Delta a$  is the allowable story drift (Table 9.5.2.8)

$$\Delta a = 0.025 h_x$$

$h_{sx}$  is the story height below level x, which is 15 ft = 180 in

$$\Delta a = 0.025 * 180 = 4.5 \text{ in}$$

$$\delta_x = C_d \delta_{xe} / I \quad (\text{Eq. 9.5.5.7.1})$$

$C_d$  = deflection amplification factor (Table 9.5.2.2)

$$C_d = 5.5 \quad (\text{Table 9.5.2.2})$$

$\delta_{xe}$  = deflection determined by an elastic analysis

$I$  = Importance factor in accordance with = 1 (Table 9.1.4)

$$\delta_x = (5.5) * (1.0974 - 0.501) / (1.0) = 3.28 \text{ in}$$

$$\delta_x = 3.28 \text{ in} < \Delta a = 4.5 \text{ in}$$

**Therefore,**

**OK**

Check P-Delta effect (9.5.5.7):

$$\theta < \theta_{\max} \quad (9.5.5.7.2)$$

$$\theta = (P_x * \Delta) / (V_x * h_{sx} * C_d) \quad (\text{Eq. 9.5.5.7.2.1})$$



Where;

$P_x$  = the total vertical design load at and above level x. When computing  $P_x$ , no individual load factor need to exceed 1.0

$$= (3 * 0.236 \text{ kips} \cdot \text{sec}^2 / \text{in} * 386 \text{ in} / \text{sec}^2) + (3 * 0.3132 \text{ kips} \cdot \text{sec}^2 / \text{in} * 386 \text{ in} / \text{sec}^2) = 635.97 \text{ kips}.$$

This is based on 1.0DL+0.5LL

$\Delta$  = the design story drift = difference between the deflections at the top and bottom of the story under consideration.

$V_x$  = seismic base shear acting between levels x and x-1 = 20 kips

$h_{sx}$  = story height below level x = 180 in

$C_d$  = deflection amplification factor = 5.5

Therefore;

$$\theta = (635.97 * (1.0974 - 0.501)) / (20 * 180 * 5.5) = 0.019$$

$$\theta_{\max} = 0.5 / (\beta * C_d) = < 0.25$$

$\beta = 1$  (conservative)

$$\theta_{\max} = 0.5 / (1 * 5.5) = 0.09$$

$$\theta = 0.019 < \theta_{\max} = 0.09$$

**Therefore,**

**OK**

Checks on Beam and Column per AISC 358 (Prequalified Connections for Special and Intermediate Steel Moment Frames for Seismic Applications)

**Beam: W18 x 40**

Flange local buckling

Flange width-thickness ratio:  $\frac{b}{t} = \frac{b_f}{2t_f} \leq 0.3 \sqrt{\frac{E}{F_y}}$

$$\frac{b}{t} = \frac{b_f}{2t_f} = \frac{6.02}{2 \cdot 0.525} = 5.73$$

$$0.3 * \sqrt{\frac{E}{F_y}} = 0.3 * \sqrt{\frac{29000}{50}} = 7.22$$

$$5.73 < 7.22$$

**Therefore,**

**OK**

Web width-thickness ratio:  $\frac{h}{t_w} \leq 2.45 \sqrt{\frac{E}{F_y}}$

$$\frac{h}{t_w} = \frac{16.85}{0.315} = 53.49$$

$$2.45 * \sqrt{\frac{E}{F_y}} = 2.45 * \sqrt{\frac{29000}{50}} = 59$$

$$53.49 < 59$$

**Therefore,**

**OK**

Check beam depth, weight and span-to-depth ratio limit per AISC 358

Maximum beam depth > W36

**W18 is used**

**Therefore,**

**OK**

Maximum beam weight > 300 lb/ft

**Beam weight is 40 lb/ft**

**Therefore, OK**

Maximum flange thickness > 1.75 in

**Flange thickness = 0.54 in**

**Therefore, OK**

Minimum Span-to-width ratio > 7

**Ratio = (30ft \*(12 in/1ft) /18 = 20**

**Therefore, OK**

Check beam lateral bracing requirements

$$L_b = \frac{0.086 * r_y * E}{F_y} = \frac{0.086 (1.27) * 29000}{50} = 63.34 \text{ in} = 5.28 \text{ ft}$$

Therefore, we need to brace every 1/6<sup>th</sup> point:  $L = 30/6 = 5$  ft on center. However, since we are analyzing a planar frame, we do not have to worry about such a requirement (i.e., for the purpose of this project, the brace does not need to be designed)

Check beam design flexure strength (AISC 360 (Chapter F.2))

$$L_P = 1.76 * r_y * \sqrt{\frac{E}{F_y}} = 5.3 \text{ ft} > 5 \text{ ft}$$

$$\therefore M_n = M_P = F_y * Z_x$$

Design Flexural Strength:  $\phi M_n = 0.9 * 50ksi * 78.4 = 3528kip.in$

Demand-capacity ratio:  $D/C = 1504 \text{ kips.in (from SAP2000)} / 3528 \text{ kips.in}$

$$D/C = 0.426 < 1$$

Therefore,

**OK**

Check nominal shear capacity

$$\frac{d}{t_w} \leq 2.45 * \sqrt{\frac{E}{F_y}}$$

$$\frac{d}{t_w} = \frac{18in}{0.315in} = 57.14$$

$$2.45 * \sqrt{\frac{E}{F_y}} = 59.00$$

$$\therefore V_n = 0.6F_y A_w C_v$$

$$C_v = 1$$

Design Shear Strength:  $\therefore \phi V_n = 0.9 * 0.6 * 50 * ((18 - (2 * 0.525)) * 0.315) * 1 = 144.15 \text{ kips}$

Demand-capacity ratio:  $D/C = 38.97 \text{ kips (from SAP2000)} / 144.15 \text{ kips}$

$$D/C = 0.27 < 1$$

Therefore,

**OK**

**Column: W14 x 159**

Flange local buckling

$$\text{Flange width-thickness ratio: } \frac{b}{t} = \frac{b_f}{2t_f} \leq 0.3 \sqrt{\frac{E}{F_y}}$$

$$\frac{b}{t} = \frac{b_f}{2t_f} = \frac{15.6}{2 * 1.19} = 6.55$$

$$0.3 * \sqrt{\frac{E}{F_y}} = 0.3 * \sqrt{\frac{29000}{50}} = 7.22$$

$$6.55 < 7.22$$

**Therefore,**

**OK**

$$\text{Web width-thickness ratio: } \frac{h}{t_w} \leq 3.14 \sqrt{\frac{E}{F_y}} (1 - 1.54 C_a)$$

$$\frac{h}{t_w} = \frac{12.62}{0.745} = 16.94$$

$$C_a = \frac{P_u}{\phi_b P_y} = \frac{P_u}{0.9 * F_y * A_g} = \frac{639 \text{ kips}}{0.9 * 50 \text{ ksi} * 46.7 \text{ in}^2} = \frac{639}{2101} = 0.304$$

$$3.14 \sqrt{\frac{E}{F_y}} (1 - 1.54 C_a) = 3.14 * \sqrt{\frac{29000}{50}} = 59 * (1 - (1.54 * 0.304)) = 28.10$$

$$16.94 < 28.10$$

**Therefore,**

**OK**

Check column depth, weight and span-to-depth ratio limit per AISC 358

Maximum beam depth > W36

**W14 is used**

**Therefore,**

**OK**

Maximum column weight = unlimited

**Therefore,**

**OK**

Maximum flange thickness = compact

**Therefore,**

**OK**

Minimum Span-to-width ratio > 7

$$\text{Ratio} = (30\text{ft} * (12 \text{ in}/1\text{ft}) / 18 = 20$$

**Therefore,**

**OK**

Check column lateral bracing requirements

Unbraced column height (taken from top of framing at bottom to mid-depth of beam at top)

$$L_p = 14.2 \text{ ft}, L_r = 73.2 \text{ ft}$$

$$h = 13.5 - (1.5/2) = 12.75 \text{ ft}$$

$$L_b = 12.75 \text{ ft} < L_p = 73.2 \text{ ft}$$

**Therefore,**

**OK**

Check column Buckling

$$G = \frac{\sum (I_c / L_c)}{\sum (I_g / L_c)}$$

$$G_{\text{top}} = \frac{2 \left( \frac{1900 \text{in}^4}{12.5 \text{ft}} \right)}{2 \left( \frac{612 \text{in}^4}{30 \text{ft}} \right)} = 7.4$$

$$G_{\text{bot}} = 1$$

Using the Monograph;  $K_x = 1.8$ , assume  $K_y = 1.2$

$$\frac{k_x L_x}{r_x} = \frac{1.8 * 12.25 * 12}{6.38} = 41.47$$

$$\frac{k_y L_y}{r_y} = \frac{1.2 * 12.25 * 12}{4} = 44.1$$

$$\text{if } \frac{k_y L_y}{r_y} \leq 4.71 \sqrt{\frac{E}{F_y}}$$

$$44.1 \leq 4.71 \sqrt{\frac{29000}{50}} = 113.43$$

$$F_e = \frac{\pi^2 E}{\left(\frac{KL}{r}\right)^2} = \frac{\pi^2 * 29000}{(44.1)^2} = 147.02 \text{ ksi}$$

$$F_{cr} = \left[ 0.658^{\frac{F_y}{F_e}} \right] F_y = [0.658^{50/147}] * 50 = 43.36 \text{ ksi}$$

The nominal design capacity is:

$$\phi P_n = \phi_c F_{cr} A_g = 0.9 * 43.36 \text{ ksi} * 46.7 \text{ in}^2 = 1822 \text{ kips} > 38 \text{ kips}$$

**Therefore,**

**OK**

Check the Flexural Strength

$$L_p = 14.2 \text{ ft} > 12.75 \text{ ft}$$

$$\text{Therefore, } M_{nx} = M_{px} = F_y * Z_x = 50 \text{ ksi} * 287 \text{ in}^3 = 14350 \text{ kips.in} = 1196 \text{ kips.ft}$$

$$M_{ny} = M_{py} = F_y * Z_y = 50 \text{ ksi} * 146 \text{ in}^3 = 7300 \text{ kips.in} = 608.33 \text{ kips.ft}$$

$$M_{cx} = \phi M_{nx} = 0.9 * 1196 \text{ kips.ft} = 1076.4 \text{ kips.ft}$$

$$M_{cy} = \phi M_{ny} = 0.9 * 608.33 \text{ kips.ft} = 547.497 \text{ kips.ft}$$

Consider second order effect

$$B_1 = \frac{C_m}{1 - \alpha P_r / P_e} \geq 1$$

$$P_r = P_{nt} + P_{lt}$$

$$\alpha = 1$$

$$C_m = 0.6 - 0.4(M_1/M_2)$$

$$C_{mx} = 0.6 - 0.4(1) = 0.2$$

$$M_{ux} = B_1 M_{nt}$$

$$M_{ux} = 0.2 * 1196 \text{ kip.ft} = 239.2 \text{ kip.ft}$$

Check moment axial interaction

$$\frac{P_u}{2\phi P_n} + \frac{M_{ux}}{\phi_b M_{nx}} \leq 1$$

$$\frac{639}{1822} + \frac{239}{1076} = 0.572 \leq 1$$

**Therefore,**

**OK**

Check Column Shear Strength

$$\frac{h}{t_w} = \frac{12.62}{0.745} = 16.94 < 2.45 * \sqrt{\frac{E}{F_y}} = 59.00$$

$$\therefore V_n = 0.6 F_y A_w C_v$$

$$C_v = 1$$

$$\therefore \phi V_n = 1 * 0.6 * 50 * 0.745 * 6.30 * 1 = 140.8 \text{ kips}$$

$$\phi V_n = 140.8 \text{ kips} > V_u = 38 \text{ kips}$$

**Therefore,**

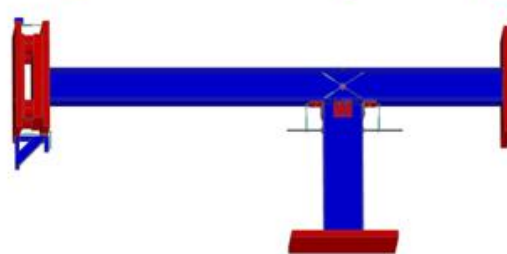
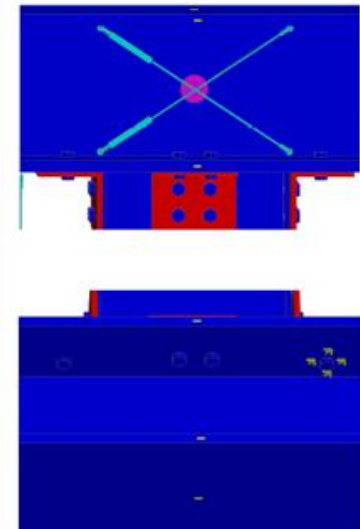
**OK**



## APPENDIX B.

### INSTRUMENTATION PLANS

*Instrumentation Plan for the 30%  $Mp_{beam}$  Connection (Typical for all specimens)*

Label	Installed By	Checked By
1-SG-C-F-24	AEM	
1-SG-C-F-25	D,B	
1-SG-C-F-26	D,B	
1-SG-C-F-27	D,B	
1-SG-C-F-28	D,B	
1-SG-C-F-29	D,B	
1-SG-C-F-30	D,B	
1-SG-C-F-31	D,B	
1-SG-C-F-32	D,B	
1-SG-C-F-33	D,B	
1-SG-C-F-168	D,B	
1-SG-C-F-169	D,B	
1-SG-C-F-170	D,B	
1-SG-C-F-171	D,B	
1-SG-C-F-172	D,B	
1-SG-C-F-173	D,B	
1-SG-C-F-174	D,B	
1-SG-C-F-175	D,B	
1-SG-C-F-176	D,B	
1-SG-C-F-177	D,B	
1-SG-C-F-178	D,B	
1-SG-C-F-179	D,B	
1-LP-C-W-39	D,B	
1-LP-C-W-40	D,B	
1-LP-B-P-37	Jce	
1-LP-B-P-38	Jce	
1-LP-B-P-167	Jce	
1-IN-C-W-182	D,B	
1-SP-F-C-34	D,B	
1-SP-F-C-35	D,B	
1-SP-F-C-36	D,B	

**BEAM-COLUMN TESTS (LARGE-SCALE)**

DATE: 07/27/09

BY: JCE


PROJECT: 07/27/09

SCALE: 1/4" = 1'-0"

AS BUILT:

Column Cover Page

SHEET NO. 2 of 26



SEISMOLOGICAL ENGINEERING CENTER  
 CENTER FOR ADVANCED EARTHQUAKE ENGINEERING AND SEISMOLOGY  
 UNIVERSITY OF MARYLAND  
 1241 UNIVERSITY COLLEGE PARK  
 COLLEGE PARK, MARYLAND 20742-1001



M&E America Engineering Center  
 MECHANICAL ENGINEERING  
 CENTER  
 UNIVERSITY OF MISSISSIPPI  
 URBAN ENGINEERING  
 1241 Research and Engineering Lab  
 205 N. Manship Avenue, Oxford, MS  
 38657

**BEAM-COLUMN  
 TESTS  
 (LARGE-SCALE)**

Sheet Notes:

1. Sensors of base shall be on centerline of column.
2. All linear pots shall be set at mid stroke.

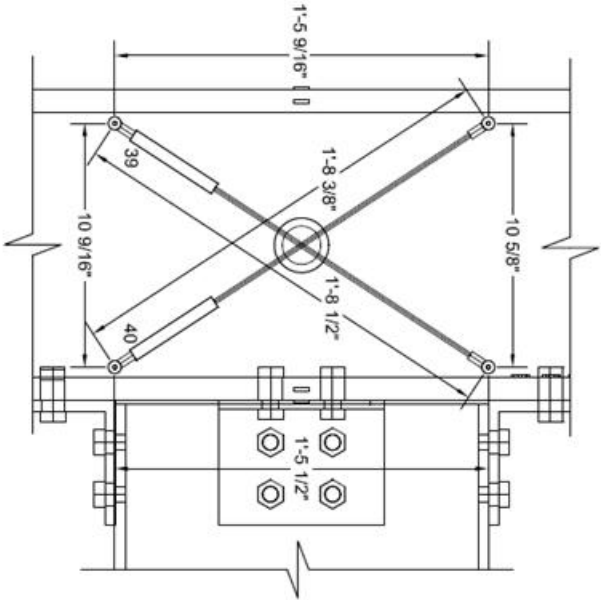
NO.	REVISION	DATE	BY

DESIGNED BY: DLE  
 DRAWN BY: DLE  
 CHECKED BY: HNW  
 SCALE: NTS  
 PROJECT NO: 727209  
 ISSUE NO: M&E-S7-01  
 SHEET TITLE:

As Built:  
 Column Linear Pots

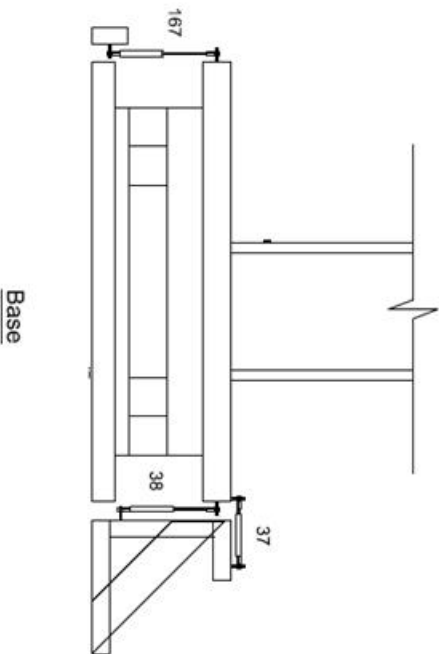
SHEET NO.:

**3 of 26**



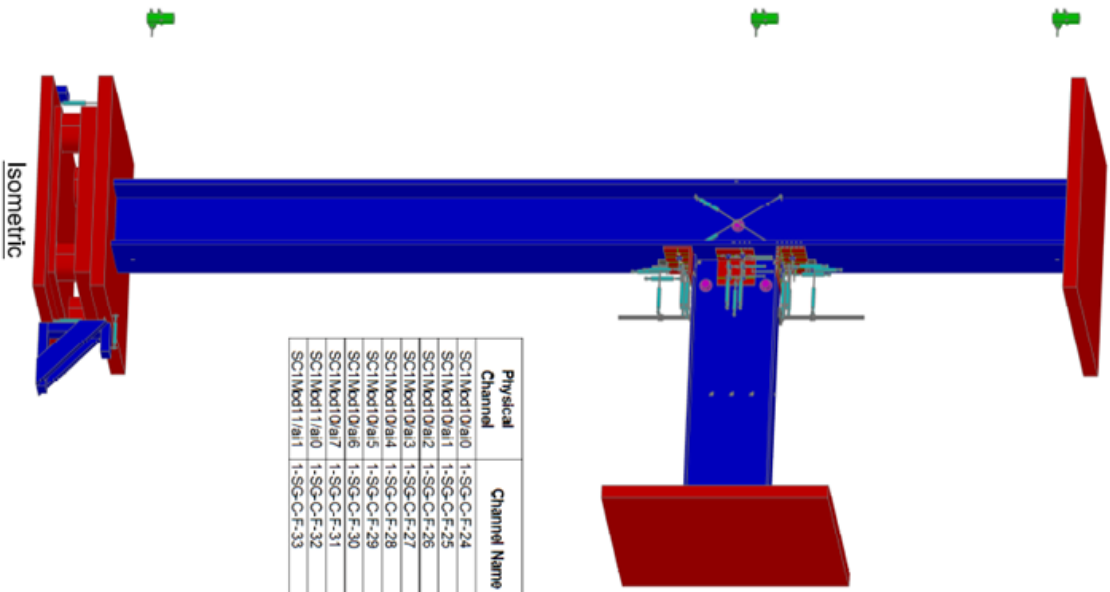
Gauge Label	Physical Channel	Serial Number
1-LP-C-W-39	SC1Mod1/a1	A1807-0006
1-LP-C-W-40	SC1Mod1/a2	A1807-0008

Gauge Label	Physical Channel	Serial Number
1-LP-B-P-37	SC1Mod1/a3	A4006-3
1-LP-B-P-38	SC1Mod1/a4	A1807-0001
1-LP-B-P-167	SC1Mod1/a5	A4006-26

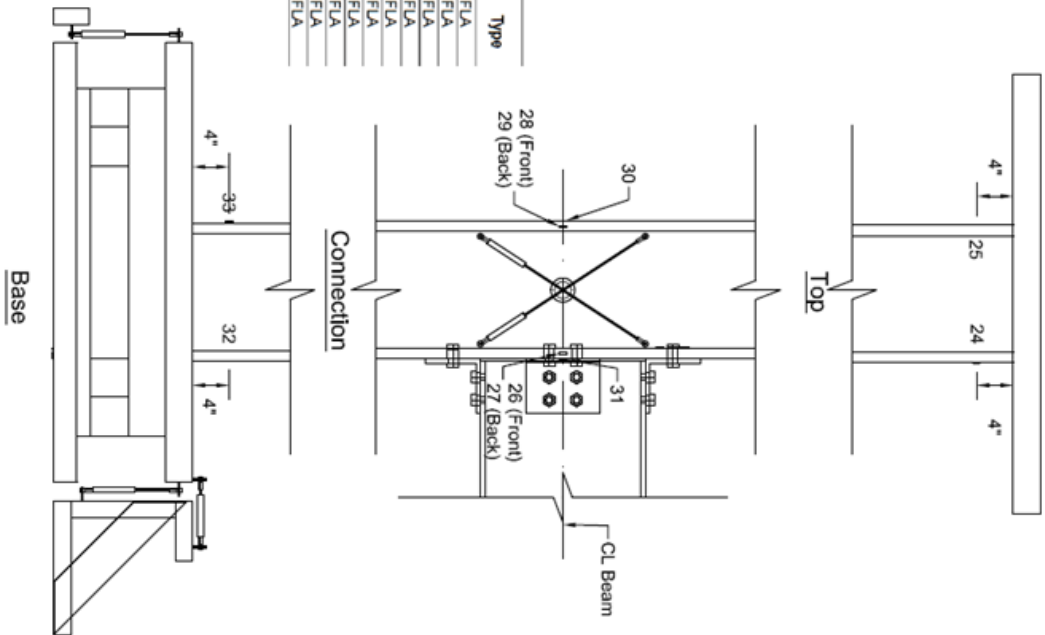


Base





Physical Channel	Channel Name	Type
SCI1Mod10/a10	1-SG-C-F-24	FLA
SCI1Mod10/a11	1-SG-C-F-25	FLA
SCI1Mod10/a12	1-SG-C-F-26	FLA
SCI1Mod10/a13	1-SG-C-F-27	FLA
SCI1Mod10/a14	1-SG-C-F-28	FLA
SCI1Mod10/a15	1-SG-C-F-29	FLA
SCI1Mod10/a16	1-SG-C-F-30	FLA
SCI1Mod10/a17	1-SG-C-F-31	FLA
SCI1Mod10/a18	1-SG-C-F-32	FLA
SCI1Mod10/a19	1-SG-C-F-33	FLA



Mid-America Earthquake Center  
 MID-AMERICA EARTHQUAKE  
 CENTER OF ILLINOIS  
 UNIVERSITY OF ILLINOIS  
 1241 Raymond, Civil Engineering Lab  
 2055 N. Mathews Avenue, Urbana, IL  
 61801

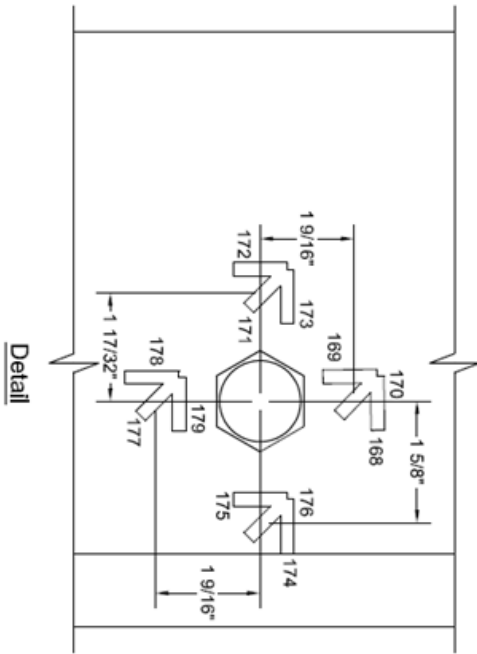
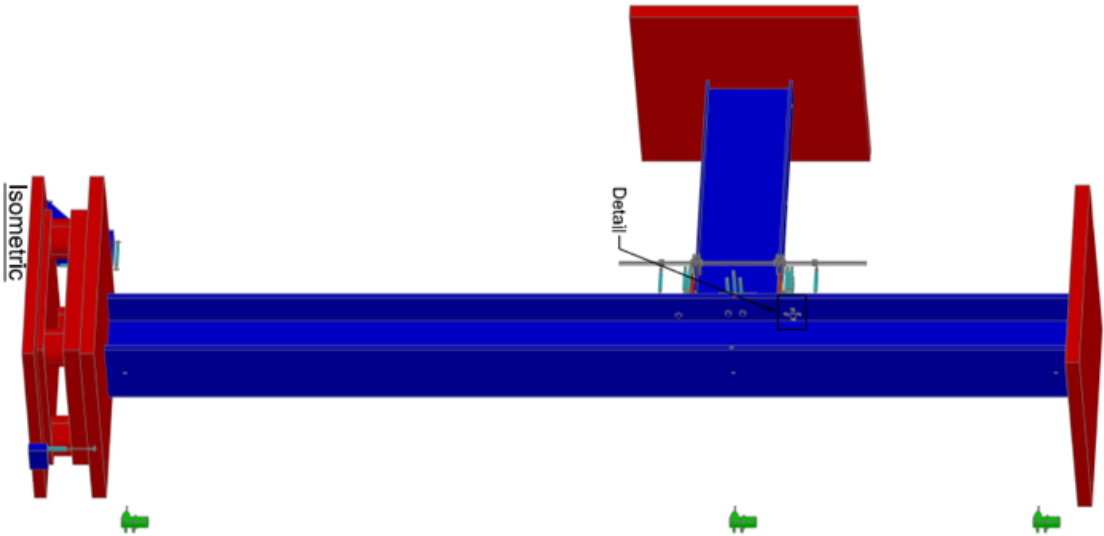
**BEAM-COLUMN TESTS (LARGE-SCALE)**

1. Channels 24, 25, 30, 31, 32, and 33 are mounted on centerline of column.

NO.	DESCRIPTION	DATE	BY

DESIGNED BY: D-JB  
 DRAWN BY: D-JB  
 CHECKED BY: HNM  
 SCALE: NTS  
 DATE: 01/27/08  
 SHEET SIZE: WIDE, 34"-0"  
 PRINT TITLE: As Built: Column Strain Gauge

SHEET NO. 5 of 26



Gauge Label	Physical Channel	Type
1-SG-C-F-168	SC1Mod11/a2	FRA
1-SG-C-F-169	SC1Mod11/a3	
1-SG-C-F-170	SC1Mod11/a4	
1-SG-C-F-171	SC1Mod11/a5	FRA
1-SG-C-F-172	SC1Mod11/a6	
1-SG-C-F-173	SC1Mod11/a7	
1-SG-C-F-174	SC1Mod12/a0	FRA
1-SG-C-F-175	SC1Mod12/a1	
1-SG-C-F-176	SC1Mod12/a2	
1-SG-C-F-177	SC1Mod12/a3	FRA
1-SG-C-F-178	SC1Mod12/a4	
1-SG-C-F-179	SC1Mod12/a5	



Mid-America Earthquake Center  
 MID-AMERICA EARTHQUAKE  
 CENTER  
 UNIVERSITY OF ILLINOIS  
 URBANA, ILLINOIS  
 1241 Simpson Civil Engineering Lab  
 200 N. Mathews Avenue, Urbana, IL  
 61801

### BEAM-COLUMN TESTS (LARGE-SCALE)

SHEET NOTES

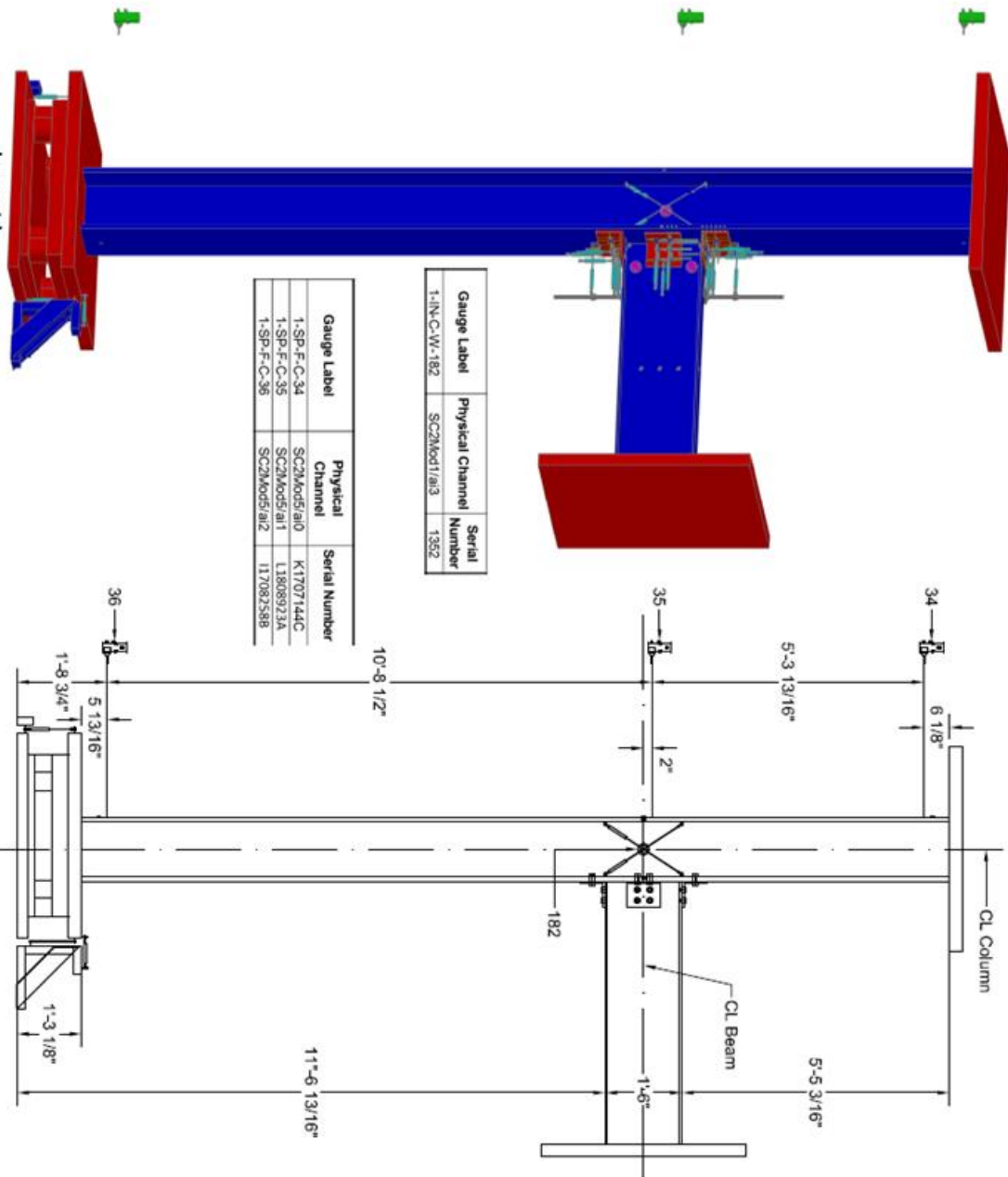
NO.	DESCRIPTION	DATE	BY

Revision:    DAB  
 Drawn by:    DAB  
 Checked by: HNM  
 Scale:        NTS  
 Date:         07/27/09  
 Project No.: MAE-SY-01  
 Panel Title:

As Built:  
 Column Strain  
 Gauges 2

SHEET NO.: **6 of 26**

Isometric



Gauge Label	Physical Channel	Serial Number
1-IN-C-W-182	SC2Mod1/813	1352
<b>Gauge Label</b>		
1-SP-F-C-34	SC2Mod5/810	K1707144C
1-SP-F-C-35	SC2Mod5/811	L1808923A
1-SP-F-C-36	SC2Mod5/812	117082588

**As Built:**  
Column Stirring Pot  
and Inclinometer

SHEET NO. **7** OF **26**

MID-AMERICA EARTHQUAKE  
UNIVERSITY OF ILLINOIS  
URBANA-CHAMPAIGN  
1241 Newman Civil Engineering Lab  
205 N. Mathews Avenue, Urbana, IL  
61801

SHEET NOTES





Mid-America Engineering Center  
 MID-AMERICA ENGINEERING  
 UNIVERSITY OF ILLINOIS  
 URBANA-CHAMPAIGN  
 1241 Newark Civil Engineering Lab  
 205 N. Matthews Avenue, Urbana, IL  
 61801

**BEAM-COLUMN TESTS (LARGE-SCALE)**

Sheet Name:

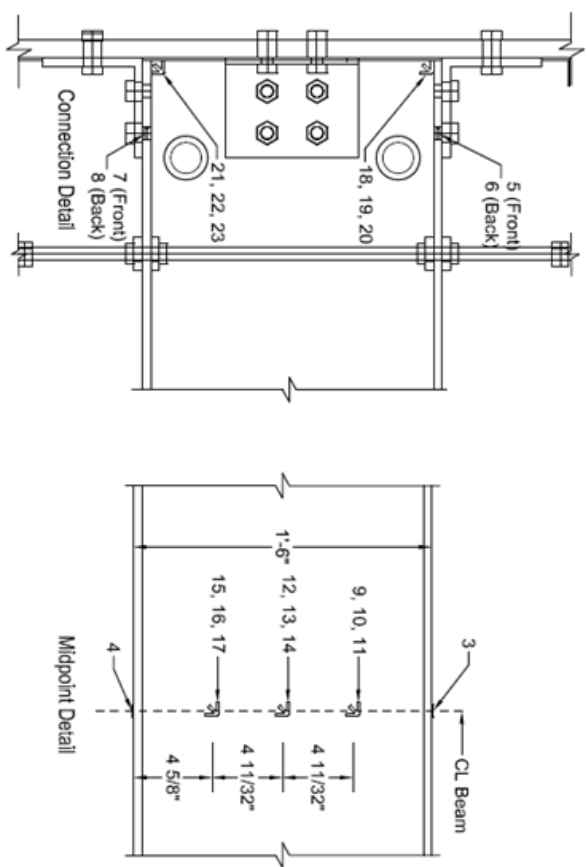
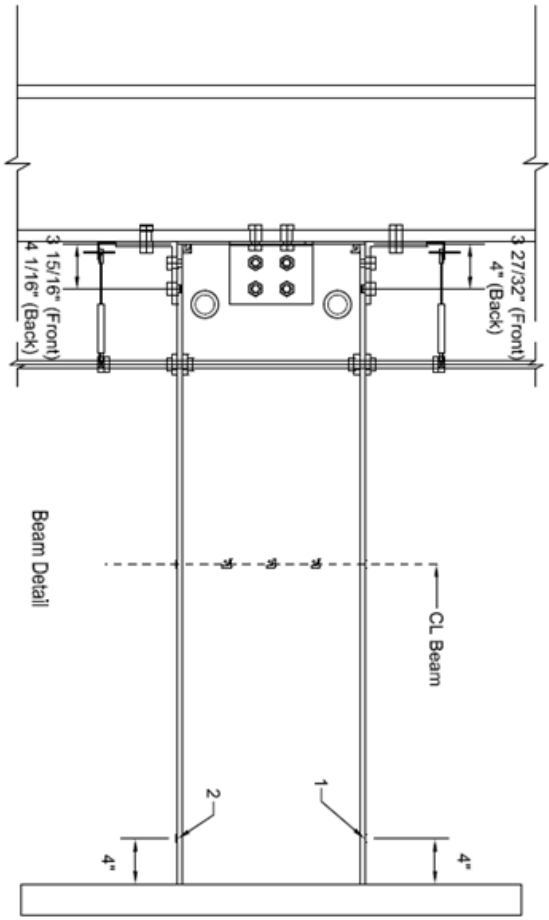
ID	DESCRIPTION	DATE	BY

DESIGNED BY: DJB  
 DRAWING NO.: N/A  
 CHECKED BY: N/A  
 DATE: 07/28/09  
 PROJECT NO.: MAF-SY-01  
 SHEET TITLE:

As Built:  
 Beam Strain Gauge

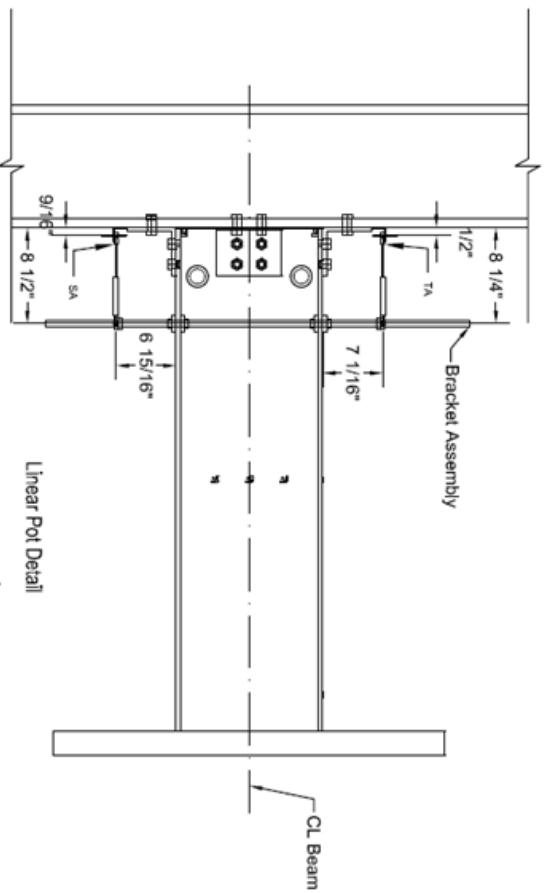
SHEET NO.:

**9 of 26**

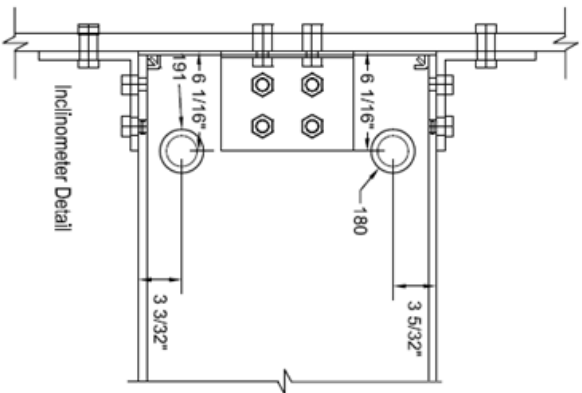


Physical Channel	Channel Name	Type
SC1Mod4/a10	1-SG-B-F-1	FLA
SC1Mod4/a11	1-SG-B-F-2	FLA
SC1Mod4/a12	1-SG-B-F-3	FLA
SC1Mod4/a13	1-SG-B-F-4	FLA
SC1Mod4/a14	1-SG-B-F-5	FLA
SC1Mod4/a15	1-SG-B-F-6	FLA
SC1Mod4/a16	1-SG-B-F-7	FLA
SC1Mod4/a17	1-SG-B-F-8	FLA
SC1Mod4/a18	1-SG-B-W-9	FRA
SC1Mod4/a19	1-SG-B-W-10	FRA
SC1Mod4/a10	1-SG-B-W-11	FRA
SC1Mod4/a11	1-SG-B-W-12	FRA
SC1Mod4/a12	1-SG-B-W-13	FRA
SC1Mod4/a13	1-SG-B-W-14	FRA
SC1Mod4/a14	1-SG-B-W-15	FRA
SC1Mod4/a15	1-SG-B-W-16	FRA
SC1Mod4/a16	1-SG-B-W-17	FRA
SC1Mod4/a17	1-SG-B-W-18	YEFRA
SC1Mod4/a18	1-SG-B-W-19	YEFRA
SC1Mod4/a19	1-SG-B-W-20	YEFRA
SC1Mod4/a20	1-SG-B-W-21	YEFRA
SC1Mod4/a21	1-SG-B-W-22	YEFRA
SC1Mod4/a22	1-SG-B-W-23	YEFRA





Linear Pot Detail



Inclinometer Detail

Gauge Label	Physical Channel	Serial Number
LP-CL-R0-SA	SC1Mod1/a13	A1807-0004
LP-CL-R0-TA	SC1Mod1/a15	A1807-0023

Gauge Label	Physical Channel	Serial Number
IN-B-W-180	SC2Mod1/a12	1349
IN-B-W-191	SC2Mod1/a112	1357



Mid-America Earthquake Center  
 MID-AMERICA EARTHQUAKE  
 CENTER  
 UNIVERSITY OF ILLINOIS  
 CHAMPAIGN-URBANA  
 1241 Newmark, Civil Engineering Lab  
 205 N. Mathews Avenue, Urbana, IL  
 61801

### BEAM-COLUMN TESTS (LARGE-SCALE)

DATE: 07/28/09

REV.	DESCRIPTION	DATE	BY

DESIGNED BY: DAB  
 DRAWN BY: DAB  
 CHECKED BY: HNR  
 DATE: 07/28/09  
 PROJECT NO.: MAE-SY-01  
 SHEET TITLE:

As Built:  
 Beam Linear Pot  
 and Inclinometer

SHEET NO.:

10 of 26

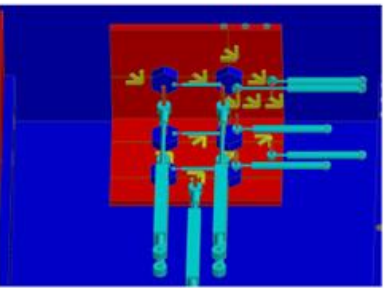
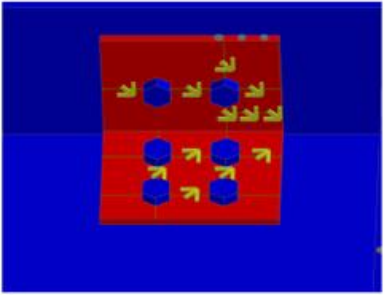


National Centre for Earthquake Engineering and Research  
 NATIONAL CENTRE FOR EARTHQUAKE ENGINEERING AND RESEARCH  
 UNIVERSITY OF LONDON  
 1241, Somerset Road, London, W1P 3AA, U.K.  
 205 N. Madison Avenue, Urbana, IL 61801

**BEAM-COLUMN  
 TESTS  
 (LARGE-SCALE)**

SHEET NUMBER

Label	Installed By	Checked By
1-SG-FWA-CF-V-89	DIB	
1-SG-FWA-CF-D-90	DIB	
1-SG-FWA-CF-H-91	DIB	
1-SG-FWA-CF-V-92	DIB	
1-SG-FWA-CF-D-93	DIB	
1-SG-FWA-CF-H-94	DIB	
1-SG-FWA-CF-V-95	DIB	
1-SG-FWA-CF-D-96	DIB	
1-SG-FWA-CF-H-97	DIB	
1-SG-FWA-CF-V-98	DIB	
1-SG-FWA-CF-D-99	DIB	
1-SG-FWA-CF-H-100	DIB	
1-SG-FWA-CF-V-101	Mark	
1-SG-FWA-CF-D-102	Mark	
1-SG-FWA-CF-H-103	Mark	
1-SG-FWA-CF-V-104	DIB	
1-SG-FWA-CF-D-105	DIB	
1-SG-FWA-CF-H-106	DIB	
1-SG-FWA-CF-V-107	DIB	



Label	Installed By	Checked By
1-SG-FWA-CF-D-108	DIB	
1-SG-FWA-CF-H-109	DIB	
1-SG-FWA-BW-H-110	DIB	
1-SG-FWA-BW-D-111	DIB	
1-SG-FWA-BW-V-112	DIB	
1-SG-FWA-BW-H-113	DIB	
1-SG-FWA-BW-D-114	DIB	
1-SG-FWA-BW-V-115	DIB	
1-SG-FWA-BW-H-116	DIB	
1-SG-FWA-BW-D-117	DIB	
1-SG-FWA-BW-V-118	DIB	
1-SG-FWA-BW-H-119	DIB	
1-SG-FWA-BW-D-120	DIB	
1-SG-FWA-BW-V-121	DIB	
1-SG-FWA-BW-H-161	DIB	
1-SG-FWA-BW-D-162	DIB	
1-SG-FWA-BW-V-163	DIB	
1-LP-FWA-BW-134	DIB	
1-LP-FWA-BW-165	DIB	
1-LP-FWA-CF-122	DIB	
1-LP-FWA-CF-123	DIB	
1-LP-FWA-BW-127	DIB	
1-LP-FWA-BW-128	DIB	
1-LP-FWA-BW-129	DIB	
1-LP-FWA-BW-130	DIB	
1-LP-FWA-BW-131	DIB	
1-LP-FWA-BW-132	DIB	
1-LP-FWA-CF-133	DIB	
1-LP-FWA-BW-164	DIB	
1-LP-FWA-BW-181	DIB	

AS BUILT:  
 FWA Cover Page

SHEET NO. 11 of 26

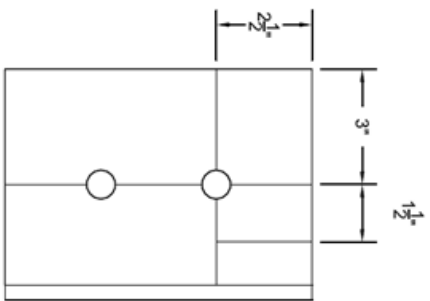


Mid-America Earthquake Center  
 MID-AMERICA EARTHQUAKE  
 CENTER - LANSING  
 UNIVERSITY OF MICHIGAN  
 LIBRARIUM-CHARLTON  
 1241 Newman Civil Engineering Lab  
 205 N. Mathews Avenue, Urbana, IL  
 61801

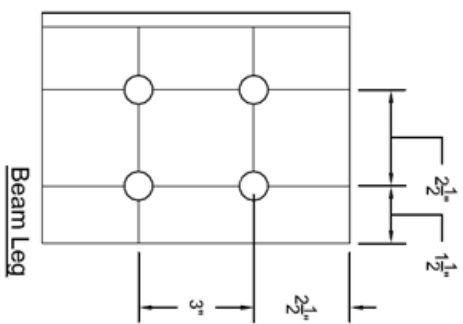
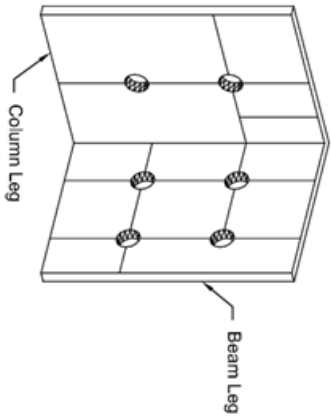
**BEAM-COLUMN  
 TESTS  
 (LARGE-SCALE)**

SHEET TITLE

1. Etch reference lines on angles.



Isometric



NO.	DESCRIPTION	DATE	BY

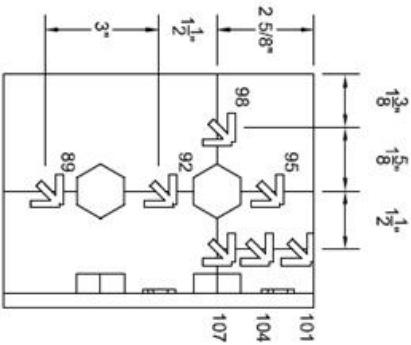
DESIGNED BY: DJS  
 DRAWING NO: D-38  
 CHECKED BY: HJM  
 SCALE: NTS  
 DATE: 07/28/09  
 PROJECT NO: WAE-SV-01  
 SHEET TITLE:

As Built:  
 Front Web Angle  
 Pre-Installation

SHEET NO.:



Multi-Axial Stress Examination Center  
 MECHANICAL ENGINEERING  
 UNIVERSITY OF ILLINOIS  
 URBANA-CHAMPAIGN  
 1241 Newark Civil Engineering Lab  
 205 N. Madonn Avenue, URBANA, IL  
 61801

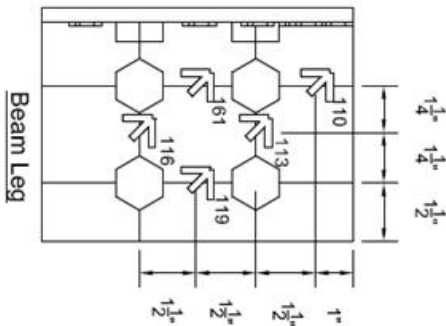


### BEAM-COLUMN TESTS (LARGE-SCALE)

1. Install strain gauges.  
 2. Channel numbers shown are the test channel of the rosette.

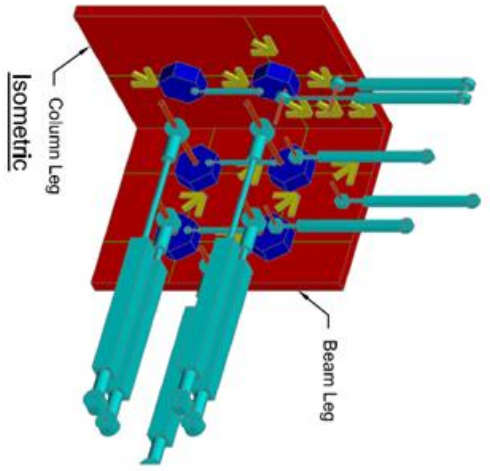
Gauge Label	Physical Channel	SN
1-SG-FWA-CF-V-89	SC1Mod5/a10	YEFRA
1-SG-FWA-CF-D-96	SC1Mod5/a11	
1-SG-FWA-CF-H-91	SC1Mod5/a12	YEFRA
1-SG-FWA-CF-V-92	SC1Mod5/a13	YEFRA
1-SG-FWA-CF-D-93	SC1Mod5/a14	
1-SG-FWA-CF-H-94	SC1Mod5/a15	YEFRA
1-SG-FWA-CF-V-95	SC1Mod5/a16	
1-SG-FWA-CF-D-96	SC1Mod5/a17	YEFRA
1-SG-FWA-CF-H-97	SC1Mod5/a18	YEFRA
1-SG-FWA-CF-V-98	SC1Mod5/a19	YEFRA
1-SG-FWA-CF-D-99	SC1Mod5/a10	
1-SG-FWA-CF-H-100	SC1Mod5/a11	YEFRA
1-SG-FWA-CF-V-101	SC1Mod5/a12	YEFRA
1-SG-FWA-CF-D-102	SC1Mod5/a13	
1-SG-FWA-CF-H-103	SC1Mod5/a14	YEFRA
1-SG-FWA-CF-V-104	SC1Mod5/a15	YEFRA
1-SG-FWA-CF-D-105	SC1Mod5/a16	
1-SG-FWA-CF-H-106	SC1Mod5/a17	YEFRA
1-SG-FWA-CF-V-107	SC1Mod5/a18	YEFRA
1-SG-FWA-CF-D-108	SC1Mod5/a19	
1-SG-FWA-CF-H-109	SC1Mod5/a20	YEFRA

Gauge Label	Physical Channel	Type
1-SG-FWA-BW-H-110	SC1Mod5/a21	YEFRA
1-SG-FWA-BW-D-111	SC1Mod5/a22	YEFRA
1-SG-FWA-BW-V-112	SC1Mod5/a23	YEFRA
1-SG-FWA-BW-H-113	SC1Mod5/a1	YEFRA
1-SG-FWA-BW-D-114	SC1Mod5/a2	
1-SG-FWA-BW-V-115	SC1Mod5/a3	YEFRA
1-SG-FWA-BW-H-116	SC1Mod5/a4	YEFRA
1-SG-FWA-BW-D-117	SC1Mod5/a5	
1-SG-FWA-BW-V-118	SC1Mod5/a6	YEFRA
1-SG-FWA-BW-H-119	SC1Mod5/a7	
1-SG-FWA-BW-D-120	SC1Mod5/a8	
1-SG-FWA-BW-V-121	SC1Mod5/a9	YEFRA
1-SG-FWA-BW-H-122	SC1Mod5/a10	
1-SG-FWA-BW-D-161	SC1Mod5/a11	YEFRA
1-SG-FWA-BW-V-162	SC1Mod5/a12	
1-SG-FWA-BW-H-163	SC1Mod5/a13	



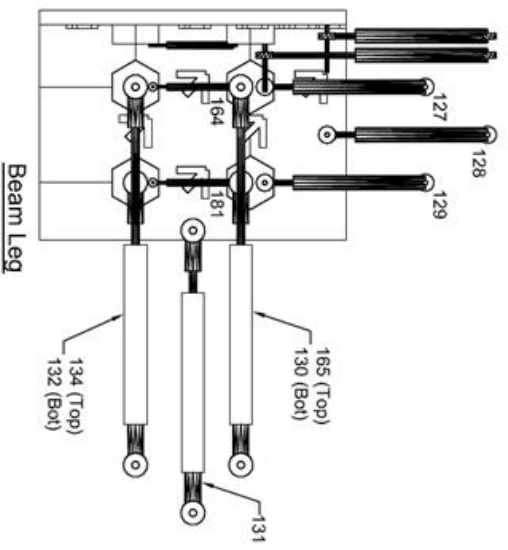
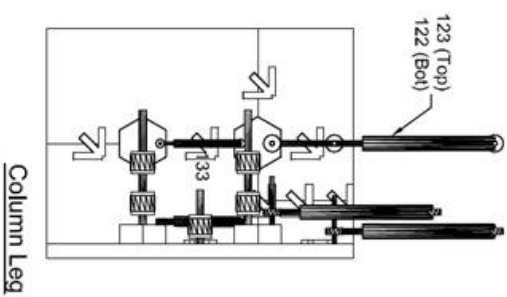
DATE: 01/28
BY: DUB
DESIGNED BY: HMM
CHECKED BY: NLS
SCALE: 07/25/08
DATE: 07/25/08
PROJECT NO. MAE SV-01
SHEET NO. 13 or 26

As Built:  
 Front Web Angle  
 Strain Gauge



Gauge Label	Physical Channel	Serial Number
1-L-P-FVA-BW-134	SC1Mod1@a14	A4006-32
1-L-P-FVA-BW-166	SC1Mod1@a16	A4006-15
1-L-P-FVA-BW-122	SC1Mod1@a18	33/07 SNO7
1-L-P-FVA-CF-123	SC1Mod1@a19	33/07 SNO5
1-L-P-FVA-BW-127	SC1Mod1@a21	33/07 SNO8
1-L-P-FVA-BW-128	SC1Mod1@a24	33/07 SNO6
1-L-P-FVA-BW-129	SC1Mod1@a25	18/07 ZNO8
1-L-P-FVA-BW-130	SC1Mod1@a26	A4006-36
1-L-P-FVA-BW-131	SC1Mod1@a27	A4006-38
1-L-P-FVA-BW-132	SC1Mod1@a28	A4006-45

Gauge Label	Physical Channel	Model Number	Serial Number
1-L-P-FVA-CF-133	SC2Mod8@a10	CD 375-50	1
1-L-P-FVA-BW-164	SC2Mod8@a11	CD 375-50	2
1-L-P-FVA-BW-181	SC2Mod8@a12	CD 375-50	3



## BEAM-COLUMN TESTS (LARGE-SCALE)

- SHEET NOTES:**
1. bracket studs as shown. CD #50. On bolts, use 2.5 #10, on specimen use 3.5 #10. CD 25: use #10 studs.
  2. Tight studs to provide clearance. Ensure that threads are protected.
  3. All linear pots shall be horizontal or vertical, as required.
  4. LVDT's 133, 164, and 181 shall be glued between bolt heads.

NO.	DESCRIPTION	DATE

DESIGNED BY: DAB  
 DRAWN BY: DAB  
 CHECKED BY: NNS  
 SCALE: 07/28/09  
 DATE: 07/28/09  
 PROJECT NO.: WAF-SY-01  
 SHEET TITLE: As Built: Front Web Angle Linear Pot



Mid-America Earthquake Center  
 MID-AMERICA EARTHQUAKE  
 CENTER  
 UNIVERSITY OF ILLINOIS  
 URBANA-CHAMPAIGN  
 1341 Newmark Civil Engineering Lab  
 205 N. McDowell Street, Urbana, IL  
 61801

**BEAM-COLUMN  
 TESTS  
 (LARGE-SCALE)**

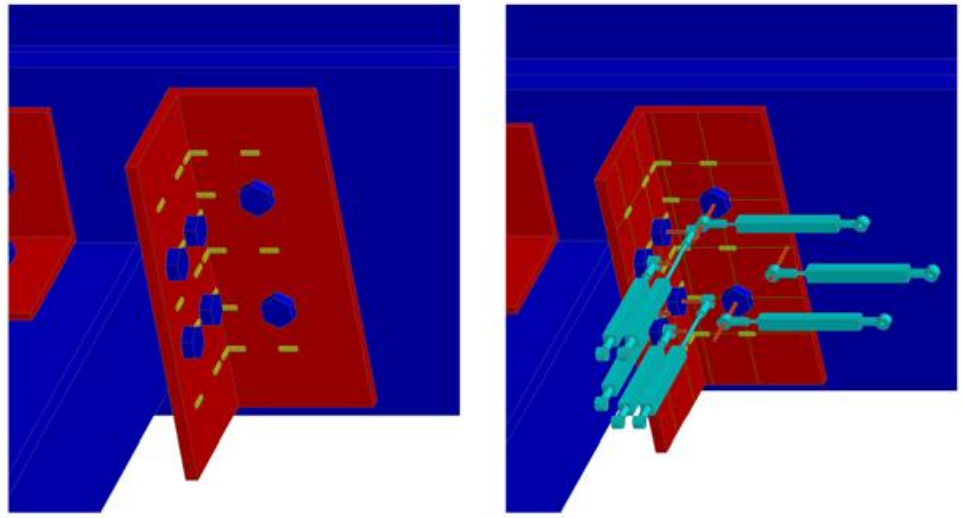
SHEET NOTES:

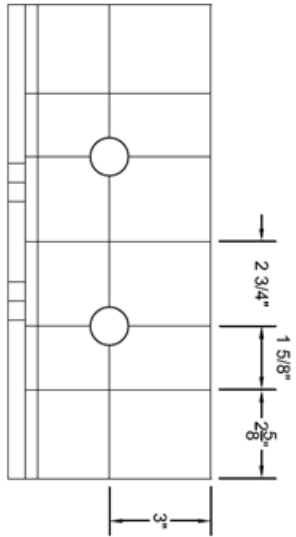
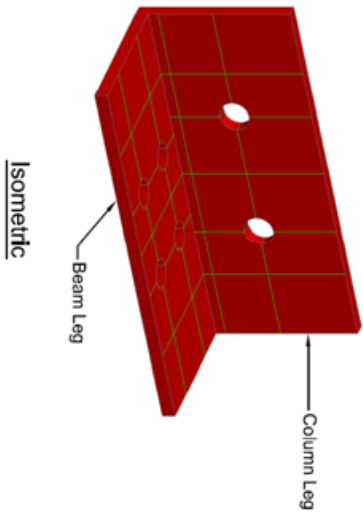
Label	Installed By	Checked By
1-SG-TA-CF-41	Joe	
1-SG-TA-CF-42	Joe	
1-SG-TA-CF-43	Joe	
1-SG-TA-CF-44	Joe	
1-SG-TA-CF-45	Joe	
1-SG-TA-CF-46	DJB	
1-SG-TA-CF-47	DJB	
1-SG-TA-CF-48	DJB	
1-SG-TA-BF-49	DJB	
1-SG-TA-BF-50	Not Installed	
1-SG-TA-BF-51	DJB	
1-SG-TA-BF-52	Not Installed	
1-SG-TA-BF-53	DJB	
1-SG-TA-BF-54	DJB	
1-SG-TA-BF-55	DJB	
1-SG-TA-BF-56	DJB	
1-SG-TA-BF-57	DJB	
1-SG-TA-BF-58	DJB	
1-SG-TA-BF-59	DJB	
1-SG-TA-BF-60	DJB	
1-SG-TA-BF-61	DJB	
1-LP-TA-BF-68	DJB	
1-LP-TA-BF-69	DJB	
1-LP-TA-CF-62	DJB	
1-LP-TA-CF-63	DJB	
1-LP-TA-CF-64	DJB	
1-LP-TA-BF-65	DJB	
1-LP-TA-BF-66	DJB	
1-LP-TA-BF-67	DJB	

As Built:  
 TA Cover Page

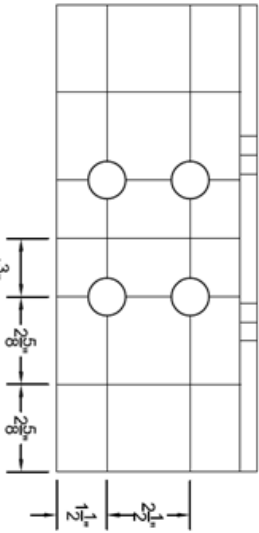
SHEET NO.:

**15 of 26**





Column Leg



Beam Leg



Mid-America Engineering Center  
 MID-AMERICA EASTTOWAEE  
 CENTER FOR BUILDINGS  
 UNIVERSITY OF ILLINOIS  
 URBANA-CHAMPAIGN  
 1241 Newmark Civil Engineering Lab  
 205 S. Mathews Avenue, Urbana, IL  
 61801

BEAM-COLUMN  
 TESTS  
 (LARGE-SCALE)

SHEET NOTES:

1. Each reference lines on angles.

NO.	DESCRIPTION	DATE	BY

SCALE DRAWING Dwg  
 REVISED DATE  
 PROJECT NO. MAE-SY-01  
 PROJECT TITLE

As Built:  
 Top Angle  
 Pre-Installation

SHEET NO.: **16 of 26**





MID-AMERICA EARTHQUAKE  
 CENTER  
 UNIVERSITY OF ILLINOIS  
 URBANA-CHAMPAIGN  
 1241 Newmark Civil Engineering Lab  
 205 S. Mathews Avenue, Urbana, IL  
 61801

**BEAM-COLUMN  
 TESTS  
 (LARGE-SCALE)**

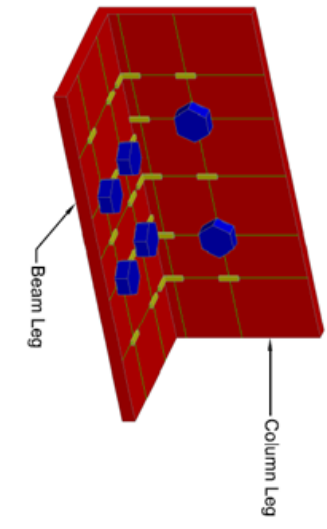
SHEET NOTES:

NO.	DESCRIPTION	DATE	BY

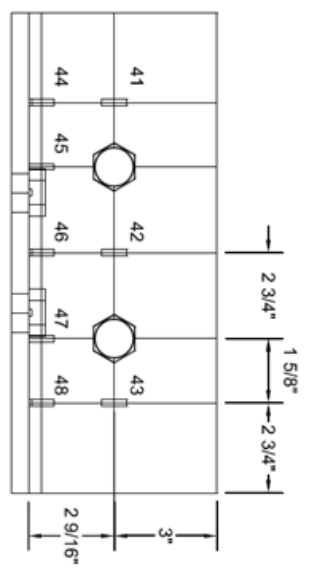
DESIGNED BY: DAB  
 DRAWN BY: DAB  
 CHECKED BY: NMS  
 SCALE: 1/2" = 1'-0"  
 PROJECT NO.: MAE-S3-01  
 PLOT TITLE:

As Built:  
 Top Angle Strain  
 Gauges

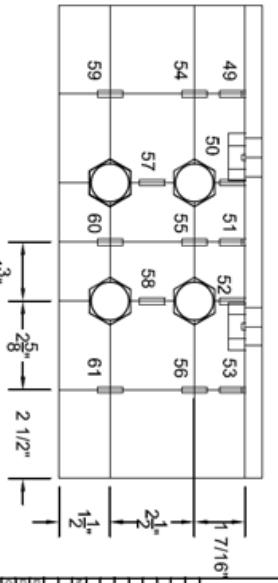
SHEET NO.:  
**17 of 26**



Isometric



Column Leg



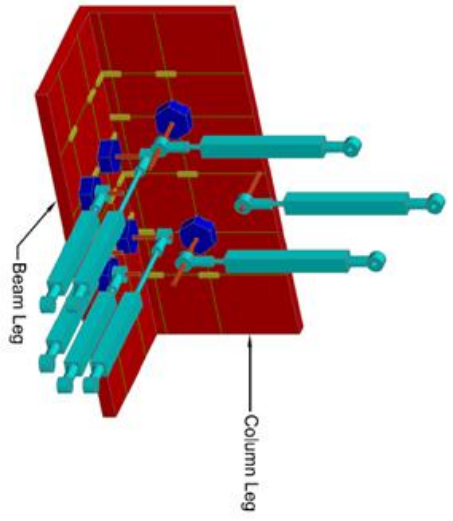
Beam Leg

Gauge Label	Physical Channel	SN
1-SG-TA-CF-41	SCIMod12/a17	YEFLLA
1-SG-TA-CF-42	SCIMod2/a11	YEFLLA
1-SG-TA-CF-43	SCIMod2/a12	YEFLLA
1-SG-TA-CF-44	SCIMod2/a13	YEFLLA
1-SG-TA-CF-45	SCIMod12/a16	YEFLLA
1-SG-TA-CF-46	SCIMod2/a15	YEFLLA
1-SG-TA-CF-47	SCIMod2/a16	YEFLLA
1-SG-TA-CF-48	SCIMod2/a17	YEFLLA
1-SG-TA-BF-49	SCIMod2/a18	YEFLLA
1-SG-TA-BF-50	SCIMod2/a19	YEFLLA
1-SG-TA-BF-51	SCIMod4/a123	YEFLLA
1-SG-TA-BF-52	SCIMod2/a111	YEFLLA
1-SG-TA-BF-53	SCIMod2/a112	YEFLLA
1-SG-TA-BF-54	SCIMod2/a113	YEFLLA
1-SG-TA-BF-55	SCIMod2/a114	YEFLLA
1-SG-TA-BF-56	SCIMod2/a115	YEFLLA
1-SG-TA-BF-57	SCIMod2/a116	YEFLLA
1-SG-TA-BF-58	SCIMod2/a117	YEFLLA
1-SG-TA-BF-59	SCIMod2/a118	YEFLLA
1-SG-TA-BF-60	SCIMod2/a119	YEFLLA
1-SG-TA-BF-61	SCIMod2/a120	YEFLLA

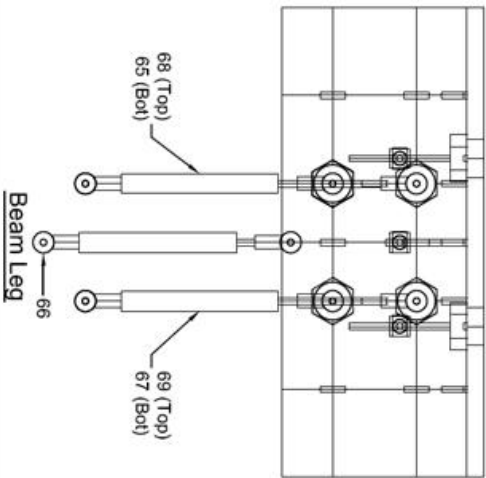
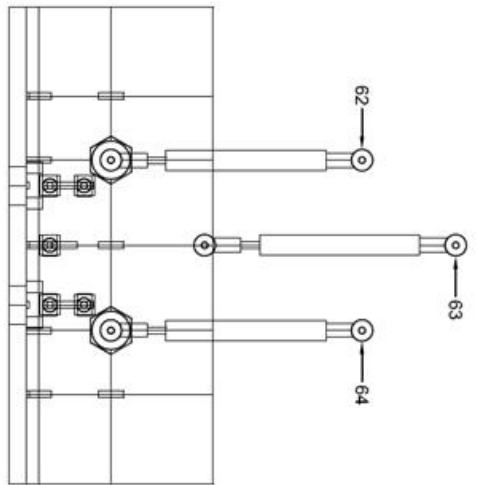
Not Used

Not Used





**Isometric**



Gauge Label	Physical Channel	Serial Number
1-LP-TA-BF-68	SC2Mod1/a6	12312147
1-LP-TA-BF-69	SC2Mod1/a7	A4006-41
1-LP-TA-CF-62	SC2Mod1/a4	12312143
1-LP-TA-CF-63	SC2Mod1/a5	A4006-28
1-LP-TA-CF-64	SC2Mod1/a6	A4006-10
1-LP-TA-BF-65	SC2Mod1/a7	A4006-11
1-LP-TA-BF-66	SC2Mod1/a8	A4006-27
1-LP-TA-BF-67	SC2Mod1/a9	A4006-42



Mid-America Earthquake Center  
 MID-AMERICA EARTHQUAKE CENTER  
 UNIVERSITY OF ILLINOIS  
 URBANA-CHAMPAIGN  
 1241 Sennock Civil Engineering Lab  
 205 N. Mathews Avenue, Urbana, IL 61801

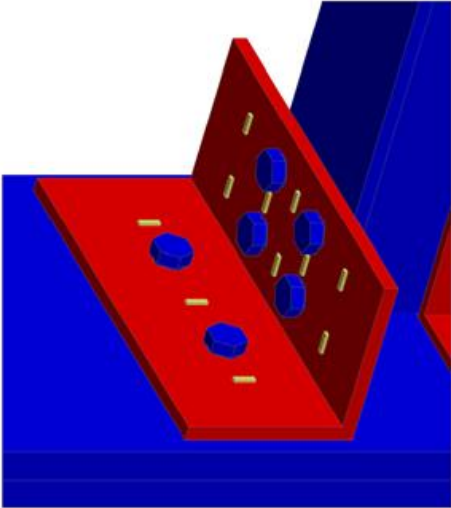
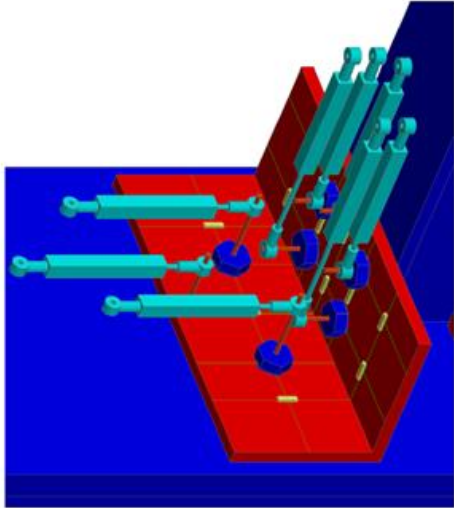
**BEAM-COLUMN TESTS (LARGE-SCALE)**

**SHEET NOTES:**

NO.	DESCRIPTION	DATE	BY

DESIGNED BY: DAB  
 DRAWN BY: DAB  
 CHECKED BY: HNM  
 SCALE: NYS  
 DATE: 07/29/09  
 PROJECT NO: MAE-SV-01  
 SHEET TITLE: **As Built: Top Angle Linear Poir**

SHEET NO.: **18 or 26**



Label	Installed By	Checked By
1-SG-SA-CF-70	AEM	
1-SG-SA-CF-71	AEM	
1-SG-SA-CF-73	AEM	
1-SG-SA-BF-74	Joe	
1-SG-SA-BF-75	Joe	
1-SG-SA-BF-76	Joe	
1-SG-SA-BF-77	Joe	
1-SG-SA-BF-78	Joe	
1-SG-SA-BF-79	Joe	
1-SG-SA-BF-80	Joe	
1-SG-SA-BF-81	Joe	
1-LP-SA-BF-87	Joe	
1-LP-SA-BF-88	Joe	
1-LP-SA-BF-84	Joe	
1-LP-SA-BF-85	Joe	
1-LP-SA-BF-86	Joe	
1-LP-SA-CF-82	Joe	
1-LP-SA-CF-83	Joe	
1-LP-SA-CF-xx	Joe	

Mid-America Earthquake Center  
 MID-AMERICA EARTHQUAKE  
 CENTER  
 UNIVERSITY OF ILLINOIS  
 URBANA-CHAMPAIGN  
 1341 Research Civil Engineering Hall  
 205 N. Mathews Avenue, Urbana, IL  
 61801

**BEAM-COLUMN TESTS (LARGE-SCALE)**

REVISIONS

NO.	DESCRIPTION	DATE

DESIGNED BY: DJB  
 DRAWING BY: AEM  
 CHECKED BY: HNM  
 SCALE: NTS  
 DATE: 07/28/09  
 PROJECT NO.: WAE-S1-01  
 SHEET TITLE: SA Cover Page

As Built: SA Cover Page

SHEET NO:



Mid-America Earthquake Center  
 MID-AMERICA EARTHQUAKE  
 CENTER  
 UNIVERSITY OF ILLINOIS  
 URBANA-CHAMPAIGN  
 1241 Newmark Civil Engineering Lab  
 205 N. Mathews Avenue, Urbana, IL  
 61801

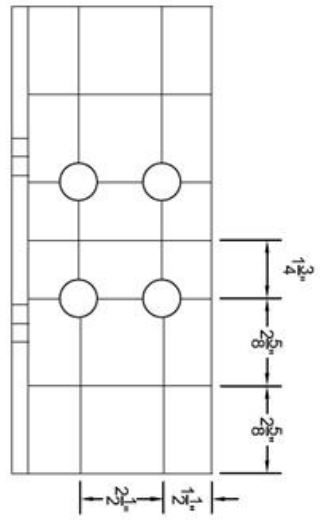
**BEAM-COLUMN  
 TESTS  
 (LARGE-SCALE)**

SHEET NUMBER:

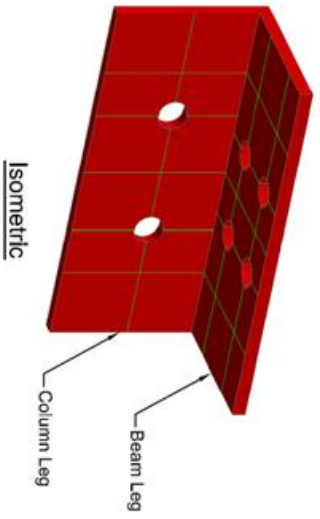
NO.	DESCRIPTION	DATE

DESIGNED BY: D.L.B.  
 DRAWN BY: D.L.B.  
 CHECKED BY: H.M.P.  
 DATE: 07/28/99  
 PROJECT NO.: MAE-SY-01  
 SHEET TITLE:  
**As Built:  
 Seat Angle  
 Pre-Installation**

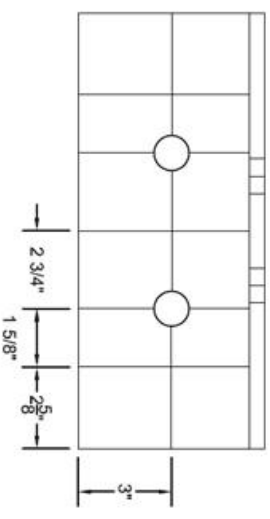
SHEET NO.:  
**20 of 26**



**Beam Leg**



**Isometric**



**Column Leg**

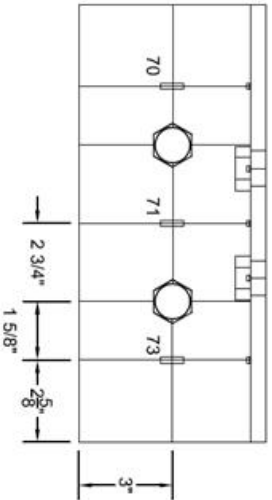
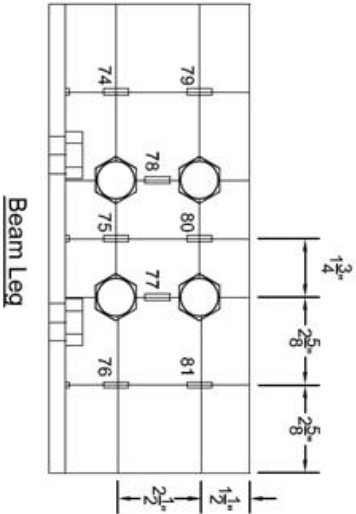
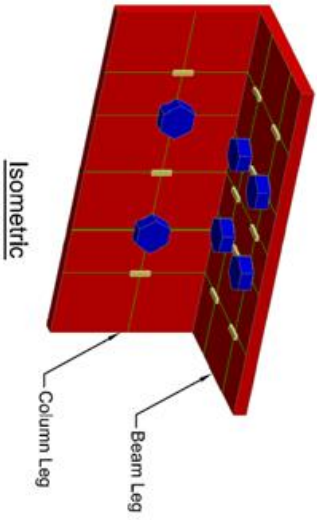


Mid-America Earthquake Center  
 MID-AMERICA EARTHQUAKE  
 CENTER  
 UNIVERSITY OF ILLINOIS  
 URBANA-CHAMPAIGN  
 1241 Newmark Civil Engineering Lab  
 208 S. Mathews Avenue, Urbana, IL  
 61801

**BEAM-COLUMN  
 TESTS  
 (LARGE-SCALE)**

SHEET NOTES:

Gauge Label	Physical Channel	Type
1-SG-SA-CF-70	SC1Mod9/a10	YEFLA
1-SG-SA-CF-71	SC1Mod9/a11	YEFLA
1-SG-SA-CF-73	SC1Mod9/a12	YEFLA
1-SG-SA-BF-74	SC1Mod9/a3	YEFLA
1-SG-SA-BF-75	SC1Mod9/a4	YEFLA
1-SG-SA-BF-76	SC1Mod9/a5	YEFLA
1-SG-SA-BF-77	SC1Mod9/a6	YEFLA
1-SG-SA-BF-78	SC1Mod9/a10	YEFLA
1-SG-SA-BF-79	SC1Mod9/a11	YEFLA
1-SG-SA-BF-80	SC1Mod9/a12	YEFLA
1-SG-SA-BF-81	SC1Mod9/a13	YEFLA



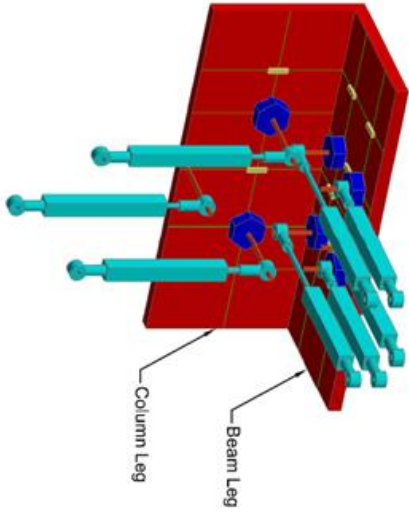
NO.	DESCRIPTION	DATE	BY

DESIGNED BY: DJB  
 DRAWN BY: DMB  
 CHECKED BY: NNS  
 SCALE: 07/28/09  
 PROJECT NO.: MAE-SY-01  
 SHEET TITLE:

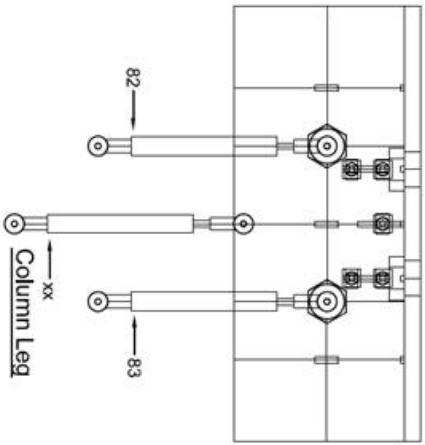
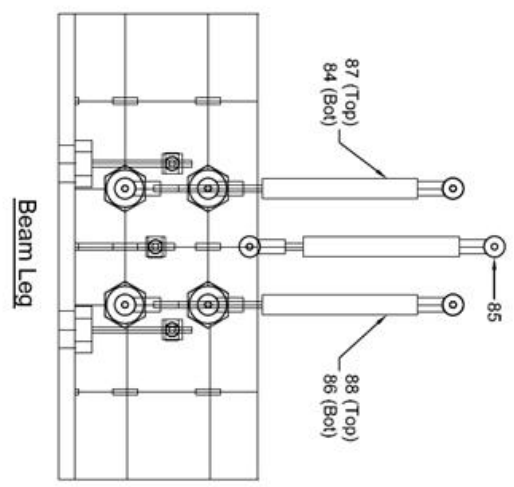
As Built  
 Seat Angle Strain  
 Gauges

SHEET NO.:

**21 of 26**



Isometric



Gauge Label	Physical Channel	Serial Number
1-1-P-SA-BF-87	SC1Mod1/a18	A4006-5
1-1-P-SA-BF-88	SC1Mod1/a19	A4006-29
1-1-P-SA-BF-84	SC1Mod1/a10	A4006-43
1-1-P-SA-BF-85	SC1Mod1/a11	A4006-18
1-1-P-SA-BF-86	SC1Mod1/a12	A4006-44
1-1-P-SA-CF-82	SC2Mod1/a10	12312159
1-1-P-SA-CF-83	SC2Mod1/a11	A4006-35
1-1-P-SA-CF-xx	SC2Mod1/a111	A4006-34



Field Advanced Composites Center  
 MID-AMERICA EASTERN  
 CENTER  
 UNIVERSITY OF ILLINOIS  
 LIBRARY-CALAMBOUS  
 1241 Newark City Engineering Lab  
 205 S. Mathews Avenue, Champaign, IL  
 61801

**BEAM-COLUMN TESTS (LARGE-SCALE)**

SHEET NUMBER

NO.	DESCRIPTION	DATE	BY

DESIGNED BY	DAB
ENGINEER	DAB
CHECKED BY	NND
DATE	07/28/09
PROJECT NO.	MAE-SY-01
SHEET TITLE	

As Built:  
 Seat Angle Linear  
 Pots

SHEET NO.:  
**22 of 26**



Multi-Axis Seismic Center  
 UNIVERSITY OF ILLINOIS  
 URBANA-CHAMPAIGN  
 1241 Kenneth Civil Engineering Lab  
 205 N. Mathews Avenue, Urbana, IL  
 61801

**BEAM-COLUMN  
 TESTS  
 (LARGE-SCALE)**

SHEET NOTES

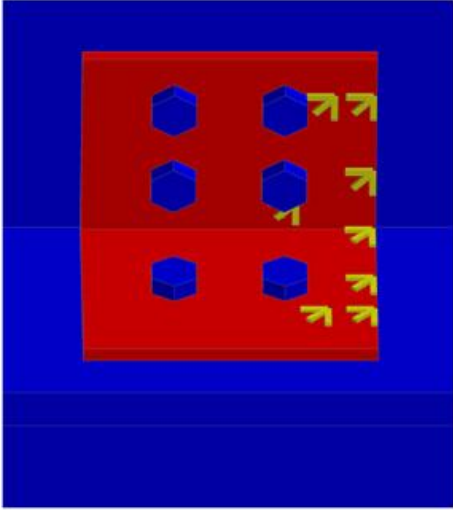
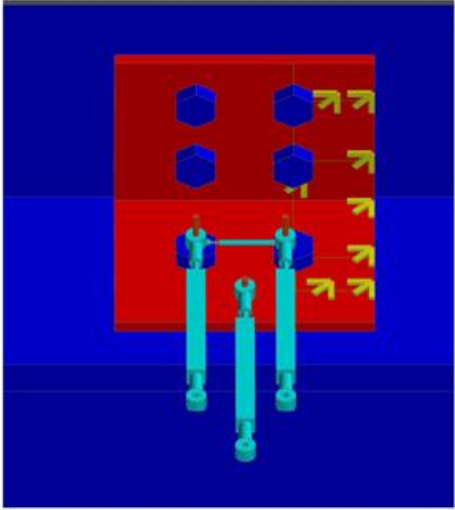
REV.	DESCRIPTION	DATE	BY

DESIGNED BY: DJB  
 DRAWN BY: ALM  
 CHECKED BY: TMM  
 DATE: 01/23/09  
 PROJECT NO.: WAE SV-CI  
 SHEET TITLE:

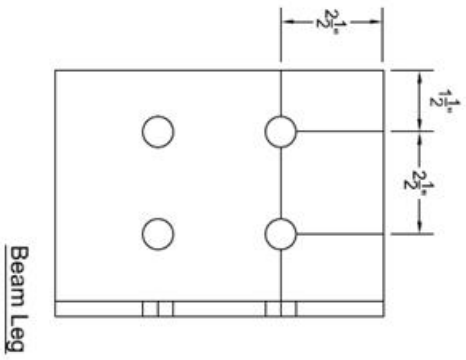
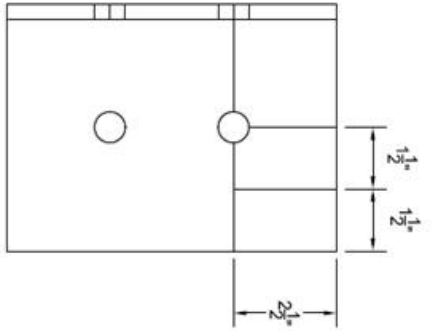
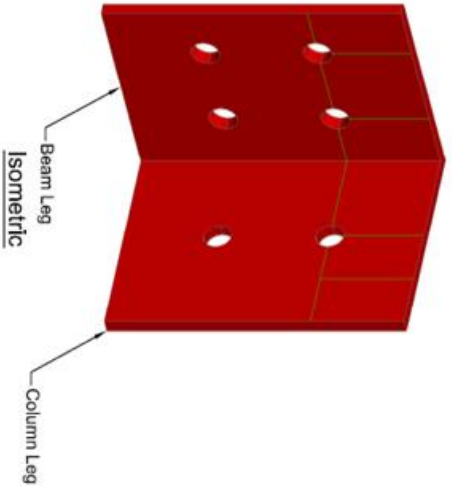
As Built:  
 BWA Cover Page

SHEET NO.:

**23 of 26**



Label	Installed By	Checked By
1-SG-BWA-BW-H-135	DJB	Dead
1-SG-BWA-BW-D-136	DJB	
1-SG-BWA-BW-V-137	DJB	
1-SG-BWA-CF-V-139	DJB	
1-SG-BWA-CF-D-140	DJB	
1-SG-BWA-CF-H-141	DJB	
1-SG-BWA-CF-V-142	DJB	
1-SG-BWA-CF-D-143	DJB	
1-SG-BWA-CF-H-144	DJB	
1-SG-BWA-CF-V-145	DJB	
1-SG-BWA-CF-D-146	DJB	
1-SG-BWA-CF-H-147	DJB	
1-SG-BWA-CF-V-148	DJB	
1-SG-BWA-CF-D-149	DJB	
1-SG-BWA-CF-H-150	DJB	
1-SG-BWA-BW-H-151	DJB	
1-SG-BWA-BW-D-152	DJB	
1-SG-BWA-BW-V-153	DJB	
1-SG-BWA-BW-H-154	DJB	
1-SG-BWA-BW-D-155	DJB	
1-SG-BWA-BW-V-156	DJB	
1-SG-BWA-BW-H-157	DJB	
1-SG-BWA-BW-D-158	DJB	
1-SG-BWA-BW-V-159	DJB	
1-LP-BWA-CF-124	DJB	
1-LP-BWA-CF-125	DJB	
1-LP-BWA-CF-126	DJB	
1-LP-BWA-CF-160	DJB	



MID-AMERICA EARTHQUAKE CENTER  
 UNIVERSITY OF ILLINOIS  
 ENGINEERING COLLEGE  
 1241 Newman Civil Engineering Lab  
 205 N. Mathews Avenue, Urbana, IL  
 61801

BEAM-COLUMN  
 TESTS  
 (LARGE-SCALE)

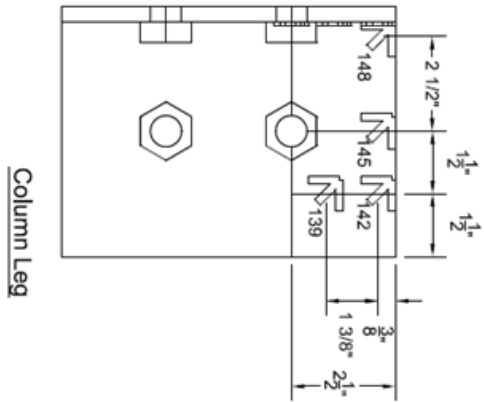
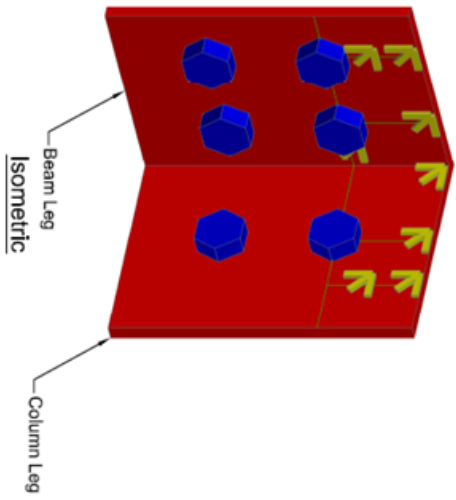
SHEET NUMBER

NO.	DESCRIPTION	DATE	BY

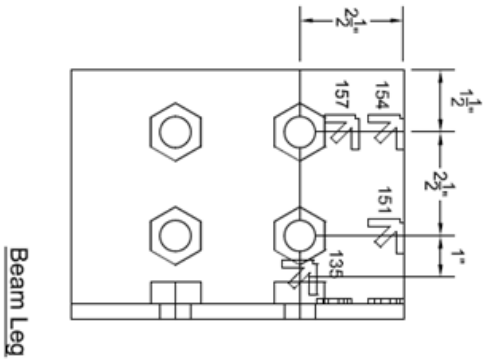
DESIGNED BY:	D.A.R.
CHECKED BY:	D.A.R.
DRAWN BY:	W.M.
SCALE:	N.T.S.
DATE:	07/28/09
PROJECT NO.:	MAE-SY-01
SHEET TITLE:	

As Built:  
 Back Web Angle  
 Pre-Installation

SHEET NO: 24 of 26



Gauge Label	Physical Channel	Type
1-56-BWA-BW-H-135	SC1Mod3/a19	YEFRA
1-56-BWA-BW-D-136	SC1Mod3/a11	
1-56-BWA-BW-V-137	SC1Mod3/a12	
1-56-BWA-CF-V-139	SC1Mod3/a13	YEFRA
1-56-BWA-CF-D-140	SC1Mod3/a14	
1-56-BWA-CF-H-141	SC1Mod3/a15	YEFRA
1-56-BWA-CF-V-142	SC1Mod3/a15	
1-56-BWA-CF-H-144	SC1Mod3/a17	
1-56-BWA-CF-V-145	SC1Mod3/a19	YEFRA
1-56-BWA-CF-D-146	SC1Mod3/a10	
1-56-BWA-CF-H-147	SC1Mod3/a11	
1-56-BWA-CF-V-148	SC1Mod3/a12	YEFRA
1-56-BWA-CF-D-149	SC1Mod3/a13	
1-56-BWA-BW-H-151	SC1Mod3/a15	YEFRA
1-56-BWA-BW-D-152	SC1Mod3/a16	
1-56-BWA-BW-H-153	SC1Mod3/a17	YEFRA
1-56-BWA-BW-V-154	SC1Mod3/a18	
1-56-BWA-BW-D-155	SC1Mod3/a19	YEFRA
1-56-BWA-BW-V-156	SC1Mod3/a20	
1-56-BWA-BW-H-157	SC1Mod3/a21	YEFRA
1-56-BWA-BW-D-158	SC1Mod3/a22	
1-56-BWA-BW-V-159	SC1Mod3/a23	



Madhavaiah Engineering Center  
 MADHAVIAH ENGINEERING  
 COLLEGE  
 UNIVERSITY OF ENGINEERS  
 (UENR) AND ARCHITECTS  
 1241 Newmark Civil Engineering Lab  
 205 S. Mathews Avenue, Urbana, IL  
 61801

**BEAM-COLUMN  
 TESTS  
 (LARGE-SCALE)**

SHEET NUMBER

NO.	DESCRIPTION	DATE	BY

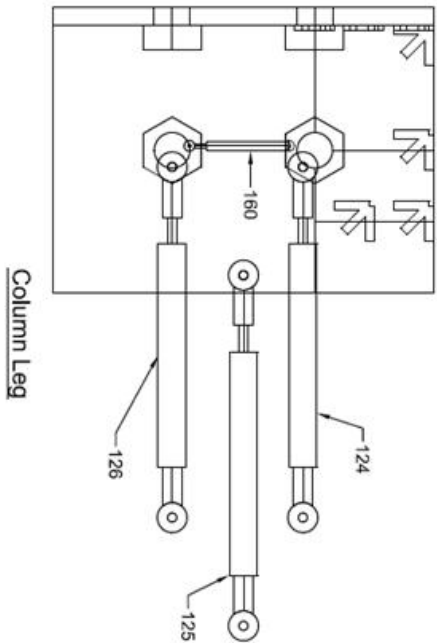
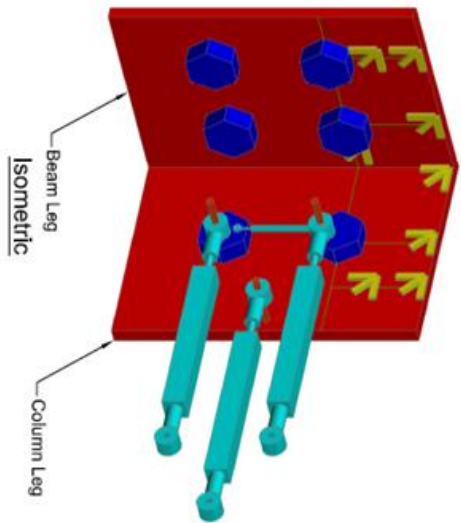
APPROVED BY: DAB  
 DRAWN BY: DAB  
 CHECKED BY: TMM  
 SCALE: 1/8" = 1'-0"  
 DATE: 07/28/09  
 PROJECT NO.: MAE-SY-01  
 SHEET TITLE:

As Built:  
 Back Web Angle  
 Strain Gauges

SHEET NO.:

25 OF 26

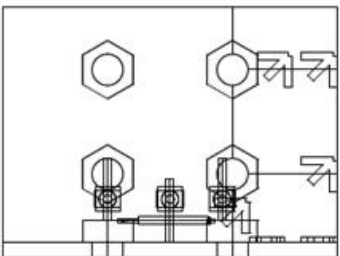




Gauge Label	Physical Channel	Serial Number
1-LP-BWA-CF-124	SC1Mod1/a120	L0206/72
1-LP-BWA-CF-125	SC1Mod1/a121	A4006-30
1-LP-BWA-CF-126	SC1Mod1/a122	L0206/50

Gauge Location on Diagram	Physical Channel	Model Number	Serial Number
1-LP-BWA-CF-160	SC2Mod7/a10	CD 375-50	4



Mid-America Engineering Center  
 MID-AMERICA ENGINEERING CENTER  
 UNIVERSITY OF ILLINOIS  
 URBANA-CHAMPAIGN  
 1241 Weirick Civil Engineering Lab  
 205 N. Mathews Avenue, Urbana, IL  
 61801

**BEAM-COLUMN TESTS (LARGE-SCALE)**

**SHEET METRIC:**  
 1. Linear pots 124, 125, and 126 will not fit on the column flange, as shown in isometric view. Clamp plate to the column to attach the linear pots.

NO.	DESCRIPTION	DATE	BY

DESIGNED BY:	D-AB
ENGINEER BY:	D-AB
CHECKED BY:	H-MM
SCALE:	NTS
DATE:	07/28/09
PROJECT NO.:	MAE-3V-01
DRAWING TITLE:	

As Built:  
 Back Web Angle  
 Linear Pots

SHEET NO: **26 of 26**



Mid-America Earthquake Center  
 MID-AMERICA EARTHQUAKE  
 CENTER  
 UNIVERSITY OF ILLINOIS  
 URBANA-CHAMPAIGN  
 1241 Kenneth C. Child Engineering Lab  
 205 N. Mathews Avenue, Urbana, IL  
 61801

**BEAM-COLUMN  
 TESTS  
 (LARGE-SCALE)**

SHEET WORKS

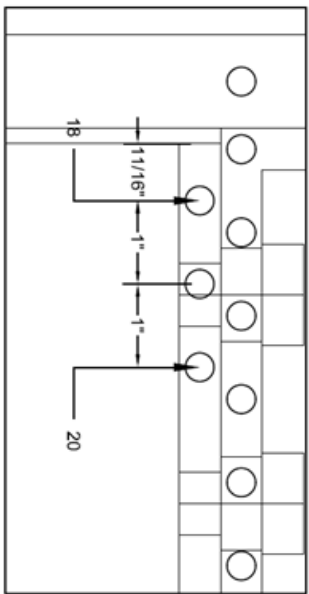
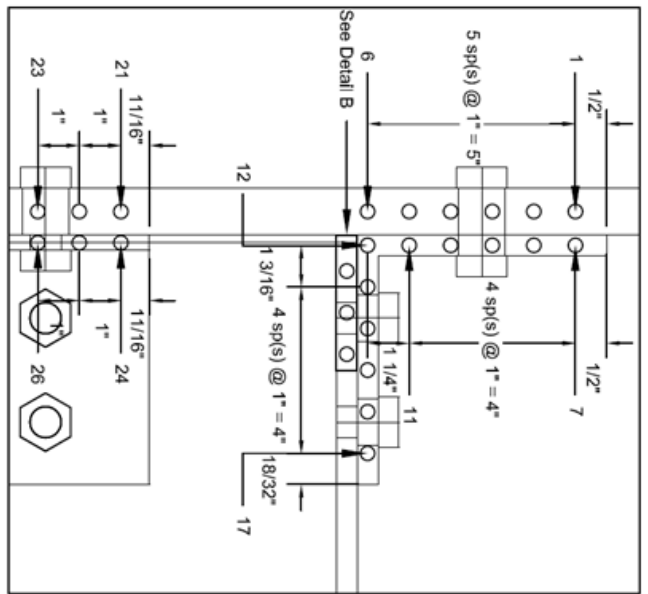
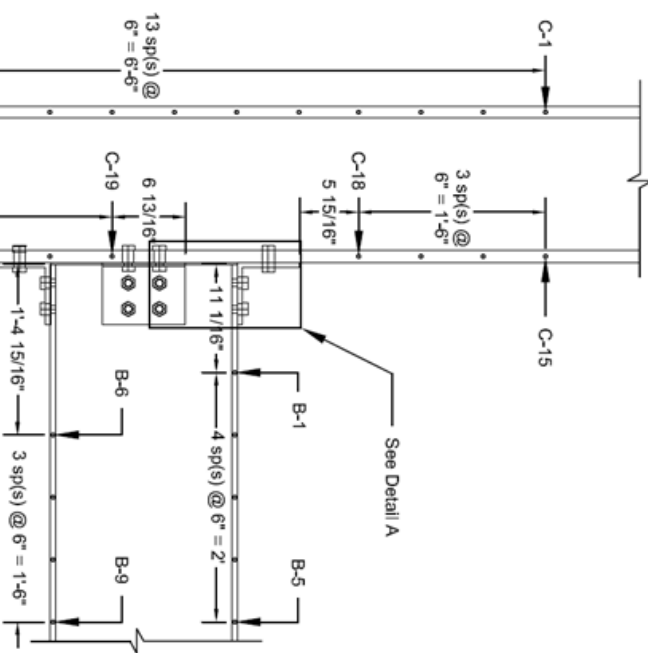
NO.	DESCRIPTION	DATE	BY

DESIGNED BY: T.S.B.  
 DRAWN BY: A.E.W.  
 CHECKED BY: B.J.S.  
 DATE: 07/27/09  
 PROJECT NO.: WAE SYC-01  
 SHEET TITLE:

As Built:  
 Krypton LEDs

SHEET NO.:

**Appendix**





Mid-America Engineering Center  
 MID-AMERICA ENGINEERING  
 UNIVERSITY OF ILLINOIS  
 URBANA-CHAMPAIGN  
 1241 Newark Civil Engineering Lab  
 205 N. Mathews Avenue, Urbana, IL  
 61801

**BEAM-COLUMN TESTS (LARGE-SCALE)**

SHEET METRIC

LED NO.	BOX NO.	BOX TERMINALS	KRYPTON CHANNELS
1	3	1	3.7
2	3	2	3.8
3	3	3	3.9
4	3	4	3.10
5	3	5	3.11
6	3	6	3.12
7	3	7	3.13
8	3	8	3.14
9	3	9	3.15
10	3	10	3.16
11	3	11	3.17
12	3	12	3.18
13	3	13	3.19
14	3	14	3.20
15	3	15	3.21
16	3	16	3.22
17	3	17	3.23
18	3	18	3.24
19	3	19	3.25
20	3	20	3.26
21	4	1	3.2
22	5	2	3.6
23	5	3	3.4
24	4	4	3.1
25	4	5	3.3
26	5	6	3.5
C1	1	1	3.47
C2	1	2	3.48
C3	1	3	3.49
C4	1	4	3.50

[ 3 . 27 - 3 . 35 ] - NULL CHANNELS

LED NO.	BOX NO.	BOX TERMINALS	KRYPTON CHANNELS
C5	1	5	3.51
C6	1	6	3.52
C7	1	7	3.53
C8	1	8	3.54
C9	1	9	3.55
C10	1	10	3.56
C11	1	11	3.57
C12	1	12	3.58
C13	1	13	3.59
C14	1	14	3.60
C15	2	11	3.37
C16	2	12	3.38
C17	2	13	3.39
C18	2	14	3.40
C19	2	15	3.41
C20	2	16	3.42
C21	2	17	3.43
C22	2	18	3.44
C23	2	19	3.45
C24	2	20	3.46
C25	2	10	3.36
B1	6	1	4.1
B2	6	2	4.2
B3	6	3	4.3
B4	6	4	4.4
B5	6	5	4.5
B6	6	6	4.5
B7	6	7	4.7
B8	6	8	4.8
B9	6	9	4.9

1 BOX - LEFT COLUMN  
 2 BOX - TOP RIGHT COLUMN  
 3 BOX - MIDDLE RIGHT COLUMN

4 BOX - RIGHT-TAPED BOTTOM RIGHT COLUMN  
 5 BOX - LEFT-TAPED BOTTOM RIGHT COLUMN  
 6 BOX - BACK OF COLUMN

As Built  
 Krypton LEDs  
 (location)

**Appendix 2**

SHEET NO.:  
 DATE:  
 PROJECT NO.:  
 DRAWING NO.:  
 SCALE: 1/8" = 1'-0"